Exponential asymptotics of parasitic capillary ripples and the complication of divergent eigenvalues

submitted by

Josh Shelton

for the degree of Doctor of Philosophy

of the

University of Bath

Department of Mathematical Sciences

December 2022


Department of
Mathematical
Sciences

DECLARATION OF ANY PREVIOUS SUBMISSION OF THE WORK

The material presented here for examination for the award of a higher degree by research has not been incorporated into a submission for another degree.

Signature of author: ....

Josh Shelton

DECLARATION OF AUTHORSHIP

I am the author of this thesis, and the work described therein was carried out by myself personally with the exception of the following sections

Chapter 3 contains a *Journal of Fluid Mechanics* article by myself, Paul Milewski, and Philippe H. Trinh.

Chapter 4 contains a *Journal of Fluid Mechanics* article by myself and Philippe H. Trinh.

Chapter 6 contains an accepted article in the *Journal of Fluid Mechanics* by myself and Philippe H. Trinh.

Chapter 7 is a to-be-submitted pre-print by myself, S. Jonathan Chapman, and Philippe H. Trinh.

Chapter 8 is a to-be-submitted pre-print by myself, Stephen D. Griffiths, S. Jonathan Chapman, and Philippe H. Trinh.

Signature of author: ....

Josh Shelton

Abstract

Many problems across fluid dynamics include effects that are exponentially small as certain parameters tend to zero. These may be visible features in the solution profiles, or solvability conditions which are obtained only when the exponentially-small components of the mathematical formulation are considered. The techniques required for the resolution of these features are known as *exponential asymptotics*.

In this thesis, special attention is placed on the limits of small surface tension and weak shear. Many physically-occurring water waves exist in the regime of small surface tension. We focus on the ideal formulation of an inviscid, irrotational, and incompressible fluid. In this formulation, the limit of small surface tension is a singular perturbative problem as the order of the governing equations differs from that found in the absence of surface tension. This is a sign that crucial exponentially small effects may appear under this limit. Numerical investigations are performed for both steadily-travelling waves and time-dependent standing waves. In fixing the energy of these waves to be large, such that their solution profiles are highly nonlinear, exponentially small *parasitic ripples* are observed in the solution profile. In both of these cases, we characterise the bifurcation space that emerges. These parasitic capillary ripples are derived asymptotically for the steadily travelling solutions; in addition to describing these using exponential asymptotic techniques, a solvability condition is also derived.

The second limit of physical importance considered in this thesis is that of weak shear, which we consider for the equatorial Kelvin wave. We demonstrate analytically that the exponentially-small component of the eigenvalue of this problem is imaginary. This is an exponentially small instability, as the imaginary component of the eigenvalue destabilises the travelling wave.

The results contained within this thesis mark a significant milestone in our understanding of exponentially-small effects in water waves, both for surface waves in low-surface tension regimes for which we have uncovered delicate structures of solutions, and geophysical waves that are destabilised by the inclusion of weak shear.

CONTENTS

INTRODUCTION

I

1.1 Summary of thesis

We begin in **Chapter 2** with an overview of the methods in exponential asymptotics that will be used and extended upon throughout this thesis. These techniques are used to determine the exponentially-small component of the asymptotic solution of various water wave problems. These exponentially small components of the asymptotic solution correspond to many of the physical effects that we seek to describe, such as high-frequency parasitic ripples in steady and unsteady water waves studied in **Part I**, and geophysical instabilities considered in **Part II**.

Part I

This first part of the thesis is motivated by the high-frequency parasitic capillary ripples that are observed experimentally to form on steep travelling water waves. We focus on the parasitic ripples which emerge on the free surface of an inviscid, irrotational, and incompressible fluid. These are studied both numerically, to classify the resultant solutions that emerge, and analytically to derive these exponentially-small effects. Fundamental issues arising from the works of Longuet-Higgins (1963), Chen and Saffman (1979), and Chen and Saffman (1980), concerning the limit of small surface tension, are resolved.

Chapter 3 contains the work of Shelton et al. (2021), in which the numerical bifurcation structure of steadily travelling gravity-capillary waves is calculated. The fluid surface, $y = \zeta(x)$, is specified by Bernoulli's equation, which demands that

$$\frac{F^2}{2}(\phi_x^2 + \phi_y^2) + y - B\frac{\zeta_{xx}}{(1+\zeta_x^2)^{\frac{3}{2}}} = 0,$$

where the Bond number, B, and Froude number, F, are constants, and ϕ is the velocity potential.

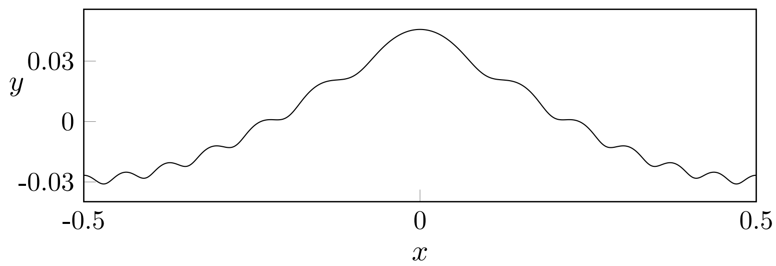

Figure 1.1: A numerical solution of the steady gravity-capillary wave equations is shown. This free surface $y = \zeta(x)$ has the values of $B = 00227$ and $F = 0.4299$.

It is demonstrated that the solutions associated with the (B, F) bifurcation space contain highly-oscillatory parasitic ripples, as shown in figure 1.1, whose amplitude is exponentially small in the surface tension parameter, B. This is the first work that has clarified the complex bifurcation structure at small values of the Bond number.

Chapter 4 contains the work by Shelton and Trinh (2022), in which steady gravity capillary waves are considered analytically. Asymptotic solutions are found for small surface tension, and these contain parasitic ripples whose amplitude,

$$y_{ripples} = O\big(\mathrm{e}^{-\chi/B}\big),$$

is exponentially small as $B \to 0$. This exponential scaling is shown in figure 1.2. Their derivation requires the use of exponential asymptotics and the understanding

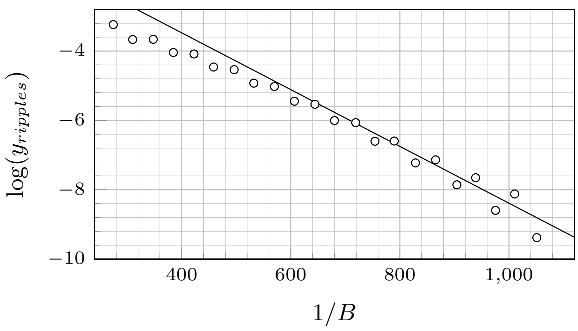

Figure 1.2: The exponential scaling of the parasitic ripple amplitude is shown for the numerical solutions of chapter 3 (circles) and the analytical prediction of chapter 4 (line).

of singularities in the analytic continuation of the leading order solution, a travelling gravity wave.

Chapter 5 considers the numerical bifurcation structure of gravity capillary standing waves. These are time-dependent water waves that oscillate vertically, whose free surface, $y = \zeta(x,t)$, is characterised by Bernoulli's equation

$$F^2\phi_t + \frac{F^2}{2}(\phi_x^2 + \phi_y^2) + y - B\frac{\zeta_{xx}}{(1+\zeta_x^2)^{\frac{3}{2}}} = 0,$$

such that the wave motion is temporally periodic in the interval between $t = 0$ and $t = 1$. The solution profiles contain high-frequency parasitic ripples, shown in

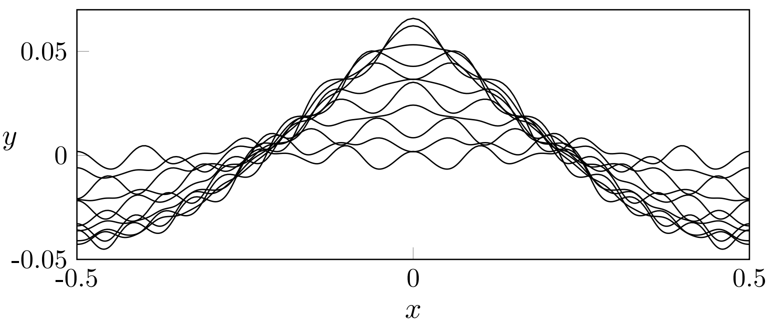

Figure 1.3: A gravity-capillary standing wave calculated numerically in chapter 5 is shown. This solution has $B = 0.002795$ and $F = 0.4161$.

figure 1.3, that visually appear to be a perturbation about the $B = 0$ standing gravity wave. the asymptotic scaling of these ripples is likely to be exponentially small as $B \to 0$.

Chapter 6 contains a pre-print by Shelton & Trinh, in which free surface waves with underlying point vortices are studied asymptotically in the low-speed limit. The vorticity is located at a single point, near to which the complex potential $f = \phi + \mathrm{i}\psi$ behaves as

$$f \sim z - \frac{\mathrm{i}\Gamma}{2\pi} \log{(z - z^*)},$$

where $z = x + \mathrm{i}y$. Here, z^* is the location of the vortex, and Γ is the circulation of the vortex. The asymptotic solutions contain high-frequency waves with an exponentially-small amplitude. The derivation of these is connected to singularities associated with the submerged point vortices. When only one submerged vortex is considered, waves in the free surface extend to the far field. For two vortices submerged at the same depth,

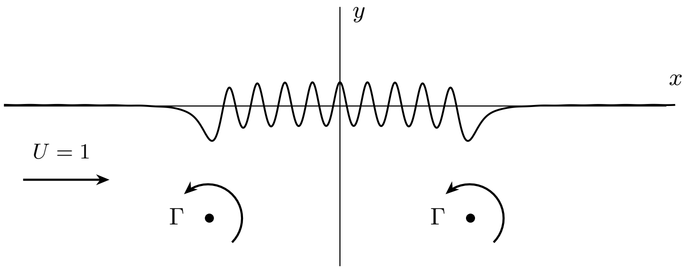

Figure 1.4: A free surface solution generated by two submerged vortices of circulation Γ is shown.

the far field oscillations produces by each vortex cancel for certain parameter values yielding trapped waves. A numerical trapped wave solution is shown in figure 1.4.

Part II

This second part of the thesis considers the weak shear limit of the equatorial Kelvin wave. This is a significant problem because while the equatorial Kelvin wave travels without change of form, the presence of a small amount of shear destabilises the travelling wave. This instability is exponentially small, and its resolution requires the use of exponential asymptotic techniques. This study is motivated by the divergent eigenvalue expansions encountered in part I, and we begin by studying this instability for a model equation before proceeding to the geophysical system.

Chapter 7 contains a pre-print by Shelton, Chapman, & Trinh, in which we study the exponential asymptotics of the Hermite-with-pole equation,

$$\frac{\mathrm{d}^2 u}{\mathrm{d}z^2} + \left[\frac{1}{z} - \lambda - \left(z - \frac{1}{\epsilon}\right)^2\right] u = 0,$$

as $\epsilon \to 0$. This linear second-order differential equation models the latitudinal shear perturbation of the equatorial Kelvin wave. In addition to the eigenfunction $u(z)$, whose asymptotic series diverges, the equation contains an eigenvalue, λ. It is demonstrated how the divergence of this eigenvalue may be captured through exponential asymptotic techniques. Furthermore, the imaginary component of the eigenvalue is shown to be exponentially small with respect to the weak shear. This component destabilises the travelling wave.

Chapter 8 contains a pre-print by Shelton, Griffiths, Chapman, & Trinh, where we study the exponentially small instability of the equatorial Kelvin wave for small latitudinal shear. In writing the solution as a travelling wave

$$u(x, y, t) = \mathrm{Re}\left[\hat{u}(y)\mathrm{e}^{\mathrm{i}k(x-ct)}\right],$$

the eigenvalue, c, contains an imaginary component given by

$$\mathrm{Im}[c] \sim \pm\frac{\mathrm{i}\epsilon^3}{4\sqrt{\pi}}\mathrm{e}^{-1/\epsilon^2}.$$

This is exponentially small as $\epsilon \to 0$, and corresponds to a growing temporal instability of the travelling solution, $u(x, y, t)$. This result is derived asymptotically with two different methods. First, the domain is restricted to real values $y \in \mathbb{R}$, for which the instability is derived by matched asymptotics performed between special function solutions. Secondly, the global behaviour is considered in the analytically continued domain $y \in \mathbb{C}$, for which the instability is derived through the application of exponential asymptotic techniques.

Appendices

Appendix A derives the time-dependent conformal map used for the numerical investigation of chapter 5.

Appendix B modifies the asymptotic work of chapter 4 to consider the late-term eigenvalue divergence for the small surface tension limit of gravity capillary waves.

Appendix C considers solitary waves in a three layer flow. Numerical solutions are found that, for certain parameter values, contain no oscillatory ripples. It is demonstrated, both numerically and analytically, that the magnitude of these ripples is algebraic with respect to the parameter distance in bifurcation space from a solution with no ripples.

2 Introduction to exponential asymptotics: the forced harmonic oscillator

2.1 Historical overview

Unsurprisingly, the *Stokes phenomenon* was first observed by George Gabriel Stokes (Stokes 1851, 1864). In his study of the Airy equation,

$$\frac{\mathrm{d}^2 u}{\mathrm{d}z^2} - 9zu = 0, \tag{2.1}$$

Stokes noted that one could solve this problem as a convergent series of the form

$$\begin{aligned} u(z) = A&\left(1 + \frac{9z^3}{2\cdot 3} + \frac{9^2 z^6}{2\cdot 3\cdot 5\cdot 6} + \cdots\right) \\ &+ B\left(z + \frac{9z^4}{3\cdot 4} + \frac{9^2 z^7}{3\cdot 4\cdot 6\cdot 7} + \cdots\right), \end{aligned} \tag{2.2}$$

where A and B are constants. Given a value of z, no matter how large in magnitude, (2.2) converges as the number of terms in the series increases. However, given the computational limitations of his time, this convergence was too slow and inspired Stokes to develop an alternative representation of the solution for large $|z|$, given by

$$\begin{aligned} u(z) = Cz^{-\frac{1}{4}}\mathrm{e}^{-2z^{3/2}}&\left(1 - \frac{5}{144 z^{3/2}} + \frac{5\cdot 7\cdot 11}{2\cdot 144^2 z^3} + \cdots\right) \\ + Dz^{-\frac{1}{4}}\mathrm{e}^{2z^{3/2}}&\left(1 + \frac{5}{144 z^{3/2}} + \frac{5\cdot 7\cdot 11}{2\cdot 144^2 z^3} + \cdots\right). \end{aligned} \tag{2.3}$$

From our modern understanding of asymptotic analysis, we recognise (2.3) as a divergent asymptotic series, for which a finite number of terms become more accurate under the limit of $|z| \to \infty$. Note that while C and D are constants, Stokes noted that they somehow must be discontinuous with respect to the domain to allow the asymptotic representation (2.3) to yield the same value upon rotation by $2\pi\mathrm{i}$. This apparent discontinuity is the Stokes phenomenon, which he verified to occur numerically through evaluation of the convergent series (2.2). Furthermore, this was justified by Stokes through the consideration of further terms of the series (2.3), in which consecutive terms may be approximately equal in magnitude as the number of them tends to infinity.

The contours across which this "discontinuous" change occurs are known as *Stokes lines*. Our modern understanding of the Stokes phenomenon stems from the work of Berry (1989), who demonstrated, by Borel resummation of the divergent expansion, that this change in fact occurs smoothly across a boundary layer of diminishing width under the asymptotic limit. This procedure is known as *Stokes smoothing*, the derivation of which relies on the understanding of the divergence of the late-terms of the asymptotic series pioneered by Dingle (1973). Throughout this thesis, we will derive the Stokes phenomenon through the application of matched asymptotic methods directly to the governing equations, which is analogous to the approach first considered by Olde Daalhuis et al. (1995).

2.2 The forced harmonic oscillator

We now provide a detailed introduction to the general procedures used in exponential asymptotics throughout this thesis. As an example, we study the forced harmonic oscillator,

$$\epsilon^2 u_{xx} - \epsilon u^2 + u = \mathrm{sech}(x), \tag{2.4a}$$

$$u(x) \sim A\cos\left(\frac{x}{\epsilon} + \delta\right) + 2\mathrm{e}^{x} \qquad \text{as } x \to -\infty, \tag{2.4b}$$

considered by Akylas and Yang (1995) and Grimshaw (2010) as a toy model for *generalised solitary waves*, which contain oscillations of finite amplitude in the far field. The solution, $u(x)$, is defined over the domain $-\infty < x < \infty$, and A and δ in (2.4b) are two specified real-valued constants. A typical asymptotic solution profile is shown in figure 2.1. As we shall demonstrate, high-frequency ripples appear in the

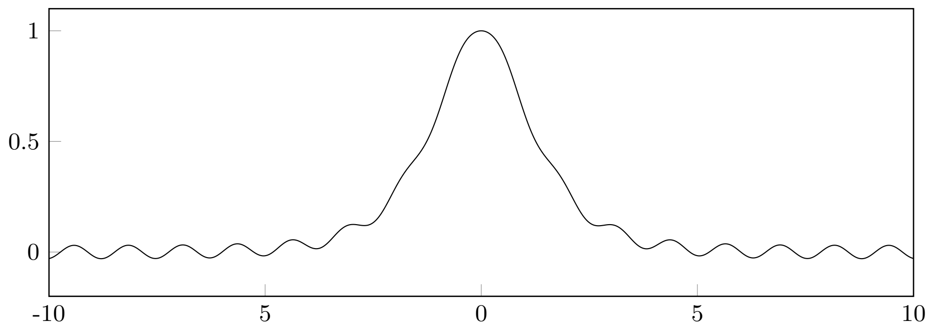

Figure 2.1: An asymptotic solution of equations (2.4a) and (2.4b), solved for in section 2.2.8, is shown for $\epsilon = 0.2$.

solution profile, and these are exponentially small as $\epsilon \to 0$. We show that a family of asymptotic solutions is obtained, corresponding to whether the exponentially-small ripples are predominantly found for $x < 0$ or $x > 0$. For instance when $A = 0$ in boundary condition (2.4b), oscillatory ripples are present only for $x > 0$.

These family of solutions, containing high-frequency ripples with an exponentially small magnitude, relate to the small surface tension limit for parasitic gravity capillary waves studied later in chapter 4, in which one solution is selected from a family of solutions by enforcing periodicity. The result is a symmetric oscillatory wave, in addition to the algebraic asymptotic series, whose amplitude is exponentially small.

2.2.1 *An initial asymptotic expansion*

We begin by considering the following asymptotic expansion for the solution,

$$u(x;\epsilon) = \sum_{n=0}^{\infty} \epsilon^n u_n(x). \tag{2.5}$$

Substituting this expansion into the governing equation (2.4a) yields distinct equations at each order of ϵ. These are given by

$$O(1): \qquad u_0(x) = \operatorname{sech}(x), \tag{2.6a}$$

$$O(\epsilon): \qquad u_1(x) = [u_0(x)]^2, \tag{2.6b}$$

$$O(\epsilon^n): \qquad u_n(x) = -u''_{n-2}(x) + \sum_{p=0}^{n-1} u_p(x)u_{n-p-1}(x), \tag{2.6c}$$

where this last equation holds for $n \geq 2$. Note that the leading order solution (2.6a) has the behaviour of $u_0(x) \sim 2\mathrm{e}^x$ as $x \to -\infty$, and is thus exponentially subdominant to the first component of behavioural condition (2.4b), $u(x) \sim A\cos(x/\epsilon + \delta) + 2\mathrm{e}^x$. Thus this solution, and all subsequent orders of the asymptotic solution, are unaffected by this behavioural condition. This is suspicious, and we will show that as $\epsilon \to 0$, the first component of condition (2.4b) must be applied to the exponentially-small terms of the asymptotic solution, requiring $A = O(\mathrm{e}^{-\pi/(2\epsilon)})$.

Note that due to the nonlinearity of the differential equation (2.4a), evaluating the higher order equations becomes considerably more difficult as n increases. However, as $n \to \infty$, only a finite number of terms in the $O(\epsilon^n)$ equation (2.6c) will form the leading order dominant balance. This is due to later orders of the asymptotic solution requiring repeated differentiation of earlier orders. Since these earlier orders of the asymptotic solution will be singular at certain points in the domain, the strength of these singularities will grow as $n \to \infty$, leading to divergence of the solution. These singular points are discussed next.

2.2.2 *Singularities of the asymptotic solution*

It is a near universality that asymptotic expansions to singularly perturbed equations, such as equation (2.4a), will diverge [cf. Dingle (1973), Chapman et al. (1998), Boyd (1999)]. This divergence of $u_n(x)$ is generated by singularities in the early orders of the asymptotic solution. However, our leading order solution, $u_0(x) = \text{sech}(x)$, is smooth across the real-valued domain, $-\infty < x < \infty$. In writing

$$u_0(x) = \text{sech}(x) = \frac{2\mathrm{e}^x}{\mathrm{e}^{2x}+1}, \tag{2.7}$$

we see that this solution is singular whenever $\mathrm{e}^{2x} + 1 = 0$. That is, these singular points exist in the complex-valued domain. Therefore, we analytically continue the domain by relabelling $x \mapsto z$, where $z \in \mathbb{C}$. This appearance of singular points in the complex-valued domain is a common feature in singular perturbative problems. For our current problem, the analytic continuation proceeds effortlessly by considering the domain to take complex values for the original differential equation (2.4a). However, for certain problems, the analytic continuation of the governing equation requires subtle considerations of singular effects when $\text{Im}[z] \to 0$. An example of this are the water-wave equations considered in part I of this thesis. Since one of the governing equations is a principal valued integral with singular behaviour in the integrand, the analytic continuation of $x \mapsto z$ yields residue contributions associated with the singular point of the principal valued integral.

The singularities of the leading order solution occur when $\mathrm{e}^{2z}+1 = 0$. This permits a countably infinite number of solutions, given by

$$z = \frac{\mathrm{i}\pi}{2}(1+2k), \tag{2.8}$$

where k takes integer values. Each of these singular points will generate divergence of the late-terms, $u_n(z)$, of the asymptotic expansion. However, since this behaviour as $n \to \infty$ will contain an integral starting from the corresponding singular point, shorter paths of integration (from the singularities closest to the real-valued domain) typically yield the dominant behaviour as $n \to \infty$. Thus, we will focus on the two singularities closest to the real axis, at $z = \mathrm{i}\pi/2$ and $z = -\mathrm{i}\pi/2$, which we denote to be the principal singularities for our problem. For convenience, we write these in compact form as $z = a\mathrm{i}/2$, where the constant a is defined by

$$a = \begin{cases} +1 & \text{for the UHP singularity,} \\ -1 & \text{for the LHP singularity.} \end{cases} \tag{2.9}$$

In Taylor expanding $u_0(z) \sim \text{sech}\,(z)$ as $z \to a\mathrm{i}\pi/2$, we find the singular behaviour of the leading order solution to be given by

$$u_0(z) \sim \frac{-a\mathrm{i}}{(z - \frac{a\mathrm{i}\pi}{2})}. \tag{2.10}$$

From this, we may also determine the singular behaviour of $u_1(z)$ as $z \to a\mathrm{i}\pi/2$, the equation for which is $u_1(z) = [u_0(z)]^2$ from (2.6b). This yields

$$u_1(z) = O\left(\left(z - \frac{a\mathrm{i}\pi}{2}\right)^{-2}\right) \quad \text{as} \quad z \to a\mathrm{i}\pi/2. \tag{2.11}$$

We see that the strength of the singular behaviour has increased. Moreover, based on the form of the $O(\epsilon^n)$ equation (2.6c), we anticipate that in general, we will have

$$u_n(z) = O\left(\left(z - \frac{a\mathrm{i}\pi}{2}\right)^{-(n+1)}\right) \quad \text{as} \quad z \to a\mathrm{i}\pi/2. \tag{2.12}$$

We demonstrated in equation (2.12) that the singular behaviour as $z \to ai\pi/2$ of the late-terms, $u_n(z)$, of the asymptotic solution increases as $n \to \infty$. Moreover, differentiation of this growing singular behaviour will result in factorial divergence, which we now demonstrate. Since successive terms in the asymptotic expansion are determined by differentiation of earlier orders, approximately by $u_n(z) \approx u''_{n-2}(z)$, we see that if $u_{n-2}(z) = O\big((z - ai\pi/2)^{-(n-1)}\big)$, then $u_n(z) = O(n^2(z - ai\pi/2)^{-(n+1)})$. This leads to factorial divergence of the asymptotic solution, which we capture in the limit of $n \to \infty$ with the factorial over power ansatz

$$u_n(z) \sim \frac{Q(z)\Gamma(n+\alpha)}{\chi(z)^{n+\alpha}}. \tag{2.13}$$

Here, both Q and χ are functions of z. We call χ the singulant as it will capture the growing singular behaviour through the condition of $\chi(z^*) = 0$ at any singular points, $z = z^*$. This condition for the singulant arises as matching criteria when the inner boundary layer analysis is considered near the singular points in z. The functional prefactor, Q, is often called the amplitude function. Note that α is assumed to be constant. This is almost universally the case, however very rarely it may be necessary to consider $\alpha = \alpha(z)$, such as in chapter 4 of Mortimer (2004).

Each singular point in the early orders of the asymptotic solution will generate a separate contribution to the late terms. Thus, in general, we will have

$$u_n(z) \sim \sum_{k\in\mathbb{Z}} \frac{Q^{(k)}(z)\Gamma(n+\alpha_k)}{\chi^{(k)}(z)^{n+\alpha_k}}, \tag{2.14}$$

where $\chi^{(k)}(z) = 0$ at $z = i\pi(1+2k)/2$. However as briefly noted earlier, closer singular points typically result in smaller values of $\chi(z)$ along the free surface $\mathrm{Im}[\chi] = 0$, and thus produce dominant contributions to the late-term divergence. Thus only the singular points of $z = ai\pi/2$ will be considered, where $a = \pm 1$.

We now find equations for the amplitude function, Q, and the singulant, χ, by substituting ansatz (2.13) into the $O(\epsilon^n)$ equation (2.6c). Due to the divergent form for u_n as $n \to \infty$, not every term in the $O(\epsilon^n)$ need be considered. Only those appearing at the first two leading orders, as $n \to \infty$, are required to obtain equations for Q and χ, yielding

$$u_n(z) = -u''_{n-2}(z) + 2u_0(z)u_{n-1}(z) + \cdots . \tag{2.15}$$

Differentiating (2.13) twice to find an expression for u''_{n-2} yields

$$u''_{n-2}(z) \sim \frac{(\chi')^2 Q\Gamma(n+\alpha)}{\chi^{n+\alpha}} - (\chi'' Q + 2\chi' Q')\frac{\Gamma(n+\alpha-1)}{\chi^{n+\alpha-1}} + \cdots , \tag{2.16a}$$

$$u_{n-1}(z) \sim \frac{Q\Gamma(n+\alpha-1)}{\chi^{n+\alpha-1}}. \tag{2.16b}$$

At the leading order of n in equation (2.15), $O(\Gamma(n+\alpha)/\chi^{n+\alpha})$, we find

$$[\chi'(z)]^2 = -1, \tag{2.17}$$

and the next order, $O(\Gamma(n+\alpha-1)/\chi^{n+\alpha-1})$, yields the equation

$$\frac{Q'(z)}{Q(z)} = -\frac{u_0(z)}{\chi'(z)}. \tag{2.18}$$

There are two solutions to the singulant equation (2.17), given by $\chi(z) = \text{const.} \pm \mathrm{i}z$. Enforcing the boundary condition $\chi(a\mathrm{i}\pi/2) = 0$ yields

$$\chi(z) = \pm\mathrm{i}\left(z - \frac{a\mathrm{i}\pi}{2}\right). \tag{2.19}$$

Thus each singular point, for instance $z = \mathrm{i}\pi/2$, generates two singulants discerned

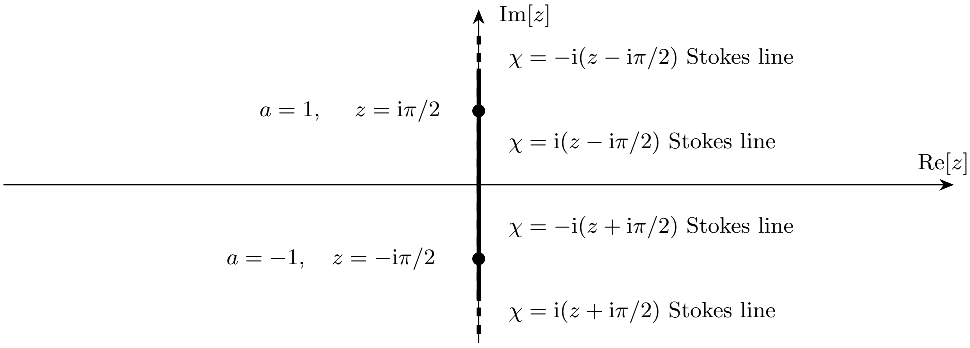

Figure 2.2: The Stokes lines (bold) which begin from each of the two singular points (circles) are shown. The singularity $z = \mathrm{i}\pi/2$ has two associated Stokes lines, both along the imaginary axis. One Stokes line has Im[z] $> \pi/2$, and the other with Im[z] $< \pi/2$ intersects with the real-axis. The singularity at $z = -\mathrm{i}\pi/2$ also has two Stokes lines along the imaginary axis. The first has Im[z] $< -\pi/2$, and the second with Im[z] $> -\pi/2$ intersects the real-axis.

by $\pm$ in the solution above. Only one of these will generate Stokes lines that intersect with the free surface. For $a = +1$, this is the $(+)$ sign, and for $a = -1$, the $(-)$ sign, demonstrated in figure 2.2. Note that the concept of a Stokes line has not yet been introduced; this will be discussed in section 2.2.7. Thus, to capture the behaviour of the relevant singulant for each singularity, we will consider the solution to be given by

$$\chi_a(z) = a\mathrm{i}\left(z - \frac{a\mathrm{i}\pi}{2}\right). \tag{2.20}$$

We now have $\chi' = a\mathrm{i}$, and therefore may solve the amplitude equation (2.18) to find the solution

$$Q_a(z) = \Lambda_a \exp\left(a\mathrm{i}\int_0^z u_0(t)\mathrm{d}t\right) = \Lambda_a \exp\left(a\mathrm{i}\int_0^z \mathrm{sech}(t)\mathrm{d}t\right). \tag{2.21}$$

Here, Λ_a is the constant of integration that depends on the starting point of integration, which has been chosen to be the origin. To conclude, we have found the functional form of the divergence of u_n to be given by

$$u_n(z) \sim \sum_{a=\pm 1} \Lambda_a \exp\left(a\mathrm{i}\int_0^z \mathrm{sech}(t)\mathrm{d}t\right) \frac{\Gamma(n+\alpha)}{\left(a\mathrm{i}\left[z - \frac{a\mathrm{i}\pi}{2}\right]\right)^{n+\alpha}}. \tag{2.22}$$

Note that while each component of (2.22) is complex-valued in general, when evaluated on the free surface, Im[z] $= 0$, they will be the complex conjugate of one another, yielding a real-valued divergent solution. Verification of this requires knowledge of the constant, Λ_a. This is determined in the next section along with the other unknown constant, α.

2.2.4 *Inner analysis at the principal singularities*

We now determine the two unknown constants in the late terms of the outer expansion by considering the inner boundary layer problem near $z = ai\pi/2$. First, we note that the early orders of the outer expansion reorder whenever $u_0(x) \sim \epsilon u_1(x)$. Since $u_1 = u_0^2$ from solution (2.6b), this yields $u_0 = \operatorname{sech}(z) \sim 1/\epsilon$. From the singular behaviour in equation (2.10), $u_0 \sim -ai/(z - ai\pi/2)$, we find

$$\epsilon \sim ai\left(z - \frac{ai\pi}{2}\right), \tag{2.23}$$

which motivates our definition of the inner variable, η, given by

$$\epsilon\eta = ai\left(z - \frac{ai\pi}{2}\right). \tag{2.24}$$

Thus, we will have $\eta = O(1)$ in the inner region.

In writing the inner limit of u_0 in terms of the inner variable, η, we have $u_0 \sim 1/(\epsilon\eta)$. Thus, we define the inner variable by

$$u_{\text{outer}} = \frac{1}{\epsilon\eta}\bar{u}_{\text{inner}}(\eta). \tag{2.25}$$

Substitution of the inner solution, $\bar{u}$, and the inner variable, η, into the outer equation (2.4a) yields the inner equation,

$$\bar{u}'' - \frac{2\bar{u}'}{\eta} + \left(\frac{2}{\eta^2} - 1\right)\bar{u} + \frac{\bar{u}^2}{\eta} + 2ai\epsilon\eta\frac{e^{-ai\epsilon\eta}}{(1 - e^{2ai\epsilon\eta})} = 0. \tag{2.26}$$

The inner limit of the outer divergent solution is calculated next in §2.2.5. It is found that the dominant divergent terms, as $n \to \infty$, reorder into the leading-order component of the inner solution. Thus, only the leading-order component of the inner equation (2.26), as $\epsilon \to 0$, must be studied in order to match with the inner limit of the outer solution.

Expanding (2.26) as $\epsilon \to 0$ yields the leading-order inner equation as

$$\bar{u}'' - \frac{2\bar{u}'}{\eta} + \left(\frac{2}{\eta^2} - 1\right)\bar{u} + \frac{\bar{u}^2}{\eta} + 1 = 0. \tag{2.27a}$$

For most of the problems contained in this thesis, only the leading-order component of the inner problem will be considered. The exception to this is the Hermite-with-pole equation in chapter 7, for which the inner limit of the late-terms of the outer expansion do not reorder into the leading-order, in ϵ, inner problem. The inner equation (2.27a) is subject to the boundary condition

$$\bar{u}(\eta) \sim 1 \qquad \text{as } \eta \to \infty, \tag{2.27b}$$

which is the value found upon taking the inner limit of the leading-order outer solution, u_0, written in inner variables.

2.2.5 *Inner limit of u_n and determination of α*

We now determine the constant α by ensuring that the factorial-over-power representation of the late term solution has the same singular behaviour as that anticipated in equation (2.12), $u_n = O((z - a\mathrm{i}\pi/2)^{-n-1})$. This inner limit is given by

$$\begin{aligned}\epsilon^n u_n &\sim \frac{2a\mathrm{i}\Lambda_a \epsilon^n \mathrm{e}^{\mathcal{P}(a\mathrm{i}\pi/2)}}{\pi}\left(z - \frac{a\mathrm{i}\pi}{2}\right)\frac{\Gamma(n+\alpha)}{\left(a\mathrm{i}\left[z - \frac{a\mathrm{i}\pi}{2}\right]\right)^{n+\alpha}} \\ &\sim \frac{2\Lambda_a \mathrm{e}^{\mathcal{P}(a\mathrm{i}\pi/2)}}{\pi\epsilon^{\alpha-1}}\frac{\Gamma(n+\alpha)}{\eta^{n+\alpha-1}},\end{aligned} \tag{2.28}$$

where the first line is the inner limit written in terms of the outer variable, z, and the second is written in terms of the inner variable, η. In order to evaluate the inner limit of the integral of $\mathrm{sech}(t)$ in the amplitude function, $Q(z)$, we have defined

$$\mathcal{P}(z) = a\mathrm{i}\int_0^z \left[\mathrm{sech}(t) + \frac{a\mathrm{i}}{(t - \frac{a\mathrm{i}\pi}{2})}\right]\mathrm{d}t. \tag{2.29}$$

Balancing the power of the singularity of u_n in (2.28), $1 - n - \alpha$, with the anticipated singularity from (2.12), $-n-1$ yields

$$\alpha = 2. \tag{2.30}$$

2.2.6 *Inner solution and determination of Λ_a*

To determine Λ_a, we will match the inner limit of the outer solution, from (2.28), with the outer limit of an inner solution. We represent this outer limit of the inner solution as a series expansion as $z \to \infty$ of the form

$$\bar{u}(\eta) = \sum_{n=0}^{\infty}\frac{\bar{u}_n}{\eta^n}. \tag{2.31}$$

Substituting this series expansion into the inner equation (2.27a) yields

$$\sum_{n=2}^{\infty}\frac{n(n-1)\bar{u}_{n-2}}{\eta^n} + \sum_{n=1}^{\infty}\sum_{m=0}^{n-1}\frac{\bar{u}_m\bar{u}_{n-m-1}}{\eta^n} - \sum_{n=0}^{\infty}\frac{\bar{u}_n}{\eta^n} + 1 = 0. \tag{2.32}$$

Equating terms of $O(\eta^0)$ and $O(\eta^{-1})$, we find that

$$\bar{u}_0 = 1 \quad \text{and} \quad \bar{u}_1 = 1. \tag{2.33a}$$

At $O(\eta^{-n})$, we find the equation

$$\bar{u}_n = n(n-1)\bar{u}_{n-2} + \sum_{m=0}^{n-1}\bar{u}_m\bar{u}_{n-m-1}, \tag{2.33b}$$

which holds for $n \geq 2$. Equations (2.33a) and (2.33b) form a recurrence relation for $\bar{u}_n$, which may be solved numerically to large values of n.

We now match the nth term of the outer limit of the inner solution from (2.31) with the inner limit of the $O(\epsilon^n)$ outer solution from (2.28), yielding

$$\frac{2\Lambda_a \mathrm{e}^{\mathcal{P}(a\mathrm{i}\pi/2)}}{\pi\epsilon}\frac{\Gamma(n+2)}{\eta^{n+1}} = \frac{\bar{u}_n}{\epsilon\eta^{n+1}}, \tag{2.34}$$

which may be rearranged to find the following expression for the constant Λ_a,

$$\Lambda_a = \frac{\pi\mathrm{e}^{-\mathcal{P}(a\mathrm{i}\pi/2)}}{2}\lim_{n\to\infty}\frac{\bar{u}_n}{\Gamma(n+2)}. \tag{2.35}$$

Recurrence relation (2.33b) may be solved numerically to $n = 150$ to find $\bar{u}_n/\Gamma(n+2) \approx 0.938$. More accurate predictions for this constant can be obtained through the implementation of Richardson extrapolation.

2.2.7 *Optimal truncation and Stokes smoothing*

The exponentially-small components of the asymptotic solution are now determined. These will display the *Stokes phenomenon*, in which they rapidly (and smoothly) change in magnitude across contours in the complex z-plane. These contours are known as *Stokes lines*, across which this change occurs in a boundary layer of diminishing width as $\epsilon \to 0$. This phenomenon was first derived analytically by Berry (1989), and the methodology presented in this section closely follows the works by Chapman et al. (1998) and Chapman and Vanden-Broeck (2006)

We consider a remainder, $\mathcal{R}_N(z)$, to a truncated asymptotic expansion by writing

$$u(z;\epsilon) = \underbrace{\sum_{n=0}^{N-1}\epsilon^n u_n(z)}_{u_r} + \mathcal{R}_N(z), \tag{2.36}$$

where we have denoted the truncated algebraic expansion by u_r. When N is chosen optimally by

$$N = \frac{|\chi|}{\epsilon} + \rho, \tag{2.37}$$

the remainder $\mathcal{R}_N$ will be exponentially small. In the above, we have introduced $0 \leq \rho < 1$ to ensure that N takes integer values. The optimal truncation point (2.37) may be derived in multiple ways. For instance, one can consider the point at which the base series reorders due to the divergence as $n \to \infty$, given by $\epsilon^n u_n \sim \epsilon^{n+1}u_{n+1}$. Alternatively, N can be left unspecified until equation (2.44) below for the particular solution of $\mathcal{R}_N$, which is minimal when N is chosen optimally in this manner.

Substitution of this truncated expansion into the original differential equation (2.4a) yields

$$\epsilon^2\mathcal{R}_N'' + (1-2\epsilon u_r)\mathcal{R}_N = -\xi_{\mathrm{eq}} + O(\mathcal{R}_N^2), \tag{2.38}$$

where the forcing term, ξ_{eq}, is defined by

$$\xi_{\mathrm{eq}}(z;\epsilon) = \epsilon^2 u_r'' - \epsilon u_r^2 + u_r - \mathrm{sech}(z). \tag{2.39}$$

Homogeneous solutions to equation (2.38), for which the forcing term ξ_{eq} is neglected, are given by

$$\mathcal{R}_N(z) = Q_a(z)\mathrm{e}^{-\chi_a(z)/\epsilon}. \tag{2.40}$$

Here, $Q_a(z)$ and $\chi_a(z)$ satisfy the same equations as that found for the late-term factorial-over-power ansatz (2.13). We will capture the Stokes phenomenon through the particular solution of equation (2.38) for $\mathcal{R}_N$, in which the forcing term ξ_{eq} is retained. Note that each order in ϵ of ξ_{eq} is identically zero, up to and including $O(\epsilon^{N-1})$. Thus, $\xi_{\text{eq}} = O(\epsilon^N)$, and this dominant component of the forcing term is given by

$$\begin{aligned} \xi_{\text{eq}} &\sim \epsilon^N \left(u''_{N-2} - 2u_0 u_{N-1} + \cdots \right) \\ &\sim \epsilon^N [\chi'_a(z)]^2 Q_a(z) \frac{\Gamma(N+\alpha)}{[\chi_a(z)]^{N+\alpha}}. \end{aligned} \tag{2.41}$$

In the above, we have also only retained the leading order divergent term as $N \to \infty$, which is given by $\epsilon^N u''_{N-2}$. The particular solution is found by variation of parameters, in which we multiply the homogeneous solution (2.40) by an unknown function, $\mathcal{S}_a(z)$, yielding

$$\mathcal{R}_N(z) = \mathcal{S}_a(z) Q_a(z) \mathrm{e}^{-\chi_a(z)/\epsilon}. \tag{2.42}$$

Here, $\mathcal{S}_a$ is denoted the Stokes prefactor, or Stokes multiplier, as it will display the Stokes phenomenon that we seek to capture.

Substitution of solution (2.42) and the dominant scaling for ξ_{eq} from (2.41) into the remainder equation (2.38) yields

$$-2\epsilon \mathrm{e}^{-\chi_a/\epsilon} \chi'_a(z) Q_a(z) \frac{\mathrm{d}\mathcal{S}_a}{\mathrm{d}z} \sim -\epsilon^N [\chi'_a(z)]^2 Q_a(z) \frac{\Gamma(N+\alpha)}{[\chi_a(z)]^{N+\alpha}}, \tag{2.43}$$

which simplifies to give

$$\frac{\mathrm{d}\mathcal{S}_a}{\mathrm{d}\chi_a} \sim \frac{1}{2} \epsilon^{N-1} \mathrm{e}^{\chi_a/\epsilon} \frac{\Gamma(N+\alpha)}{\chi_a^{N+\alpha}}. \tag{2.44}$$

First we substitute for $\chi_a = r_a \mathrm{e}^{\mathrm{i}\vartheta_a}$, change derivatives to ϑ_a, and expand as $N \to \infty$ using Stirlings approximation for the gamma function to find

$$\begin{aligned} \frac{\mathrm{d}\mathcal{S}_a}{\mathrm{d}\vartheta_a} &\sim \mathrm{i} r_a \mathrm{e}^{\mathrm{i}\vartheta_a} \frac{\sqrt{2\pi}\epsilon^{N-1} \mathrm{e}^{-N-\alpha+r_a \mathrm{e}^{\mathrm{i}\vartheta_a}/\epsilon} (N+\alpha)^{N+\alpha-1/2}}{2 r_a^{N+\alpha} \mathrm{e}^{\mathrm{i}\vartheta_a (N+\alpha)}}, \\ &\sim \frac{\sqrt{\pi} \mathrm{i} \epsilon^{r_a/\epsilon+\rho-1} \mathrm{e}^{-\rho-\alpha+r_a(\mathrm{e}^{\mathrm{i}\vartheta_a}-1)/\epsilon} r_a^{r_a/\epsilon+\rho+\alpha-1/2}}{\sqrt{2} r_a^{r_a/\epsilon+\rho+\alpha-1} \mathrm{e}^{\mathrm{i}\vartheta_a(r_a/\epsilon+\rho+\alpha-1)} \epsilon^{r_a/\epsilon+\rho+\alpha-1/2}} \left(1 + \frac{\epsilon(\rho+\alpha)}{r_a}\right)^{\frac{r_a}{\epsilon}}, \\ &\sim \frac{\sqrt{\pi} \mathrm{i} r_a^{1/2} \mathrm{e}^{-r_a(1-\mathrm{e}^{\mathrm{i}\vartheta_a})/\epsilon}}{\sqrt{2} \mathrm{e}^{\mathrm{i}\vartheta_a(r_a/\epsilon+\rho+\alpha-1)} \epsilon^{\alpha+1/2}}. \end{aligned} \tag{2.45}$$

In the second approximation above, we substituted for the optimal truncation point, $N = r_a/\epsilon + \rho$ specified earlier in equation (2.37). The right-hand side of (2.45) is exponentially small on account of the $\exp\left(-r_a(1-\mathrm{e}^{\mathrm{i}\vartheta_a})/\epsilon\right)$ component. The exception to this is near $\vartheta_a = 0$, for which we expand $\mathrm{e}^{\mathrm{i}\vartheta_a} \sim 1 + \mathrm{i}\vartheta_a - \vartheta_a^2/2 + \cdots$ to find

$$\frac{\mathrm{d}\mathcal{S}_a}{\mathrm{d}\vartheta_a} \sim \frac{\sqrt{\pi} \mathrm{i} r_a^{1/2}}{\sqrt{2}\epsilon^{\alpha+1/2}} \exp\left(-\frac{r_a \vartheta_a^2}{2\epsilon}\right). \tag{2.46}$$

Thus, we have demonstrated that the main change in the Stokes multiplier, $\mathcal{S}_a$, occurs about $\vartheta_a = 0$. This condition, $\arg[\chi_a] = 0$, yields the conditions by Dingle (1973) of

$$\mathrm{Im}[\chi_a] = 0 \quad \text{and} \quad \mathrm{Re}[\chi_a] > 0. \tag{2.47}$$

Contours along which (2.47) are satisfied are the Stokes lines for our problem. Furthermore, we may integrate differential equation (2.46) to find a solution for $\mathcal{S}_a$, which closely resembles the error function. Since the dominant change across the Stokes line is confined to the region where $\vartheta_a = O(\epsilon^{1/2})$, we may integrate across this boundary layer to find that

$$\mathcal{S}_a(z) = S_a + \frac{\sqrt{2\pi}\mathrm{i}}{2\epsilon^\alpha} \int_{-\infty}^{\frac{\vartheta_a \sqrt{r_a}}{\sqrt{\epsilon}}} \mathrm{e}^{-t^2/2}\mathrm{d}t, \tag{2.48}$$

where S_a is a constant. On one side of the Stokes line, $\vartheta_a < 0$, we have $\mathcal{S}_a = S_a$ as $\epsilon \to 0$. On the other side, $\vartheta_a > 0$, integration of the error function yields $\mathcal{S}_a = S_a + \pi\mathrm{i}/\epsilon^\alpha$. We have thus predicted the jump condition of

$$\mathcal{S}_a(\vartheta_a \to 0^+) - \mathcal{S}_a(\vartheta_a \to 0^-) = \frac{\pi\mathrm{i}}{\epsilon^\alpha} \tag{2.49}$$

across the Stokes lines. This switching is shown in figure 2.3.

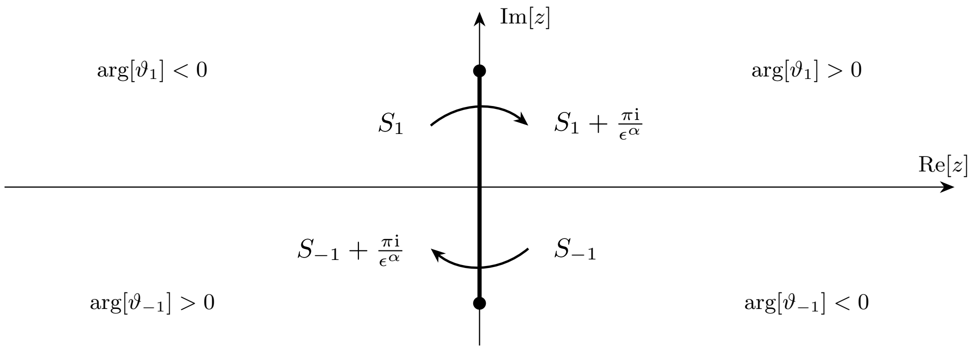

Figure 2.3: The Stokes lines (bold) that intersect with the real-axis are shown. Their associated Stokes switching contribution, from equation (2.49), is shown across both of these lines.

2.2.8 *The exponentially small solution*

The exponentially-small component of the asymptotic solution is given by combining both contributions, one with $a = 1$ from the UHP singularity, and the other with $a = -1$ from the LHP singularity. This yields

$$\mathcal{R}_N(z) \sim \mathcal{S}_1(z)Q_1(z)\mathrm{e}^{-\chi_1(z)/\epsilon} + \mathcal{S}_{-1}(z)Q_{-1}(z)\mathrm{e}^{-\chi_{-1}(z)/\epsilon}, \tag{2.50}$$

which we may write as an outer solution on either side of the Stokes lines by writing

$$\mathcal{R}_N \sim \begin{cases} S_1 Q_1(z)\mathrm{e}^{-\chi_1(z)/\epsilon} + \left(S_{-1} + \dfrac{\pi\mathrm{i}}{\epsilon^\alpha}\right)Q_{-1}(z)\mathrm{e}^{-\chi_{-1}(z)/\epsilon} & \text{for } z < 0, \\ \left(S_1 + \dfrac{\pi\mathrm{i}}{\epsilon^\alpha}\right)Q_1(z)\mathrm{e}^{-\chi_1(z)/\epsilon} + S_{-1}Q_{-1}(z)\mathrm{e}^{-\chi_{-1}(z)/\epsilon} & \text{for } z > 0. \end{cases} \tag{2.51}$$

We may now substitute for each of the components appearing in (2.51). It is seen from solution (2.35) for the constant amplitude, Λ_a, that $\mathcal{P}(\mathrm{i}\pi/2) = \mathcal{P}(-\mathrm{i}\pi/2)$, yielding $\Lambda_1 = \Lambda_{-1}$. Evaluation of (2.51) for $\mathrm{Im}[z] = 0$ yields firstly for $x < 0$,

$$\mathcal{R}_N \sim \Lambda_1 \mathrm{e}^{-\frac{\pi}{2\epsilon}} \left[\left(S_1^{(r)} + S_{-1}^{(r)} \right) \cos\left(f(x)\right) - \left(S_1^{(i)} - S_{-1}^{(i)} - \frac{\pi}{\epsilon^\alpha} \right) \sin\left(f(x)\right) \right]$$
$$+ \mathrm{i}\Lambda_1 \mathrm{e}^{-\frac{\pi}{2\epsilon}} \left[\left(S_1^{(i)} + S_{-1}^{(i)} + \frac{\pi}{\epsilon^\alpha} \right) \cos\left(f(x)\right) + \left(S_1^{(r)} - S_{-1}^{(r)} \right) \sin\left(f(x)\right) \right], \tag{2.52a}$$

and secondly for $x > 0$,

$$\mathcal{R}_N \sim \Lambda_1 \mathrm{e}^{-\frac{\pi}{2\epsilon}} \left[\left(S_1^{(r)} + S_{-1}^{(r)} \right) \cos\left(f(x)\right) - \left(S_1^{(i)} - S_{-1}^{(i)} + \frac{\pi}{\epsilon^\alpha} \right) \sin\left(f(x)\right) \right]$$
$$+ \mathrm{i}\Lambda_1 \mathrm{e}^{-\frac{\pi}{2\epsilon}} \left[\left(S_1^{(i)} + S_{-1}^{(i)} + \frac{\pi}{\epsilon^\alpha} \right) \cos\left(f(x)\right) + \left(S_1^{(r)} - S_{-1}^{(r)} \right) \sin\left(f(x)\right) \right]. \tag{2.52b}$$

In the above, we have defined

$$f(x) = -\frac{x}{\epsilon} + \int_0^x \operatorname{sech}(t)\mathrm{d}t, \tag{2.53}$$

and written $S_1 = S_1^{(r)} + \mathrm{i}S_1^{(i)}$ and $S_{-1} = S_{-1}^{(r)} + \mathrm{i}S_{-1}^{(i)}$ for the real and imaginary parts of each of these constants. Condition (2.4b) requires that $\mathrm{Im}[\mathcal{R}_N] = 0$ for $x \leq 0$, yielding

$$S_1^{(r)} - S_{-1}^{(r)} = 0 \qquad \text{and} \qquad S_1^{(i)} + S_{-1}^{(i)} + \frac{\pi}{\epsilon^\alpha} = 0. \tag{2.54}$$

Substitution of these solutions for $S_{-1}^{(r)}$ and $S_{-1}^{(i)}$ back into equations (2.52a) and (2.52b) yields the real-valued solution,

$$\mathcal{R}_N \sim \begin{cases} 2\Lambda_1 \mathrm{e}^{-\frac{\pi}{2\epsilon}} \left[S_1^{(r)} \cos\left(f(x)\right) - S_1^{(i)} \sin\left(f(x)\right) \right] & \text{for } x < 0, \\ 2\Lambda_1 \mathrm{e}^{-\frac{\pi}{2\epsilon}} \left[S_1^{(r)} \cos\left(f(x)\right) - \left(S_1^{(i)} + \frac{\pi}{\epsilon^\alpha} \right) \sin\left(f(x)\right) \right] & \text{for } x > 0, \end{cases} \tag{2.55}$$

for which there are two free constants. These constants may be related to boundary condition (2.4b), $u \sim A\cos(x/\epsilon + \delta)$ as $x \to -\infty$. Since $f(x) \sim -x/\epsilon - \pi/2$ as $x \to -\infty$, we enforce this boundary condition on $\mathcal{R}_N$ from (2.55) as $x \to -\infty$ to find

$$A\cos(\delta) = 2\Lambda_1 S_1^{(i)} \mathrm{e}^{-\frac{\pi}{2\epsilon}} \quad \text{and} \quad A\sin(\delta) = 2\Lambda_1 S_1^{(r)} \mathrm{e}^{-\frac{\pi}{2\epsilon}}, \tag{2.56}$$

yielding

$$S_1^{(i)} = \frac{A\cos(\delta)}{2\Lambda_1}\mathrm{e}^{\frac{\pi}{2\epsilon}} \quad \text{and} \quad S_1^{(r)} = \frac{A\sin(\delta)}{2\Lambda_1}\mathrm{e}^{\frac{\pi}{2\epsilon}}. \tag{2.57}$$

Regardless of the value of these constants, there is always a switching of

$$-\frac{2\pi\Lambda_1}{\epsilon^\alpha}\mathrm{e}^{-\frac{\pi}{2\epsilon}} \sin\left(-\frac{x}{\epsilon} + \int_0^x \operatorname{sech}(t)\mathrm{d}t \right) \tag{2.58}$$

incurred in $\mathcal{R}_N$ as we pass from $x < 0$ to $x > 0$. Three asymptotic solutions, $u(x) \sim u_0(x) + \mathcal{R}_N(x)$, are shown in figure 2.4 for different values of $S_1^{(r)}$ and $S_1^{(i)}$.

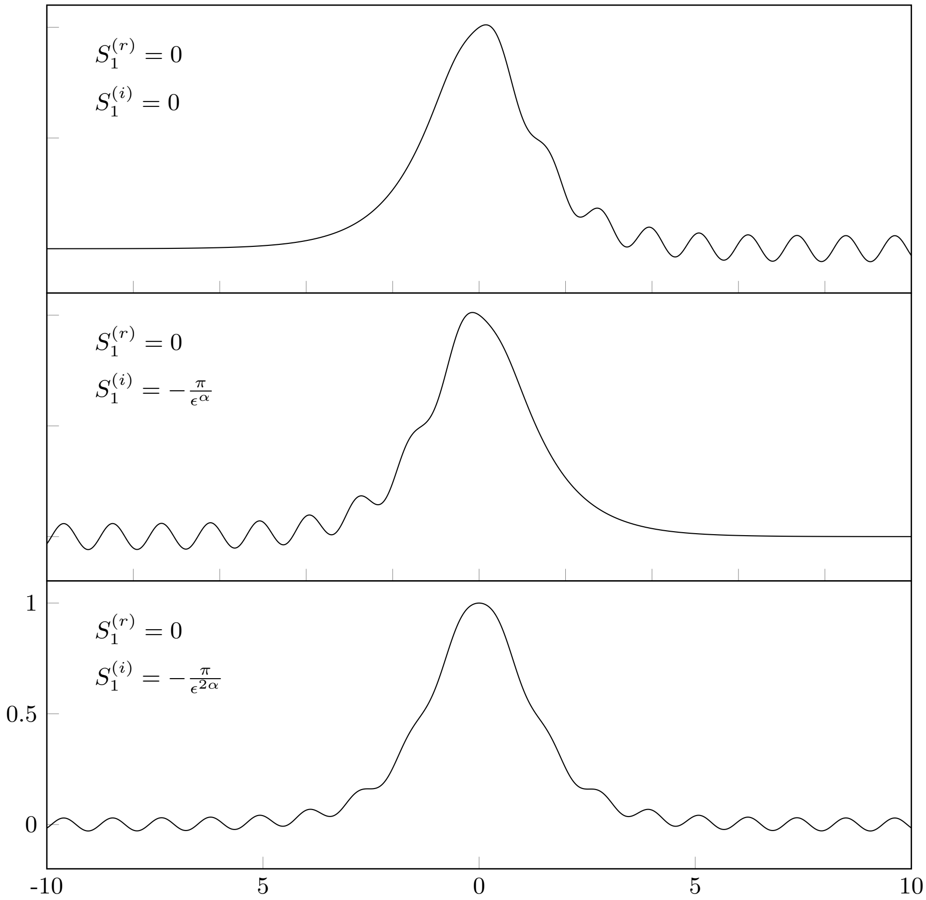

Figure 2.4: Three asymptotic solutions, $u \sim u_0 + \bar{u}$, are shown for $\epsilon = 0.18$ and different values of the constants $S_1^{(r)}$ and $S_1^{(i)}$.

2.2.9 *Conclusion*

We have demonstrated how the divergent asymptotic expansion for the solution of a singularly perturbed equation yields an exponentially small remainder upon optimal truncation of the initial expansion. This exponentially-small remainder displays the Stokes phenomenon across Stokes lines for $z \in \mathbb{C}$, and these Stokes lines begin at singular points of the asymptotic expansion. The boundary layer analysis across each Stokes line predicts only a local change in the magnitude of the exponentially-small term, and determination of the outer behaviour of these terms thus requires an additional constraint. We have imposed a behavioural condition as $x \to -\infty$ to characterise the exponentially-small component of the asymptotic solution in this outer region.

2.2.10 *Discussion*

Each of the problems discussed in this thesis contain various complications to the exponential asymptotic techniques introduced in this chapter. These are:

(i) **Chapters 3 and 4**, in which the small surface tension limit of periodic gravity-capillary waves is firstly considered numerically, and then asymptotically.

This asymptotic solution contains at leading order a nonlinear travelling gravity wave, whose form is not known analytically. Numerical values are required to determine the singular points in the analytic continuation, which in section 2.2.2 we determined analytically, that generate Stokes lines and the Stokes phenomenon.

(ii) **Chapter 5**, in which time-dependent standing gravity-capillary waves are considered numerically. Their future analytical treatment would require the extension of these techniques to a nonlinear set of PDEs.

(iii) **Chapter 6**, for which we consider the small Froude number (speed) limit of waves generated by submerged point vortices. This formulation requires the exponentially-small solution to three coupled equations. When two submerged point vortices are considered, trapped waves confined to lie between the two vortices emerge for certain values of the Froude number, due to the Stokes phenomenon of section 2.2.7 generated by these cancelling out exactly in the far field.

(iv) **Part II**, in which the exponentially-small instability of the equatorial Kelvin wave is derived analytically. This problem contains an eigenvalue, whose asymptotic expansion also diverges. While the base expansion for the eigenvalue is real-valued, the exponentially-small component is imaginary. This corresponds to a growing temporal instability of the travelling wave solution. This problem displays two additional features. First, the *higher-order Stokes phenomenon* in which the late-terms of the asymptotic series display the Stokes phenomenon of section 2.2.7 across higher-order Stokes lines. This can lead to naive Stokes lines, found by evaluating Dingle's condition (2.47) on the singulant, being either inactive or partially active. Second, in addition to the classical Stokes phenomenon generated by a divergent base expansion for the solution, there is an additional Stokes phenomenon generated by the exponentially-small component of the eigenvalue. This second feature is analogous to the *second-generation Stokes phenomenon*, in which exponentials turned on by the primary Stokes phenomenon themselves generate an additional Stokes switching. However, our additional Stokes switching is generated by exponentially-small terms that are universally present, and thus we do not use the second-generation terminology for this.

PART I

The small surface tension limit of gravity capillary waves


Chapter 2
Introduction to exponential asymptotics:
the forced harmonic oscillator


Chapter 3
On the structure of steady parasitic gravity-capillary waves in the small surface tension limit


Chapter 4
Exponential asymptotics for steady parasitic capillary ripples on steep gravity waves


Chapter 5
On the structure of gravity-capillary standing waves in the small surface tension limit

THE NUMERICAL BIFURCATION STRUCTURE OF TRAVELLING WAVES

3

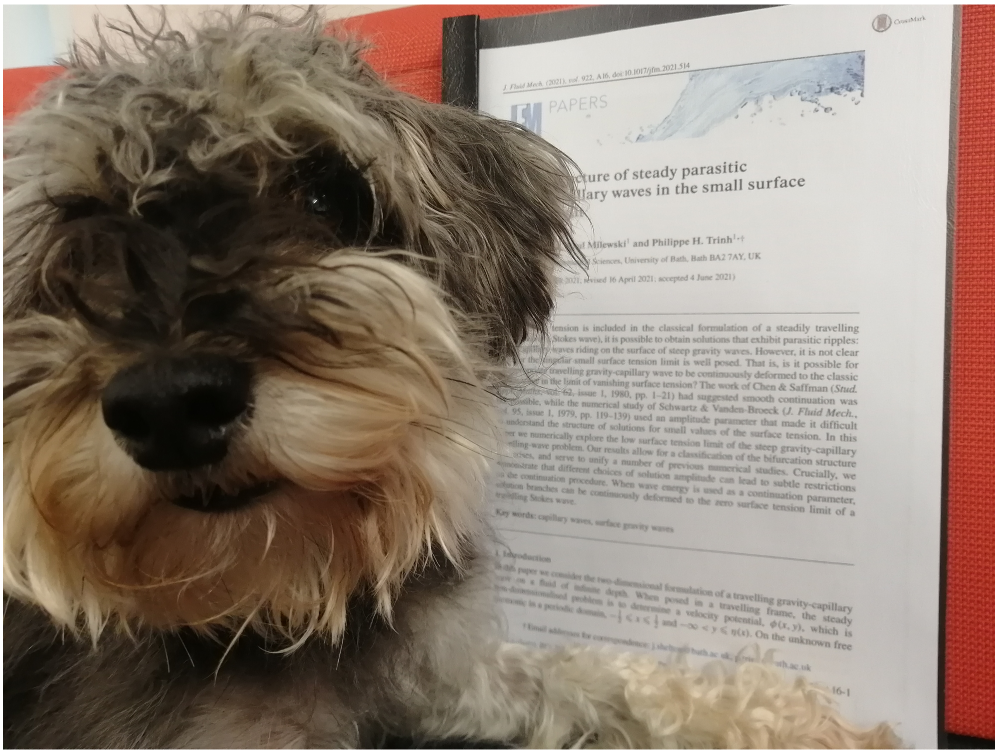

3.1 Introduction

In the introduction to exponential asymptotics of chapter 2, highly oscillatory ripples appeared in the solution profile, which were shown to be exponentially small as $\epsilon \to 0$. This exponentially small behaviour arose due to the singularly perturbed nature of the governing equation as $\epsilon \to 0$. That is, the order of the differential equation with $\epsilon = 0$ differed from that with $\epsilon \neq 0$, no matter how small this value was taken.

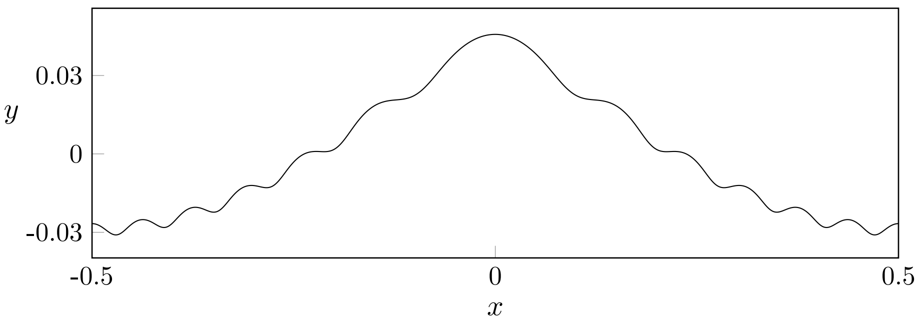

Figure 3.1: A numerical solution of the steady gravity-capillary wave equations is shown. This profile has $B = 00227$ and $F = 0.4299$.

Free surface water waves are also singularly perturbed for small surface tension. In this section we consider Bernoulli's equation for the steadily travelling free surface of an inviscid, irrotational, and incompressible fluid,

$$\frac{F^2}{2}(\phi_x^2+\phi_y^2)+y-B\frac{\eta_{xx}}{(1+\eta_x^2)^{\frac{3}{2}}}=0.$$

Here, the Bond number, B, represents the surface tension. We see that the differential equation is first order for $B = 0$ and second order for $B \neq 0$, and hence the limit of $B \to 0$ is a singular perturbation. We therefore anticipate that exponentially small effects may be present in travelling gravity-capillary wave solutions when the Bond number, B, is small. Note that this is not guaranteed to be the case. While these exponentially-small effects will be present in the analytic continued solution on account of the anticipated Stokes lines and Stokes phenomenon, these Stokes lines may not intersect with the real-valued free surface.

The first indication that these exponentially small effects may be present in the solution profile of a steadily travelling gravity capillary wave was numerically detected by Schwartz and Vanden-Broeck (1979). In addition to presenting a preliminary bifurcation picture of the solutions for small values of the surface tension, they presented one very interesting solution profile in their figure 10, analogous to that shown in figure 3.1. This profile, with $B \neq 0$, was very close in value to the $B = 0$ solution, but with one crucial difference: the appearance of high-frequency ripples on the wave surface, with 11 peaks in the periodic domain. This raised two interesting questions:

(i) First, can one explore the branch of solutions in the bifurcation space starting from this solution, and what does this look like?

(ii) Second, are there solutions containing high-frequency ripples that contain a different number of peaks (for instance 12, 13, and so forth) within the periodic domain, and how do these behave as the number of peaks tends to infinity?

The purpose of the paper by Shelton et al. (2021) presented in this chapter is to answer these questions by characterising the numerical branches of solutions, for fixed amplitude, each of which corresponds to a certain number of peaks in the high-frequency ripple. It is also observed that the amplitude of these ripples is exponentially small as $B \to 0$.

Appendix B: Statement of Authorship

This declaration concerns the article entitled:									
On the structure of steady parasitic gravity-capillary waves in the small surface tension limit									
Publication status:									
Draft manuscript	☐	**Submitted**	☐	**In review**	☐	**Accepted**	☐	**Published**	●
Publication details	Journal - Journal of Fluid Mechanics, 922, A16 Authors - Josh Shelton, Paul Milewski, Philippe H. Trinh								
Copyright status:									
The material has been published with a CC-BY license	●					The publisher has granted permission to replicate the material included here	☐		
Candidate's contribution to the paper	All authors contributed equally to the conceptualisation and methodology used in the article (33%) All analytical calculations were performed by the author of this thesis (100%) All numerical computations were performed by the author of this thesis (100%) The original draft and bulk of the final presentation has been written by the author of this thesis (90%)								
Statement from Candidate	This paper reports on original research I conducted during the period of my Higher Degree by Research candidature.								
Signed						**Date**	30/12/22		

J. Fluid Mech. (2021), *vol.* 922, A16, doi:10.1017/jfm.2021.514

JFM PAPERS

On the structure of steady parasitic gravity-capillary waves in the small surface tension limit

Josh Shelton[1,†], **Paul Milewski**[1] **and Philippe H. Trinh**[1,†]

[1]Department of Mathematical Sciences, University of Bath, Bath BA2 7AY, UK

(Received 19 January 2021; revised 16 April 2021; accepted 4 June 2021)

When surface tension is included in the classical formulation of a steadily travelling gravity wave (a Stokes wave), it is possible to obtain solutions that exhibit parasitic ripples: small capillary waves riding on the surface of steep gravity waves. However, it is not clear whether the singular small surface tension limit is well posed. That is, is it possible for an appropriate travelling gravity-capillary wave to be continuously deformed to the classic Stokes wave in the limit of vanishing surface tension? The work of Chen & Saffman (*Stud. Appl. Maths*, vol. 62, issue 1, 1980, pp. 1–21) had suggested smooth continuation was not possible, while the numerical study of Schwartz & Vanden-Broeck (*J. Fluid Mech.*, vol. 95, issue 1, 1979, pp. 119–139) used an amplitude parameter that made it difficult to understand the structure of solutions for small values of the surface tension. In this paper we numerically explore the low surface tension limit of the steep gravity-capillary travelling-wave problem. Our results allow for a classification of the bifurcation structure that arises, and serve to unify a number of previous numerical studies. Crucially, we demonstrate that different choices of solution amplitude can lead to subtle restrictions on the continuation procedure. When wave energy is used as a continuation parameter, solution branches can be continuously deformed to the zero surface tension limit of a travelling Stokes wave.

Key words: capillary waves, surface gravity waves

1. Introduction

In this paper we consider the two-dimensional formulation of a travelling gravity-capillary wave on a fluid of infinite depth. When posed in a travelling frame, the steady non-dimensionalised problem is to determine a velocity potential, $\phi(x, y)$, which is harmonic in a periodic domain, $-\frac{1}{2} \leqslant x \leqslant \frac{1}{2}$ and $-\infty < y \leqslant \eta(x)$. On the unknown free

† Email addresses for correspondence: j.shelton@bath.ac.uk, p.trinh@bath.ac.uk

surface, $y = \eta(x)$, Bernoulli's condition requires that

$$\frac{F^2}{2}|\nabla\phi|^2 + \eta - B\kappa = \text{const.} \tag{1.1}$$

Here, the Froude number, F, characterises the balance between inertia and gravity, and the inverse Bond number, B, characterises the balance between gravity and surface tension; with this latter effect depending on the surface curvature, κ. These non-dimensional constants are given by

$$F = c/\sqrt{gL_\lambda} \quad \text{and} \quad B = \sigma/\rho g L_\lambda^2, \tag{1.2a,b}$$

where c is the wave speed, g is the gravitational constant, L_λ is the wavelength, ρ is the fluid density and σ is the coefficient of surface tension.

Typically, a wave energy or amplitude parameter, $\mathscr{E}$, is fixed and prescribes the degree of nonlinearity. Solutions are then characterised by bifurcation curves in (B, F) or $(B, F, \mathscr{E})$-solution space. The small surface tension limit corresponds to $B \to 0$.

Extensive results are known for the case with $B = 0$ when surface tension is neglected, and this originates from the seminal work of Stokes (1847); cf. the reviews by Okamoto & Shõji (2001) and Toland (1996). Intuitively, we might expect that the inclusion of a small amount of surface tension results in a small change in the profile of the pure gravity wave. However, since the limit of $B \to 0$ is singularly perturbed, this is not necessarily the case, and it is known that the introduction of surface tension has a significant impact on the existence and uniqueness of solutions, their bifurcations and their profiles.

The goal of this paper is to present a numerical study of nonlinear solutions in the singular limit of $B \to 0$, for which we know one solution to be the Stokes wave. We demonstrate the numerical existence of a cohesive structure of branches of solutions existing under this limit. Importantly this suggests that, with fixed wave energy, $\mathscr{E}$, only one of a family of solutions approaches the classical Stokes wave as $B \to 0$.

We firstly discuss the analytical and numerical difficulties of the $B \to 0$ limit.

1.1. *Longuet-Higgins and parasitic ripples*

It is well-known observationally that under the action of both gravity and surface tension, ripples of small wavelength form on the forward face of a propagating wave. As shown by the experimental results of Cox (1958) and Ebuchi *et al.* (1987) for instance, the amplitude of these parasitic capillary ripples increases when the overall amplitude of the wave (measured by crest to trough displacement) increases. An example of such parasitic ripples, as photographed by Ebuchi *et al.* (1987), is shown in figure 1, where it is seen that these ripples are asymmetric about the wave crest and unsteady in the frame of the propagating wave. Note that in this paper we shall refer to solutions exhibiting parasitic capillary ripples as those where a short wavelength and small amplitude wave is present on what appears to be a gravity-dominated water wave.

A seminal advance in the modelling of these parasitic capillary waves arose from the methodology of Longuet-Higgins (1963), who predicted that for small surface tension these parasitic ripples would be exponentially small in both amplitude and wavelength. In this simplest steady framework one assumes that the parasitic ripples are fixed to the same travelling frame of reference as the underlying gravity wave. However, it was noted by Perlin, Lin & Ting (1993) that these analytical predictions produced poor agreement with both experimental wave profiles and numerical solutions of the steady nonlinear equations, a result of asymptotic inconsistencies in his method. We shall provide a preliminary

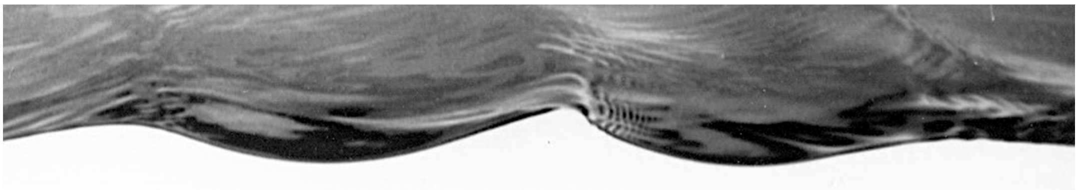

Figure 1. Experimental picture showing parasitic ripples located near the crests of steep gravity waves from Ebuchi, Kawamura & Toba (1987) (reproduced with permission).

discussion of these issues in § 7, in which we comment that the Longuet-Higgins approximation can be improved through the use of exponential asymptotics.

Nevertheless, it remains an open question as to whether parasitic capillary ripples similar to those shown in figure 1 may be found as either symmetric or asymmetric solutions of the steady framework of (1.1). In this work we present clear numerical evidence that steady symmetric parasitic ripples do exist within the solution space of the classical potential framework in the $B \to 0$ limit.

1.2. *Schwartz & Vanden-Broeck and the complexity of* (B, F)*-space*

In their seminal work Schwartz & Vanden-Broeck (1979) developed a numerical scheme using a series truncation method to compute periodic gravity-capillary waves of the exact nonlinear equations. Imposing symmetry at $x = 0$ and an amplitude condition on the crest-to-trough displacement, they presented a preliminary classification of solutions in (B, F)-space of types 1, 2, 3 and 4. Each type number was associated with a distinct branch of solutions, and corresponded to the number of observed 'dimples' or inflexion points on a (half) wave profile.

A reproduction of their original bifurcation diagram, which is computed at fixed crest-to-trough amplitude, is shown in figure 2(*b*). Our intention in reproducing this figure is to convince the reader that indeed the bifurcation space of the gravity-capillary problem is certainly non-trivial, and it is difficult to observe any clear structure. We also show the computed (Schwartz & Vanden-Broeck 1979) bifurcation curves in figure 2 alongside our solutions of fixed energy.

One of their solutions, Schwartz & Vanden-Broeck (1979, figure 10), is of particular interest in the context of parasitic ripples. This profile, similar to that shown in figure 3, appears to contain small-scale capillary ripples as a perturbation to the main Stokes wave. This is one of the types of solution that we will be expanding upon in this work. Note in addition that the type 1 to 4 branches, as shown in their figure, have a non-trivial and unstructured shape in the bifurcation diagram; it is not obvious if a more consistent pattern emerges upon increasing the type number, or whether these solution curves can be taken as $B \to 0$. We shall explain the reason for these issues in this work.

Later, in seeking to compare new experimental data with the previous analytical approximations of Longuet-Higgins (1963) and numerical solutions of Schwartz & Vanden-Broeck (1979), Perlin *et al.* (1993) made extensive remarks on the challenges of navigating the solution space of the full nonlinear problem, noting that 'there is no known method for determining the number of solutions to the numerical formulation. . . ' (p. 618). Indeed, they state that (p. 598),

> Surprisingly little information is available on these waves of disparate scales, presumably due to the analytical/numerical, as well as experimental, difficulties involved.
>
> Perlin *et al.* (1993)

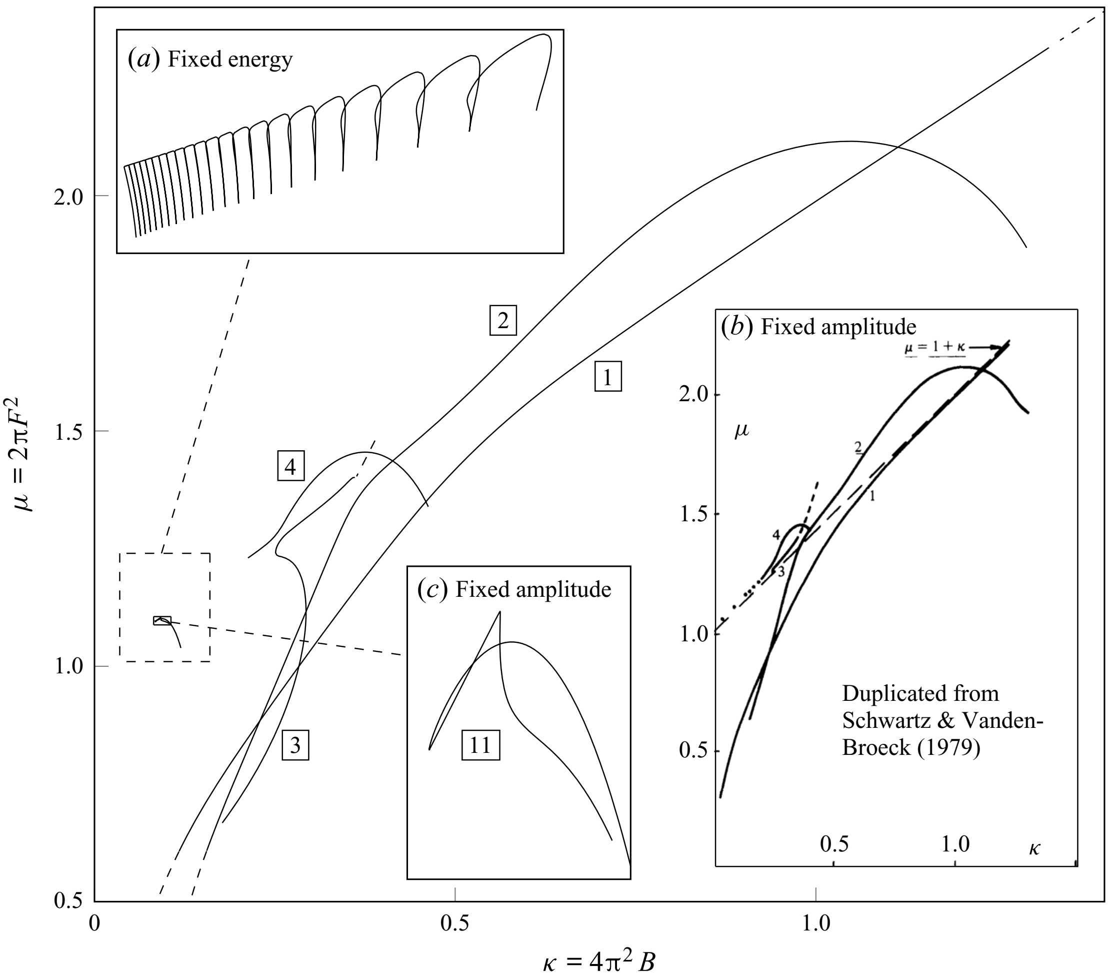

Figure 2. Our solutions of fixed energy from § 5 are shown in (*a*). Panel (*b*) shows a reproduction of the fixed amplitude results previously published in Schwartz & Vanden-Broeck (1979) (reproduced with permission). These branches of fixed amplitude are shown in the (κ, μ)-plane, where the boxed type number indicates the number of observed 'dimples' or inflexion points on a (half) wave profile. In (*c*) we show the type-11 fixed amplitude branch.

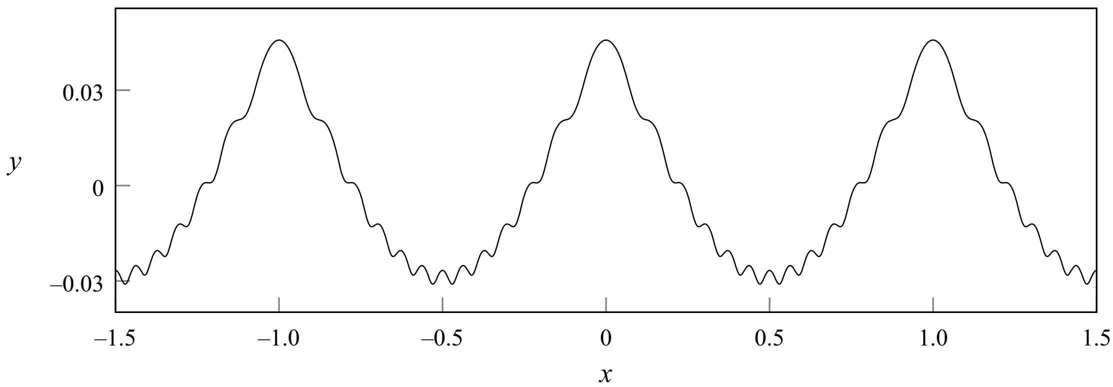

Figure 3. A numerical solution of (4.1*a*) and (4.1*b*) is displayed in physical (x, y)-space, with non-dimensional parameters $F = 0.4299$, $B = 0.002270$ and energy $\mathscr{E} = 0.3804$. This has been computed using the scheme described in § 4. The periodic solution has been repeated three times.

1.3. *Chen & Saffman and the impossibility of the $B \to 0$ limit*

Nearly in parallel with the work by Schwartz & Vanden-Broeck (1979), Chen & Saffman (1979, 1980*a*,*b*) produced a series of works where they examined the Stokes wave problem, largely from the perspective of weakly nonlinear theory (and its numerical consequences on the full nonlinear problem).

In Chen & Saffman (1979) they considered weakly nonlinear solutions of (1.1) in powers of a small wave amplitude, ϵ. Expressing the solution, $y = \eta(x)$, as a Fourier series, this permits analytical solutions for the Fourier coefficients, A_n. They discovered that in fixing the point of symmetry of the wave profile to be at $x = 0$, the branches of solutions in the (κ, A_n)-bifurcation space (where $\kappa = 4\pi^2 B$) are discontinuous either side of the point $\kappa = 1/n$. Due to this discontinuity and the analytical criterion, they commented (p. 204):

> The gravity wave ($\kappa = 0$) is therefore a singular limit which cannot be reached smoothly by applying the limit $\kappa \to 0$ to a gravity capillary wave. Chen & Saffman (1979)

In our work we will note how this statement is misleading since their non-smoothness is a consequence of their initial assumption of a fixed point of symmetry at $x = 0$. We demonstrate this in § 6.4, noting that this is due to the presence of a symmetry shifting bifurcation. Thus, if their enforced symmetry at $x = 0$ were to be relaxed, the branches of solutions in (κ, A_n)-space either side of the point $\kappa = 1/n$ would be continuous.

In a second work by Chen & Saffman (1980*b*), the numerical solution space was explored for waves of finite amplitude. Their choice of amplitude was a linear combination of Fourier coefficients, typically chosen to be that of the fundamental mode, A_1, or the nth mode A_n. Nonlinear solutions were computed. However, the resultant branches of solutions in their bifurcation diagram did not connect, from which they concluded:

> These results confirm the impossibility of going continuously from a pure capillary-gravity wave to a gravity wave by letting $\kappa \to 0$. Chen & Saffman (1980*b*)

We later note in § 6.2 that if the wave energy instead is fixed as an amplitude parameter then the continuous set of solutions as $B \to 0$, discovered within this paper, bifurcate from solutions with fundamental mode $A_1 = 0$. Hence, if A_1 is fixed to be a non-zero constant, as in the numerical work of Chen & Saffman (1980*b*), this bifurcation point would remain undiscovered. We shall conclude that in order to achieve a continuous transition as $B \to 0$, the first Fourier coefficient should not be fixed.

1.4. *Outline of the paper*

In this work we shall consider the numerical behaviour of steady symmetric parasitic ripples for small values of the Bond number, B. Starting in § 2, we introduce the governing equations for the gravity-capillary wave problem, which we transform to depend on the velocity potential, ϕ, alone. In § 3 the well-known linear solutions are derived. These form a starting point for our numerical method of § 4. Solutions are presented in § 5, which we use to demonstrate that as $B \to 0$ for fixed energy, $\mathscr{E}$, this bifurcation structure appears to form a countably infinite number of connecting branches of solutions in the (B, F)-plane. Each branch forms a 'finger' in the solution space, which is connected continuously to the proceeding branch. These branches then accumulate in the limit of $B \to 0$ such that solutions are conjectured to exist in an $O(1)$ interval in the Froude number, F. These branches of solutions are connected at the point where they bifurcate from a wave with smaller fundamental wavelength, resulting in numerical evidence for the $B \to 0$ limit of the steep gravity-capillary wave problem having a continuous set of solutions.

This allows us to show why previous authors have failed to reveal this underlying structure, which we comment upon in §§ 6 and 6.5. Lastly, in § 7 we comment upon the asymptotic properties as $B \to 0$ of our discovered solutions, and how this uncovered structure is likely to be present in other numerical problems for small values of the Bond number, B.

2. Mathematical formulation

Consider a two-dimensional free surface flow of an inviscid, irrotational and incompressible fluid of infinite depth. The velocity potential, ϕ, is defined by $\boldsymbol{u} = \nabla \phi$. We assume that, in the lab frame, the free surface, $y = \eta(x, t)$, is periodic in x with wavelength L_λ, and moves to the right with wave speed c. We non-dimensionalise with unit length, L_λ, and velocity, c. We consider steady travelling-wave solutions by introducing a subflow of unit horizontal velocity in the opposite direction of wave propagation. This negates the movement of the free surface. Then $\eta_t = 0 = \phi_t$ yields the steady governing equations (compare with Vanden-Broeck 2010, (2.48)–(2.55) for example),

$$\phi_{xx} + \phi_{yy} = 0 \quad \text{for } y \leqslant \eta, \tag{2.1a}$$

$$\phi_y = \eta_x \phi_x \quad \text{at } y = \eta, \tag{2.1b}$$

$$\frac{F^2}{2}(\phi_x^2 + \phi_y^2) + y - B\frac{\eta_{xx}}{(1+\eta_x^2)^{3/2}} = 0 \quad \text{at } y = \eta, \tag{2.1c}$$

$$\phi_y \to 0 \quad \text{and} \quad \phi_x \to -1 \quad \text{as } y \to -\infty, \tag{2.1d}$$

for the travelling wave now in $x \in [-\frac{1}{2}, \frac{1}{2})$. Thus, the system is governed by Laplace's equation (2.1a) within the fluid, kinematic and dynamic conditions on the free surface (2.1b) and (2.1c), and uniform flow conditions in the deep-water limit (2.1d). The horizontal velocity condition (2.1d), our subflow, indicates a uniform flow moving towards the left. The spatial subscripts in (2.1) correspond to partial differentiation.

Remark on terminology: note that in the mathematical formulation above, we have non-dimensionalised lengths by a fixed physical wavelength, L_λ, and, hence, we shall seek solutions that are 1-periodic in the non-dimensional travelling frame. However, these solutions may have a smaller wavelength which is less than unity. We thus define λ to be the non-dimensional fundamental wavelength (the smallest such wavelength). Moreover, in this work we shall refer to a wave with fundamental wavenumber $k = 1/\lambda$ as a pure k-wave. Thus, a pure k-wave has a dimensional wavelength of λL_λ.

2.1. *The conformal mapping to the (ϕ, ψ)-plane*

We now formulate the governing equations (2.1) in the potential (ϕ, ψ)-plane, as shown in figure 4. We assume that the free surface is located along $\psi = 0$, and introduce the notation of X and Y for the fluid quantities evaluated on the free surface. Thus,

$$X(\phi) \equiv x(\phi, 0) \quad \text{and} \quad Y(\phi) \equiv \eta(x(\phi, 0)). \tag{2.2a,b}$$

We may now obtain expressions for the surface derivative and curvature by differentiating (2.2a,b). This yields

$$\eta_x = \frac{Y_\phi}{X_\phi} \quad \text{and} \quad \eta_{xx} = \frac{X_\phi Y_{\phi\phi} - Y_\phi X_{\phi\phi}}{X_\phi^3}. \tag{2.3a,b}$$

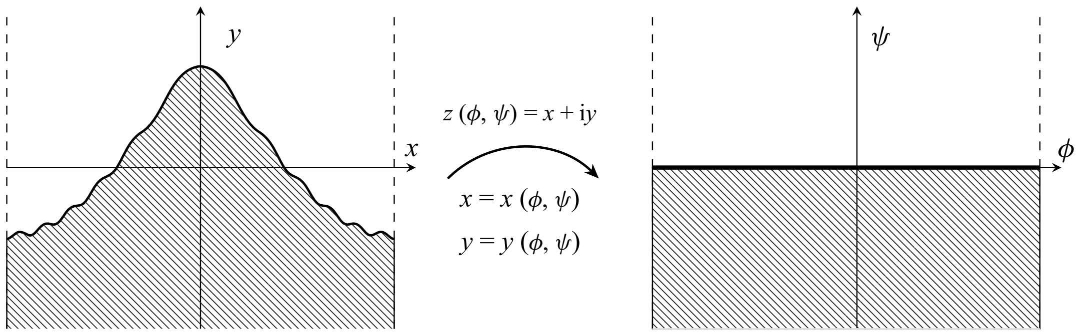

Figure 4. The conformal mapping from (x, y) to (ϕ, ψ) is shown.

We now seek to rewrite the kinematic (2.1*b*) and dynamic (2.1*c*) boundary conditions on the surface in terms of the conformal variables X and Y. First, the velocities, ϕ_x and ϕ_y, may be inverted, yielding

$$\phi_x = \frac{x_\phi}{x_\phi^2 + y_\phi^2} \quad \text{and} \quad \phi_y = \frac{y_\phi}{x_\phi^2 + y_\phi^2}. \tag{2.4a,b}$$

Finally, substitution of (2.4*a,b*) for ϕ_x and ϕ_y, (2.3*a,b*) for η_x and η_{xx}, and $Y(\phi) = \eta(x(\phi, 0))$ into Bernoulli's equation (2.1*c*) and setting $\psi = 0$ yields our governing equation (compare with (6.12) of Vanden-Broeck 2010)

$$\frac{F^2}{2J} + Y + B\frac{(Y_\phi X_{\phi\phi} - X_\phi Y_{\phi\phi})}{J^{3/2}} = 0. \tag{2.5}$$

Above we have introduced the surface Jacobian, J, via

$$J(\phi) = X_\phi^2 + Y_\phi^2. \tag{2.6}$$

Note that in the conformal formulation, the kinematic condition (2.1*b*) can be verified to be satisfied identically once (2.3*a,b*) and (2.4*a,b*) are used on the streamline $\psi = 0$.

In addition to Bernoulli's equation (2.5), in order to close the system, we require a harmonic relationship between X and Y. Note that within the fluid, $y(\phi, \psi)$ can be written as a Fourier series of the form

$$y(\phi, \psi) = \psi + A_0 + \sum_{n=1}^{\infty} \mathrm{e}^{2n\pi\psi} \left[A_n \cos(2n\pi\phi) + B_n \sin(2n\pi\phi)\right], \tag{2.7}$$

where A_n and B_n are real-valued for all n. Indeed, the above ansatz satisfies $y_{\phi\phi} + y_{\psi\psi} = 0$ along with the depth condition $y \sim \psi$ as $\psi \to -\infty$.

We define the Hilbert transform on Y by

$$\mathscr{H}[Y](\phi') = \fint_{-\infty}^{\infty} \frac{Y(\phi)}{\phi - \phi'}\, \mathrm{d}\phi, \tag{2.8}$$

where the integral is of principal-value type. Then by the assumed periodicity of the solution, this implies that

$$\mathscr{H}[Y](\phi') = \fint_{-1/2}^{1/2} Y(\phi) \cot[\pi(\phi - \phi')]\, \mathrm{d}\phi. \tag{2.9}$$

We can then verify that the individual Fourier modes can be related using $\mathscr{H}[\sin(2n\pi\phi)] = \cos(2n\pi\phi)$ and $\mathscr{H}[\cos(2n\pi\phi)] = -\sin(2n\pi\phi)$. From using the

Cauchy–Riemann relations of $x_\phi = y_\psi$ and $x_\psi = -y_\phi$, we obtain the harmonic relationships between X and Y on the free surface via

$$X_\phi(\phi) = 1 - \mathscr{H}[Y_\phi(\phi)] \quad \text{and} \quad Y_\phi(\phi) = \mathscr{H}[X_\phi(\phi) - 1]. \tag{2.10a,b}$$

A choice of any one of the relations in (2.10a,b), combined with Bernoulli's equation (2.5) allows X and Y to be solved.

2.2. *The energy constraint*

In order to fully close the formulation, we shall impose an energy constraint on the solution, which can be viewed as equivalent to a measurement of the wave amplitude. We define the wave energy, E, to be

$$E = \frac{F^2}{2}\int_{-1/2}^{1/2} Y(X_\phi - 1)\,\mathrm{d}\phi + B\int_{-1/2}^{1/2}(\sqrt{J} - X_\phi)\,\mathrm{d}\phi + \frac{1}{2}\int_{-1/2}^{1/2} Y^2 X_\phi\,\mathrm{d}\phi, \tag{2.11}$$

where the first integral on the right-hand side corresponds to the kinetic energy, the second to the capillary potential energy and the third to the gravitational potential energy. The derivation of (2.11) from the bulk energy is given in Appendix A.

For comparison purposes, it will be convenient for us to rescale the energy in (2.11) by the energy of the highest (fundamental) gravity wave, E_{hw}. Thus, we write

$$\mathscr{E} = \frac{E}{E_{hw}}, \tag{2.12}$$

where $E_{hw} \approx 0.00184$ (to 5 decimal places) is calculated using the numerical scheme of § 4 applied to the pure gravity wave using $n = 4096$ Fourier coefficients.

The choice of how to define an amplitude or energy condition for the wave is a subtle one. In this paper we shall comment on the following three choices of amplitude:

$$\mathscr{A} = \begin{cases} \mathscr{E} & \text{[energy definition from (2.11)]}, \\ A_1 & \text{[first Fourier coefficient from (2.7)]}, \\ Y(0) - Y(1/2) & \text{[crest-to-trough displacement]}. \end{cases} \tag{2.13}$$

The second choice of A_1, as used in Chen & Saffman (1980b), designates the amplitude to be the first Fourier coefficient, while the third choice of $Y(0) - Y(1/2)$, as used by Schwartz & Vanden-Broeck (1979), is a sensible choice to measure the physical wave height of the fundamental Stokes wave.

Note that both definitions of amplitude, A_1 and $Y(0) - Y(1/2)$, have the problem that strongly nonlinear waves (as measured by a lack of decay in the Fourier coefficients) can occur, even at small amplitude values. This is particularly affected by the fact that gravity-capillary waves may take a variety of shapes beyond the simple fundamental wave considered by Stokes (1847). Similar difficulties were encountered by Chen & Saffman (1979, 1980b), who chose $\mathscr{A} = A_1$ but commented that:

> We found from experience that none of these parameters were universally useful for describing the bifurcation phenomenon to be described in this work, and in fact we have been unable to construct a parameter which characterized the magnitude of the wave for all the phenomena in a satisfactory way. Chen & Saffman (1979)

It may be that using the energetic definition of amplitude with $\mathscr{A} = \mathscr{E}$ is the modification required to fix these issues; indeed within the context of our numerical investigations this does seem to be the case in the small surface tension limit.

3. Linear theory, Wilton ripples and type (n, m)-waves

It will be useful for us to review linear solutions in the notation of § 2.1. The results of linear theory are found from the first two terms of a Stokes expansion in powers of a small amplitude parameter, ϵ (see, e.g. Vanden-Broeck 2010, § 2.4.2). Thus, we shall consider equations (4.1*a*) and (4.1*b*) and take $X \sim X_0 + \epsilon X_1$ and $Y \sim Y_0 + \epsilon Y_1$. Solving the resultant equations yields $X_0 = \phi$ and $Y_0 = 0$ at leading order. At $O(\epsilon)$, we write X_1 and Y_1 as Fourier series and assume that the two solutions are respectively odd and even about $\phi = 0$. This yields the necessary equation that

$$\sum_{k=1}^{\infty} \left[F^2(2k\pi) - 1 - (2k\pi)^2 B\right] a_k \cos(2k\pi\phi) = 0. \tag{3.1}$$

In order to obtain non-trivial solutions, we require the linear dispersion relation of

$$2k\pi F^2 - 1 - 4k^2\pi^2 B = 0, \tag{3.2}$$

and obtain $X_1 = a_k \sin(2k\pi\phi)$ and $Y_1 = a_k \cos(2k\pi\phi)$. Thus, the linear solution, a pure-k wave, is approximated by

$$X \sim \phi + \epsilon \left[a_k \sin(2k\pi\phi)\right] \quad \text{and} \quad Y \sim \epsilon \left[a_k \cos(2k\pi\phi)\right], \tag{3.3a,b}$$

to the first two orders. Substitution into the energy expression (2.12) yields

$$\mathscr{E} \sim \epsilon^2 \frac{2K^2\pi^2 B a_k^2}{E_{hw}}. \tag{3.4}$$

The linear solution (3.3*a*,*b*) was assumed to satisfy the single dispersion relation (3.2) for the kth Fourier mode only. Note that other solutions may be constructed that satisfy the dispersion relation for more than one mode. For instance, if the modes with $k = 1$ and $k = n$ are assumed to be non-degenerate, then we require that both $2\pi F^2 - 1 - 4\pi^2 B = 0$ and $2n\pi F^2 - 1 - 4n^2\pi^2 B = 0$. This yields the so-called Wilton ripples predicted by Wilton (1915), located wherever

$$B_{\text{wilton}} = \frac{1}{4\pi^2 n} \quad \text{and} \quad F^2_{\text{wilton}} = \frac{(1+n)}{2\pi n}, \tag{3.5a,b}$$

with $n \in \mathbb{Z}^+$. The Wilton ripples are then given by

$$X_1 = a_1 \sin(2\pi\phi) + a_n \sin(2n\pi\phi) \quad \text{and} \quad Y_1 = a_1 \cos(2\pi\phi) + a_n \cos(2n\pi\phi). \tag{3.6a,b}$$

In the numerics of § 4, we shall often initialise the numerical continuation method with the linear solution (3.3*a*,*b*) using a small value of ϵa_k. Crucially, since this linear solution is invalid near points (3.5*a*,*b*), we must ensure that our initial choice lies away from the critical numbers of B_{wilton} and/or F_{wilton}.

As introduced by Chen & Saffman (1979), linear solutions that consist of a combination of pure n- and m-waves, and with fundamental wavelengths of $\lambda = 1/n$ and $1/m$, respectively, are described as a type (n, m)-wave. Thus, under this terminology, Wilton's solution in (3.5*a*,*b*) is an example of a type $(1, n)$-wave. Our numerical results presented in § 5 will contain solutions that are the nonlinear analogue of a type $(1, n)$-wave.

4. The numerical method

In this section we describe the numerical procedure for solving Bernoulli's equation (2.5) and the harmonic relationship (2.10*a*,*b*) for $X(\phi)$ and $Y(\phi)$ subject to a given value of the energy, $\mathscr{E}$, from (2.11). Thus,

$$\frac{F^2}{2J} + Y + B\frac{(Y_\phi X_{\phi\phi} - X_\phi Y_{\phi\phi})}{J^{3/2}} = 0, \tag{4.1a}$$

$$X_\phi(\phi) = 1 - \mathscr{H}[Y_\phi(\phi)], \tag{4.1b}$$

$$\mathscr{E} = \frac{F^2}{2E_{hw}}\int_{-1/2}^{1/2} Y(X_\phi - 1)\,\mathrm{d}\phi + \frac{B}{E_{hw}}\int_{-1/2}^{1/2}(\sqrt{J} - X_\phi)\,\mathrm{d}\phi + \frac{1}{2E_{hw}}\int_{-1/2}^{1/2} Y^2 X_\phi\,\mathrm{d}\phi. \tag{4.1c}$$

Recall we define E_{hw} as the energy of the highest Stokes wave ($E_{hw} \approx 0.00184$).

Solutions of the above problem are regarded as lying within $(B, F, \mathscr{E})$-space. We solve these equations using Newton iteration on a truncated Fourier series using the fast Fourier transform. The procedure is as follows.

(i) An initial guess for $Y(\phi)$ is carefully chosen using either linear theory (3.3*a*,*b*) or from a previously computed solution (cf. § 5 for specific details).

(ii) Of the triplet $(B, F, \mathscr{E})$, we choose to fix two parameters and treat the last parameter as an unknown.

(iii) The collocation variable, ϕ, is discretised using N grid points, with $\phi_k = -1/2 + k\Delta\phi$ for $k = 0, \ldots, N-1$ and $\Delta\phi = 1/N$. We define the solution $Y(\phi_k) = Y_k$ at each of these points. Note that once Y_k is known for all k, X_k can be calculated using the harmonic relation (4.1*b*).

(iv) Combined with the unknown parameter (either B, F or $\mathscr{E}$), this yields $N+1$ unknowns. Bernoulli's equation (4.1*a*), evaluated at ϕ_k, provides N equations and the system is closed with the additional energy constraint (4.1*c*). Newton iteration is then used to solve the nonlinear system of equations until a certain tolerance (typically 10^{-11}) on the norm of the residual is met.

In our numerical scheme we leverage the Fourier transform for efficient manipulation of the solutions. In particular, note that the Hilbert transform, $\mathscr{H}$, needed for the harmonic relation (4.1*b*), can be evaluated via $\mathscr{H}[Y] = \mathscr{F}^{-1}[\mathrm{i}\cdot \mathrm{sgn}(k)\mathscr{F}[Y]]$, where $\mathscr{F}$ denotes the Fourier transform and sgn is the signum function. Both the Fourier and inverse-Fourier transforms are calculated with the fast Fourier transform algorithm. The derivatives of Y are also computed in Fourier space using the relationship $Y^{(n)}(\phi) = \mathscr{F}^{-1}[(2\pi\mathrm{i}k)^n\mathscr{F}[Y]]$. In order to obtain the numerical results presented in § 5, we find it sufficient to use $N = 1024$ mesh points. The computations are performed using a desktop computer and individual solutions are typically computed in under a second.

In essence, our goal will be to study the $(B, F, \mathscr{E})$-solution space, particularly as $B \to 0$. We start from a low-energy solution, and increase the parameter $\mathscr{E}$ until the desired value is reached. In order to initialise this continuation procedure at small values of $\mathscr{E}$, we select an initial Bond number which is chosen away from the Wilton ripples value of B_{wilton} in (3.5*a*,*b*). Then the Froude number is approximated by the linear dispersion relation (3.2) with $k = 1$, and we use the linear approximations of X and Y from (3.3*a*,*b*) with a small arbitrary choice of ϵa_k (typically 10^{-5}). For this linear solution, $\mathscr{E}$ is then calculated; the above serves as the initialisation procedure for the Newton scheme which solves for values of Y_i and F.

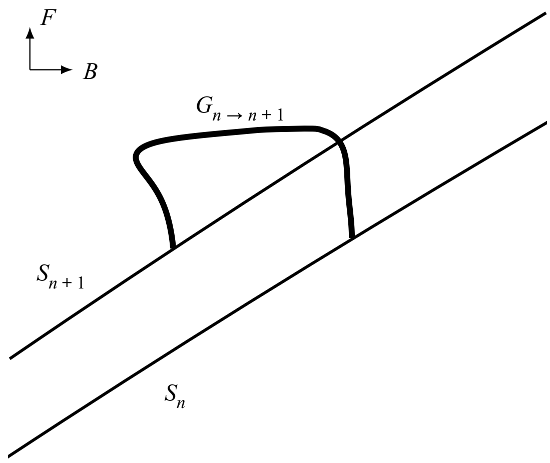

Figure 5. A typical component of the bifurcation diagram illustrated in (B, F)-space consisting of a single finger, $G_{n\to n+1}$, (shown bolded) and two side curves S_n and S_{n+1}. This is considered at a fixed value of the energy, $\mathscr{E}$.

Once solutions are found at desired values of $\mathscr{E}$, we establish the (B, F)-bifurcation space by continuation from a previously calculated solution. Note that in some cases, it will be necessary to fix B or F and solve for the other value, depending on the gradient of the bifurcation curves.

5. Numerical results for fixed energy, $\mathscr{E}$

The numerical results we now present suggest that at a fixed value of $\mathscr{E}$, certain solutions in the (B, F)-bifurcation space can be classified according to 'finger'-type structures and 'side-branch'-type structures. An example of this structure, as drawn in the (B, F)-plane, is shown in figure 5.

First, let us first define the side branch, S_n, as

$$S_n = \{\text{Bifurcation curve of solutions analogous to type (0, n)-waves}\}. \tag{5.1}$$

Thus, S_n corresponds to those points in (B, F)-space associated with a certain type of solution. These solutions are pure n-waves ($1/n$-periodic solutions in the interval); they are the nonlinear analogue of the linear type $(0, n)$-waves introduced in § 3, i.e. a sine or cosine wave with wavenumber n about a constant mean value.

In addition, adjacent side branches are connected by fingers, say $G_{n\to n+1}$. We define such a structure as

$$G_{n\to n+1} = \{\text{Bifurcation curve of solutions connecting } S_n \text{ to } S_{n+1}\}. \tag{5.2}$$

The finger can be interpreted as follows. Along S_n, solutions are pure (n)-waves; following this set of solutions, there exists a bifurcation point where the 1-mode grows. Following this new branch, which is labelled $G_{n\to n+1}$, yields a solution analogous to a type $(1, n)$-wave. Continuing along $G_{n\to n+1}$, the solution transitions to type $(1, n + 1)$ and then finally to a pure-$(n + 1)$ wave where it connects to S_{n+1}. An illustration of these classifications is shown in figure 5.

In the following sections we present solutions along the side branches, S_n, and fingers, $G_{n\to n+1}$, for waves that are approximately half the height of the highest fundamental gravity wave. For our choice of energy in (4.1*c*), this occurs at $\mathscr{E} = 0.3804$. Starting in § 5.1, we describe the structure of solutions across a prototypical finger, $G_{13\to 14}$, and then

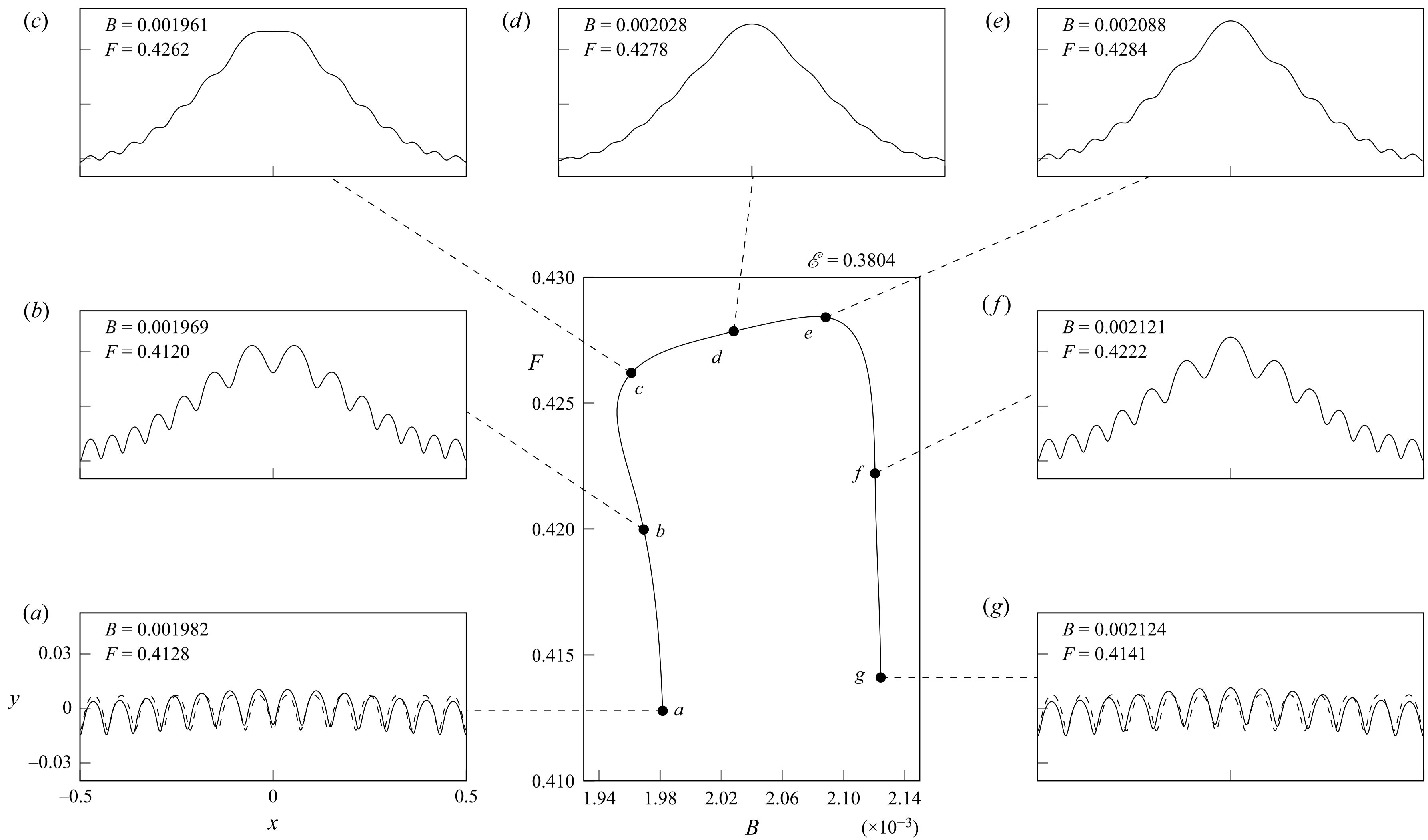

Figure 6. A single finger of solutions, $G_{13\to 14}$, is displayed in the (B, F)-plane for a value of $\mathscr{E} = 0.3804$. The dashed profiles in (a) and (g) are solutions from branches S_{13} and S_{14} near the bifurcation point. The (b)–(g) axis limits are the same as inset (a).

in § 5.2 we demonstrate how this finger bifurcates from side branches S_{13} and S_{14}. Multiple fingers are then shown in § 5.3 for $n = 7$ to 28, demonstrating their behaviour as $B \to 0$.

5.1. *Analysis of a single finger, $G_{n\to n+1}$*

The prototypical finger $G_{13\to 14}$ is shown in figure 6 for a value of $\mathscr{E} = 0.3804$. Note that solutions near the 'tip' of the finger seem to correspond to the phenomena of parasitic ripples discussed in § 1; that is, we observe a series of small-scale capillary-dominated ripples riding on the surface of a steep gravity wave. This is shown in insets (*c*), (*d*) and (*e*) in figure 6. Below, we will continue to refer to solutions as being separated into capillary ripples and an underlying gravity wave, even though this classification may be ambiguous.

As we move down either side of $G_{13\to 14}$ by decreasing the Froude number, the amplitude of the ripples increases while the amplitude of the underlying gravity wave decreases. This is shown in figure 6 via the transitions $(c) \to (b) \to (a)$ and $(e) \to (f) \to (g)$. It becomes extremely challenging to numerically compute solutions below (*a*) and (*g*).

Finally, as we travel from right to left across the finger, the wavelength of the ripples decreases as an extra ripple is formed. This can be seen by comparing solutions in insets (*g*) and (*a*), where (*g*) has 13 maxima and (*a*) has 14 maxima. The increase in the number of ripples can be observed as occurring near the tip of the finger between insets (*c*) and (*e*). We will discuss the structure of this process in § 7.

5.2. *Analysis of side branches S_n and S_{n+1}*

We now discuss the side branches. In the case of the prototypical finger, $G_{13\to 14}$, displayed in figure 6, we observe that this finger connects two side branches S_{13} and S_{14}, as shown in figure 7. The branch S_{13} contains pure (13)-waves, which have a fundamental wavelength of $\lambda = 1/13$. The branch S_{14} consists of pure 14-solutions, which have $\lambda = 1/14$.

We next observe that at fixed energy, $\mathscr{E} = 0.3804$, the solutions in S_{13} and S_{14} reach a limiting configuration through the trapping of bubbles, shown by solutions (*a*) and (*c*). These branches of solutions are the large amplitude analogue of those predicted by linear theory in § 3, given by

$$F^2 \sim 1/(2n\pi) + (2n\pi)B \quad \text{and} \quad F^2 \sim 1/(2\pi(n+1)) + 2\pi(n+1)B. \qquad (5.1a,b)$$

These were obtained by taking the values of $k = n$ and $k = n + 1$ in the linear dispersion relation (3.2).

In order to compute these branches numerically, an initial pure–n solution was taken from linear theory with the dispersion relation (3.2) satisfied for $k = n$. This gives a cosine profile with n peaks across the periodic domain. Slowly increasing the energy of this solution across multiple runs yields a single solution for each branch at $\mathscr{E} = 0.3804$, from which these branches were calculated by continuation at fixed $\mathscr{E}$.

The location along the branch for which solutions reach a limiting configuration through a trapped bubble can be numerically predicted by the results of Appendix B. These points are shown in figure 7 for $n \geqslant 15$.

We see that as the value of n for these limiting solutions increases, the value of F at these points increases beyond that of the original finger. Thus, below a certain value of the Bond number, we expect that each finger will instead bifurcate from self-intersecting solutions. As we then proceed to increase the Froude number and transverse the side of each of these fingers for $B < B_{crit}$, we anticipate that the solutions will turn physical. This would result in the tip of each finger consisting of purely physical solutions.

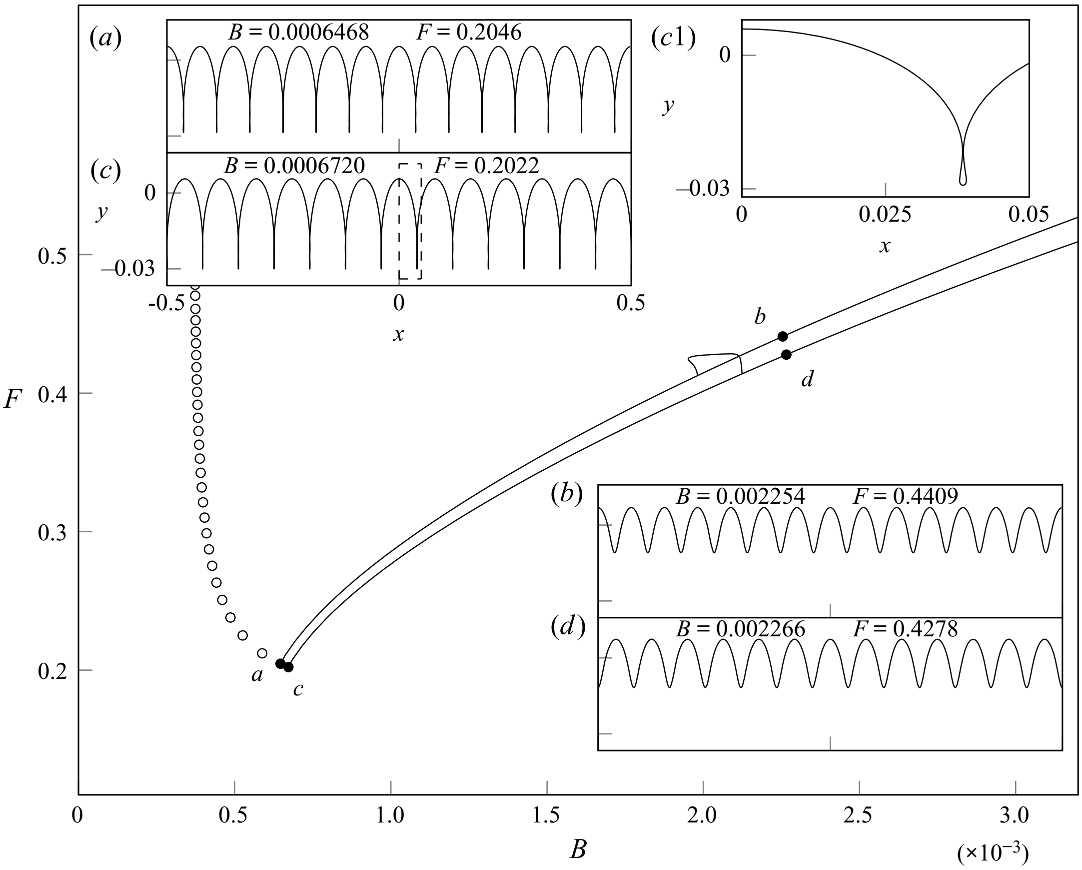

Figure 7. The finger $G_{13\to14}$ is shown against the two side branches S_{13} and S_{14}. The two side branches terminate at points a and c (black circle) through the trapping of bubbles. Circles represent the locations where solutions of S_n for $n \geqslant 15$, shown for every fifth point, become self-intersecting, found from the numerical predictions of Appendix B. The (*b*)–(*d*) axis limits are the same as inset (*c*).

5.3. *The unveiled structure for* $B \to 0$

This process of generating an individual finger may be repeated across different values of the Bond number, resulting in a remarkable structure that holds in the limit of $B \to 0$. Many of these fingers are shown in figure 8 from $n = 7$ to $n = 28$; for clarity, the side branches have been omitted from this figure. As the Bond number decreases over each finger, the wavelength of the ripples decreases from $1/n$ to $1/(n+1)$, resulting in the formation of an additional crest. Consecutive fingers are connected at the point from which they bifurcate from the side branches of pure n-waves, demonstrated previously in § 5.2 and shown by solutions ($d1$) and ($d2$) in figure 8. The solutions at these bifurcation points display a phase shift of $1/n$ between them. Due to this phase shift, the nth Fourier coefficient changes sign between these solutions at this bifurcation point. It is this phase shift that led Chen & Saffman (1979) to misleadingly state (on p. 204) that the weakly nonlinear solutions are discontinuous with respect to the nth Fourier coefficient at this point.

From solutions ($a1$), (b) and (c), labelled at the top of the fingers in figure 8, we observe that as $B \to 0$, the amplitude of the ripples decreases and the overall solution appears to tend towards the fundamental Stokes wave with energy $\mathscr{E}$. Although the profile in figure 8($a1$) seems to indicate a pure gravity wave, the capillary ripples can be detected under closer inspection. In order to quantify this, we isolate the pure gravity wave solution,

https://doi.org/10.1017/jfm.2021.514 Published online by Cambridge University Press

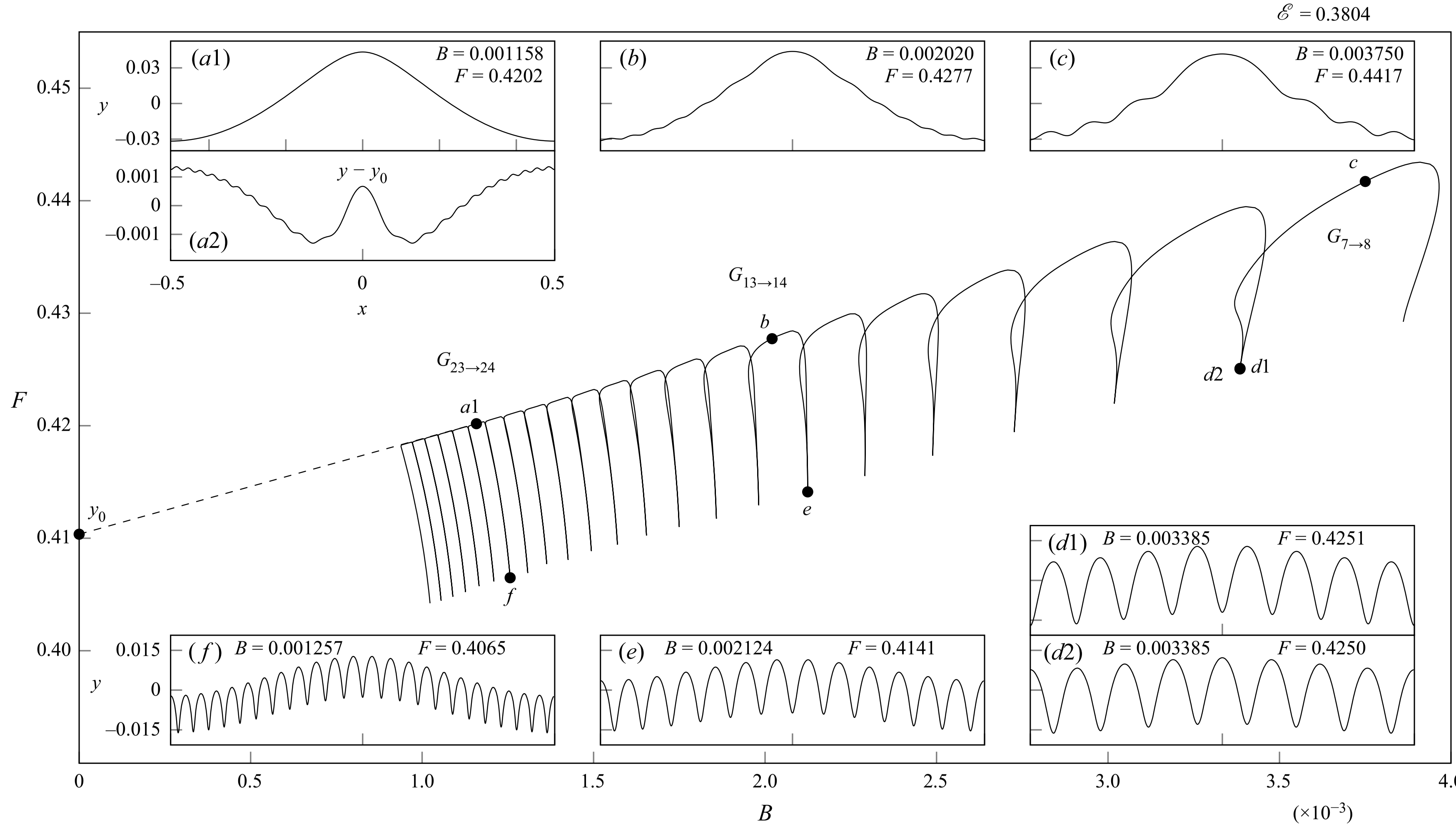

Figure 8. Multiple fingers $G_{7\to 8}$ to $G_{28\to 29}$ are shown to form one connected branch in the (B, F)-plane at fixed $\mathscr{E} = 0.3804$. The (b)–(c) axes limits are the same as inset (a1) and the (e)–(d) limits are the same as inset (f).

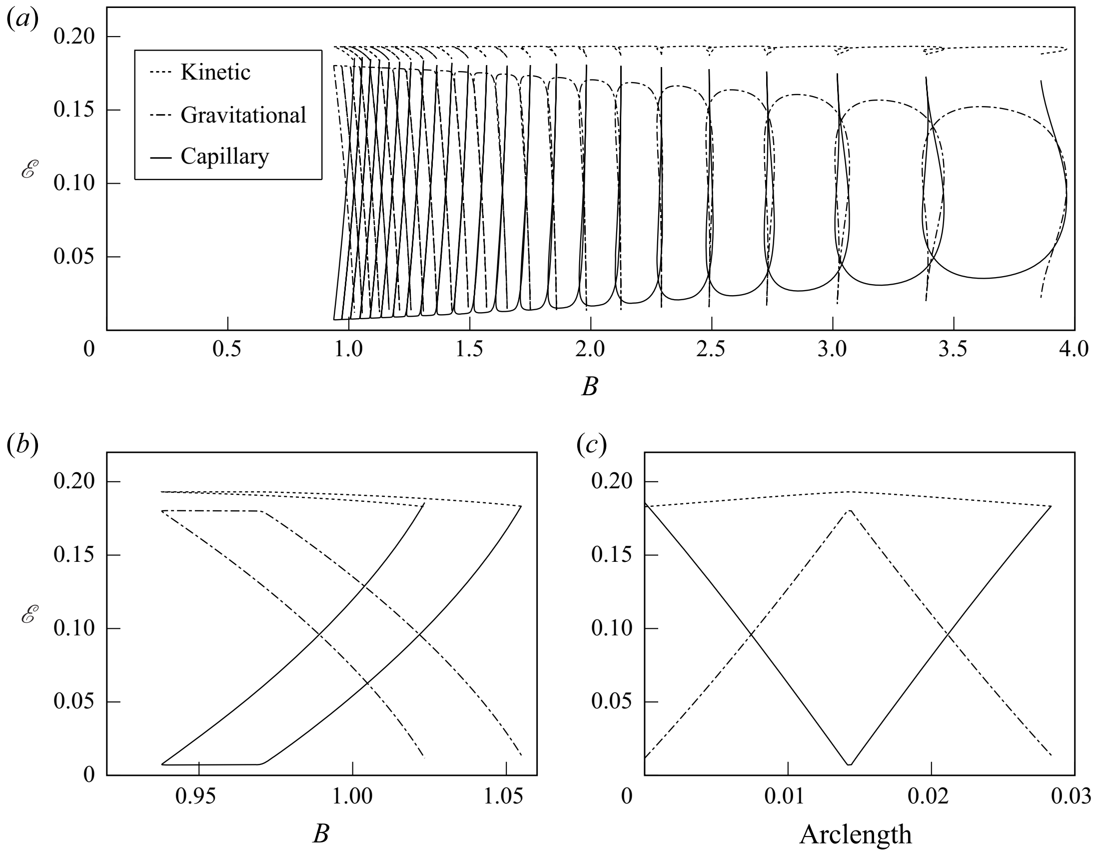

Figure 9. (*a*) The corresponding kinetic (dotted), gravitational (dash–dotted) and capillary (solid) energies for the solutions from figure 8. In the two lower figures, the kinetic, capillary and gravitational energies are also shown for (*b*) B vs $\mathscr{E}$ and (*c*) branch arclength vs $\mathscr{E}$ for the solutions corresponding to the single finger $G_{28\to29}$.

y_0, and plot $y - y_0$ in figure 8($a2$). This shows that the ripples are still present in the solution, but with a very small amplitude. Moreover, one can verify that the profile norm, $|y - y_0|$, is of $O(B)$ by repeating this procedure for multiple solutions along the top of the fingers in figure 8. We shall comment on this algebraic error and the exponentially small ripples in § 7.

We note that the presence of this bifurcation from the side branches S_n to the fingers $G_{n\to n+1}$ can be observed by a change in sign of the Jacobian along S_n as the bifurcation point is passed. Solutions close to this bifurcation point are shown by (a) and (g) in figure 6 for S_n (dashed) and $G_{n\to n+1}$ (solid). A further change of sign in the Jacobian occurs at the top of each of the fingers. Since our numerical scheme permits asymmetric solutions through the retention of the asymmetric coefficients in the Fourier series expression (2.7), it may be that this additional bifurcation involves symmetry breaking. A brief overview of gravity-capillary works containing asymmetry is provided in § 7. However, no such solutions were found during our investigation.

Furthermore, the range of F between the tip of each finger and the bottom remains of $O(1)$ as $B \to 0$ for the solutions calculated in figure 8. Consider, for instance, the range between solutions ($a1$) and (f). This suggests the existence of an interval of solutions holding under the $B \to 0$ limit. The solution with the largest value of F is expected to be the fundamental Stokes wave with $B = 0$ and $\mathscr{E} = 0.3804$, shown by the point y_0 in figure 8. We predict that, as $B \to 0$, the solutions with the smallest Froude number in this interval will contain a self-intersecting free surface. This is because, for

$B < B_{crit}$, the pure n-solutions near the bifurcation point on the side branches are also anticipated to self-intersect. The interval would then contain a range of solutions, which transition from unphysical to physical as the Froude number increases. A further detail of the structure of these solutions may be seen from figure 9, which shows the exchange between the three components of kinetic, capillary and gravitational potential energies. For the parasitic solutions at the top of each of the fingers, which resemble a perturbation about a gravity-dominated wave, the capillary energy is small and appears to decrease to zero as $B \to 0$. Conversely, for the highly oscillatory solutions close to the bifurcation point between adjacent fingers, the capillary and kinetic energies are seen to tend to an $O(1)$ constant while the gravitational potential energy tends to zero. Thus, these highly oscillatory solutions of $G_{n\to n+1}$, as well as those on the side branch S_n, appear to tend towards a pure-capillary solution as $B \to 0$. The asymptotic properties of the solutions on $G_{n\to n+1}$ and S_n will be discussed in § 7 for the limit of $B \to 0$.

6. Relation to previous numerical attempts

A key challenge is to understand the relationship between our solutions of fixed energy, $\mathscr{E}$, and those of previous authors with a different amplitude condition, say $\mathscr{A}$. In this section we demonstrate that a key limitation of previous choices of amplitude is the existence of highly energetic (and subsequently nonlinear) solutions at small values of $\mathscr{A}$. Thus, somewhat surprisingly, alternative choices of the amplitude measure may admit nonlinear solutions in the naive linear limit of $\mathscr{A} \to 0$ – this occurs due to the singular nature of $B \to 0$ and, in particular, the nature of the solutions between adjacent fingers.

6.1. *Solutions at different values of the energy $\mathscr{E}$*

In the previous section we demonstrated the structure of the bifurcation diagram and associated solutions at fixed energy $\mathscr{E} = 0.3804$. In fact, this bifurcation structure is only perturbed in a regular fashion as the energy changes near this value. Thus, the full structure of solutions, which holds as $B \to 0$, can be computed for different values of $\mathscr{E}$ in a straightforward manner.

We show an example of this in figure 10, where we display the finger $G_{11\to 12}$ and the side branches S_{11} and S_{12} for three different values of $\mathscr{E}$. In the figure the value of $\mathscr{E}$ decreases from $\mathscr{E} = 0.67$ in (*a*) to $\mathscr{E} = 0.3804$ in (*b*) to $\mathscr{E} = 0.046$ in (*c*). The following three changes to either the solution or branch structure are noticeable as $\mathscr{E}$ decreases:

(i) the amplitude of the ripples decreases;
(ii) the range of F between the top and bottom of the finger decreases; and
(iii) the finger becomes more rectangular.

In (*c*) the amplitude of the ripples has decreased to the point at which they are no longer observable visually.

6.2. *Choice of amplitude parameters in previous works*

We now revisit the alternative choices of the amplitude or energy parameter in (2.13). A few of the solutions displayed in figure 8 are similar to those previously calculated by Schwartz & Vanden-Broeck (1979), who plotted remnants of this figure at larger values of

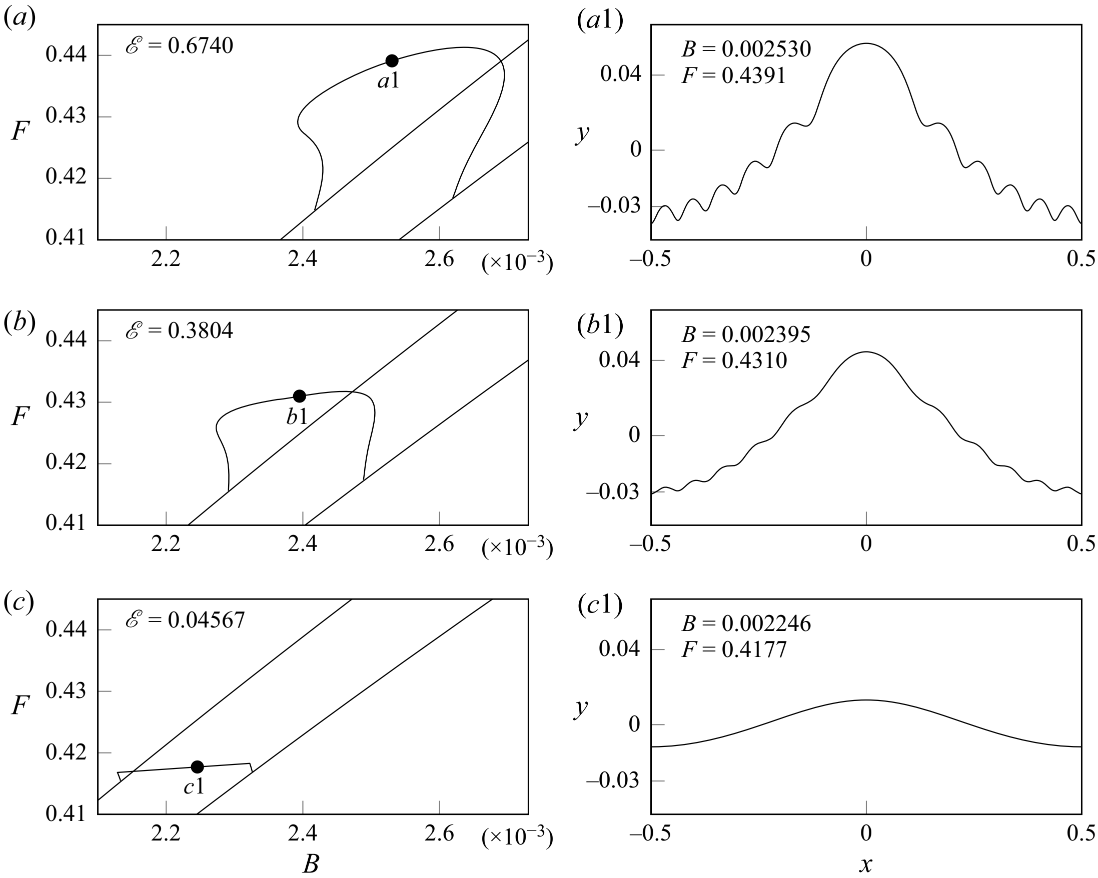

Figure 10. Shown in the left subplots are the fingers $G_{11\to 12}$ and the side branches S_{11} and S_{12}, plotted in the (B, F)-plane, for (*a*) $\mathscr{E} = 0.67$; (*b*) $\mathscr{E} = 0.3804$; (*c*) $\mathscr{E} = 0.046$. Example solutions, near the tops of the fingers, are shown in the corresponding right subplots labelled (*a*1), (*b*1) and (*c*1).

B for a different amplitude parameter. Since their choice of amplitude,

$$\mathscr{A} = A \equiv [y(0) - y(\pi)]/2\pi, \tag{6.1}$$

relies on local values at the centre and edge of the periodic domain, they found these branches to behave somewhat differently than how we have described them in our § 5.

Notice that according to their choice of norm (6.1), waves with an even number of crests that are equally spaced throughout the domain will have $y(0) = y(\pi)$ and, consequently, $A = 0$. This corresponds to every other branch of solutions with a fundamental wavelength smaller than the periodic domain, S_n with n even. Hence, for the branch of solutions $G_{n\to n+1}$ at fixed $\mathscr{E}$, A grows smaller tending towards solutions near the bifurcation points of S_{n+1} and S_n – despite the high nonlinearity of these solutions. This is demonstrated for $n = 13$ in figure 6 with solution (*a*), which approaches S_{14}, and solution (*g*), which approaches S_{13}. Thus, the bifurcation from S_{14} connecting finger $G_{14\to 15}$ to $G_{13\to 14}$ will occur from an amplitude value of $A = 0$. This is one reason why the full structure of solutions was not revealed through smooth continuation at fixed A by the investigations of Schwartz & Vanden-Broeck (1979).

Next, let us turn to the numerical investigation of the $B \to 0$ limit performed by Chen & Saffman (1980*b*), who fixed the first Fourier coefficient,

$$\mathscr{A} = A_1, \tag{6.2}$$

as an amplitude parameter. We now know that, since the bifurcation between distinct fingers in the (B, F)-plane occurs via the side branches S_n, which have a first Fourier coefficient of zero for $n \geqslant 2$, it is impossible to recover the structure shown in figure 8 with a fixed value of A_1. Chen & Saffman (1980*b*) had indicated the impossibility of a continuous deformation to the pure Stokes gravity wave as $B \to 0$, but we now see that this occurred as a direct consequence of their chosen amplitude parameter.

6.3. *An insufficient number of Fourier coefficients*

As we have noted, it is crucial to select the right continuation parameter in order to recover the $B \to 0$ limit. There are other possible reasons why others may have struggled to reproduce an accurate structure of the parasitic ripple phenomena. In particular, a large number of Fourier modes are required in order to capture the regions between adjacent fingers, and this is primarily due to the bifurcation occurring from the side branches, S_n, which contains solutions that approach pure n-waves. Thus, solutions within the finger $G_{n\to n+1}$, which are located near to side branches are then dominated by the nth Fourier coefficient. If in our numerical scheme we consider a series truncation at the Nth Fourier coefficient, then the main coefficients contributing to the capillary-dominated ripples will be a multiple of n. Hence, an effective number of N/n Fourier coefficients will describe the behaviour of the wave near to this bifurcation point.

For the computation of the gravity-capillary wave with the parasitic ripples, Schwartz & Vanden-Broeck (1979) (their figure 10) used $N = 40$ in order to capture a wave with $n = 11$ ripples. Thus, in order to investigate the side branch bifurcation associated with this solution, their Fourier expansions would have contained an effective number of $N/n \approx 4$ Fourier coefficients – which is insufficient. Within this work, we have been using 1024 Fourier coefficients, which corresponds to 35 effective coefficients for solutions near the bifurcation point of the finger with the smallest Bond number in figure 8.

6.4. *The symmetry shifting bifurcation*

In addition to the importance of selecting an appropriate amplitude measure, let us discuss the relationship between the bifurcation structure presented earlier (e.g. in our figure 8) with the constraint on the symmetry in the travelling-wave frame. For the solutions displayed in figure 8, each finger is computed beginning with an initial solution that lies on the finger and then, with a fixed $\mathscr{E}$, solutions are obtained by continuation to either side of the starting point until the entire finger is computed. As a result of this continuation scheme, the solutions at the bottom of adjacent fingers are out of phase with one another; this can be seen in solutions (*d*1) and (*d*2) in figure 8. This method of continuation is depicted more clearly in figure 11(*a*), where (*a*1) and (*a*2) are two starting solutions, while (*a*3) and (*a*4) are out of phase. Note also that this phase shift is observable between the profiles (*g*) and (*e*) in figures 6 and 8, respectively, as these are solutions either side of the same bifurcation point.

Alternatively, we could formulate a continuation scheme where the solutions in each finger are connected to those in adjacent fingers in a continuous fashion, depicted in figure 11(*b*). Thus, for example, the scheme is started with a single initial point, (*b*1), shown in figure 11. This finger is then found via the typical continuation method. Having located a solution, (*b*3), at the bifurcation point, the adjacent finger is completed by using (*b*3) as a starting solution for continuation. This alternative method shown in figure 11(*b*) results in solutions (*b*3) and (*b*4) at the bottom of consecutive fingers with no phase shift. The result of this approach is a continuous set of solutions as $B \to 0$.

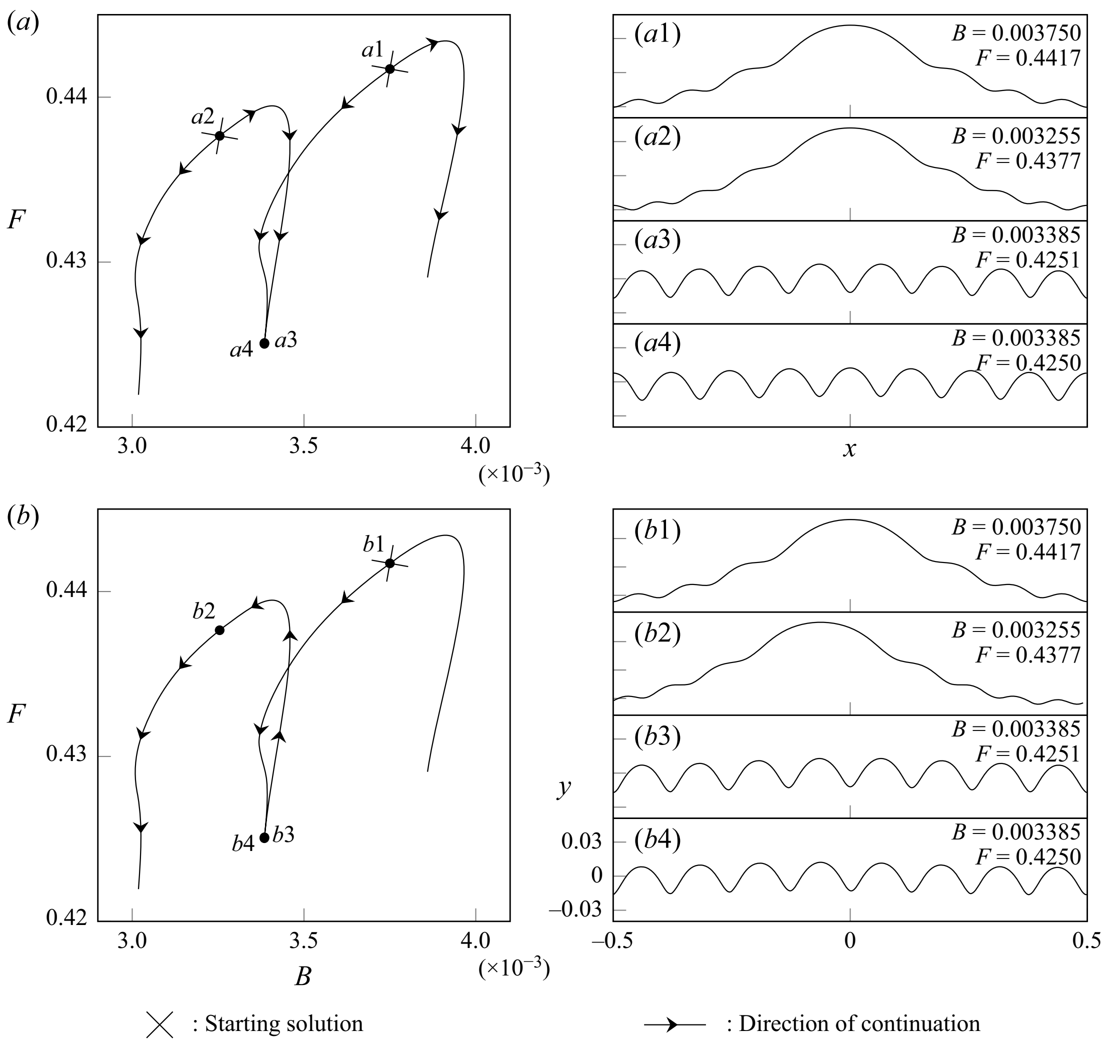

Figure 11. Two methods for numerical continuation are depicted. The starting location for continuation is denoted by a cross, and the arrows indicate the direction travelled by continuation.

In using this alternative method, solutions at the top of consecutive fingers have a shifted point of symmetry, as demonstrated by comparing solutions ($b1$) and ($b2$) in figure 11. This point of symmetry has been moved from $x = 0$ to $x = -1/n$ for all solutions on the new finger. We denote this to be a symmetry shifting bifurcation, which is unable to be captured if the point of symmetry of the wave is prespecified. This assumption of a fixed point of symmetry is often used in the two following methods.

(i) Numerical procedures that solve for the half-domain $x = [0, 1/2]$ and enforce a turning point at $x = 0$, such as that by Schwartz & Vanden-Broeck (1979).

(ii) The analytical work of Chen & Saffman (1979), who posit a weakly nonlinear solution with assumed symmetry at $x = 0$.

Both of these methods will be unable to capture this $B \to 0$ limit with continuous solutions at the bifurcation point.

The relaxation of the fixed point of symmetry, in contrast to the assumption in Chen & Saffman (1979), is the modification required to correct their earlier statement on the validity of the $B \to 0$ limit for gravity-capillary waves.

6.5. *Conclusions*

We have studied the bifurcation structures derived in the previous works by Schwartz & Vanden-Broeck (1979) and Chen & Saffman (1979, 1980*b*), and have highlighted the following three core issues that are important for unifying and extending their diagrams to the small Bond number regime.

(i) The chosen amplitude parameters, relying either on local values of the wave height or specific Fourier coefficients (cf. § 6.2).
(ii) A small number of Fourier coefficients retained in the numerical schemes, the issues for which become more prominent near the bifurcation points (cf. § 6.3).
(iii) Assumptions made on the point of symmetry of the wave profile (usually fixed to be at $x = 0$), due to the symmetry shifting bifurcation connecting adjacent fingers (cf. § 6.4).

In being aware of these, we have introduced alternative methods, either by solving or mitigating the issues. For instance, we have used the wave energy, $\mathscr{E}$, as an amplitude parameter. This has allowed us to be able to find a number of different types of solutions to the steep gravity-capillary wave problem existing under the limit of $B \to 0$. One of these, the steady symmetric parasitic ripple, is similar to the asymmetric parasitic waves encountered physically and will be the focus of our forthcoming analytical work.

7. Discussion

In § 5.3 we described the two types of solutions that are found as $B \to 0$. The first of these are found along the sides of the fingers and the side branches; they can be described by a multiple-scales type expansion that captures the rapid oscillations about a slowly varying mean. As they become increasingly oscillatory (with diminishing F), they reach an unphysical configuration through the trapping of bubbles for $B < B_{crit}$ (cf. end of § 5.2). These highly oscillatory solutions near the bifurcation point between adjacent fingers are very interesting. This is because a multiple-scales ansatz yields Crapper's pure-capillary equation, that is, Bernoulli's equation (2.1*c*) in the absence of gravity, at leading order for the small-scale ripples. Since an exact solution for this is well known by the work of Crapper (1970), it may be possible that once the boundary conditions of periodicity and energy have been applied to the solvability condition (obtained at the next order) our snaking structure of the fingers can be found analytically. This multiple-scales approach will be the focus of future analytical work by the current authors. We note that this snaking structure is very similar to that found by Chapman & Kozyreff (2009) for a version of the Swift–Hohenberg equation appearing in nonlinear optics.

Our focus has been more on the second of these types of solutions – those which correspond to waves with parasitic ripples lying on a gravity wave; these solutions are found near the tops of each finger. In a forthcoming work, Shelton & Trinh (2021), we shall present an asymptotic theory for the description of these parasitic ripples.

The essential details are as follows. For those solutions that correspond to parasitic ripples on gravity waves, we may expand their form as a naive expansion in powers of the Bond number,

$$y(x) = \sum_{n=0}^{\infty} B^n y_n(x), \tag{7.1}$$

such that in the limit of $B \to 0$ we recover the pure gravity wave, y_0. However, as it turns out, the magnitude of the short wavelength parasitic ripples is exponentially small in the

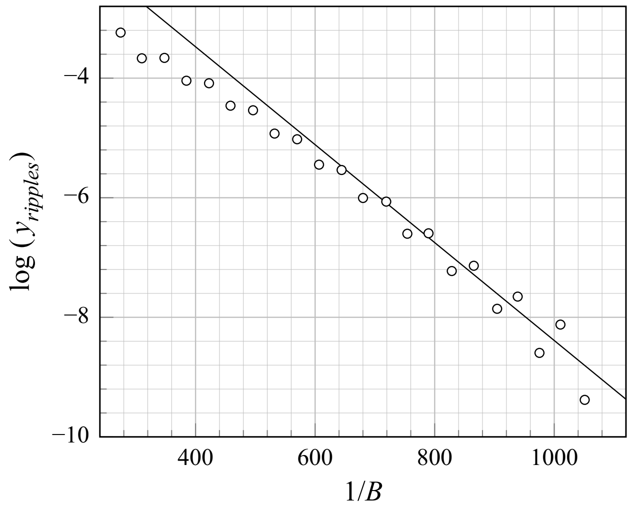

Figure 12. The exponential scaling in (7.2) is shown (circles) for our numerical solutions by plotting $1/B$ vs $\log(y_{ripples})$. One numerical solution is chosen from each finger, corresponding to that of minimal ripple amplitude. From our forthcoming work, the analytical prediction (line), which depends on the value of $\mathscr{E}$, predicts a gradient of approximately -8.2×10^{-3}.

Bond number, B. Thus,

$$|y_{ripples}| \sim \exp\left(-\frac{\text{const.}}{B}\right). \tag{7.2}$$

The above can be validated based on our numerical computations in the following way. For each finger, $G_{n\to n+1}$, a solution profile is calculated at the tip of the finger (i.e. the vertex in the (B, F)-plane). At this point, the magnitude of the parasitic ripple is approximated by examining $y - y_0$ and measuring the crest-to-trough amplitude for the oscillation nearest to the edge of the domain, $x = 1/2$ (a typical profile is shown in ($a2$) of figure 8). The result of this numerical experiment is shown in figure 12; indeed, the ripple amplitude lies approximately on a straight line in the semilog plot, confirming the exponential smallness of the ripples as $B \to 0$.

Thus, in light of (7.2) these parasitic ripples will fail to be captured by (7.1) and must be found beyond-all-orders of the naive asymptotic expansion. Consequently, the use of specialised tools in asymptotic analysis, known as exponential asymptotics, are required (see, e.g. Chapman, King & Adams 1998; Chapman & Vanden-Broeck 2006; Trinh & Chapman 2013). Here, the necessary theory for prediction of the parasitic ripples is analogous, in spirit, to theories for the prediction of generalised solitary waves (Boyd 1998), but there are a number of additional challenges due to the more involved boundary-integral framework and the lack of a closed-form leading-order Stokes solution, y_0. Similar bifurcation structures have also been noted in the context of wave-structure interactions of gravity waves, as seen in the works of , for example, Dias & Vanden-Broeck (2004), Binder, Dias & Vanden-Broeck (2008), Holmes *et al.* (2013), Hocking, Holmes & Forbes (2013); we would expect that our work here with freely propagating waves can be related to more complex problems where the bottom topography has an appreciable effect.

We remark, in addition, that the idea of exponentially small parasitic capillary ripples in the classic Stokes wave problem is not a new one. Indeed, as we discussed in § 1.1, Longuet-Higgins (1963) had proposed an analytical methodology for the derivation of parasitic ripples (followed by a similar approach in Longuet-Higgins 1995). However, both of these approaches are *ad hoc* in nature, and as noted by Perlin *et al.* (1993), fail to predict the correct magnitude of the ripples. Other theories, such as the averaged Lagrangian methodology of Crapper (1970), exhibit similar difficulties in providing rigorous comparison to numerical results – the latter author notes that '... [the theory] is not very accurate, but at the timing of writing is probably the best available' (p. 154). Consequently, the point we emphasise is that the systematic $B \to 0$ results we have presented in this paper are crucial for validation of the small surface tension limit. The presentation of a complete exponential asymptotics treatment of $B \to 0$ and the importance of prior approaches in inspiring such a methodology will be the focus of our forthcoming work.

Finally, we have only found symmetric solutions of the parasitic ripples problem in this work. For general values of B and F, and not necessarily only for the regime of small B, we note that there are extensive efforts to search for steady asymmetric solutions. See, for instance, the works on gravity-capillary waves by Zufiria (1987*b*) for finite depth, Shimizu & Shōji (2012) for infinite depth, and Zufiria (1987*a*) for pure gravity on infinite depth. Indeed, many of the asymmetric profiles in the works of, for example, Shimizu & Shōji (2012) exhibit similarities to the profiles shown in our work. Thus, it seems likely that the bifurcation structures we have presented in this work form a subset of a much more complicated structure that includes the potential for asymmetry. It remains to be seen if this asymmetry of the steady system would account for that observed in the experimental results, or whether it is necessary to consider unsteady flows, such as the time-dependent Navier–Stokes formulation considered numerically by Mui & Dommermuth (1995) and Hung & Tsai (2009). We further note that asymmetric wave profiles have also been found with the unsteady potential flow formulation considered by Moreira & Peregrine (2010) over a submerged cylinder.

Acknowledgements. We are grateful to Professor N. Ebuchi for generously providing the photo displayed in figure 1, captured during the experimental work of Ebuchi *et al.* (1987). We also thank the anonymous reviewers for their suggestions to improve the clarify of this manuscript.

Declaration of interests. The authors report no conflict of interest.

Author ORCIDs.
Josh Shelton https://orcid.org/0000-0001-6257-5190;
Paul Milewski https://orcid.org/0000-0003-4454-8441;
Philippe H. Trinh https://orcid.org/0000-0003-3227-1844.

Appendix A. The wave energy

The non-dimensionalised bulk energy in the physical domain is given by

$$\bar{E} = \frac{F^2}{2}\int_{-1/2}^{1/2}\int_{-\infty}^{\eta}(\phi_x^2+\phi_y^2)\,\mathrm{d}y\,\mathrm{d}x + B\int_{-1/2}^{1/2}\left([1+\eta_x^2]^{1/2}-1\right)\mathrm{d}x + \int_{-1/2}^{1/2}\int_{-\infty}^{\eta} y\,\mathrm{d}y\,\mathrm{d}x. \tag{A1}$$

On the right-hand side, the three groups correspond to the kinetic, capillary potential and gravitational potential energies.

Note that due to our subflow (where $\phi_x \to -1$ as $y \to -\infty$), the first and third integrals on the right-hand side of (A1) will be unbounded. We thus define the energy, E, to be the difference between (A1) and 'no-flow', $\eta = 0$, energy, which yields a finite value. This is then transformed to act on the free surface, $\psi = 0$, only by the method of Longuet-Higgins (1989), with which we change variables from (x, y) to find the wave energy under the

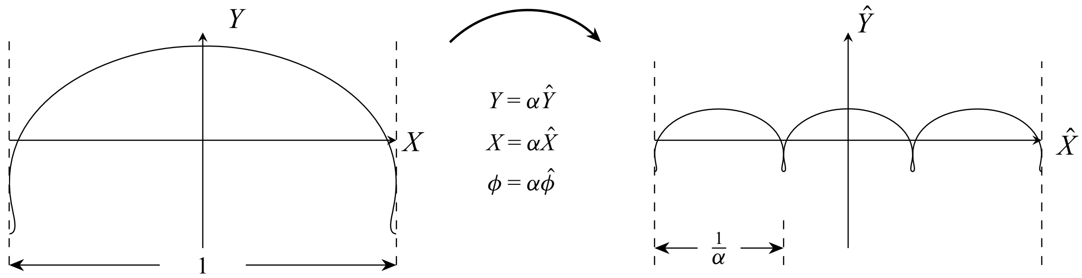

Figure 13. The rescaling used to produce another solution with a smaller fundamental wavelength is shown.

(ϕ, ψ) mapping,

$$E = \frac{F^2}{2}\int_{-1/2}^{1/2} Y(X_\phi - 1)\,\mathrm{d}\phi + B\int_{-1/2}^{1/2}(\sqrt{J} - X_\phi)\,\mathrm{d}\phi + \frac{1}{2}\int_{-1/2}^{1/2} Y^2 X_\phi\,\mathrm{d}\phi. \qquad \text{(A2)}$$

With this choice of amplitude parameter, $E_{hw} \approx 0.00184$ corresponds to the fundamental Stokes wave of maximum height. We rescale the energy by this value to obtain the amplitude parameter, $\mathscr{E}$, used within this report, given by $\mathscr{E} = E/E_{hw}$, in (4.1*c*).

Appendix B. Limiting solutions of smaller fundamental wavelength

If one solution is known to the gravity-capillary wave problem with fundamental wavelength $\lambda = 1$, another can be constructed with $\lambda = 1/\alpha$, where α is a positive integer. This is visualised in figure 13. Suppose we have a solution to Bernoulli's equation (4.1*a*) and the harmonic relation (4.1*b*). In rescaling $Y = \alpha\hat{Y}$, $X = \alpha\hat{X}$ and $\phi = \alpha\hat{\phi}$, we repeat the first solution α times to map the original domain from $\phi \in [-\alpha/2, \alpha/2)$ to the new domain $\hat{\phi} \in [-1/2, 1/2)$. This new solution, $\hat{X}$ and $\hat{Y}$, also satisfies the two governing equations with rescaled Froude and Bond numbers $\hat{F}$ and $\hat{B}$, given by

$$\hat{F} = \frac{F}{\sqrt{\alpha}} \quad \text{and} \quad \hat{B} = \frac{B}{\alpha^2}. \qquad \text{(B1}a,b\text{)}$$

The energy of this new solution can be found by substituting the rescaled variables $\hat{X}$, $\hat{Y}$, $\hat{F}$ and $\hat{B}$ into (4.1*c*), yielding

$$\hat{\mathscr{E}} = \frac{\mathscr{E}}{\alpha^2}. \qquad \text{(B1}c\text{)}$$

Since $\alpha > 1$, the energy of the new pure α-wave, $\hat{\mathscr{E}}$, will always be smaller than that of the original wave, $\mathscr{E}$.

This ability to construct new solutions with a fundamental wavelength shorter than the periodic domain allows us to numerically predict the point at which solutions in the side branches S_α begin to trap a bubble through a self-intersecting free surface. These locations are shown in the bifurcation diagram of figure 7. As all of these side branch solutions have the same energy, $\hat{\mathscr{E}} = 0.3804$, but different values of α, the energy of the original wave is given by $\mathscr{E} = \alpha^2\hat{\mathscr{E}}$.

The procedure to find the location at which solutions in S_α become self-intersecting is as follows.

(i) First, we numerically calculate the (B, F)-solution space of pure 1-waves with a single trapped bubble amplitude condition. The energy of these solutions will vary.

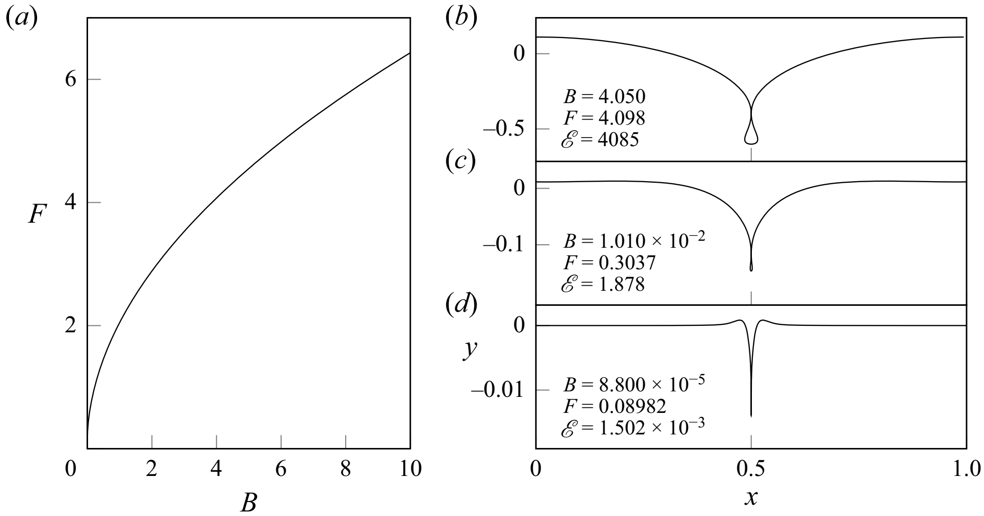

Figure 14. (*a*) The branch of pure-1 solutions displaying an enclosed bubble is shown in the (B, F)-bifurcation diagram. Note that we have displayed the domain $x \in [0, 1]$ to demonstrate this limiting behaviour.

(ii) Second, we select the profile with $\mathscr{E} = \alpha^2\hat{\mathscr{E}}$ and obtain values for B and F.

(iii) Third, we rescale these by using (B1*a*) to find $\hat{F}$ and $\hat{B}$. This yields the location at which solutions within the side branch, S_α, become self-intersecting.

Repeating this process for multiple values of α yields the predictions displayed with the circles in figure 7. With this method we are able to calculate solutions with a large value of α while keeping the number of Fourier coefficients used during Newton iteration fixed, and, thus, do not encounter the issue discussed in § 6.3.

It would also be possible to use this method to compute all of the solutions along the side branch S_α. However, this requires the entire sheet of pure 1-wave solutions to be found in the three-dimensional $(B, F, \mathscr{E})$-solution space, which we consider to be prohibitively expensive computationally. By restricting only to profiles displaying a single trapped bubble, this solution space simplifies to a single branch throughout the $(B, F, \mathscr{E})$-bifurcation diagram, which we projected to the (B, F)-plane for simplicity.

B.1. *Limiting pure*-1 *solution space*

This branch of limiting solutions is displayed in figure 14(*a*). These solutions were found from the same numerical procedure as in § 4. An initial limiting solution, displaying one trapped bubble, is found by increasing $\mathscr{E}$. The energy constraint is then replaced by a trapped bubble condition, which forces the second turning point of $X(\phi)$ to a value of -0.5. We then explore the (B, F)-solution space by continuation.

We note that as $B \to \infty$ along this branch, the wave profile approaches the limiting pure-capillary solution found by Crapper (1957) (see their figure 1) with an amplitude of 0.730. Solution (*b*), with $B = 4.050$, is an example of this. As $B \to 0$ along the same branch, the solution approaches a depressive solitary wave, demonstrated by solution (*d*). This is since the small B limit is related to the solitary wave limit of $L_\lambda \to \infty$. The solutions calculated by Schwartz & Vanden-Broeck (1979) (see their figure 2) form the intermediate range between these two limits.

References

Binder, B.J., Dias, F. & Vanden-Broeck, J.-M. 2008 Influence of rapid changes in a channel bottom on free-surface flows. *IMA J. Appl. Maths* **73** (1), 254–273.

Boyd, J.P. 1998 *Weakly Nonlocal Solitary Waves and Beyond-All-Orders Asymptotics*. Kluwer Academic.

Chapman, S.J., King, J.R. & Adams, K.L. 1998 Exponential asymptotics and Stokes lines in nonlinear ordinary differential equations. *Proc. R. Soc. Lond.* A **454**, 2733–2755.

Chapman, S.J. & Kozyreff, G. 2009 Exponential asymptotics of localised patterns and snaking bifurcation diagrams. *Physica* D **238** (3), 319–354.

Chapman, S.J. & Vanden-Broeck, J.-M. 2006 Exponential asymptotics and gravity waves. *J. Fluid Mech.* **567**, 299–326.

Chen, B. & Saffman, P.G. 1979 Steady gravity-capillary waves on deep water–1. Weakly nonlinear waves. *Stud. Appl. Maths* **60** (3), 183–210.

Chen, B. & Saffman, P.G. 1980*a* Numerical evidence for the existence of new types of gravity waves of permanent form on deep water. *Stud. Appl. Maths* **62** (1), 1–21.

Chen, B. & Saffman, P.G. 1980*b* Steady gravity-capillary waves on deep water–II. Numerical results for finite amplitude. *Stud. Appl. Maths* **62** (2), 95–111.

Cox, C.S. 1958 Measurements of slopes of high-frequency wind waves. *J. Mar. Res.* **16**, 199–225.

Crapper, G.D. 1957 An exact solution for progressive capillary waves of arbitrary amplitude. *J. Fluid Mech.* **2** (6), 532–540.

Crapper, G.D. 1970 Non-linear capillary waves generated by steep gravity waves. *J. Fluid Mech.* **40** (1), 149–159.

Dias, F. & Vanden-Broeck, J.-M. 2004 Trapped waves between submerged obstacles. *J. Fluid Mech.* **509**, 93–102.

Ebuchi, N., Kawamura, H. & Toba, Y. 1987 Fine structure of laboratory wind-wave surfaces studied using an optical method. *Boundary-Layer Meteorol.* **39** (1–2), 133–151.

Hocking, G.C., Holmes, R.J. & Forbes, L.K. 2013 A note on waveless subcritical flow past a submerged semi-ellipse. *J. Engng Maths* **81** (1), 1–8.

Holmes, R.J., Hocking, G.C., Forbes, L.K. & Baillard, N.Y. 2013 Waveless subcritical flow past symmetric bottom topography. *Eur. J. Appl. Maths* **24** (2), 213–230.

Hung, L.-P. & Tsai, W.-T. 2009 The formation of parasitic capillary ripples on gravity–capillary waves and the underlying vortical structures. *J. Phys. Oceanogr.* **39** (2), 263–289.

Longuet-Higgins, M.S. 1963 The generation of capillary waves by steep gravity waves. *J. Fluid Mech.* **16**, 138–159.

Longuet-Higgins, M.S. 1989 Capillary–gravity waves of solitary type on deep water. *J. Fluid Mech.* **200**, 451–470.

Longuet-Higgins, M.S. 1995 Parasitic capillary waves: a direct calculation. *J. Fluid Mech.* **301**, 79–107.

Moreira, R.M. & Peregrine, D.H. 2010 Nonlinear interactions between a free-surface flow with surface tension and a submerged cylinder. *J. Fluid Mech.* **648**, 485.

Mui, R.C.Y. & Dommermuth, D.G. 1995 The vortical structure of parasitic capillary waves. *Trans. ASME J. Fluids Engng* **117**, 355–361.

Okamoto, H. & Shōji, M. 2001 *The Mathematical Theory of Permanent Progressive Water-Waves*. World Scientific.

Perlin, M., Lin, H. & Ting, C.-L. 1993 On parasitic capillary waves generated by steep gravity waves: an experimental investigation with spatial and temporal measurements. *J. Fluid Mech.* **255**, 597–620.

Schwartz, L.W. & Vanden-Broeck, J.-M. 1979 Numerical solution of the exact equations for capillary–gravity waves. *J. Fluid Mech.* **95** (1), 119–139.

Shelton, J. & Trinh, P.H. 2021 Exponential asymptotics for steady-state parasitic gravity-capillary waves. arXiv:2106.09495.

Shimizu, C. & Shoji, M. 2012 Appearance and disappearance of non-symmetric progressive capillary–gravity waves of deep water. *Japan J. Ind. Appl. Maths* **29** (2), 331–353.

Stokes, G.G. 1847 On the theory of oscillatory waves. *Trans. Camb. Phil. Soc.* **8**, 441–455.

Toland, J.F. 1996 Stokes waves. *Topol. Method. Nonlinear Anal.* **7** (1), 1.

Trinh, P.H. & Chapman, S.J. 2013 New gravity-capillary waves at low speeds. Part 1: linear theory. *J. Fluid Mech.* **724**, 367–391.

Vanden-Broeck, J.-M. 2010 *Gravity-Capillary Free-Surface Flows*. Cambridge University Press.

Wilton, J.R. 1915 On ripples. *Phil. Mag.* **29** (173), 688–700.

Zufiria, J.A. 1987*a* Non-symmetric gravity waves on water of infinite depth. *J. Fluid Mech.* **181**, 17–39.

Zufiria, J.A. 1987*b* Symmetry breaking in periodic and solitary gravity-capillary waves on water of finite depth. *J. Fluid Mech.* **184**, 183–206.

EXPONENTIAL ASYMPTOTICS FOR NONLINEAR TRAVELLING WAVES

4

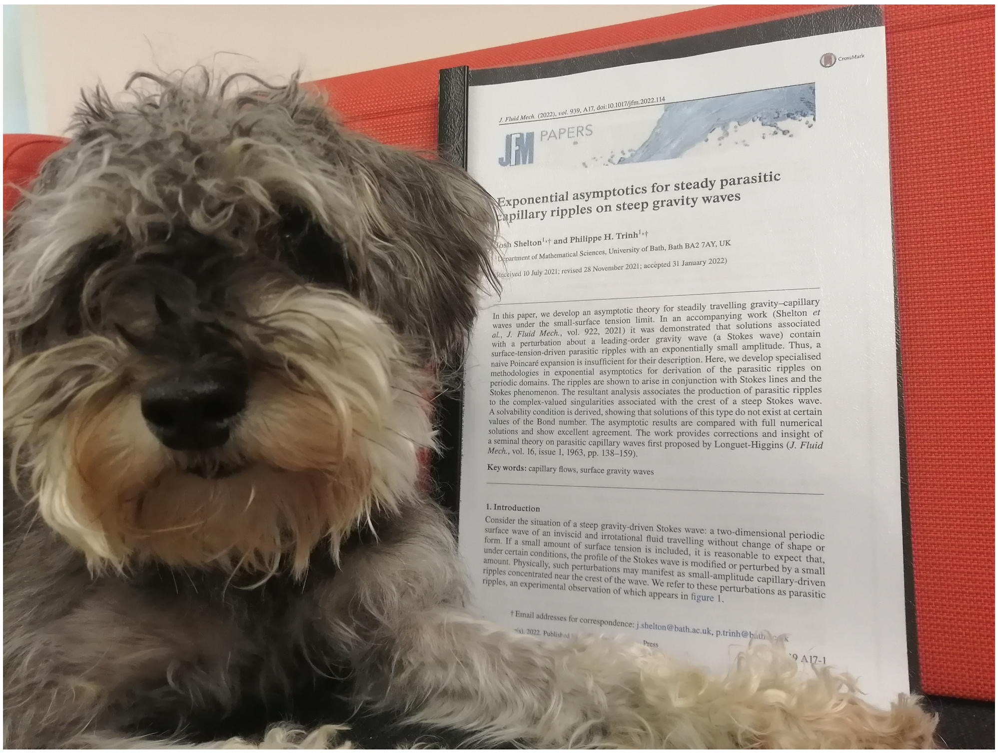

4.1 Introduction

We saw in chapter 3 that the steady gravity capillary wave problem has solutions containing exponentially-small parasitic ripples. As the surface tension parameter, B, approached zero, this yielded a discrete set of solution branches, each of which corresponded to a fixed number of peaks in the oscillatory ripple.

In this chapter, the asymptotic behaviour of these solutions, derived by Shelton and Trinh (2022), is presented. Recall from the introduction on exponential asymptotics of chapter 2 that the exponentially small components of an asymptotic series are derived through the understanding of the Stokes phenomenon that occurs across Stokes lines which emanate from singularities of the early orders of the asymptotic expansion. In the gravity capillary wave problem, these singularities are also located in the analytic continuation of the leading order asymptotic solution (with $B = 0$). However, this leading order solution (a nonlinear gravity/Stokes wave) is known only numerically. The consequent asymptotic study that we present must be performed without explicit knowledge of the asymptotic series.

Appendix B: Statement of Authorship

This declaration concerns the article entitled:	
Exponential asymptotics for steady parasitic capillary ripples on steep gravity waves	
Publication status: Draft manuscript ☐ Submitted ☐ In review ☐ Accepted ☐ Published ●	
Publication details	Journal - Journal of Fluid Mechanics, 939, A17-36 Authors - Josh Shelton, Philippe H. Trinh
Copyright status: The material has been published with a CC-BY license ● The publisher has granted permission to replicate the material included here ☐	
Candidate's contribution to the paper	All authors contributed equally to the conceptualisation and methodology used in the article (50%) All analytical calculations were performed by the author of this thesis (100%) All numerical computations were performed by the author of this thesis (100%) The original draft and bulk of the final presentation has been written by the author of this thesis (90%)
Statement from Candidate	This paper reports on original research I conducted during the period of my Higher Degree by Research candidature.
Signed	**Date** 30/12/22

J. Fluid Mech. (2022), *vol.* 939, A17, doi:10.1017/jfm.2022.114

JFM PAPERS

Exponential asymptotics for steady parasitic capillary ripples on steep gravity waves

Josh Shelton[1,†] and Philippe H. Trinh[1,†]

[1]Department of Mathematical Sciences, University of Bath, Bath BA2 7AY, UK

(Received 10 July 2021; revised 28 November 2021; accepted 31 January 2022)

In this paper, we develop an asymptotic theory for steadily travelling gravity–capillary waves under the small-surface tension limit. In an accompanying work (Shelton *et al.*, *J. Fluid Mech.*, vol. 922, 2021) it was demonstrated that solutions associated with a perturbation about a leading-order gravity wave (a Stokes wave) contain surface-tension-driven parasitic ripples with an exponentially small amplitude. Thus, a naive Poincaré expansion is insufficient for their description. Here, we develop specialised methodologies in exponential asymptotics for derivation of the parasitic ripples on periodic domains. The ripples are shown to arise in conjunction with Stokes lines and the Stokes phenomenon. The resultant analysis associates the production of parasitic ripples to the complex-valued singularities associated with the crest of a steep Stokes wave. A solvability condition is derived, showing that solutions of this type do not exist at certain values of the Bond number. The asymptotic results are compared with full numerical solutions and show excellent agreement. The work provides corrections and insight of a seminal theory on parasitic capillary waves first proposed by Longuet-Higgins (*J. Fluid Mech.*, vol. 16, issue 1, 1963, pp. 138–159).

Key words: capillary flows, surface gravity waves

1. Introduction

Consider the situation of a steep gravity-driven Stokes wave: a two-dimensional periodic surface wave of an inviscid and irrotational fluid travelling without change of shape or form. If a small amount of surface tension is included, it is reasonable to expect that, under certain conditions, the profile of the Stokes wave is modified or perturbed by a small amount. Physically, such perturbations may manifest as small-amplitude capillary-driven ripples concentrated near the crest of the wave. We refer to these perturbations as parasitic ripples, an experimental observation of which appears in figure 1.

† Email addresses for correspondence: j.shelton@bath.ac.uk, p.trinh@bath.ac.uk

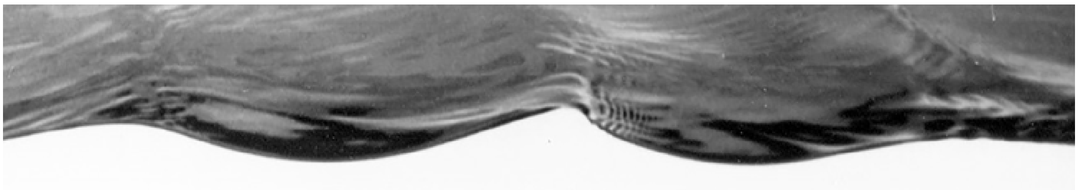

Figure 1. Experimental picture showing parasitic ripples located near the crests of a steep gravity-dominated wave. Note that the ripples appear in an asymmetric manner; mechanisms that produce asymmetry are discussed in § 9.2. Image used with permission from Professor N. Ebuchi (Hokkaido University).

The purpose of this work is to develop a precise asymptotic theory for the parasitic ripples that arise in the permanently progressive framework of a travelling water wave. In particular, we demonstrate that for small surface tension, the parasitic ripples are described by an exponentially small remainder to the base water wave, which is given by a typical asymptotic expansion in algebraic powers of the surface tension parameter. Their description requires the use of exponential asymptotics and, indeed, it is this requirement that distinguishes this work from the previous analytical treatments.

1.1. *Steady parasitic solutions for small surface tension*

Here, we provide a brief overview of how our treatment differs from previous works. To begin, the water-wave problem can be formulated in terms of an unknown streamline speed, q, and streamline angle, θ, considered as functions of the velocity potential, ϕ, over the periodic domain $-\frac{1}{2} < \phi \leqslant \frac{1}{2}$. The free surface is then governed by Bernoulli's equation,

$$F^2 q^2 \frac{\mathrm{d}q}{\mathrm{d}\phi} + \sin(\theta) - Bq\frac{\mathrm{d}}{\mathrm{d}\phi}\left(q\frac{\mathrm{d}\theta}{\mathrm{d}\phi}\right) = 0, \tag{1.1}$$

where F is the Froude number and B is the (inverse) Bond number. These non-dimensional constants are given by

$$F = \frac{c}{\sqrt{g\lambda}} \quad \text{and} \quad B = \frac{\sigma}{\rho g \lambda^2}, \tag{1.2a,b}$$

where c is the wave speed, g is the constant acceleration due to gravity, λ is the wavelength, ρ is the fluid density and σ is the coefficient of surface tension. The limit of small-surface tension is given by $B \to 0$. A list of variables, parameters and notation used in the main text is provided in table 1.

As it turns out, the structure of the solution space for the free-surface gravity–capillary wave problem is remarkably sophisticated. Recently, a portion of this solution space was investigated numerically by Shelton, Milewski & Trinh (2021) for fixed energy, with a focus on determining the small-surface tension limit of $B \to 0$. Multiple branches of solutions were found, each of which can be indexed by the number of capillary-driven ripples that appear in the periodic domain. This solution space is shown in figure 2 and the structure of 'fingers' (as introduced in the previous work) can be observed.

Two different asymptotic limits are visible in these solutions. The first limit is observed from the solutions in figures 2(*d*)–2(*f*) at the lower parts of each of the fingers, which are highly oscillatory with some modulation across the domain. In this region, the solution

	Symbol	Notes
Dimensional quantities	c	Wave speed
	g	Constant acceleration due to gravity
	ρ	Fluid density
	λ	Wavelength
	σ	Constant coefficient of surface tension
Parameters	q	Streamline speed
	θ	Streamline angle
	$\phi + \mathrm{i}\psi$	Complex potential comprised of velocity potential ϕ and streamfunction ψ
	f	Complex valued domain, relabeled from the analytically continued velocity potential ϕ_c
	a	Direction of analytic continuation, where $a = \pm 1$
	$\mathscr{E}$	Energy
	B	Bond number
	F	Froude number
Subscript notation	x_ϕ	Partial derivative of x with respect to ϕ
	q_n	nth order of the asymptotic series $\sum_{n=0}^{\infty} B^n q_n$
	E_{hw}	Text, used for hw (highest wave), homog (homogeneous) and phys (physical)
	Q_a	Direction of analytic continuation of the free-surface solution, $Q(f)$
Further notation	$\hat{\mathscr{H}}$	Complex-valued Hilbert transform
	f^*	Location of the principal singularity of the analytically continued Stokes wave
	$\bar{q}$	Overbar, denoting the remainder to a truncated asymptotic series
	$\mathfrak{q}$	Frankerscript, denoting the combined solution $q\vert_{a=-1} + q\vert_{a=1}$
	ξ	Forcing terms which appear in the equation for the remainder, $\bar{q}$
	$\hat{q}$	Hats denote an inner asymptotic solution within a boundary layer associated with the singularity at $f = af^*$

Table 1. List of variables, parameters and notation used in the main text.

can be approximated by a multiple-scales framework, with

$$q(\phi) = \sum_{n=0}^{\infty} B^n q_n(\phi, \hat{\phi}), \tag{1.3}$$

where $\hat{\phi} = \phi/B$ is the fast scale. Substitution of this ansatz into Bernoulli's equation (1.1) yields, at order $1/B$, the pure-capillary equation of Crapper (1957) for the small-scale ripples

$$F_0^2 q_0^2 \frac{\partial q_0}{\partial \hat{\phi}} - q_0 \frac{\partial}{\partial \hat{\phi}} \left(q_0 \frac{\partial \theta_0}{\partial \hat{\phi}} \right) = 0. \tag{1.4}$$

Thus, for these multiple-scale solutions, the highly oscillatory parasitic ripples appear in the leading-order term, $q_0(\phi, \hat{\phi})$, of the expansion. We will focus on this asymptotic regime in future work.

The second asymptotic limit can be observed in figures 2(*a*)–(*c*). As these solutions approach the pure-gravity (Stokes) solution with the same fixed value of the energy as

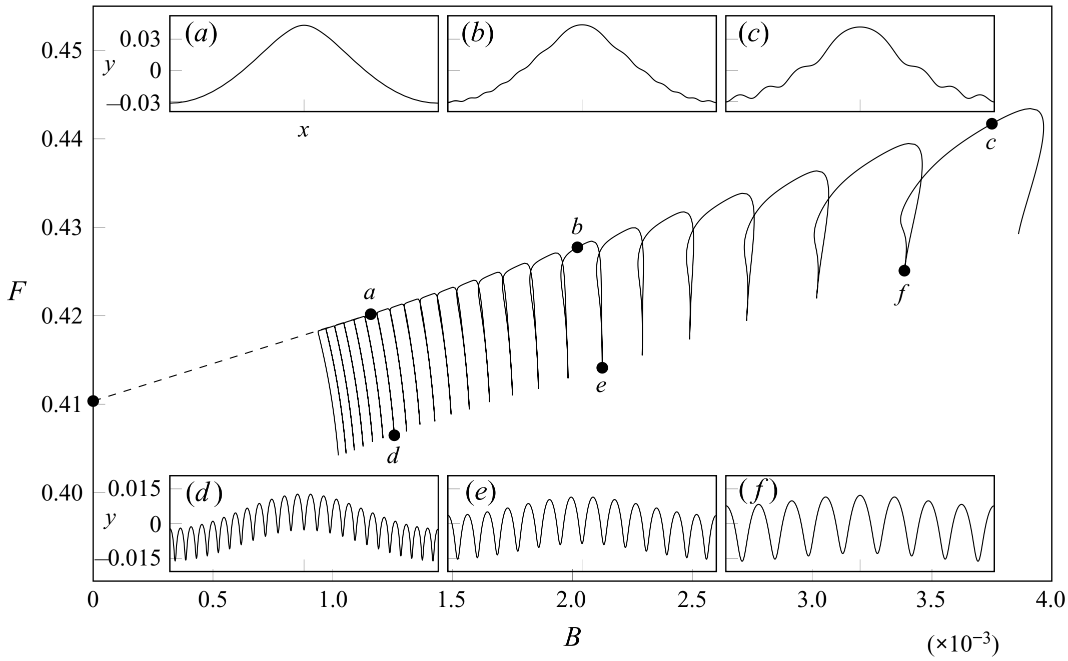

Figure 2. The numerical (B, F) solution space calculated by Shelton *et al.* (2021) is shown for a fixed energy of $\mathscr{E} = 0.3804$. Insets (a)–(c) show the physical free surface for those cases corresponding to exponentially small parasitic ripples on Stokes waves; insets (d)–(f) show a different multiple-scales regime.

$B \to 0$, the leading order solution q_0 contains no ripples. Moreover, a standard perturbative series of the form

$$q(\phi) = \sum_{n=0}^{\infty} B^n q_n(\phi) \tag{1.5}$$

will also not contain the parasitic ripples observed in the numerical solutions. This is due to the exponential smallness of the amplitude of these ripples, which was confirmed numerically by Shelton *et al.* (2021) and is shown to form a straight line in the semi-log plot in figure 3.

Thus, in the $B \to 0$ limit, the capillary-driven ripples exhibit different behaviours according to two distinct asymptotic limits of:

(i) a multiple-scales solution, for which the ripples appear in the leading-order approximation of the solution; and
(ii) a standard perturbative series about a Stokes wave, for which the parasitic ripples appear beyond all orders.

It is this latter asymptotic regime that we focus on in this work.

In the context of the second scenario, an early analytical theory for the generation of these parasitic ripples was proposed by Longuet-Higgins (1963), who considered a small surface-tension perturbation about a base Stokes wave. Although Longuet-Higgins' seminal work provides a crucial basis for our analysis in this paper, we also demonstrate that there are a number of key asymptotic inconsistencies that appear in the historical 1963 work. These inconsistencies turn out to be connected with modern understanding of exponential asymptotics (Berry 1989; Olde Daalhuis *et al.* 1995; Chapman, King & Adams 1998), and may have led to the poor agreement noted by Perlin, Lin & Ting

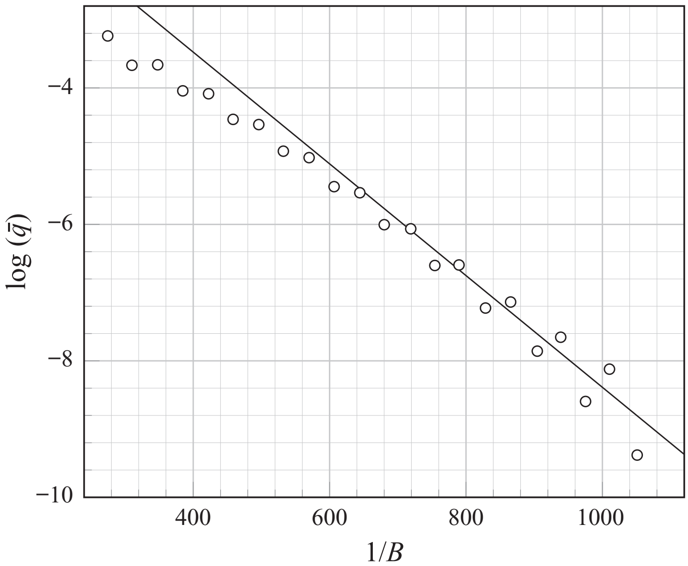

Figure 3. Our analytical prediction of the exponential-scaling of the parasitic ripple magnitude, $\bar{q}$, (line) is compared with numerical results of the full nonlinear equations (circles). These results have both been calculated with an energy of $\mathscr{E} = 0.3804$ and the gradient of the analytical result is -0.0082.

(1993) in comparison with numerical solutions of the full nonlinear problem. One of the primary objectives of our work is to provide a critical re-examination of the seminal Longuet-Higgins (1963) paper, which we perform in § 3. Note that we provide a more complete literature review of theories and research on the parasitic capillary problem in our discussion of § 9.

As we demonstrate, the intricate difficulties involved in formulating a corrected theory for the $B \to 0$ limit are linked to the presence of singularities in the analytical continuation of the leading-order gravity-wave solution. Due to the singularly perturbed nature of Bernoulli's equation (1.1), successive terms in the asymptotic expansion of the solution require repeated differentiation of the singularity in the leading-order solution. This causes the expansion to diverge. In studying this divergence, a form for the exponentially small correction terms to the asymptotic series is found by truncating the series optimally and these corrections correspond to the anticipated parasitic ripples.

1.2. *Outline of the paper*

We begin in § 2 with the mathematical formulation of the non-dimensional gravity–capillary wave system, which is analytically continued into the complex potential plane. In § 3 we provide a detailed overview of the Longuet-Higgins (1963) analytical methodology. In § 4, we consider a perturbation expansion for small values of the surface tension, B. Subsequent terms in this expansion rely on differentiation of the leading-order gravity-wave solution. Thus, singularities in the analytic continuation of the free-surface gravity-wave produce a divergence in the asymptotic series as further terms are considered. The scaling of the principal upper-half and lower-half singularities are derived in § 5. The divergence of the late terms of the asymptotic expansion is then considered in § 6. This allows us to find the Stokes lines for our problem, which are shown in § 7 to produce the switching of exponentially small terms of the solution via Stokes phenomenon. Application of the periodicity conditions then yields an analytical solution for these parasitic ripples and an accompanying solvability condition. These solutions and the

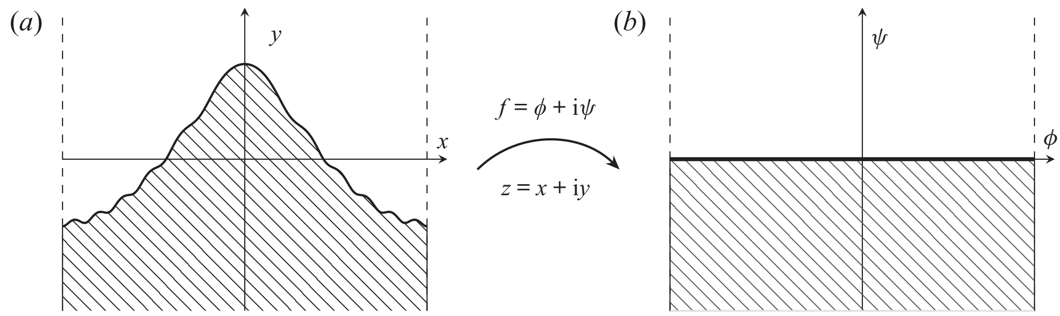

Figure 4. The conformal map from (*a*) the physical $z = x + \mathrm{i}y$-plane to (*b*) the complex $f = \phi + \mathrm{i}\psi$-plane. The boundary, $y = \eta(x)$, is mapped to the line $\psi = 0$.

solvability condition are then compared with numerical solutions of the full nonlinear equations in § 8. Our findings are summarised in § 10, and discussion of further work occurs in § 9.

2. Mathematical formulation

We begin by considering the two-dimensional free-surface flow of an inviscid, irrotational and incompressible fluid of infinite depth. The effects of gravity and surface tension are included. We assume the free surface to be periodic with wavelength λ, and it is chosen to move to the right with wave speed c. Imposing a sub-flow within the fluid in the opposite direction cancels out the lateral movement; this results in a steady free surface when $\partial_t = 0$, now assumed to be located at $y = \eta(x)$. A typical configuration is shown in figure 4. The system is non-dimensionalised using λ and c for the units of length and velocity, respectively, and the set of governing equations is taken to be the same as those considered by Shelton *et al.* (2021):

$$\phi_{xx} + \phi_{yy} = 0 \quad \text{for } y \leqslant \eta, \tag{2.1a}$$

$$\phi_y = \eta_x \phi_x \quad \text{at } y = \eta, \tag{2.1b}$$

$$\frac{F^2}{2}(\phi_x^2 + \phi_y^2) + y - B\frac{\eta_{xx}}{(1+\eta_x^2)^{3/2}} = \frac{F^2}{2} \quad \text{at } y = \eta, \tag{2.1c}$$

$$\phi_y \to 0 \quad \text{and} \quad \phi_x \to -1 \quad \text{as } y \to -\infty. \tag{2.1d}$$

Thus, the flow is governed by Laplace's equation (2.1*a*), kinematic and dynamic boundary conditions in (2.1*b*) and (2.1*c*), respectively, at the free surface, and the deep-water condition (2.1*d*). The constants F and B are the Froude and Bond numbers, introduced earlier in (1.2*a*,*b*). Periodicity of the flow and wave profile is specified by enforcing

$$\nabla\phi\left(x - \tfrac{1}{2}, y\right) = \nabla\phi\left(x + \tfrac{1}{2}, y\right) \quad \text{and} \quad \eta\left(x - \tfrac{1}{2}\right) = \eta\left(x + \tfrac{1}{2}\right). \tag{2.1e}$$

In addition to the governing equations in (2.1), we also enforce an amplitude parameter as a measure of nonlinearity of the solution. This is derived from the physical bulk energy of the wave via Appendix A of Shelton *et al.* (2021). This yields

$$\mathscr{E} = \frac{1}{E_{hw}}\int_{-1/2}^{1/2}\left[\frac{F^2}{2}y(x_\phi - 1) + B\left(\sqrt{(x_\phi^2 + y_\phi^2)} - x_\phi\right) + \frac{1}{2}y^2 x_\phi\right]\mathrm{d}\phi, \tag{2.2}$$

where the three groupings of terms correspond to the kinetic, capillary and gravitational potential energies. In (2.2), we have rescaled with the energy of the limiting classical

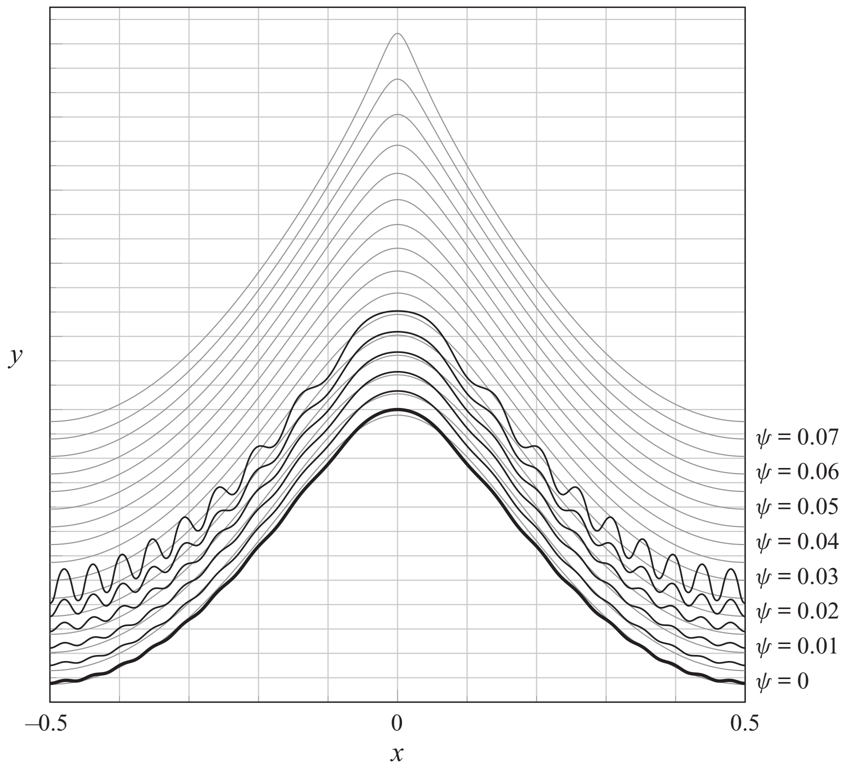

Figure 5. The analytic continuation into the upper-half plane is calculated numerically for two solutions of (2.1) with $\psi = 0$. The first is a gravity wave with $B = 0$, $F = 0.4104$ and $\mathscr{E} = 0.3804$ (thin grey lines) and the second a gravity–capillary wave with $B = 0.001$, $F = 0.4188$ and $\mathscr{E} = 0.3804$ (bold lines). The solutions with $\psi > 0$ satisfy the analytically continued equations (2.9) and Re[x] versus Re[y] is shown. This image can be compared with figure 11 of Longuet-Higgins & Fox (1978), which provides a streamline plot of the pure-gravity solution in the analytically continued plane.

Stokes wave, $E_{hw} \approx 0.00184$. A central idea in Shelton *et al.* (2021) concerned the importance of choosing an amplitude condition on the water waves, and we refer readers to § 2.2 of that work for further discussion.

Finally, based on the previous study in Shelton *et al.* (2021), we note that once the energy condition (2.2) is imposed, there is only a single degree of freedom in specifying either F or B. We typically consider the Bond number as a free parameter, which results in the Froude number as an eigenvalue that must be determined via the system (2.1).

2.1. *The* (q, θ) *formulation*

In this section, we repose the two-dimensional governing system (2.1) as a one-dimensional boundary-integral formulation in terms of the free-surface speed and angle. Following the traditional treatment of potential free-surface flows, we introduce the complex potential $f = \phi + \mathrm{i}\psi$. Rather than consider $f = f(z)$, we instead consider $z = z(f)$ and, hence, the flow region is known in the potential plane. The complex potential plane is shown in figure 4. From this definition, the complex velocity can be found to be $\mathrm{d}f/\mathrm{d}z = u - \mathrm{i}v$, where (u, v) are the horizontal and vertical velocities.

Introducing q as the streamline speed and θ as the streamline angle by the relationship $q\mathrm{e}^{-\mathrm{i}\theta} = u - \mathrm{i}v$ then yields

$$\frac{\mathrm{d}f}{\mathrm{d}z} = q\mathrm{e}^{-\mathrm{i}\theta}. \tag{2.3}$$

https://doi.org/10.1017/jfm.2022.114 Published online by Cambridge University Press

In this form, Bernoulli's equation (2.1c) is written as

$$F^2 q^2 \frac{\mathrm{d}q}{\mathrm{d}\phi} + \sin(\theta) - Bq\frac{\mathrm{d}}{\mathrm{d}\phi}\left(q\frac{\mathrm{d}\theta}{\mathrm{d}\phi}\right) = 0. \tag{2.4a}$$

By the analyticity of $\log q - \mathrm{i}\theta$, we introduce the boundary-integral equation which relates q to the Hilbert transform of θ operating over the free surface. For our periodic domain from $-1/2$ to $1/2$, we integrate $\log q - \mathrm{i}\theta$ using Cauchy's theorem and use the periodicity conditions

$$q\left(\phi - \tfrac{1}{2}\right) = q\left(\phi + \tfrac{1}{2}\right) \quad \text{and} \quad \theta\left(\phi - \tfrac{1}{2}\right) = \theta\left(\phi + \tfrac{1}{2}\right), \tag{2.4b}$$

which follow from (2.1e), and the deep-water conditions (2.1d) to derive the periodic Hilbert transform given by

$$\log(q) = \mathscr{H}[\theta](\phi) = \mathop{⨍}_{-1/2}^{1/2} \theta(\phi')\cot[\pi(\phi' - \phi)]\mathrm{d}\phi'. \tag{2.4c}$$

In the above, $⨍$ is the Cauchy principal-value integral. The above provides the crucial relationship between the components q and θ, and further details on the derivation of the boundary-integral relations can be found in chapter 6 of Vanden-Broeck (2010).

Finally, the energy expression (2.2) is also considered in terms of (q, θ). Noting that $x_\phi = q^{-1}\cos(\theta)$ and $y_\phi = q^{-1}\sin\theta$, we substitute $y = (F^2/2)(1 - q^2) + Bq\theta_\phi$ from Bernoulli's equation to find

$$\mathscr{E} = \frac{1}{E_{hw}}\int_{-1/2}^{1/2}\left[\mathcal{G}_0(\phi) + B\mathcal{G}_1(\phi) + B^2\mathcal{G}_2(\phi)\right]\mathrm{d}\phi, \tag{2.4d}$$

where we have defined components

$$\left.\begin{aligned} \mathcal{G}_0(\phi) &= \frac{F^4}{8q}(1 - q^2)(3\cos\theta - 2q - q^2\cos\theta), \\ \mathcal{G}_1(\phi) &= \frac{(1 - \cos\theta)}{q} + \frac{F^2\theta_\phi}{2}(2\cos\theta - q - q^2\cos\theta), \\ \mathcal{G}_2(\phi) &= \frac{q\theta_\phi^2\cos\theta}{2}. \end{aligned}\right\} \tag{2.5}$$

In summary, the water-wave problem, as formulated for q and θ, involves the solution of (2.4a)–(2.4d). Note that the above sets of equations all involve the evaluation of q and θ on the streamline $\psi = 0$.

2.2. *Analytic continuation*

As we show, the exponential asymptotics procedure of § 7 requires the continuation of the free-surface solutions, $q(\phi + 0\mathrm{i})$ and $\theta(\phi + 0\mathrm{i})$, into the complex plane, where $\phi \in \mathbb{C}$. This free-surface continuation procedure is depicted in figure 6. Hence, we analytically continue Bernoulli's equation (2.4a) and the boundary-integral equation (2.4c) into the complex ϕ-plane. The independent variable ϕ is complexified by considering $\phi \mapsto \phi_c \in \mathbb{C}$ and, hence, q and θ are analytically continued. For convenience, we relabel ϕ_c as f. Thus, Bernoulli's equation remains in an identical form to (2.4a), but with the variable ϕ replaced by f.

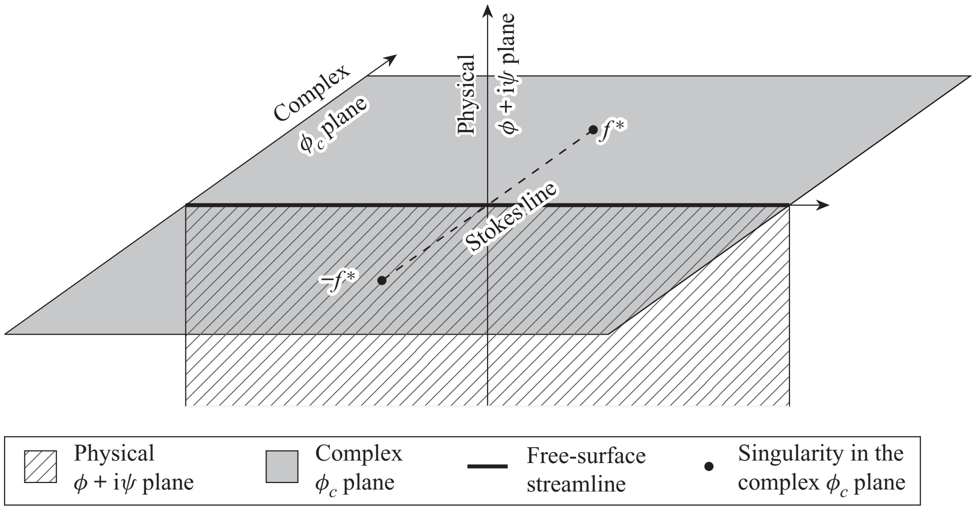

Figure 6. A schematic of our analytic continuation procedure demonstrates the difference between the physical $\phi + \mathrm{i}\psi$ plane and our complexified ϕ_c space. The location of the principle upper- and lower-half singularities at f^* and $-f^*$ of the leading-order flow field are shown by circles, and the main Stokes line from § 7 is shown dashed.

For the boundary-integral equation (2.4*c*), we must consider the complexification of the Hilbert transform. Let us write

$$\mathscr{H}[\theta] = \hat{\mathscr{H}}[\theta] - a\mathrm{i}\theta, \tag{2.6}$$

where $\hat{\mathscr{H}}[\theta]$ is the complex-valued Hilbert transform,

$$\hat{\mathscr{H}}[\theta](f) = \int_{-1/2}^{1/2} \theta(\phi') \cot\left[\pi(\phi' - f)\right] \mathrm{d}\phi'. \tag{2.7}$$

Note that the integral above is only evaluated along the physical free surface, parameterised in terms of ϕ', where θ takes real values.

In (2.6), we have also introduced the parameter, a, which is defined by

$$a = \begin{cases} +1 & \text{for } \mathrm{Im}(f) > 0, \\ -1 & \text{for } \mathrm{Im}(f) < 0. \end{cases} \tag{2.8}$$

When the Hilbert transform relationship is extended into the upper-half-f-plane, $a = 1$, whereas $a = -1$ for continuation into the lower-half-f-plane. The validity of (2.6) as a legitimate complexification of the Hilbert transform is verified by taking $\mathrm{Im}(f) \to 0$ on the right-hand side. Then $\hat{\mathscr{H}}[\theta]$ yields a principal value integral and residue. The residue contribution changes sign between $\mathrm{Im}(f) \to 0^+$ and $\mathrm{Im}(f) \to 0^-$, yielding the constant a.

In summary, the governing equations for the analytically continued q and θ values are given by

$$F^2 q^2 q' + \sin(\theta) - Bq(q\theta')' = 0, \tag{2.9a}$$

$$\log(q) + a\mathrm{i}\theta = \hat{\mathscr{H}}[\theta], \tag{2.9b}$$

$$\mathscr{E} = \frac{1}{E_{hw}} \int_{-1/2}^{1/2} \left[\mathcal{G}_0(\phi) + B\mathcal{G}_1(\phi) + B^2\mathcal{G}_2(\phi)\right] \mathrm{d}\phi, \tag{2.9c}$$

$$q\left(-\tfrac{1}{2}\right) = q\left(\tfrac{1}{2}\right) \quad \text{and} \quad q'\left(-\tfrac{1}{2}\right) = q'\left(\tfrac{1}{2}\right). \tag{2.9d}$$

Note that although (2.9*a*) and (2.9*b*) are evaluated through complex f-space, the energy condition is most easily evaluated on the physical free surface. Here and henceforth, we use primes ($'$) to denote differentiation in f. This system will be solved in § 4 with an expansion holding under the limit of $B \to 0$.

3. A critical examination of the Longuet-Higgins (1963) theory

Longuet-Higgins (1963) proposed a theory for the generation of steady parasitic ripples by considering an asymptotic expansion for small surface tension such that a gravity wave was obtained at leading order. In § 3 he wrote the following perturbative form for the solutions,

$$q(\phi, \psi) = q_0 + \bar{q}, \quad \theta(\phi, \psi) = \theta_0 + \bar{\theta}, \quad y(\phi, \psi) = y_0 + \bar{y}, \tag{3.1a–c}$$

with y denoting the wave height. All quantities are dimensional and functions of the potential, ϕ, and stream function, ψ. Let us introduce the logarithm of the speed by $\tau = \log(q/c)$, where c is the wave speed. In writing $\tau = \tau_0 + \bar{\tau}$, this yields $q_0 = c\mathrm{e}^{\tau_0}$ and $\bar{q} = q_0\bar{\tau}$ for $\bar{\tau}$ assumed small.

The expression that Longuet-Higgins produced for the capillary ripples was [cf. equation (5.18) in Longuet-Higgins 1963]

$$\bar{\tau} - \mathrm{i}\bar{\theta} \sim F(\phi)\exp(-\mathrm{i}c\alpha(\phi)/T') \quad \text{for } \phi > 0, \tag{3.2a}$$

where the functional prefactor, $F(\phi)$, and exponent, $\alpha(\phi)$, are given by

$$F(\phi) = 4\mathrm{i}\exp\left(\mathrm{i}\int_0^{\phi} \frac{\partial \tau_0}{\partial \psi}\mathrm{d}\phi\right)\int_0^{\infty}\left(\frac{\partial \tau_0}{\partial \psi}\cos\left(\alpha c/T'\right)\right)\mathrm{d}\phi, \tag{3.2b}$$

$$\alpha(\phi) = \int_0^{\phi} \mathrm{e}^{\tau_0}\,\mathrm{d}\phi. \tag{3.2c}$$

Here, T' is the dimensional surface tension coefficient, assumed to be small. Note that $\alpha(\phi)$ involves integration of a real-valued e^{τ_0} over real-valued ϕ and, hence, α is also real.

One of the main contributions of our work is to provide an improvement on the above formulae, which contains a number of problems related to the capture of small ripples. The three most important issues are as follows.

(i) The functional form of the prefactor, $F(\phi)$, in (3.2*c*) is incorrect; the form written above emerges as a consequence of certain asymptotic inconsistencies in the derivation.

(ii) Longuet-Higgins predicted correctly that the capillary ripples would exhibit wavelengths scaling with T', but in closer examination of (3.2*a*), the expression predicts a wave amplitude that is of $O(1)$ and independent of T'. We find that for small values of the surface tension, the wave amplitude is exponentially small in T' (indeed this should be clear from figure 3).

(iii) The above formulation does not provide any restriction on the solution space (i.e. the existence of a solvability condition observed in the full numerical simulations). It particular, it does not capture any of the observed bifurcation structure seen in figure 2.

Note that a portion of the work of Longuet-Higgins (1963) is devoted to studying the addition of viscosity and also incorporating the almost-highest wave theory of Longuet-Higgins & Fox (1977) into (3.2). However, in the present authors' view, the treatment following § 6 of the 1963 work becomes increasingly *ad hoc* and difficult to analyse in view of the fundamental issues with (3.2).

We now discuss these key issues (i)–(iii) in detail.

3.1. *Asymptotic inconsistencies in Longuet-Higgins (1963)*

Numerical evidence was provided by Shelton *et al.* (2021) (see figure 3) to demonstrate that, for those solutions exhibiting small-scale ripples on an underlying gravity wave, the amplitude of these parasitic ripples is exponentially small as $T' \to 0$. Solutions that display such exponentially small behaviour cannot be described purely by a typical Poincaré expansion which contains only algebraic powers of the small parameter; their description will instead appear beyond all orders of the standard Poincaré expansion.

We now review Longuet-Higgins' approach in our non-dimensional formulation (using the Bond number, B, and Froude number, F, in (1.2*a,b*) instead of T' and c). We start with the integrated form of Bernoulli's equation from (1.1) given in terms of y and the streamline speed, q, as

$$\frac{F^2}{2}q^2 + y - B\frac{\partial q}{\partial \psi} = \text{const.}, \tag{3.3}$$

where the derivative in the ψ direction can be converted into a derivative the ϕ direction via the Cauchy–Riemann equations. In his §3, Longuet-Higgins considered a perturbation $(\bar{y}, \bar{q})$ about the gravity-wave (y_0, q_0) with the truncations from (3.1*a–c*) to find

$$\frac{F^2}{2}(q_0^2 + 2q_0\bar{q} + \bar{q}^2) + (y_0 + \bar{y}) - B\left(\frac{\partial q_0}{\partial \psi} + \frac{\partial \bar{q}}{\partial \psi}\right) = \text{const.} \tag{3.4}$$

Here, the $O(1)$ terms, $F^2 q_0^2/2 + y_0 = \text{const.}$, are satisfied exactly as this is the gravity-wave equation with solutions (y_0, q_0). Thus, we obtain

$$\underbrace{F^2 q_0\bar{q} + \bar{y} - B\frac{\partial q_0}{\partial \psi}}_{O(B)} - \underbrace{B\frac{\partial \bar{q}}{\partial \psi}}_{O(B^2)} = -\underbrace{\frac{F^2\bar{q}^2}{2}}_{O(B^2)}. \tag{3.5}$$

The asymptotic behaviour indicated by the under-braced quantities follows by making the standard assumption that the leading corrections, $\bar{y}$ and $\bar{q}$, are both of $O(B)$. Consequently, $\bar{q} \ll q_0$, and so Longuet-Higgins neglected the nonlinear term $\bar{q}^2$ on the right-hand side of this equation. However, the $O(B^2)$ term on the left-hand side was not neglected. This assumption, which appears in his (5.1), is asymptotically inconsistent. In fact, this inconsistency is how Longuet-Higgins was able to produce approximations to an *a priori* exponentially small capillary ripple, because, otherwise, all corrections are ripple-free and algebraic in B.

The above asymptotic inconsistency is somewhat typical in early models of many exponential asymptotic problems. There are two (formally correct) methods to proceed with (3.5).

(i) We may correctly treat $\bar{y}$ and $\bar{q}$ to both be of $O(B)$. The leading-order terms in (3.5) are, thus,

$$F^2 q_0\bar{q} + \bar{y} - B\frac{\partial q_0}{\partial \psi} = 0, \tag{3.6}$$

and would yield the $O(B)$ capillary correction term. The procedure could be continued to quadratic orders of B and higher, but the resultant perturbative solution would never yield an exponentially small ripple. In essence, this is a derivation of the regular perturbative expansion and leads to the analysis of § 4.

(ii) Alternatively, we may consider $\bar{y}$ and $\bar{q}$ to both scale as $\sim \mathrm{e}^{-\alpha/B}$, i.e. for solutions to be of Wentzel–Kramers–Brillouin–Jeffreys (WKBJ) type. As differentiation of this ansatz yields a factor of $1/B$, the dominant terms in (3.5) change to

$$\underbrace{F^2 q_0 \bar{q} - B\frac{\partial \bar{q}}{\partial \psi}}_{O(\mathrm{e}^{-\alpha/B})} = \underbrace{Bq_0'}_{O(B)}. \tag{3.7}$$

The form of the above equation would allow for the correct prediction of the WKBJ phase, α, but not the correct prefactor (amplitude); this is on account of the fact the right-hand side is the result of a one-term truncation of the Poincaré expansion (3.1*a–c*). Instead, the correct procedure must involve additional terms of the regular expansion. In general, the right-hand side is of $O(B^N)$ with $N \to \infty$ as $B \to 0$. In order to derive the exponentially small ripples, we must optimally truncate with N chosen carefully (Chapman *et al.* 1998).

Longuet-Higgins had worked with the asymptotically inconsistent (3.5), with the right-hand side set to zero, and this was used to derive the solution (3.2).

As shown in § 7.3, the ripples have the analytical behaviour

$$q_{exp}(\phi) = \Lambda \mathcal{F}(\phi) \exp\left(-\frac{\chi(\phi)}{B}\right), \tag{3.8}$$

where Λ is a constant coefficient, $\mathcal{F}(\phi)$ is a functional prefactor and $\chi(\phi)$ is the exponentially small dependence of the solution, which is related to the quantity $\alpha(\phi)$. These components will be significantly different than those derived by Longuet-Higgins in (3.2). In order to be correct, the above expression must be derived through optimal truncation of the standard asymptotic expansion, rather than using the one-term truncation in (3.1*a–c*).

We note that it is still nevertheless possible to capture exponentially small behaviour with the truncation (3.1*a–c*) used by Longuet-Higgins. A comprehensive review of truncations of this type, for the case of free-surface flows, was given by Trinh (2017) who, aided by the use of exponential asymptotics, discussed how the functional form of the exponentially small waves changes when different truncations are made. The type utilised here by Longuet-Higgins in (3.1*a–c*) is an $N = 1$ truncation as only one term of the asymptotic series is included. Although this truncation (if dealt with in an asymptotically consistent manner) can predict the correct exponentially small scaling of the solution, the functional form of the prefactor and its magnitude [cf. (3.2*b*)] will be incorrect.

3.2. *The choice of integration in the exponential argument*

We now discuss the second issue with Longuet-Higgins' analytical solution, which is that (3.2) predicts an $O(1)$ solution magnitude. For real values of ϕ, α takes purely real values. Thus, as his solution contains $\mathrm{e}^{-\mathrm{i}c\alpha/T'}$, only a rapidly oscillating waveform of wavelength $O(\epsilon)$ is predicted. The issue is not precisely related to the functional form of the exponential argument, because modulo the scalings, it can be confirmed via our work that

$$-\frac{1}{B}\frac{\mathrm{d}\chi}{\mathrm{d}\phi} \propto -\frac{\mathrm{i}c}{T'}\frac{\mathrm{d}\alpha}{\mathrm{d}\phi}. \tag{3.9}$$

However, Longuet-Higgins restricts ϕ to take real values and forces the starting point of integration in $\alpha(\phi)$ to be at $\phi = 0$. This is later matched to an *ad hoc* simplification near the crest of the wave. This misses a fundamental step in the determination of the parasitic ripples because, as we show, their existence is intimately connected with the singularities of $\chi'(\phi)$ in the analytic continuation of the free surface. In order to correctly resolve the Stokes phenomenon in § 7, integration in our expression for χ must begin from such singularities, and results in a path of integration through the complex-valued domain. The final result produces a complex-valued q_{exp}, which is paired with a conjugate contribution to in order to produce a real-valued solution with both exponentially small phase and amplitude.

4. The expansion for small surface tension, B

In the limit of $B \to 0$, we consider the traditional series expansions for q and θ, given by

$$q = \sum_{n=0}^{\infty} B^n q_n \quad \text{and} \quad \theta = \sum_{n=0}^{\infty} B^n \theta_n. \tag{4.1a,b}$$

These expansions will satisfy both Bernoulli's equation (2.9*a*) and the boundary-integral equation (2.9*b*) to each order in B. As noted in the discussion following (2.4*d*), specifying B and enforcing the energy constraint requires that F be treated as an eigenvalue. Hence, we also consider an expansion of the Froude number by

$$F = \sum_{n=0}^{\infty} B^n F_n. \tag{4.1c}$$

At leading order in (2.9*a*), (2.9*b*) and (2.4*d*) this results in the gravity-wave equations

$$F_0^2 q_0^2 \frac{\mathrm{d}q_0}{\mathrm{d}f} + \sin(\theta_0) = 0, \tag{4.2a}$$

$$\log(q_0) + a\mathrm{i}\theta_0 = \hat{\mathscr{H}}[\theta_0], \tag{4.2b}$$

$$\mathscr{E} = \frac{1}{E_{hw}} \int_{-1/2}^{1/2} \frac{F_0^4}{8q_0}(1 - q_0^2)(3\cos\theta_0 - 2q_0 - q_0^2\cos\theta_0)\,\mathrm{d}\phi, \tag{4.2c}$$

where we remind the reader that $a = \pm 1$ via the choice of analytic continuation into the upper- or lower-half planes, respectively [cf. (2.8)]. Here, the Hilbert transform in (4.2*b*) acts on the free surface for which f is real. The energy, $\mathscr{E}$, is a specified $O(1)$ constant, which we take to be less than unity.

At $O(B)$, we have for Bernoulli's equation,

$$F_0^2 q_0^2 \frac{\mathrm{d}q_1}{\mathrm{d}f} + 2F_0^2 q_0 q_0' q_1 + 2F_0 F_1 q_0^2 q_0' + \theta_1 \cos\theta_0 - q_0\left(q_0\theta_0'\right)' = 0, \tag{4.3a}$$

for the boundary-integral equation,

$$\frac{q_1}{q_0} + a\mathrm{i}\theta_1 = \hat{\mathscr{H}}[\theta_1], \tag{4.3b}$$

and finally for the energy constraint,

$$0 = \int_{-1/2}^{1/2} \left[\frac{(1-\cos\theta_0)}{q_0} + \frac{F_0^2\theta_0'}{2}(2\cos\theta_0 - q_0 - q_0^2\cos\theta_0) \right.$$
$$+ (3\cos\theta_0 - 2q_0 - q_0^2\cos\theta_0)\left(\frac{F_0^3F_1(1-q_0^2)}{2q_0} - \frac{F_0^4 q_1}{8q_0}(1+q_0^2) \right)$$
$$\left. + \frac{F_0^4(1-q_0^2)}{8q_0}(-3\theta_1\sin\theta_0 - 2q_1 + q_0^2\theta_1\sin\theta_0 - 2q_0q_1\cos\theta_0) \right] \mathrm{d}\phi. \tag{4.3c}$$

We now consider the $O(B^n)$ components of (2.9*a*) and (2.9*b*). The solutions of these, q_n, θ_n and F_n, are denoted the late terms of the asymptotic expansions (4.1*a,b*) and (4.1*c*). An important feature of these solutions is that they diverge as $n \to \infty$. This is a consequence of the singularities in the leading-order solutions, q_0 and θ_0, which are derived in § 5. Evidently, the $O(B^n)$ equations will contain an unbounded number of terms as $n \to \infty$. However, due to the divergent nature of the late terms, only a few of these terms will influence the leading-order solution as $n \to \infty$.

Starting with Bernoulli's equation (2.9*a*), we retain the two leading orders in n, yielding

$$\left[F_0^2\left(q_0^2 q_n' + 2q_0q_1q_{n-1}' + 2q_0q_0'q_n + \dots \right) + 2F_0F_1q_0^2q_{n-1}' + 2F_0F_nq_0^2q_0' + \dots \right]$$
$$+ [\theta_n\cos\theta_0 + \dots] - \left[q_0^2\theta_{n-1}'' + 2q_0q_1\theta_{n-2}'' + q_0\theta_0'q_{n-1}' + q_0q_0'\theta_{n-1}' + \dots \right] = 0. \tag{4.4a}$$

At $O(B^n)$, we expand the logarithm in the boundary-integral equation (2.9*b*) in order to obtain

$$\frac{q_n}{q_0} - \frac{q_1q_{n-1}}{q_0^2} + \dots + ai\theta_n = \hat{\mathscr{H}}[\theta_n]. \tag{4.4b}$$

5. On the singularities of the leading-order flow

A crucial element of the exponential asymptotics analysis relies upon the understanding that the series (4.1*a,b*) will diverge on account of singularities (such as poles or branch points) in the analytic continuation of q and θ. More specifically, we shall find that the leading-order solution, q_0, which corresponds to the pure Stokes gravity wave via (4.2), contains branch points in the complex plane. As the determination of each subsequent order generally relies upon differentiating the previous, the result is that the order of the singularity increases as $n \to \infty$. This is shown in § 6.

On the assumption that the leading-order Stokes wave possesses a singularity in the complex plane, previously Grant (1973) derived the local asymptotic behaviour using a dominant balance. That is, by considering the complex velocity $\mathrm{d}f/\mathrm{d}z$ from (2.3), he showed that near to a point $f^* \in \mathbb{C}$ directly 'above' the wave crest

$$\frac{\mathrm{d}f}{\mathrm{d}z} \sim (f - f^*)^{1/2}. \tag{5.1}$$

In the exponential asymptotics to follow, we require the singular behaviour of the individual components of q_0 and θ_0. This is derived in the following analysis, along with a discussion of the difference between Grant's singularity in $\mathrm{d}f/\mathrm{d}z$ and those of (q_0, θ_0).

5.1. *Singularities in the analytic continuation of q_0 and θ_0*

The singular scaling of q_0 and θ_0 is now considered. We let f^* denote the 'crest' singularity in the upper-half-f-plane. We leave the constant, a, unspecified and take the limit of $f \to af^*$. First, it can be verified *a posteriori* that as $f \to af^*$, $|\operatorname{Im}\theta_0| \to \infty$ and

$$\sin\theta_0 = \frac{1}{2\mathrm{i}}\left[\mathrm{e}^{\mathrm{i}\theta_0} - \mathrm{e}^{-\mathrm{i}\theta_0}\right] \sim \frac{a}{2\mathrm{i}}\mathrm{e}^{a\mathrm{i}\theta_0}. \tag{5.2}$$

We multiply Bernoulli's equation (4.2*a*) by q_0, and use the above scaling for $\sin\theta_0$ to find

$$F_0^2 q_0^3 \frac{\mathrm{d}q_0}{\mathrm{d}f} = -q_0 \sin\theta_0 \sim -\frac{a}{2\mathrm{i}} q_0 \mathrm{e}^{a\mathrm{i}\theta_0}. \tag{5.3}$$

However, in taking the exponential of the boundary-integral equation (4.2*b*), we have

$$q_0 \mathrm{e}^{a\mathrm{i}\theta_0} = \mathrm{e}^{\hat{\mathscr{H}}[\theta_0]}. \tag{5.4}$$

Note that the complex Hilbert transform is applied to θ_0 and integrated over the free surface, where $\theta_0 = O(1)$. Thus $q_0\mathrm{e}^{a\mathrm{i}\theta_0}$ is also of order unity and we conclude from (5.3) that $q_0^3 q_0'$ tends to a constant as $f \to af^*$. Integration then yields the following singular behaviour for q_0,

$$q_0 \sim c_a (f - af^*)^{1/4}. \tag{5.5}$$

In addition, the scaling for $\mathrm{e}^{a\mathrm{i}\theta_0}$ is found from (5.3), giving

$$\mathrm{e}^{a\mathrm{i}\theta_0} \sim \frac{-a\mathrm{i}F_0^2 c_a^3}{2}(f - af^*)^{-1/4}. \tag{5.6}$$

Combining these results for q_0 in (5.5) and θ_0 in (5.6) gives the scaling for the complex velocity,

$$\frac{\mathrm{d}f}{\mathrm{d}z} \sim c_a \left(\frac{-a\mathrm{i}F_0^2 c_a^3}{2}\right)^{-a} (f - af^*)^{(a+1)/4}. \tag{5.7}$$

Note that $a = 1$ recovers the same singular behaviour of Grant (1973) in the upper-half plane, shown in (5.1).

5.2. *The apparent paradox of a singularity in the lower-half plane*

We see from (5.5) for q_0 that a singularity exists 'within the fluid' in the lower-half plane at $f = -f^*$. This is in contrast to the regular behaviour near the same location provided by Grant's result. Our apparent prediction of singular behaviour in the flow field can readily be resolved by noting that this singularity is for the analytically continued variable, originally relabelled from $q_c \to q$ in § 2.2. It is, thus, important to distinguish between the complexified and 'physical' streamline speeds q_c and q_{phys}, and angles θ_c and θ_{phys}. These physical variables are found by taking the magnitude and argument of the complex velocity $q_0\mathrm{e}^{-\mathrm{i}\theta_0}$ as in (5.7), which is regular for $a = -1$, yielding

$$q_{phys} = \left|q_c \mathrm{e}^{-\mathrm{i}\theta_c}\right| \quad \text{and} \quad \theta_{phys} = \operatorname{Arg}\left(q_c \mathrm{e}^{-\mathrm{i}\theta_c}\right). \tag{5.8a,b}$$

Thus, as $f \to -f^*$ these physical values are regular for the leading-order Stokes wave solution. Only by recombining $q_0\mathrm{e}^{-\mathrm{i}\theta_0}$ to find the physical values within the fluid have these singular terms cancelled out.

6. Exponential asymptotics

As we show in § 7, the exponentially small ripples are intimately connected with the later term divergence of the asymptotic series (4.1*a*,*b*). In this section, we seek to characterise this divergence.

As we have noted in the previous section, the leading-order solution, q_0 and θ_0, which represents a pure gravity wave, contains singularities at the points $f = af^*$, where $a = \pm 1$ (and further singularities on subsequent Riemann sheets; cf. Crew & Trinh 2016). As later orders depend on successive differentiation of the previous orders, we intuit that as $n \to \infty$, the late terms of q_n and θ_n diverge. In this limit of $n \to \infty$, the divergence can be described by a factorial-over-power ansatz of

$$q_n \sim \frac{Q(f)\Gamma(n+\gamma)}{\chi(f)^{n+\gamma}} \quad \text{and} \quad \theta_n \sim \frac{\Theta(f)\Gamma(n+\gamma)}{\chi(f)^{n+\gamma}}. \tag{6.1a,b}$$

Here, Q, Θ and χ are all functions of f, and γ is assumed to be constant. Note that, more generally, there is a summation of contributions of factorial-over-power type: one for each singularity in $f \in \mathbb{C}$. Typically, the nearest singularities determine the leading-order divergence. As the late terms are determined through a linear perturbative procedure, it is sufficient to consider the general ansatz (6.1*a*,*b*) and add the appropriate contributions once the general forms of Q, Θ and χ are derived.

A consequence of enforcing the $O(B^n)$ energy condition with these solutions is that the Froude number, F_n, is determined as an eigenvalue of the system. Thus, F_n in (4.1*c*) will also diverge in a similar factorial-over-power manner, given by

$$F_n \sim \frac{\delta(n)\Gamma(n+\gamma)}{\Delta^{n+\gamma}}. \tag{6.2}$$

This unusual divergent form arises from satisfying the boundary conditions on the complete solution. The presence of a divergent eigenvalue is a feature typically neglected in similar studies and it will not affect the solvability condition we derive in this work. However, we discuss some subtle considerations of this property in § 9.

The $O(B^n)$ component of Bernoulli's equation (4.4*a*) is a linear differential equation for q_n and θ_n, where terms containing the divergent Froude number, F_n, appear as a forcing term. We solve the homogeneous Bernoulli equation, for which the divergent eigenvalue F_n does not appear. In the discussion of § 9 we provide a more detailed justification of why it is sufficient to neglect the divergent eigenvalue, F_n, and the $O(B^n)$ energy condition. This yields

$$\begin{aligned} F_0^2\left(q_0^2 q_n' + 2q_0 q_1 q_{n-1}' + 2q_0 q_0' q_n + \cdots\right) + 2F_0 F_1 q_0^2 q_{n-1}' + \cdots \\ + \theta_n \cos\theta_0 - q_0^2\theta_{n-1}'' - 2q_0 q_1 \theta_{n-2}'' - q_0\theta_0' q_{n-1}' - q_0 q_0' \theta_{n-1}' + \cdots = 0. \end{aligned} \tag{6.3a}$$

In the above equation, we have explicitly written those terms that are necessary to correctly determine the leading- and first-order analysis of the late terms as $n \to \infty$. In particular, note that if the ansatz (6.1*a*,*b*) is differentiated once, then because $(n+\gamma)\Gamma(n+\gamma) = \Gamma(n+\gamma+1)$, the order in n increases by one. Thus, for example, $q_{n-1}' = O(q_n)$ as $n \to \infty$.

Next, we use the boundary-integral equation (4.4*b*) to substitute for θ_n in (6.3*a*). A key idea here, used in previous works on exponential asymptotics and water waves, is that the term that involves the complex Hilbert transform, $\hat{\mathscr{H}}[\theta_n]$, is evaluated on the real axis, and hence away from the singularities $f = af^*$. As a consequence, the contribution is exponentially subdominant to the left-hand side of (4.4*b*) as $n \to \infty$. This idea of neglecting $\hat{\mathscr{H}}[\theta_n]$ is a classic step in exponential asymptotics applications of many boundary-integral problems in interfacial flows (cf. § 3 of Chapman (1999), § 5.3 of Trinh, Chapman & Vanden-Broeck (2011) and Trinh (2017)) and can be rigorously justified in such cases (Tanveer & Xie 2003).

With this in mind, we rearrange the boundary-integral equation (4.4*b*) to find

$$\theta_n \sim \frac{\mathrm{a}\mathrm{i}q_n}{q_0} - \frac{a\mathrm{i}q_1 q_{n-1}}{q_0^2} + \cdots . \tag{6.3b}$$

From this form, θ''_{n-1}, θ''_{n-2} and θ'_{n-1} are found in terms of q_n and its derivatives. Next, we substitute these into Bernoulli's equation (6.3*a*) and consider the divergent ansatz (6.1*a*,*b*). The leading order in n, which comes from the terms q'_n and q''_{n-1}, is seen to be of order $\Gamma(n+\gamma+1)/\chi^{n+\gamma+1}$. Dividing out by this divergence yields terms that are of $O(1)$, $O(1/n)$, and so on as $n \to \infty$.

Combining (6.3*a*) and (6.3*b*), we obtain at leading order

$$\chi'(q_0 F_0^2 + a\mathrm{i}\chi') = 0. \tag{6.4}$$

We seek the non-trivial function χ that forces the divergence of the asymptotic expansion and, hence, takes the value of $\chi = 0$ at the singularities in f. Assuming that $\chi' \neq 0$, we integrate to find

$$\chi(f) = \chi_a(f) = a\mathrm{i}F_0^2 \int_{af^*}^{f} q_0(f')\,\mathrm{d}f'. \tag{6.5}$$

Here, we have chosen the starting point of integration to be the upper/lower-half singularity at $f = af^*$ where $a = \pm 1$. The function χ, denoted the singulant, plays a pivotal role in the form of the exponentially small terms and the associated Stokes smoothing procedure of § 7. It will be convenient to distinguish between the two singulants using the sub-index a.

At the next order in Bernoulli's equation, $O(1/n)$, we use $\chi' = a\mathrm{i}F_0^2 q_0$ and $\chi'' = a\mathrm{i}F_0^2 q'_0$ to find

$$\frac{Q'}{Q} = 2\frac{q'_0}{q_0} - a\mathrm{i}F_0^2 q_1 - 2a\mathrm{i}F_0 F_1 q_0 + a\mathrm{i}\theta'_0 + \frac{a\mathrm{i}\cos\theta_0}{F_0^2 q_0^3}. \tag{6.6}$$

Thus, by integration, we find

$$Q(f) = Q_a(f) = \Lambda_a q_0^2 \exp\left(a\mathrm{i}\theta_0 + a\mathrm{i}\int_0^f \left[\frac{\cos\theta_0}{F_0^2 q_0^3} - F_0^2 q_1 - 2F_0 F_1 q_0\right]\mathrm{d}f'\right). \tag{6.7}$$

The starting point of integration has been chosen to be on the free surface at $f = 0$ for convenience. Other points may be chosen, which alters the value of the constant Λ_a. We note that this constant may take different values for $a = 1$ and $a = -1$. Similarly, the form of Θ is found using (6.3*b*) and, thus,

$$\Theta(f) = \Theta_a(f) = \frac{a\mathrm{i}Q_a(f)}{q_0(f)}. \tag{6.8}$$

Substitution of this solution for $Q(f)$ into ansatz (6.1*a,b*) then yields

$$q_n(f) \sim \Lambda_a q_0^2 \exp\left(a\mathrm{i}\theta_0 + a\mathrm{i}\int_0^f \left[\frac{\cos\theta_0}{F_0^2 q_0^3} - F_0^2 q_1 - 2F_0F_1q_0\right]\mathrm{d}f'\right)\frac{\Gamma(n+\gamma)}{\chi^{n+\gamma}}, \tag{6.9}$$

with χ given by (6.5). A similar form for θ_n may also be found by using the expression for Θ given in (6.8).

6.1. *Determination of γ and Λ*

At this point, we have determined the key components, Q, Θ and χ, that appear in the factorial-over-power ansatz (6.1*a,b*). This leaves the value of the constants γ and Λ_a. Note that our asymptotic series (4.1*a,b*) reorders as $f \to af^*$ (for which $q_0 = O(Bq_1)$ for instance) and the matched asymptotics procedure that results in investigating this limit yields γ and Λ_a.

In order to determine the constant γ, we take the limit $f \to af^*$ and match the order of the singularity of the divergent ansatz, valid for n large, to the low-order behaviour. Setting $n = 0$ in (6.9) and taking the limit of $f \to af^*$ yields

$$q_n|_{n=0} = O\left(\frac{q_0^2}{\chi^\gamma}\exp\left(a\mathrm{i}\theta_0 + a\mathrm{i}\int_0^f \left[\frac{\cos\theta_0}{F_0^2 q_0^3} - F_0^2 q_1 - 2F_0F_1q_0\right]\mathrm{d}f'\right)\right). \tag{6.10}$$

From the scalings of q_0 and θ_0 in § 5.1, and the scaling of q_1 in Appendix A we find that

$$\left.\begin{aligned} \chi^\gamma &= O((f - af^*)^{5\gamma/4}), \\ q_0^2\exp\left(a\mathrm{i}\int_0^f \left[\frac{\cos\theta_0}{F_0^2 q_0^3} - F_0^2 q_1 - 2F_0F_1q_0\right]\mathrm{d}f\right) &= O\left((f - af^*)^{5/4}\right). \end{aligned}\right\} \tag{6.11}$$

We substitute the above into (6.10) and match to $q_0 = O(f - af^*)^{1/4}$ to find

$$\gamma = \tfrac{4}{5}. \tag{6.12}$$

As is the case in many exponential asymptotic analyses, the determination of the constant prefactor, Λ_a, is often the most troublesome aspect of the procedure. For our purposes, it will be sufficient to know that Λ_a is a non-zero constant, and can be determined via the solution of a numerical recursion relation. Specifically, it is found by matching the 'inner' limit of q_n from the divergent form (6.9) with the 'outer' limit of the inner solution for q near $f = af^*$. This analysis is performed in Appendix B, yielding

$$\Lambda_a = -\frac{2\mathrm{i}f^*}{F_0^2 c_a^4}\mathrm{e}^{-\mathcal{P}(af^*)}\left(\frac{4a\mathrm{i}F_0^2 c_a}{5}\right)^{4/5}\lim_{n\to\infty}\frac{\hat{q}_n}{\Gamma(n+\gamma)}. \tag{6.13}$$

Here, $\hat{q}_n$ is the nth term of the outer limit of an inner solution holding near $f = af^*$, and can be determined by recurrence relation (B14). The constant c_a is the prefactor of the singular scaling of q_0 from (5.6) whereas $\mathcal{P}(af^*)$ is given in (A7). We do not need to work with the precise value of Λ_a; however, later in §§ 6.2 and 7.3, the fact that Λ_1 and Λ_{-1} are complex conjugates will be crucial to obtain a real-valued solution on the free surface. As the prefactor, Λ_a, only has a scaling effect on the solutions (and is independent of B), it will be convenient to choose a specific value for visualisation purposes in § 8.

6.2. *The divergence along the free surface*

In order to capture the divergence of q_n along the free surface, $\mathrm{Im}[f] = 0$, we must include the effects of the two symmetrically placed crest singularities indexed by $a = \pm 1$. We thus write

$$\mathfrak{q}_n = q_n|_{a=1} + q_n|_{a=-1}. \tag{6.14}$$

By the results of § B.3, the constants Λ_1 and Λ_{-1} are the complex conjugates of one another. With regards to the two singulants, χ_1 and χ_{-1}, we may split the path of integration via

$$\chi_a(\phi) = a\mathrm{i}F_0^2 \left[\int_{af^*}^{0} + \int_{0}^{\phi} \right] q_0(f')\,\mathrm{d}f', \tag{6.15}$$

for $f = \phi$ along the real axis. As q_0 takes real values on the free-surface, $\mathrm{Im}[f] = 0$, the second integral above is seen to take purely imaginary values. By the Schwarz reflection principle, q_0 evaluated on the imaginary axis between $-af^*$ and af^* is purely real and symmetric about the origin. Therefore the first integral on the right-hand side of (6.15) is purely real and takes the same value regardless of the choice of a. Thus, χ_{-1} and χ_1 are also the complex conjugates of one another on the free surface.

Due to this behaviour of Λ_a and χ_a, we write

$$\Lambda_a = |\Lambda_1| \exp[a\mathrm{i} \arg \Lambda_1] \quad \text{and} \quad \chi_a(\phi) = |\chi_1(\phi)| \exp[a\mathrm{i} \arg \chi_1(\phi)], \tag{6.16a,b}$$

which upon substitution into $\mathfrak{q}_n = q_n|_{a=1} + q_n|_{a=-1}$ yields

$$\mathfrak{q}_n(\phi) = \frac{2|\Lambda_1| q_0^2 \Gamma(n+\gamma)}{|\chi_1(\phi)|^{n+\gamma}} \cos\left[\arg \Lambda_1 - (n+\gamma) \arg \chi_1(\phi) + \theta_0 + I(\phi)\right], \tag{6.17}$$

where we have defined

$$I(\phi) = \int_0^{\phi} \left(\frac{\cos\theta_0}{F_0^2 q_0^3} - F_0^2 q_1 - 2F_0F_1q_0 \right) \mathrm{d}\phi'. \tag{6.18}$$

Thus, the above form (6.17) captures the real-valued divergence on the free-surface.

We have successfully derived an expression for the late term divergence on the axis in (6.17) and off the axis in (6.9).

7. Stokes line smoothing

One of the key ideas of exponential asymptotics is that there exists a link between the factorial-over-power form of the divergences, given (6.1a,b) and (6.17), and the exponentially small terms we wish to derive. Following the work of Dingle (1973), Stokes lines are contours in the f-plane for which both

$$\mathrm{Im}[\chi_a(f)] = 0 \quad \text{and} \quad \mathrm{Re}[\chi_a(f)] \geqslant 0. \tag{7.1a,b}$$

Across and in the vicinity of these contours, exponentially small terms in the solution smoothly change in magnitude across a boundary layer. This is known as the

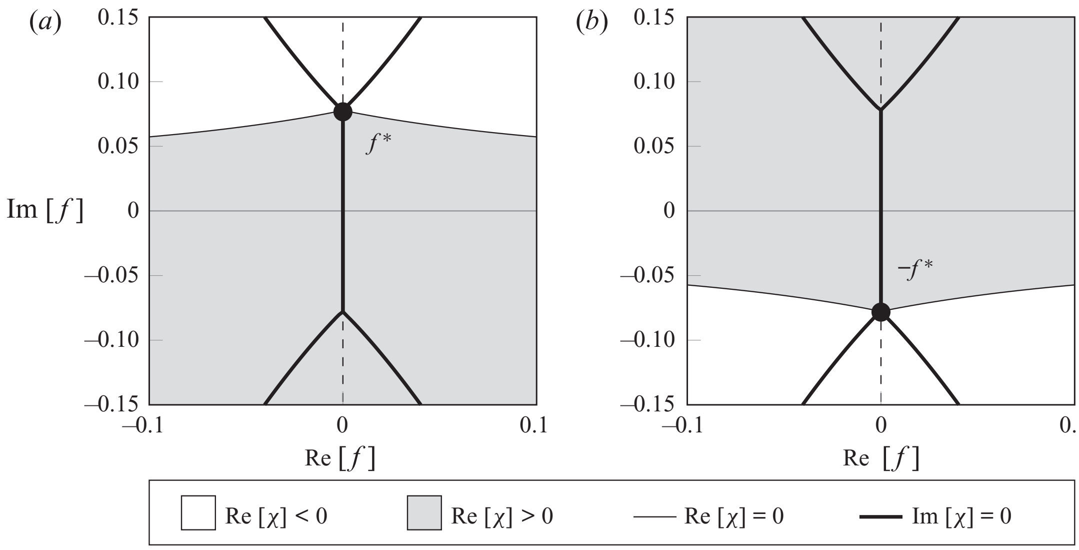

Figure 7. Values of the singulant, χ_a, are shown from the upper-half singularity in (*a*), with $a = 1$, and from the lower-half singularity in (*b*), with $a = -1$. The Stokes lines, which satisfy conditions (7.1*a*,*b*), are shown by the thick lines in the grey-shaded regions. This configuration corresponds to the energy $\mathscr{E} = 0.3804$ for which the upper-half plane singularity is at $f^* \approx 0.07776\mathrm{i}$. The chosen branch cuts for each of these singularities are shown by dashed lines.

Stokes phenomenon. In this section, we discuss the configuration of Stokes lines, and then perform the optimal truncation and Stokes-line-smoothing procedures needed to derive the exponentially small capillary ripples.

7.1. *Analysis of the Stokes lines*

To find the Stokes lines for our problem, we apply conditions (7.1*a*,*b*) to our expression for the singulant, χ_a, given in (6.5) as

$$\chi_a(f) = a\mathrm{i}F_0^2 \int_{af^*}^{f} q_0(f')\,\mathrm{d}f'. \tag{7.2}$$

Here, integration begins at the principal singularity, $f' = af^*$, that lies in the analytic continuation of the free surface. Note that unlike many traditional studies in exponential asymptotics, the determination of the singulant function requires the leading-order solution, q_0, for which there does not exist a closed-form analytical solution. We use numerical values of q_0 to evaluate the singulant, χ_a.

The procedure is as follows. Given a fixed value of the energy, we obtain numerical values of q_0 and θ_0 along the free-surface $\mathrm{Im}[f] = 0$ using the numerical computations of Shelton *et al.* (2021) or any standard procedure for calculating gravity Stokes waves (cf. Vanden-Broeck 1986). Next, the analytic continuation method of Crew & Trinh (2016) is used to find q_0 and θ_0 in the complex f-plane. Values for χ_a are then found across the domain by integrating q_0 along paths originating at either singularity. Graphs of the critical contours of $\mathrm{Im}[\chi_a]$ and $\mathrm{Re}[\chi_a]$ are given in figure 7 for the two choices of $a = 1$ and $a = -1$. We see that there are two Stokes lines along the imaginary axis from $f = -f^*$ to $f = f^*$, one for $a = 1$ and another for $a = -1$, which intersect with the free surface at the wave crest $\phi = 0$.

Note that only the Stokes lines that intersect with the free-surface, $\mathrm{Im}[f] = 0$, are considered; other Stokes lines would indicate a switching on or switching off of exponentials in the general complex plane, but are not associated with the physical production of surface ripples.

7.2. *Optimal truncation*

In order to capture the exponentially small components of the solution, which do not appear in the Poincaré series (4.1*a*,*b*), we truncate the series at $n = N - 1$ by considering

$$q = \underbrace{\sum_{n=0}^{N-1} B^n q_n}_{q_r} + \bar{q}, \quad \theta = \underbrace{\sum_{n=0}^{N-1} B^n \theta_n}_{\theta_r} + \bar{\theta} \quad \text{and} \quad F = \underbrace{\sum_{n=0}^{N-1} B^n F_n}_{F_r} + \bar{F}, \tag{7.3a–c}$$

and, thus, we have introduced the notation of q_r, θ_r and F_r for the truncated regular expansions of the solutions and eigenvalue.

We demonstrate that when truncated optimally at the point where two consecutive terms are of the same order, that is, choose N such that $|B^N q_N| \sim |B^{N+1} q_{N+1}|$, the remainders $\bar{q}$, $\bar{\theta}$ and $\bar{F}$ will be exponentially small. This point of optimal truncation is given by

$$N = \frac{|\chi_a|}{B} + \rho, \tag{7.4}$$

where $\rho \in [0, 1)$ is a bounded number to ensure N is an integer.

Substituting these into the boundary-integral equation (2.9*b*) yields a relationship between $\bar{\theta}$ and $\bar{q}$, given by

$$\bar{\theta} = \frac{a\mathrm{i}\bar{q}}{q_r} - a\mathrm{i}\xi_{int} - a\mathrm{i}\hat{\mathscr{H}}[\bar{\theta}] + O(\bar{q}^2). \tag{7.5}$$

Similarly we can insert the truncations (7.3*a*–*c*) into Bernoulli's equation (2.9*a*). This gives a second-order differential equation for $\bar{q}$ and $\bar{\theta}$. Upon substituting for $\bar{\theta}$ from (7.5), this is reduced down to an equation for $\bar{q}$ only. Furthermore, we neglect the Hilbert transform of the remainder, $\hat{\mathscr{H}}[\bar{\theta}]$, as this is anticipated to be exponentially subdominant. This yields

$$\begin{aligned} &\left[a\mathrm{i}Bq_r\right]\bar{q}'' + \left[-F_r^2 q_r^2 - a\mathrm{i}Bq_r' + Bq_r\theta_r' - a\mathrm{i}Bq_r\xi_{int}'\right]\bar{q}' \\ &\quad + \left[-\frac{a\mathrm{i}\cos\theta_r}{q_r} - 2F_r^2 q_r q_r' + \frac{a\mathrm{i}B(q_r')^2}{q_r} + Bq_r'\theta_r' \right. \\ &\quad \left. - a\mathrm{i}Bq_r'' + 2Bq_r\theta_r'' - a\mathrm{i}Bq_r'\xi_{int}' - 2a\mathrm{i}Bq_r\xi_{int}''\right]\bar{q} - 2F_r q_r^2 q_r'\bar{F} = \mathcal{R} + O(\bar{q}^2). \end{aligned} \tag{7.6}$$

This is a second-order differential equation for $\bar{q}$, in which the forcing terms on the right-hand side are of $O(B^N)$. A similar equation was derived by Trinh (2017) for the low-Froude limit of gravity waves. Here, we have introduced the forcing terms ξ_{int} and ξ_{bern} arising from the Poincaré expansion in the boundary-integral and Bernoulli's equations as

$$\xi_{int} = \hat{\mathscr{H}}[\theta_r] - a\mathrm{i}\theta_r - \log q_r, \tag{7.7a}$$

$$\xi_{bern} = F_r^2 q_r^2 q_r' + \sin(\theta_r) - B(q_r^2\theta_r'' + \theta_r' q_r' q_r), \tag{7.7b}$$

$$\mathcal{R} = \xi_{bern} - a\mathrm{i}\cos\theta_r\xi_{int} + a\mathrm{i}Bq_r q_r'\xi_{int}' + a\mathrm{i}Bq_r^2\xi_{int}''. \tag{7.7c}$$

Due to the truncation at $n = N - 1$, equation (7.6) is satisfied exactly for every order up to and including B^{N-1} because $\xi_{int} = O(B^N)$ and $\xi_{bern} = O(B^N)$.

7.3. *Stokes line smoothing*

We now seek a closed-form asymptotic expression for $\bar{q}$ and the terms switched-on across Stokes lines. We start with the homogeneous form of (7.6), in which the terms on the right-hand side and $\bar{F}$ are neglected. Following the exponential asymptotics methodology established in, e.g., § 4 of Chapman & Vanden-Broeck (2006), we note that the homogeneous problem has solutions of the form,

$$\bar{q}_{homog} \sim Q_a(f) \exp\left(-\frac{\chi_a(f)}{B}\right), \tag{7.8}$$

where $\chi_a(f)$ and $Q_a(f)$ satisfy those same equations as found for the late-term ansatz via (6.4) and (6.6). To observe the Stokes phenomenon and the switching of exponentials, we now include the forcing terms on the right-hand side of (7.6) for $\bar{q}$. We consider a solution of the form

$$\bar{q}(f) = A_a(f) Q_a(f) \exp\left(-\frac{\chi_a(f)}{B}\right), \tag{7.9}$$

where the Stokes multiplier $A_a(f)$ is introduced to capture the switching behaviour that occurs across the Stokes lines. When the truncation point, N, is chosen optimally as in (7.4), $\bar{q}$ will be seen to be exponentially small and will change in magnitude across the lines where $\mathrm{Im}[\chi_a] = 0$ and $\mathrm{Re}[\chi_a] \geqslant 0$.

The algebra for this procedure follows very similarly to, e.g., Chapman *et al.* (1998), Chapman & Vanden-Broeck (2006) and Trinh (2017). Thus, when the exponential form of (7.9) for $\bar{q}$ is substituted into (7.6), the dominant balance at leading order is identically satisfied by our choice of χ determined in (6.4). The first non-trivial balance occurs at $O(\mathrm{e}^{-\chi/B})$, which also involves the forcing terms on the right-hand side. We extract the $O(B^N)$ terms from $\mathcal{R}$ in (7.7*c*), and this yields $\mathcal{R} \sim -q_0^2 \theta_{N-1}'' B^N$. The governing equation for A_a is then given by

$$\left[F_0^2 q_0^2 Q_a \mathrm{e}^{-\chi_a/B}\right] \frac{\mathrm{d}A_a}{\mathrm{d}f} \sim -a\mathrm{i} q_0 q_{N-1}'' B^N, \tag{7.10}$$

where we have used $\theta_{N-1}'' \sim a\mathrm{i} q_0^{-1} q_{N-1}''$ from the boundary-integral equation (6.3*b*).

By substituting in the factorial-over-power form for q_{N-1}'' from (6.1*a*,*b*), and using the chain rule to change differentiation to be in terms of χ_a, we find

$$\frac{\mathrm{d}A_a}{\mathrm{d}\chi_a} = \frac{B^N \mathrm{e}^{\chi_a/B} \Gamma(N+1+\gamma)}{\chi_a^{N+1+\gamma}}. \tag{7.11}$$

This is now of an equivalent form to that found by Chapman & Vanden-Broeck (2006) for the low-Froude limit of gravity waves (cf. their (4.4)). In brief, the procedure is as follows. First, we write $\chi_a = r_a \mathrm{e}^{\mathrm{i}\vartheta_a}$ and truncate optimally via (7.4) with $N = r_a/B + \rho$. Examination of the differential equation (7.11) shows that there exists a boundary layer at $\vartheta_a = 0$ and indeed this is the anticipated Stokes line where $\mathrm{Im}[\chi_a] = 0$. The appropriate inner variable near the Stokes line is $\vartheta_a = B^{1/2}\overline{\vartheta}_a$ and (7.11) can then be integrated to show

$$A_a(f) = C_a + \frac{\sqrt{2\pi}\mathrm{i}}{B^\gamma} \int_{-\infty}^{\overline{\vartheta}_a \sqrt{r_a}} \exp(-t^2/2)\, \mathrm{d}t, \tag{7.12}$$

where C_a is constant. Taking the outer limit of $\bar{\vartheta} \to \infty$, we then see that across the Stokes line, there is a jump of

$$A_a(\vartheta_a \to 0-) - A_a(\vartheta_a \to 0+) = \frac{2\pi\mathrm{i}}{B^\gamma}. \tag{7.13}$$

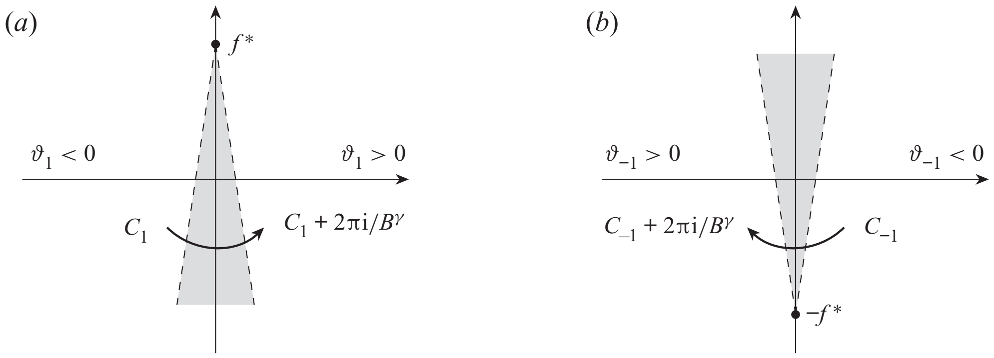

Figure 8. The Stokes smoothing procedure is visualised in the f-plane for (*a*) $a = 1$ and (*b*) $a = -1$.

As concerns the relationship between Stokes-line contributions from $f = f^*$ and $f = -f^*$, note that as χ_1 is the complex conjugate of χ_{-1}, we have $\vartheta_1 = -\vartheta_{-1}$. Thus, we anticipate that C_1 switches to $C_1 + 2\pi\mathrm{i}/B^\gamma$ as one proceeds from left-to-right across the Stokes line from $f = f^*$. This is shown in figure 8(*a*). On the other hand, C_{-1} switches to $C_{-1} + 2\pi\mathrm{i}/B^\gamma$ proceeding from right-to-left across the Stokes line from $f = -f^*$. This is shown in figure 8(*b*). We emphasise that the above Stokes smoothing procedure only provides the local change of the prefactor, A_a, across the Stokes line. Determination of the constant, C_a, will follow from imposition of the boundary conditions.

Returning now to (7.9), we write the leading-order exponentials on the axis, $\mathrm{Im}[f] = 0$, via $\bar{\mathfrak{q}} = \bar{q}|_{a=1} + \bar{q}|_{a=-1}$, either as an inner solution

$$\bar{\mathfrak{q}}(\phi) = A_1(\phi)Q_1(\phi)\exp\left(-\frac{\chi_1(\phi)}{B}\right) + A_{-1}(\phi)Q_{-1}(\phi)\exp\left(-\frac{\chi_{-1}(\phi)}{B}\right), \tag{7.14a}$$

for which $A(\phi)$ is given by (7.12), or as an outer solution by

$$\bar{\mathfrak{q}}(\phi) \sim \begin{cases} C_1\left(Q_a\mathrm{e}^{-\chi_a/B}\right)\Big|_{a=1} + \left\{C_{-1} + \dfrac{2\pi\mathrm{i}}{B^\gamma}\right\}\left(Q_a\mathrm{e}^{-\chi_a/B}\right)\Big|_{a=-1} & \text{for } \phi < 0, \\ \left\{C_1 + \dfrac{2\pi\mathrm{i}}{B^\gamma}\right\}\left(Q_a\mathrm{e}^{-\chi_a/B}\right)\Big|_{a=1} + C_{-1}\left(Q_a\mathrm{e}^{-\chi_a/B}\right)\Big|_{a=-1} & \text{for } \phi > 0. \end{cases} \tag{7.14b}$$

In (7.14*b*), the constants, C_1 and C_{-1}, will be determined by enforcing periodicity on $\bar{\mathfrak{q}}$ and $\bar{\mathfrak{q}}'$, as given by

$$\bar{\mathfrak{q}}\left(-\tfrac{1}{2}\right) = \bar{\mathfrak{q}}\left(\tfrac{1}{2}\right) \quad \text{and} \quad \bar{\mathfrak{q}}'\left(-\tfrac{1}{2}\right) = \bar{\mathfrak{q}}'\left(\tfrac{1}{2}\right). \tag{7.15a,b}$$

The second relation above arose by evaluating the derivative of periodicity condition (2.4*b*) at $\phi = 0$. In writing $C_1 = C_1^R + \mathrm{i}C_1^I$ and $C_{-1} = C_{-1}^R + \mathrm{i}C_{-1}^I$, we have four unknowns balancing the four equations from the real and imaginary parts of (7.15*a*,*b*). Using $\varLambda_a = |\varLambda_1|\mathrm{e}^{a\mathrm{i}\arg\varLambda_1}$ from (6.16*a*,*b*) and $\chi_a = \mathrm{Re}[\chi_1] + a\mathrm{i}\,\mathrm{Im}[\chi_1]$ then yields the solutions

$$\left.\begin{aligned} C_1^I &= -\frac{\pi}{B^\gamma}, \quad C_1^R = -\frac{\pi}{B^\gamma}\frac{\cos[G(1/2)]}{\sin[G(1/2)]}, \\ C_{-1}^I &= -\frac{\pi}{B^\gamma}, \quad C_{-1}^R = -\frac{\pi}{B^\gamma}\frac{\cos[G(1/2)])}{\sin[G(1/2)]}, \end{aligned}\right\} \tag{7.16}$$

where

$$G(\phi) = \theta_0(\phi) + \int_0^\phi\left[\frac{\cos\theta_0}{F_0^2q_0^3} - F_0^2q_1 - 2F_0F_1q_0 - \frac{F_0^2q_0}{B}\right]\mathrm{d}\phi. \tag{7.17}$$

Solutions are not possible when $\sin[G(1/2)] = 0$, from which we obtain the following discrete set of values of B,

$$B_n = \frac{F_0^2 \displaystyle\int_0^{1/2} q_0 \, \mathrm{d}\phi}{\theta_0(1/2) + \displaystyle\int_0^{1/2} \left[\frac{\cos\theta_0}{F_0^2 q_0^3} - F_0^2 q_1 - 2F_0F_1q_0 \right] \mathrm{d}\phi + n\pi} \quad \text{for } n \in \mathbb{Z}^+. \tag{7.18}$$

Formula (7.18) provides the crucial eigenvalue condition for the non-existence of solutions. Recall that the 'parameters' in this formula, e.g. $\{F_0, F_1, q_0, q_1, \theta_0\}$, are dependent on the chosen energy, $\mathscr{E}$, in (2.9*c*). Note that $\theta_0(1/2) = 0$ and, in addition, only solutions with positive integer values of n correspond to positive values of the Bond number. Thus, for instance, it is predicted that solutions do not exist at a countably infinite set of discrete values,

$$B_1(\mathscr{E}) > B_2(\mathscr{E}) > B_3(\mathscr{E}) > \cdots > B_n(\mathscr{E}) > \cdots > 0. \tag{7.19}$$

In the next section, we show that these values of B are associated with points between adjacent 'fingers' of solutions in the bifurcation diagram.

Substitution of (7.16) for C_1 and C_{-1} into (7.14*b*) then gives a real-valued solution on the free surface. First, for $\phi < 0$, we have

$$\bar{\mathfrak{q}}(\phi) = -\frac{2\pi}{B^\gamma}|\Lambda_1| q_0^2 \mathrm{e}^{-\mathrm{Re}[\chi_1]/B} \left[\frac{\cos(G(1/2))}{\sin(G(1/2))} \cos[\arg \Lambda_1 + G(\phi)] - \sin[\arg \Lambda_1 + G(\phi)] \right], \tag{7.20a}$$

whereas for values on the positive real axis $\phi > 0$,

$$\bar{\mathfrak{q}}(\phi) = -\frac{2\pi}{B^\gamma}|\Lambda_1| q_0^2 \mathrm{e}^{-\mathrm{Re}[\chi_1]/B} \left[\frac{\cos(G(1/2))}{\sin(G(1/2))} \cos[\arg \Lambda_1 + G(\phi)] + \sin[\arg \Lambda_1 + G(\phi)] \right]. \tag{7.20b}$$

Note that the above forms for $\bar{\mathfrak{q}}$ are valid away from the boundary layer surrounding the Stokes line at $\phi = 0$.

8. Numerical comparisons with the full water-wave model

We now compare the asymptotic results of § 7.3 with the numerical solutions of the fully nonlinear equations (2.1*a*)–(2.1*d*) found by Shelton *et al.* (2021). These numerical solutions were calculated using a spectral method on a domain, ϕ, uniformly discretised with $N = 1024$ points (cf. § 4 of Shelton *et al.* (2021) for details).

8.1. *Finding values for our analytical solution*

To obtain precise values for our analytical solution, $\bar{\mathfrak{q}}$, across the domain, we use the form given in (7.14*a*). This form includes the local change across the boundary layer at $\phi = 0$ and requires known values of q_0, θ_0, F_0, q_1 and F_1 for a specified value of the energy, $\mathscr{E}$.

In order to calculate values for these nonlinear solutions, we employ Newton iteration on the $O(1)$ and $O(B)$ (4.2) and (4.3) with an even discretisation of the domain, ϕ. With these values known, the three components of $\bar{\mathfrak{q}}$, the Stokes prefactor, $A_a(\phi)$, the functional prefactor, $Q_a(\phi)$, and the singulant, $\chi_a(\phi)$, may then be calculated individually with a specified value of B.

(i) For $Q_a(\phi)$ given in (6.7), we take the previously computed values for θ_0, q_0, F_0, q_1 and F_1 and employ numerical integration across the domain. As noted in § 6.1, it is convenient to choose a value of $|\Lambda_a|$ in order to facilitate visualisation of the ripples. In figures 9 and 11, we plot $\bar{\mathfrak{q}}$ with $|\Lambda_a| = 1$. In figure 10, in order to compare between asymptotic and numerical solutions, we have chosen $|\Lambda_a| = 0.006$, which is estimated by numerical fitting. It can be verified that fitting to other fingers changes the constant by only a small amount.

(ii) To determine $\chi_a(\phi)$, we split the range of integration as in (6.15). This allows for $\mathrm{Re}[\chi_a]$ to be calculated by integrating q_0 through the complex-valued domain from the singularity at $f = af^*$ to the wave crest at $f = 0$. Next, $\mathrm{Im}[\chi_a]$ is found by integrating q_0 over the free surface from $f = 0$ to $f = \phi$. Values for the integrand, q_0, are found with the analytic continuation method from Crew & Trinh (2016) described in § 7.1.

(iii) To find the Stokes prefactor, $A_a(\phi)$, from (7.12), the upper limit of the integral is determined by using $r_a = |\chi_a|$ and $\bar{\vartheta} = \arg \chi_a / B$ from the known values of χ_a. The integral is then calculated with known values of the error function. The constants C_a are then found by calculating $G(1/2)$ from (7.17).

This process yields values for our exponentially small component of the solution, $\bar{\mathfrak{q}}$, for specified values of B and $\mathscr{E}$. The values of B_n where the solvability condition fails from (7.18) are also found with the same method used for Q_a above.

8.2. *Comparisons*

We begin by comparing the values of B_n (where the solvability condition fails) with the (B, F) bifurcation space computed numerically by Shelton *et al.* (2021). In taking the same value of the energy, $\mathscr{E} = 0.3804$, we visualise these points in the (B, F)-plane by approximating F_n by $F_n \approx F_0 + B_n F_1$ (an error of $O(B^2)$). This comparison is shown in figure 9. These locations where perturbation solutions are non-existent show excellent agreement with the points between adjacent branches of solutions where numerical solutions could not be calculated.

In addition, four of our analytical solution profiles, $\bar{\mathfrak{q}}$, are shown in insets (*a*)–(*d*) of this figure. These solutions have been selected to lie in the midpoint of the solution branch, with a Bond number of $(B = (B_n + B_{n+1})/2)$. They demonstrate that the ripples obtain their greatest magnitude at the edge of the periodic domain. Note that these ripples are plotted on a zero background state. These same solutions are also shown in figure 10, which includes the first two terms of the asymptotic expansion, $q_0 + Bq_1$. These have been provided to compare the magnitude of the ripples in relation to the leading-order Stokes wave.

In our previous numerical work, we demonstrated that as one of the solution branches was transversed, the solution develops an extra wavelength, and this was seen to occur near the top of the solution branch. We observe that the same effect occurs with our analytical solutions. This is demonstrated in figure 11, in which we provide eight solution profiles equally spaced in the Bond number between two adjacent values of B_n. From these, we see that as we travel from right to left across the solution branch by decreasing the value of B, an additional ripple forms in the centre of the domain.

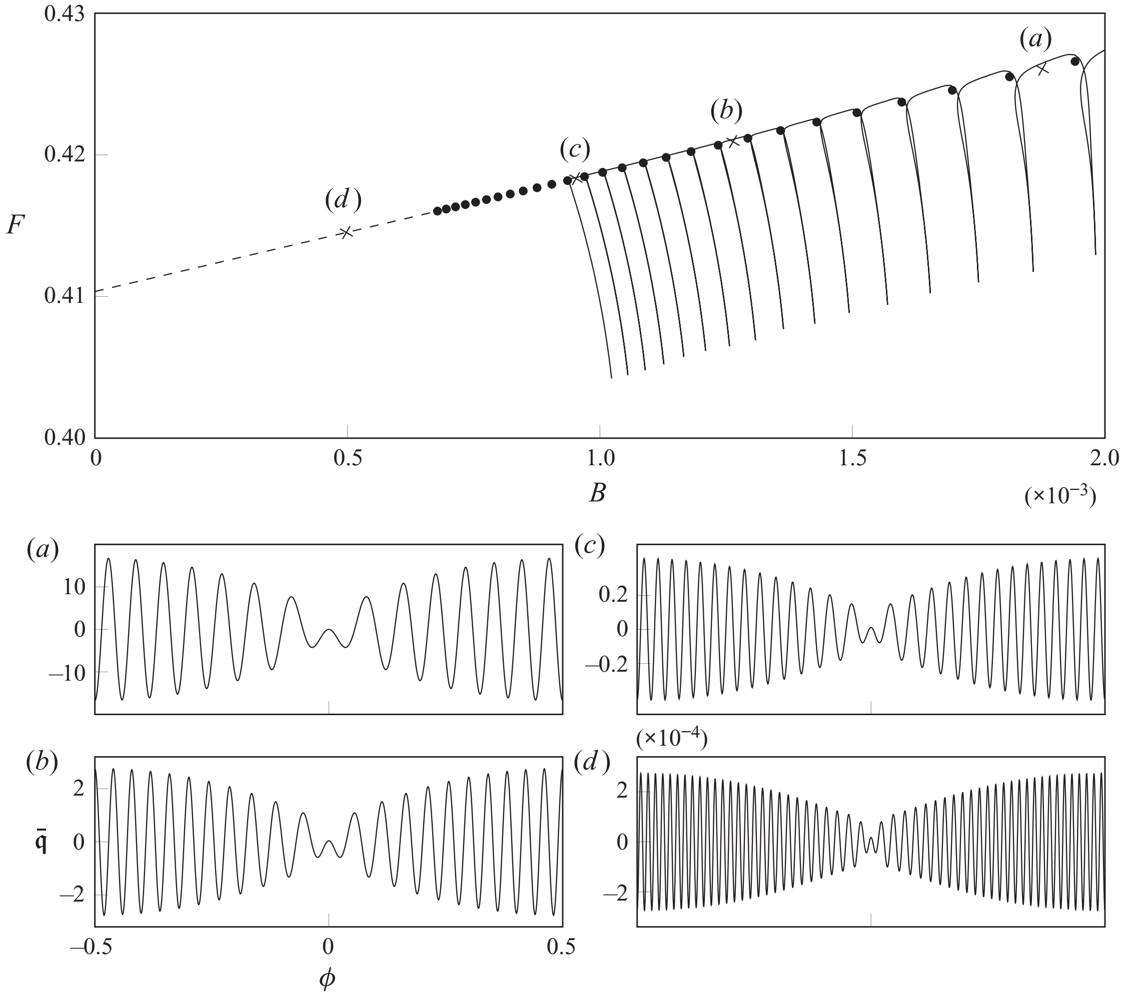

Figure 9. A comparison between the numerical solution branches of Shelton *et al.* (2021) (shown solid) and the analytical approximations of B_n from (7.18) (shown as black circles). Insets (*a*)–(*d*) show the exponentially small ripples, $\bar{\mathrm{q}}$, from (7.20) for the four locations of $B = 0.001876$, $B = 0.001264$, $B = 0.0009527$ and $B = 0.0004978$ (shown as crosses in the main inset). The solutions are all computed at $\mathscr{E} = 0.3804$. A value of $|\Lambda_a| = 1$ has been used for the constant prefactor.

8.3. *The effects of changing the energy,* $\mathscr{E}$

All of the above solutions have been computed for the same fixed value of the energy, $\mathscr{E} = 0.3804$. We now relax this restriction by considering values of $\mathscr{E}$ between 0 and 0.9. Note that the limiting Stokes wave is not the most energetic (cf. § 6 of Longuet-Higgins & Fox 1978) and for values of $\mathscr{E}$ very close to unity, there are multiple possible solutions beyond the classical Stokes wave. We do not consider solutions too close to the highest wave ($\mathscr{E} > 0.9$) in this work.

In figure 12 we show how the locations where the solvability condition fails, $B_n(\mathscr{E})$, change with the energy for values of $n \leqslant 40$. We note that as the energy deceases to zero and we enter the linear regime, these lines tend towards the predictions by Wilton (1915). These are the discrete values of the Bond number for which two linear solutions of wavenumbers 1 and n also have the same Froude number. Thus, a single leading-order gravity wave of the type assumed in this work is insufficient for describing Wilton's linear solutions, and is why we recover his values under this limit.

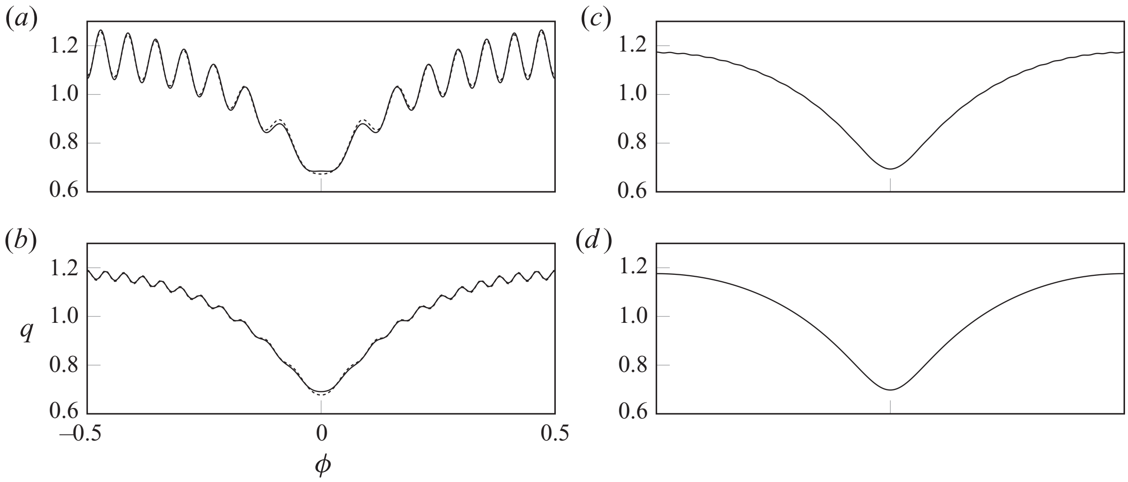

Figure 10. The analytical solution, $q = q_0 + Bq_1 + \bar{q}$, is shown (line) for the four profiles calculated in figure 9. For comparison, numerical solutions with the same value of B and $\mathscr{E}$ are shown dashed in insets (a) and (b). A value of $|\Lambda_a| = 0.006$ has been used for these comparisons, estimated from numerical comparisons.

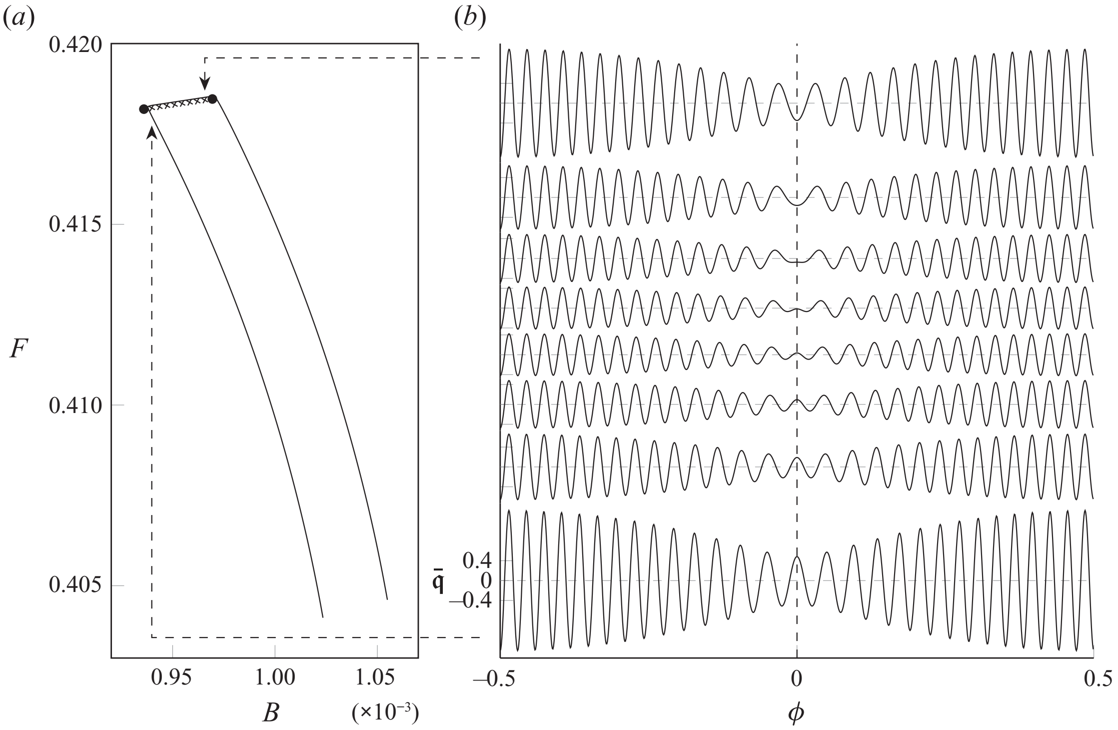

Figure 11. Here, for $\mathscr{E} = 0.3804$, we plot the exponentially small solution, $\bar{\mathrm{q}}$, from (7.20) between the two values of $B_{29} = 0.0009360$ and $B_{28} = 0.0009694$. Note that the base gravity wave is thus not shown. The eight chosen values of B (crosses) are equally spaced between the values of B_{29} and B_{28}. This corresponds to the finger $G_{28\to 29}$ found numerically by Shelton *et al.* (2021). A value of $|\Lambda_a| = 1$ has been used for the constant prefactor.

We have also chosen to provide values of $\mathrm{Re}[\chi]$ for different values of $\mathscr{E}$, as this controls the exponential behaviour of the magnitude of our parasitic ripples. This is shown in figure 13, and shows that the constant controlling the exponential behaviour of our solution increases with the energy, $\mathscr{E}$.

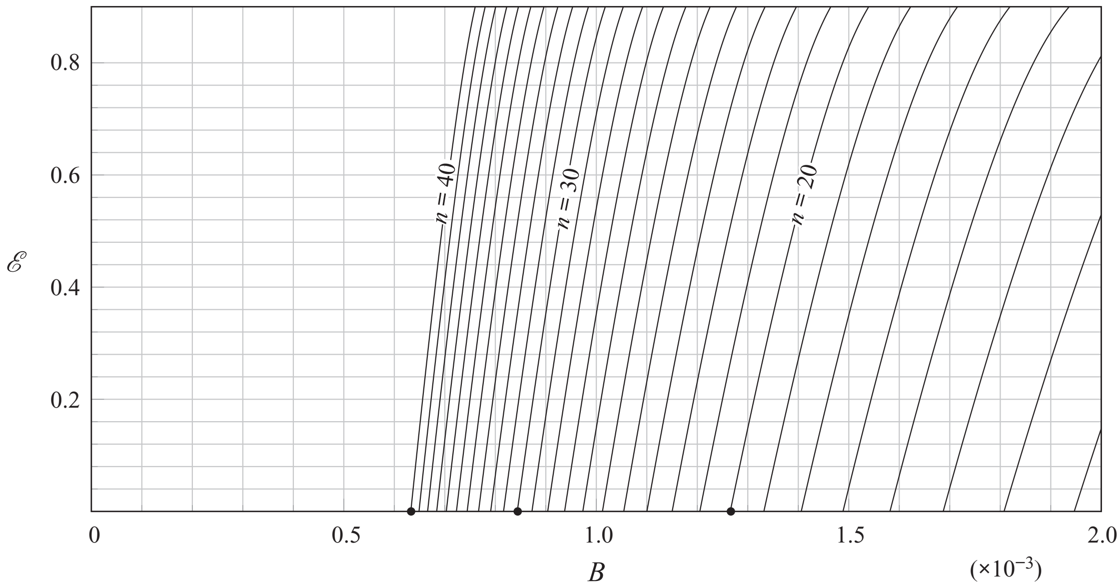

Figure 12. Values for B_n, where the solvability condition fails, are shown for different values of the energy, $\mathscr{E}$. The small-$\mathscr{E}$ predictions by Wilton (1915) are shown by the black dots at $\mathscr{E} = 0$ for $n = 20$, 30 and 40.

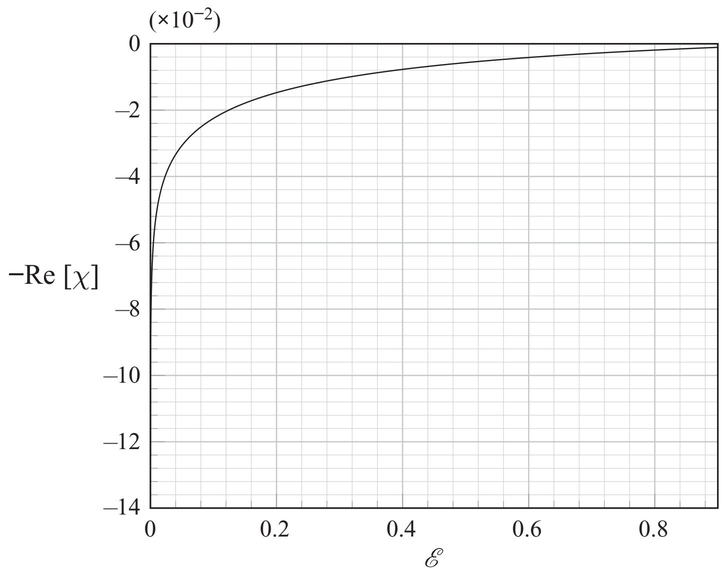

Figure 13. The value of $-\mathrm{Re}[\chi]$ from (6.15) is shown for different values of the energy, $\mathscr{E}$.

9. Discussion

9.1. *Open and resolved challenges in exponential asymptotics*

Over the past 20 years, the application of exponential asymptotics to fluid mechanical problems has been very successful in the discovery and development of new analytical methodologies (Boyd 1998). However, there are a number of distinguishing features in our treatment of the parasitic ripples problem that are particularly interesting.

First, the majority of preceding works in exponential asymptotics typically rely upon the derivation of a crucial singulant function, χ, for which an exact analytical form is known. In our analysis, however, the singulant in (6.5) requires the complex integration of a nonlinear gravity wave, which must be precomputed. Moreover, the values of χ and the associated Stokes lines must be determined in the complex plane, and this has necessitated a separate study of the distribution and properties of the singularities of the Stokes wave problem (Crew & Trinh 2016) as a precursor to the present work.

Second, there are a number of challenging steps in the exponential asymptotics analysis that we highlight here. The reader should note two interesting features.

(i) The eigenvalues, F_n, are divergent, but we have not had to rely upon their form in the derivation of $\mathfrak{q}_n$ in § 6.

(ii) Our factorial-over-power expression for $\mathfrak{q}_n$, valid only in the limit $n \to \infty$, satisfies neither the energy condition nor the periodicity conditions on q_n and q_n'. This is because our approximation of this divergence is only valid in the vicinity of the Stokes line about which the Stokes phenomenon occurs, rather than globally.

Through a more detailed analysis, it is possible to derive both a factorial-over-power ansatz for F_n, as well as the additional terms necessary so that the late-term approximation satisfies the energetic and periodicity conditions. We provide a brief comment on the procedure, but some of these issues are more easily observed in a simpler eigenvalue problem exhibiting divergence; this will be the focus of future work by the current authors (authors' unpublished observations).

In essence, the eigenvalue divergence produces inhomogeneous contributions to Bernoulli's equation depending on F_n, F_{n-1}, ... (compare (6.3*a*) with (4.4*a*)). These contributions, of the form (6.2), will force additional components in the late-term representation of the solution. Both the periodicity and energy constraints can then be satisfied with the inclusion of further components associated with $\chi' = 0$, currently neglected following (6.4). Once these additional divergences are included, a prediction for the eigenvalue, F_n, is obtained.

As it turns out, however, these additional components are subdominant to the divergent ansatz (6.1*a*,*b*) with $\chi = \chi_a(f)$ given by (6.5) near the relevant Stokes lines. Consequently, these components will not influence the Stokes smoothing procedure derived in § 7. We note that this is analogous to how the complex Hilbert transform, $\hat{\mathscr{H}}[\theta_n]$, is neglected in the discussion following (6.3*a*).

9.2. *Asymmetry in steady and temporal water-waves*

It is important to note that in this work, following Longuet-Higgins (1963), we have focused on a fairly restricted view of parasitic ripples that correspond to the classical potential flow formulation of a steadily travelling wave composed of a perturbation about a symmetric nonlinear gravity wave. This assumption also follows from the class of solutions first detected by Shelton *et al.* (2021).

We would expect that within this steady potential framework, it is possible to obtain general asymmetric gravity–capillary solutions exhibiting small-scale ripples in the $B \to 0$ limit. Indeed, solutions resembling this anticipated structure have been calculated by previous authors; for instance Zufiria (1987*b*) considered symmetry breaking in gravity–capillary waves for moderately small values of the surface-tension coefficient. The properties of the waves in that study match those presented in this paper, as some appear to be perturbations about the asymmetric gravity waves found in Zufiria (1987*a*). The general detection of asymmetric gravity–capillary waves remains a challenging problem (cf. Gao, Wang & Vanden-Broeck 2017).

However, it is likely that the above relaxation of symmetry in the solutions does not lead to the typical distribution of asymmetric capillary ripples that appear on the forward face of a steep travelling wave. In order to produce the asymmetry viewed in experimental results, it is likely necessary to consider further modifications to this theory (cf. Perlin & Schultz 2000). Possible extensions include accounting for the additional effects of time dependence, viscosity or vorticity.

The problem of time-dependent parasitic waves has been studied numerically by multiple authors, such as Hung & Tsai (2009), Murashige & Choi (2017) and Wilkening & Zhao (2021). For instance, Hung & Tsai (2009) studied a time-dependent formulation that includes vortical effects; a pure gravity wave is chosen as the initial condition and time-evolution results in the formation of parasitic ripples ahead of the wave crest. Similar methodologies have been implemented by, e.g., Deike, Popinet & Melville (2015) in order to study the formation of time-dependent parasitic ripples in the full Navier–Stokes system using a volume-of-fluid method. We note that small-scale ripples can also occur near the crest of gravity waves as they approach a limiting formulation, as shown by Chandler & Graham (1993) for solutions close to the steady Stokes wave of extreme form and Mailybaev & Nachbin (2019) for finite-depth breaking waves. In our present work, the authors are examining the application of exponential asymptotic techniques to the description of time-dependent parasitic ripples. The inclusion of time dependence in asymptotics beyond-all-orders remains a poorly understood problem, and very few authors including Chapman & Mortimer (2005), Lustri (2013) and Lustri, Pethiyagoda & Chapman (2019), have considered such a complication.

Analogously, the extension of models of gravity–capillary waves to include non-zero viscosity, vorticity or finite depth have been considered by various authors. For instance Longuet-Higgins (1963, 1995) and Fedorov & Melville (1998) considered viscous gravity–capillary waves which exhibit asymmetry. Furthermore, we would expect that a similar application of exponential asymptotics to the case of periodic finite-depth flows could be achieved; in the shallow-water limit, the results would match those presented in seminal works on generalised solitary waves in Kortewe–de Vries equations (see e.g. Yang & Akylas (1996, 1997) and chapter 10 of Boyd 1998). It is an interesting question to consider the equivalent exponential asymptotic analysis for these more complex problems where we expect similar phenomena to arise.

10. Conclusions

We have considered the small surface-tension limit of gravity–capillary waves of infinite depth. This results in gravity-wave solutions at leading order. The parasitic ripples, which have a wavelength much smaller than that of the base gravity wave, appear beyond all orders of the asymptotic expansion as their amplitude is exponentially small in the Bond number. The analytical solution for these from (7.20) has been found by

(i) observing the divergence of the Poincaré series $q = q_0 + Bq_1 + \ldots$, a consequence of singularities in the analytic continuation of the leading-order solution, q_0;

(ii) optimally truncating the divergent expansion at $N \sim 1/B$ and considering the exponentially small remainder $\bar{q}$ by a solution of the form $q = q_0 + Bq_1 + \cdots + B^N q_N + \bar{q}$;

(iii) identifying the Stokes lines (which depend on q_0) and calculating the effect of Stokes phenomenon on the exponentially small terms.

We have also found a solvability condition for our problem, which fails at discrete values of the Bond number given by (7.18). These points were shown in figure 9 to coincide with the discrete nature of the numerical solution branches. Moreover, we have demonstrated that if the leading-order gravity wave is taken to be symmetric, these parasitic ripples must also exhibit symmetry about the wave crest; presenting a fundamental improvement in our understanding of the structure of these parasitic waves.

Our results provide an analytical theory and framework for the numerical solutions detected in Shelton *et al.* (2021). Moreover, we have shown that, although certain details of Longuet-Higgins (1963) theory of parasitic capillary ripples are correct, an exponential asymptotics approach provides verifiable asymptotic predictions, corrected functional relationships, and connection of the ripples to Stokes lines and the Stokes phenomenon.

Acknowledgements. We thank Professors P. Milewski and J. Toland (Bath) for helpful discussions, and the anonymous reviewers for their insightful comments on our work.

Funding. This work was supported by the Engineering and Physical Sciences Research Council (EP/V012479/1).

Declaration of interests. The authors report no conflict of interest.

Author ORCIDs.
Josh Shelton https://orcid.org/0000-0001-6257-5190;
Philippe H. Trinh https://orcid.org/0000-0003-3227-1844.

Appendix A. Singular scaling of the order B quantities

In § 6.1, the inner limit of q_n as $f \to af^*$ relied on the singular behaviour of the $O(B)$ term q_1. Taking the $O(B)$ equations, we substitute θ_1 from the boundary-integral equation (4.3*b*) into Bernoulli's equation (4.3*a*) to find

$$F_0^2 q_0^2 \frac{\mathrm{d}q_1}{\mathrm{d}f} + \left[2F_0^2 q_0 q_0' + \frac{a\mathrm{i}\cos\theta_0}{q_0}\right] q_1 + 2F_0F_1 q_0^2 q_0' - a\mathrm{i}\hat{\mathscr{H}}[\theta_1]\cos\theta_0 - q_0(q_0\theta_0')' = 0. \tag{A1}$$

The singular scaling of $\cos\theta_0$ can be found from (5.6) to be

$$\cos\theta_0 \sim \frac{1}{2}\mathrm{e}^{a\mathrm{i}\theta_0} \sim \frac{-a\mathrm{i}F_0^2 c_a^3}{4}(f - af^*)^{-1/4}. \tag{A2}$$

Thus, the term involving the complex-valued Hilbert transform $\hat{\mathscr{H}}[\theta_1]$, which acts on the free surface upon which $\theta_1 \sim O(1)$, is subdominant in (A1). The same is true for the term containing $2F_0F_1q_0^2q_0'$. The singular scaling of the four remaining dominant terms in (A1) can then be found by the results of § 5.1, yielding

$$\left.\begin{aligned} F_0^2 q_0^2 \frac{\mathrm{d}q_1}{\mathrm{d}f} &\sim F_0^2 c_a^2 (f - af^*)^{1/2}\frac{\mathrm{d}q_1}{\mathrm{d}f}, \quad 2F_0^2 q_0 q_0' q_1 \sim \frac{F_0^2 c_a^2}{2}(f - af^*)^{-1/2} q_1, \\ \frac{a\mathrm{i}\cos\theta_0}{q_0} q_1 &\sim \frac{F_0^2 c_a^2}{4}(f - af^*)^{-1/2} q_1, \quad -q_0(q_0\theta_0')' \sim \frac{3a\mathrm{i}c_a^2}{16}(f - af^*)^{-3/2}. \end{aligned}\right\} \tag{A3}$$

In substituting the ansatz $q_1 \sim A(f - af^*)^n$ into (A1), we then find

$$q_1 \sim \frac{3a\mathrm{i}}{4F_0^2}(f - af^*)^{-1}. \tag{A4}$$

A.1. *Inner limit of* $Q_a(f)$

To determine the value of the constant Λ_a, the analysis of which is performed in Appendix B, we require the inner limit of the prefactor, $Q_a(f)$, of the naive solution. Taking $Q_a(f)$ from (6.7), we consider the singular behaviour of q_0 and $\mathrm{e}^{ai\theta_0}$ from (5.5) and (5.6) to find

$$Q_a(f) \sim \frac{-\Lambda_a a \mathrm{i} F_0^2 c_a^5}{2}(f - af^*)^{1/4} \times \exp\left(\int_0^f ai\left[\frac{\cos\theta_0}{F_0^2 q_0^3} - F_0^2 q_1 - 2F_0F_1q_0\right]\mathrm{d}f\right) \quad \text{as } f \to af^*. \tag{A5}$$

It remains to evaluate the integral in the above equation as $f \to af^*$. In considering the singular behaviour of the integrand, we find

$$ai\left[\frac{\cos\theta_0}{F_0^2 q_0^3} - F_0^2 q_1 - 2F_0F_1q_0\right] \sim (f - af^*)^{-1} + O(1). \tag{A6}$$

In writing

$$\mathcal{P}(f) = \int_0^f ai\left[\frac{\cos\theta_0}{F_0^2 q_0^3} - F_0^2 q_1 - 2F_0F_1q_0\right] - (f - af^*)^{-1}\,\mathrm{d}f, \tag{A7}$$

and noting that $q_1 \sim 3a\mathrm{i}/4F_0^2(f - af^*)^{-1} + O(1)$, we see that $\mathcal{P}(f) \sim O(1)$ as $f \to af^*$. This formulation yields

$$\int_0^f ai\left[\frac{\cos\theta_0}{F_0^2 q_0^3} - F_0^2 q_1 - 2F_0F_1q_0\right]\mathrm{d}f = \mathcal{P}(f) + \log(f - af^*) - \log(-af^*), \tag{A8}$$

from which we find the singular behaviour of $Q_a(f)$ to be

$$Q_a(f) \sim \frac{\Lambda_a \mathrm{i} F_0^2 c_a^5}{2f^*}\mathrm{e}^{\mathcal{P}(af^*)}(f - af^*)^{5/4} \quad \text{as } f \to af^*. \tag{A9}$$

Appendix B. An inner solution at the principal singularities

The constant Λ_a appearing in the prefactor of q_n in (6.9) is determined by matching the inner limit of q_n with the outer limit of a solution holding near the singularity at $f = af^*$. In the inner region near this point, Bernoulli's equation (2.9*a*) holds,

$$F^2 q^2 \frac{\mathrm{d}q}{\mathrm{d}f} + \frac{1}{2\mathrm{i}}(\mathrm{e}^{\mathrm{i}\theta} - \mathrm{e}^{-\mathrm{i}\theta}) - Bq\frac{\mathrm{d}}{\mathrm{d}f}\left(q\frac{\mathrm{d}\theta}{\mathrm{d}f}\right) = 0. \tag{B1}$$

We also have the boundary-integral equation (2.9*b*) applying in this inner region. As the complex-valued Hilbert transform $\hat{\mathscr{H}}[\theta]$ appearing in the right-hand side of this operates on values of θ from the free surface in the outer region, away from the singularity, we can use the outer expansion in powers of B. At each order in B, $\hat{\mathscr{H}}[\theta_n]$ is then related to the outer solutions of q_n and θ_n by evaluating the boundary-integral equation at this order.

This gives

$$\begin{aligned}\log(q) + a\mathrm{i}\theta &= \hat{\mathscr{H}}[\theta] \\ &= \hat{\mathscr{H}}[\theta_0] + B\hat{\mathscr{H}}[\theta_1] + O(B^2) \\ &= (\log q_0 + a\mathrm{i}\theta_0) + B(q_1/q_0 + a\mathrm{i}\theta_1) + O(B^2).\end{aligned} \tag{B2}$$

To evaluate this in the inner region, we take the inner limit of $f \to af^*$ on the right-hand side. Exponentiating (B2) and using the scaling of q_0 and $\mathrm{e}^{a\mathrm{i}\theta_0}$ from (5.5) and (5.6) gives

$$q\mathrm{e}^{a\mathrm{i}\theta} \sim -\frac{a\mathrm{i}F_0^2c^4}{2} + O(B). \tag{B3}$$

From this, we find at leading order both $\mathrm{e}^{\mathrm{i}\theta} - \mathrm{e}^{-\mathrm{i}\theta} = 2q/(\mathrm{i}F_0^2c^4) - (\mathrm{i}F_0^2c^4)/2q$ and $q\theta' = a\mathrm{i}q'$. Substituting these into Bernoulli's equation (B1) then gives the inner equation

$$F^2q^2\frac{\mathrm{d}q}{\mathrm{d}f} - \frac{q}{F_0^2c^4} - \frac{F_0^2c^4}{4q} - a\mathrm{i}Bq\frac{\mathrm{d}^2q}{\mathrm{d}f^2} = 0. \tag{B4}$$

B.1. *Boundary layer scalings*

The width of the boundary layer at the principal upper- and lower-half plane singularities is determined by the reordering of the outer expansion $q_{outer} = q_0 + Bq_1 + O(B^2)$ when consecutive terms become comparable. Balancing $q_0 \sim Bq_1$ for simplicity, where $q_0 \sim c_a(f - af^*)^{1/4}$ from (5.5) and $q_1 \sim 3a\mathrm{i}/4F_0^2(f - af^*)^{-1}$ from (A4), we find the width of the boundary layer to be $B^{4/5}$. Thus, we introduce the inner variable η by

$$(f - af^*) = B^{4/5}\eta. \tag{B5}$$

In addition, in the inner region $\bar{q}_{inner} \sim q_0$. By incorporating the inner variable η with our scaling for q_0, we have $q_0 \sim c_a(f - af^*)^{1/4} \sim c_aB^{1/5}\eta^{1/4}$. This tells us how to rescale q_{outer} to produce an $O(1)$ quantity, $\bar{q}_{inner}$, in the inner region, given by

$$q_{outer} = c_aB^{1/5}\eta^{1/4}\bar{q}_{inner}. \tag{B6}$$

To find the outer limit of $\bar{q}_{inner}$, we consider a series expansion as $\eta \to \infty$. The form of this series is determined by substituting the inner limit of the expansion for q_{outer} into (B6), giving

$$\begin{aligned} q_{outer} = \sum_{n=0}^{\infty} B^n q_n &\sim \sum_{n=0}^{\infty} \frac{B^n Q_a \Gamma(n+\gamma)}{\chi_a^{n+\gamma}} \\ &\sim \sum_{n=0}^{\infty} \frac{\mathrm{i}\Lambda_a B^n F_0^2 c_a^5\,\mathrm{e}^{\mathcal{P}(af^*)}(f-af^*)^{5/4}\Gamma(n+\gamma)}{2f^*\left[\dfrac{4a\mathrm{i}F_0^2c_a}{5}(f-af^*)^{5/4}\right]^{n+\gamma}} \\ &\sim \sum_{n=0}^{\infty} \frac{\mathrm{i}\Lambda_a B^{1/5}F_0^2c_a^5\,\mathrm{e}^{\mathcal{P}(af^*)}\Gamma(n+\gamma)\eta^{1/4}}{2f^*\left(\dfrac{4a\mathrm{i}F_0^2c_a}{5}\eta^{5/4}\right)^n\left(\dfrac{4a\mathrm{i}F_0^2c_a}{5}\right)^{4/5}}.\end{aligned} \tag{B7}$$

Here, we have used $\chi_a \sim 4a\mathrm{i}F_0^2c_a/5(f - af^*)^{5/4}$, $\gamma = 4/5$, the singular behaviour of Q_a from (A9) and the inner variable η introduced in (B5). In denoting the constant prefactor of χ_a to be $X = 4a\mathrm{i}F_0^2c_a/5$, we find by (B6) the expected series form for $\bar{q}_{inner}$,

$$\bar{q}_{inner} \sim \sum_{n=0}^{\infty} \frac{\mathrm{i}\Lambda_a F_0^2 c_a^4\, \mathrm{e}^{\mathcal{P}(af^*)}\Gamma(n+\gamma)}{2f^*(X\eta^{5/4})^n X^{4/5}}. \tag{B8}$$

This suggests that in taking

$$z = X\eta^{5/4}, \tag{B9}$$

the anticipated series for $\bar{q}_{inner}$ will be of the form

$$\bar{q}_{inner} = \sum_{n=0}^{\infty} \frac{\hat{q}_n}{z^n}. \tag{B10}$$

B.2. *Inner expansion*

Substituting both the inner variable η from (B5), and $\bar{q}_{inner}$ from (B6) into the governing equation for the inner region (B4) gives

$$c_aF_0^2\bar{q}^3\left(\eta\frac{\mathrm{d}\bar{q}}{\mathrm{d}\eta} + \frac{\bar{q}}{4}\right) - \frac{a\mathrm{i}\bar{q}^2}{\eta^{5/4}}\left(\eta^2\frac{\mathrm{d}^2\bar{q}}{\mathrm{d}\eta^2} + \frac{\eta}{2}\frac{\mathrm{d}\bar{q}}{\mathrm{d}\eta} - \frac{3\bar{q}}{16}\right) = \frac{c_aF_0^2}{4}. \tag{B11}$$

Using the substitution $z = 4a\mathrm{i}F_0^2c_a\eta^{5/4}/5$ presented in (B9) results in a more convenient expansion in integer powers of $1/z$. With this, (B11) becomes

$$\bar{q}^3\left(5z\frac{\mathrm{d}\bar{q}}{\mathrm{d}z} + \bar{q}\right) + \frac{\bar{q}^2}{z}\left(5z^2\frac{\mathrm{d}^2\bar{q}}{\mathrm{d}z^2} + 3z\frac{\mathrm{d}\bar{q}}{\mathrm{d}z} - \frac{3\bar{q}}{5}\right) = 1. \tag{B12}$$

The outer limit of the inner solution to this equation as $z \to \infty$ is considered by the series (B10). Substituting this into the inner equation (B12) yields at leading order

$$\hat{q}_0^4 = 1. \tag{B13}$$

By considering the $O(z^{-n})$ term in (B12), the following recurrence relation is found for $\hat{q}_n$,

$$\begin{aligned}
&(5n-4)\hat{q}_0^3\hat{q}_n \\
&\quad = \sum_{k=1}^{n-1}\hat{q}_{n-k}\left[\hat{q}_0^2\hat{q}_k + \sum_{p=1}^{k}\hat{q}_{k-p}\left(\frac{(5p-6)(5p-2)}{5}\hat{q}_{p-1} + \sum_{j=0}^{p}(1-5j)\hat{q}_j\hat{q}_{p-j}\right)\right] \\
&\qquad + \hat{q}_0\sum_{p=1}^{n-1}\hat{q}_{n-p}\left(\frac{(5p-6)(5p-2)}{5}\hat{q}_{p-1} + \sum_{j=0}^{p}(1-5j)\hat{q}_j\hat{q}_{p-j}\right) \\
&\qquad + \frac{(5n-6)(5n-2)}{5}\hat{q}_0^2\hat{q}_{n-1} + \hat{q}_0^2\sum_{j=1}^{n-1}(1-5j)\hat{q}_j\hat{q}_{n-j}.
\end{aligned} \tag{B14}$$

B.3. *Determining the constant $\varLambda_a$*

In comparing the nth term of $\bar{q}_{inner}$ between representations (B8) and (B10), we find the following expression for the constant $\varLambda_a$:

$$\varLambda_a = \frac{-2\mathrm{i}f^*}{F_0^2 c_a^4}\mathrm{e}^{-\mathcal{P}(af^*)}\left(\frac{4a\mathrm{i}F_0^2 c_a}{5}\right)^{4/5}\lim_{n\to\infty}\frac{\hat{q}_n}{\varGamma(n+\gamma)}. \tag{B15}$$

By applying Schwartz reflection principle to q_0, which is real valued on the free surface, $\mathrm{Im}[f] = 0$, we see that $c_{a=1}$ and $c_{a=-1}$ are the complex conjugates of one another.

The recurrence relation (B14) may then be solved numerically and yields $\lim_{n\to\infty}\hat{q}_n/\varGamma(n+\gamma) \approx 1.4\times 10^{-3}$. Once the secondary components of (B15) are computed, this gives a numerical value for $\varLambda_a$.

References

Berry, M.V. 1989 Uniform asymptotic smoothing of Stokes's discontinuities. *Proc. R. Soc. Lond.* A **422** (1862), 7–21.

Boyd, J.P. 1998 *Weakly Nonlocal Solitary Waves and Beyond-All-Orders Asymptotics*. Kluwer Academic.

Chandler, G.A. & Graham, I.G. 1993 The computation of water waves modelled by Nekrasov's equation. *SIAM J. Numer. Anal.* **30** (4), 1041–1065.

Chapman, S.J. 1999 On the role of Stokes lines in the selection of Saffman–Taylor fingers with small surface tension. *Eur. J. Appl. Maths* **10** (6), 513–534.

Chapman, S.J., King, J.R. & Adams, K.L. 1998 Exponential asymptotics and Stokes lines in nonlinear ordinary differential equations. *Proc. R. Soc. Lond.* A **454**, 2733–2755.

Chapman, S.J. & Mortimer, D.B. 2005 Exponential asymptotics and Stokes lines in a partial differential equation. *Proc. R. Soc. Lond.* A **461** (2060), 2385–2421.

Chapman, S.J. & Vanden-Broeck, J.-M. 2006 Exponential asymptotics and gravity waves. *J. Fluid Mech.* **567**, 299–326.

Crapper, G.D. 1957 An exact solution for progressive capillary waves of arbitrary amplitude. *J. Fluid Mech.* **2** (6), 532–540.

Crew, S.C. & Trinh, P.H. 2016 New singularities for Stokes waves. *J. Fluid Mech.* **798**, 256–283.

Deike, L., Popinet, S. & Melville, W.K. 2015 Capillary effects on wave breaking. *J. Fluid Mech.* **769**, 541–569.

Dingle, R.B. 1973 *Asymptotic Expansions: Their Derivation and Interpretation*. Academic.

Fedorov, A.V. & Melville, W.K. 1998 Nonlinear gravity–capillary waves with forcing and dissipation. *J. Fluid Mech.* **354**, 1–42.

Gao, T., Wang, Z. & Vanden-Broeck, J.-M. 2017 Investigation of symmetry breaking in periodic gravity–capillary waves. *J. Fluid Mech.* **811**, 622–641.

Grant, M.A. 1973 The singularity at the crest of a finite amplitude progressive Stokes wave. *J. Fluid Mech.* **59** (2), 257–262.

Hung, L.-P. & Tsai, W.-T. 2009 The formation of parasitic capillary ripples on gravity–capillary waves and the underlying vortical structures. *J. Phys. Oceanogr.* **39** (2), 263–289.

Longuet-Higgins, M.S. 1963 The generation of capillary waves by steep gravity waves. *J. Fluid Mech.* **16**, 138–159.

Longuet-Higgins, M.S. 1995 Parasitic capillary waves: a direct calculation. *J. Fluid Mech.* **301**, 79–107.

Longuet-Higgins, M.S. & Fox, M.J.H. 1977 Theory of the almost-highest wave: the inner solution. *J. Fluid Mech.* **80** (04), 721–741.

Longuet-Higgins, M.S. & Fox, M.J.H. 1978 Theory of the almost-highest wave. Part 2. Matching and analytic extension. *J. Fluid Mech.* **85** (04), 769–786.

Lustri, C.J., Pethiyagoda, R. & Chapman, S.J. 2019 Three-dimensional capillary waves due to a submerged source with small surface tension. *J. Fluid Mech.* **863**, 670–701.

Lustri, C.J. 2013 Exponential asymptotics in unsteady and three-dimensional flows. PhD thesis, Oxford University.

Mailybaev, A.A. & Nachbin, A. 2019 Explosive ripple instability due to incipient wave breaking. *J. Fluid Mech.* **863**, 876–892.

Murashige, S. & Choi, W. 2017 A numerical study on parasitic capillary waves using unsteady conformal mapping. *J. Comput. Phys.* **328**, 234–257.

Olde Daalhuis, A.B., Chapman, S.J., King, J.R., Ockendon, J.R. & Tew, R.H. 1995 Stokes phenomenon and matched asymptotic expansions. *SIAM J. Appl. Maths* **55** (6), 1469–1483.

Perlin, M., Lin, H. & Ting, C.-L. 1993 On parasitic capillary waves generated by steep gravity waves: an experimental investigation with spatial and temporal measurements. *J. Fluid Mech.* **255**, 597–620.

Perlin, M. & Schultz, W.W. 2000 Capillary effects on surface waves. *Annu. Rev. Fluid Mech.* **32** (1), 241–274.

Shelton, J., Milewski, P. & Trinh, P.H. 2021 On the structure of steady parasitic gravity–capillary waves in the small surface tension limit. *J. Fluid Mech.* **922**, A16.

Tanveer, S. & Xie, X. 2003 Analyticity and nonexistence of classical steady Hele-Shaw fingers. *Commun. Pure Appl. Maths* **56** (3), 353–402.

Trinh, P.H. 2017 On reduced models for gravity waves generated by moving bodies. *J. Fluid Mech.* **813**, 824–859.

Trinh, P.H., Chapman, S.J. & Vanden-Broeck, J.-M. 2011 Do waveless ships exist? Results for single-cornered hulls. *J. Fluid Mech.* **685**, 413–439.

Vanden-Broeck, J.-M. 1986 Steep gravity waves: Havelock's method revisited. *Phys. Fluids* **29** (9), 3084–3085.

Vanden-Broeck, J.-M. 2010 *Gravity-Capillary Free-Surface Flows*. Cambridge University Press.

Wilkening, J. & Zhao, X. 2021 Quasi-periodic travelling gravity–capillary waves. *J. Fluid Mech.* **915**, A7.

Wilton, J.R. 1915 On ripples. *Phil. Mag.* **29** (173), 688–700.

Yang, T.-S. & Akylas, T.R. 1996 Weakly nonlocal gravity–capillary solitary waves. *Phys. Fluids* **8** (6), 1506–1514.

Yang, T.-S. & Akylas, T.R. 1997 On asymmetric gravity–capillary solitary waves. *J. Fluid Mech.* **330**, 215–232.

Zufiria, J.A. 1987*a* Non-symmetric gravity waves on water of infinite depth. *J. Fluid Mech.* **181**, 17–39.

Zufiria, J.A. 1987*b* Symmetry breaking in periodic and solitary gravity–capillary waves on water of finite depth. *J. Fluid Mech.* **184**, 183–206.

5 THE NUMERICAL BIFURCATION STRUCTURE OF STANDING WAVES

5.1 Introduction

In this chapter, gravity-capillary standing waves are considered numerically. These are time-dependent water waves that oscillate in time. Most previous numerical studies have focused upon gravity standing waves, for which the surface tension is neglected by setting $B = 0$. Exceptions to this for instance are the numerical studies by Vanden-Broeck (1984) and Schultz et al. (1998), the latter of which computed a few highly nonlinear solutions for small values of the surface tension.

Since Bernoulli's equation (5.1c) with $B = 0$ is a first-order PDE, and that with small B is of second order, the limit of $B \to 0$ results in a singular perturbative problem. We anticipate based on the introduction of chapter 2 and the asymptotics of chapter 4 that as $B \to 0$, the solutions will contain exponentially small effects.

In the following section, we formulate this problem mathematically as a temporally periodic water wave that returns to the initial $\hat{t} = 0$ profile at $\hat{t} = T$. Numerical solutions are then calculated in section 5.4 by Newton iteration, for which the periodicity of the solution allows for the computation of derivatives and Hilbert transforms spectrally. We show that branches of solutions emerge for fixed energy; these are then classified in a similar way to that seen in the steadily travelling numerical results of chapter 3.

5.2 Mathematical formulation

We consider the time-dependent free-surface flow of a two-dimensional, inviscid, irrotational, and incompressible fluid of infinite depth. Temporally periodic solutions are sought, such that the free-surface, $\hat{\zeta}(\hat{x}, \hat{t})$, and velocity potential, $\hat{\phi}(\hat{x}, \hat{y}, \hat{t})$ return a to phase shift of their original profiles from $\hat{t} = 0$ at $\hat{t} = T$. We non-dimensionalise length scales by the assumed wavelength λ, time by the physical time interval T, and the velocity potential $\hat{\phi}$ by λ^2/T. The nondimensional governing equations are taken to be

$$
\begin{aligned}
\phi_{xx} + \phi_{yy} &= 0 \qquad \text{for} \quad y \leq \zeta, && (5.1a)\\
\zeta_t &= \phi_y - \zeta_x \phi_x \qquad \text{at} \quad y = \zeta, && (5.1b)\\
F^2 \phi_t + \frac{F^2}{2}(\phi_x^2 + \phi_y^2) + y - B\frac{\zeta_{xx}}{(1+\zeta_x^2)^{\frac{3}{2}}} &= 0 \qquad \text{at} \quad y = \zeta, && (5.1c)\\
\phi_x \to 0 \quad \text{and} \quad \phi_y &\to 0 \qquad \text{as} \quad y \to -\infty, && (5.1d)
\end{aligned}
$$

where the non-dimensional constants,

$$
F = \frac{\sqrt{\lambda}}{T\sqrt{g}} \qquad \text{and} \qquad B = \frac{\sigma}{\rho g \lambda^2}, \tag{5.2}
$$

are the Froude and (inverse)-Bond numbers, respectively. The Froude number characterises the balance between inertia and gravity, and the Bond number characterises the balance between gravity and surface tension. Here, g is the gravitational constant, ρ is the fluid density, σ is the constant coefficient of surface tension, and T and λ are constants introduced from our choice of non-dimensionalisation. Note that if we have a wave-speed $c = \lambda/T$ associated with purely travelling waves as in chapter 3, then our expression for the Froude number, F, in (5.2) becomes $F = c/\sqrt{g\lambda}$.

To consider solutions $\zeta(x, y, t)$ and $\phi(x, y, t)$ which are spatially periodic for $x \in [-1/2, 1/2)$ and temporally periodic with a horizontal phase shift of θ for $t \in [0, 1)$, we enforce the following two conditions:

$$
\nabla\phi\left(x - \frac{1}{2}, y, t\right) = \nabla\phi\left(x + \frac{1}{2}, y, t\right) \quad \text{and} \quad \zeta\left(x - \frac{1}{2}, t\right) = \zeta\left(x + \frac{1}{2}, t\right), \tag{5.3a}
$$

for periodicity in the horizontal coordinate x, and

$$
\nabla\phi(x, y, 0) = \nabla\phi(x + \theta, y, T) \qquad \text{and} \qquad \zeta(x, 0) = \zeta(x + \theta, T), \tag{5.3b}
$$

to ensure periodicity in time.

This results in a system with the three unknown constants F, B, and θ, two of which will be determined as eigenvalues of the problem through the imposition of two additional constraints specified later in equations (5.16d) and (5.16e). These will be the total energy, E, to measure the nonlinearity of the solution, and a parameter β

that distinguishes between travelling and standing components of the solution. Note that this current formulation permits temporally periodic solutions with both travelling and standing components. In the numerical results of section 5.4, focus will be placed upon standing waves by specifying the value of the travelling/standing parameter β, for which $\theta = 0$.

5.2.1 The time dependent conformal mapping

The difficulty in computing solutions numerically to equations (5.1) is that Bernoulli's equation (5.1c) holds along the unknown free-surface, $y = \zeta(x,t)$, which is also a function of time. We employ the time-dependent conformal mapping from Dyachenko et al. (1996) and Choi and Camassa (1999a), which maps the physical fluid domain $-\infty < y \leq \zeta(x,t)$ to the lower-half (ξ,η)-plane. Under this mapping, the free-surface streamline $y = \zeta(x,t)$ maps to the line $\eta = 0$. The following formulation follows closely to that presented by Milewski et al. (2010), and a full derivation occurs in Appendix A.

We now formulate the governing equations for the free surface under this conformal mapping. The free-surface variables, Y and Φ, are defined by evaluating $y = \zeta(x,t)$ and $\phi(x,y,t)$ on $\eta = 0$, yielding

$$Y(\xi,t) = \zeta(x(\xi,0,t),t) \qquad \text{and} \qquad \Phi(\xi,t) = \phi(x(\xi,0,t),y(\xi,0,t),t). \tag{5.4}$$

Differentiation of (5.4) with respect to ξ and t yields equations that may be solved to obtain expressions for ζ_t, ϕ_x, ϕ_y, ζ_x, and ζ_{xx} in terms of these free-surface variables evaluated on $\eta = 0$. Substitution of these resultant equations into the kinematic and dynamic boundary conditions (5.1b) and (5.1c) yields the time evolution equations

$$Y_t = Y_\xi \mathcal{H}\left[\frac{\Psi_\xi}{J}\right] - X_\xi\left(\frac{\Psi_\xi}{J}\right), \tag{5.5a}$$

$$\Phi_t = \frac{1}{2}\left(\frac{\Psi_\xi^2 - \Phi_\xi^2}{J}\right) + \Phi_\xi \mathcal{H}\left[\frac{\Psi_\xi}{J}\right] - \frac{Y}{F^2} + \frac{B}{F^2}\frac{(X_\xi Y_{\xi\xi} - Y_\xi X_{\xi\xi})}{J^{3/2}}, \tag{5.5b}$$

where $J = X_\xi^2 + Y_\xi^2$. In addition to the unknown functions Y and Φ, equations (5.5a) and (5.5b) also involve $X(\xi,t)$ and $\Psi(\xi,t)$, which are the harmonic conjugates of y and ϕ, x and ψ, evaluated on the free-surface $\eta = 0$. These can be calculated by the harmonic relations of

$$X_\xi = 1 - \mathcal{H}[Y_\xi] \qquad \text{and} \qquad \Psi_\xi = \mathcal{H}[\Phi_\xi], \tag{5.5c}$$

where $\mathcal{H}$ denotes the Hilbert transform, defined by the integral

$$\mathcal{H}[Y](\xi) = \int_{-\infty}^{\infty} \frac{Y(\phi)}{\phi - \xi}\,\mathrm{d}\phi = \int_{-1/2}^{1/2} Y(\phi)\cot[\pi(\phi - \xi)]\,\mathrm{d}\phi, \tag{5.6}$$

where the second equality follows from periodicity of $Y(\phi)$. System (5.5) consists of the two coupled time-evolution integro-differential equations for $Y(\xi,t)$ and $\Phi(\xi,t)$. Furthermore, we also enforce the spatial periodicity conditions,

$$\Phi\big(\xi - 1/2, t\big) = \Phi(\xi + 1/2, t) \quad \text{and} \quad Y(\xi - 1/2, t) = Y(\xi + 1/2, t)\,, \tag{5.7}$$

and temporal periodicity conditions,

$$\Phi(\xi,0)=\Phi(\xi+\theta,1) \qquad \text{and} \qquad Y(x,0)=Y(x+\theta,1)\,, \tag{5.8}$$

which follow from evaluating the physical conditions (5.3a) and (5.3b) for $\zeta(x,t)$ and $\phi(x,y,t)$ on $\eta=0$ and substituting for Y and Φ defined in (5.4).

5.2.2 *Linear theory*

We consider the first two terms of a Stokes expansion by writing $Y = Y_0+\epsilon Y_1$, $X=X_0+\epsilon X_1$, $\Phi=\Phi_0+\epsilon\Phi_1$, and $\Psi=\Psi_0+\epsilon\Psi_1$. At $O(\epsilon^0)$ in equations (5.5a) to (5.5c), we find the solutions $Y_1=0$, $X_0=\xi$, $\Phi_0=0$, and $\Psi_0=0$. Next at $O(\epsilon)$ we have the equations

$$Y_{1t}=-\mathcal{H}[\Phi_{1\xi}] \qquad \text{and} \qquad F^2\Phi_{1t}=-Y_1+BY_{1\xi\xi}. \tag{5.9}$$

In writing the solutions as a Fourier series of the form

$$Y_1(\xi,t)=a_0(t)+\sum_{k=1}^{\infty}\Big[a_k(t)\cos\left(2k\pi\xi\right)+b_k(t)\sin(2k\pi\xi)\Big], \tag{5.10}$$

with a similar expansion for $\Phi_1(\xi,t)$ in terms of the Fourier coefficients $c_k(t)$ and $d_k(t)$, we find for $k\geq 1$ the two second order differential equations

$$\begin{pmatrix} a_k''(t)\\ b_k''(t)\end{pmatrix} = -\frac{2k\pi}{F^2}\Big(1+(2k\pi)^2B\Big)\begin{pmatrix} a_k(t)\\ b_k(t)\end{pmatrix}. \tag{5.11}$$

Note that we necessarily have $a_0(t)=0$ in order for the $k=0$ mode in $\Phi_1(\xi,t)$ to be temporally-periodic.

We now express the solutions to (5.11), $a_k(t)$ and $b_k(t)$, as a Fourier series in time of the form

$$a_k(t)=\hat{a}_0^{(k)}+\sum_{m=1}^{\infty}\Big[\hat{a}_m^{(k)}\cos\left(2m\pi t\right)+\bar{a}_m^{(k)}\sin(2m\pi t)\Big], \tag{5.12}$$

with a similar expansion for $b_k(t)$ in terms of the Fourier coefficients $\hat{b}_m^{(k)}$ and $\bar{b}_m^{(k)}$. Substitution of (5.12) into the differential equation (5.11) yields the dispersion relation

$$F^2-\frac{k}{2\pi m^2}\Big(1+(2k\pi)^2B\Big)=0. \tag{5.13}$$

Here, $k\geq 1$ is the spatial mode, and $m\geq 1$ is the temporal mode. Note that if $m=k$, (5.13) reduces to the steady dispersion relation for gravity-capillary waves derived in chapter 3. When (5.13) is satisfied, a non-zero mth mode in the Fourier series expansions for $a_k(t)$ and $b_k(t)$ is permitted. Furthermore, the symmetry condition (5.7) for $Y(\xi,0)$ requires that $\hat{b}_m^{(k)}=0$. Asymmetry on $\Phi(\xi,0)$, through the equation $a_k'(t)=2k\pi c_k(t)$, yields $\bar{a}_m^{(k)}=0$. This gives a linear solution of the form

$$\left.\begin{aligned} Y_1(\xi,t)&=\hat{a}_m^{(k)}\cos\left(2m\pi t\right)\cos\left(2k\pi\xi\right)+\bar{b}_m^{(k)}\sin\left(2m\pi t\right)\sin\left(2k\pi\xi\right),\\ \Phi_1(\xi,t)&=-\frac{m\hat{a}_m^{(k)}}{k}\sin\left(2m\pi t\right)\cos\left(2k\pi\xi\right)+\frac{m\bar{b}_m^{(k)}}{k}\cos\left(2m\pi t\right)\sin\left(2k\pi\xi\right).\end{aligned}\right\} \tag{5.14}$$

Multiple Fourier modes may be non-zero in the solution if the linear dispersion relation (5.13) is satisfied for two values of $k = \{k_1, k_2\}$ and $m = \{m_1, m_2\}$. This yields

$$B = \frac{1}{4\pi^2}\left(\frac{m_1^2 k_2 - m_2^2 k_1}{m_2^3 k_1^3 - m_1^2 k_2^3}\right) \quad \text{and} \quad F^2 = \frac{1}{2\pi}\left(\frac{k_1 k_2 (k_1 + k_2)(k_1 - k_2)}{m_2^3 k_1^3 - m_1^2 k_2^3}\right), \tag{5.15}$$

which reduces down to the prediction of Wilton (1915) when $m_1 = k_1$ and $m_2 = 1 = k_2$.

5.3 The numerical method

Our governing equations are the time evolution dynamic and kinematic conditions,

$$Y_t = Y_\xi \mathcal{H}\left[\frac{\Psi_\xi}{J}\right] - X_\xi\left(\frac{\Psi_\xi}{J}\right), \tag{5.16a}$$

$$\Phi_t = \frac{1}{2}\left(\frac{\Psi_\xi^2 - \Phi_\xi^2}{J}\right) + \Phi_\xi \mathcal{H}\left[\frac{\Psi_\xi}{J}\right] - \frac{Y}{F^2} + \frac{B}{F^2}\frac{(X_\xi Y_{\xi\xi} - Y_\xi X_{\xi\xi})}{J^{3/2}}, \tag{5.16b}$$

with the harmonic relations $X_\xi = 1 - \mathcal{H}[Y_\xi]$ and $\Psi_\xi = \mathcal{H}[\Phi_\xi]$ from (5.5c). The spatial and temporal periodicity conditions are

$$\left.\begin{aligned} \Phi(\xi - 1/2, t) &= \Phi(\xi + 1/2, t)\,, \qquad & Y(\xi - 1/2, t) &= Y(\xi + 1/2, t)\,, \\ \Phi(\xi, 0) &= \Phi(\xi + \theta, 1)\,, & Y(\xi, 0) &= Y(\xi + \theta, 1)\,. \end{aligned}\right\} \tag{5.16c}$$

Furthermore, as an amplitude condition, we fix the energy, E, and as a travelling/standing constraint we fix the constant β, both of which are given by

$$\mathscr{E} = \frac{1}{E_{\text{hw}}}\int_{-1/2}^{1/2}\left[\frac{F^2}{2}\Psi\Phi_\xi + B(J^{1/2} - X_\xi) + \frac{1}{2}Y^2 X_\xi\right]\mathrm{d}\xi, \tag{5.16d}$$

$$\beta = \mathrm{Arg}\Big[\mathcal{F}[Y(\xi, 0)] + \mathrm{i}\mathcal{F}[Y(\xi, 1/4)]\Big]. \tag{5.16e}$$

Here, the normalisation constant $E_{\text{hw}} = 0.00184$ is chosen to be approximately that of the highest steadily travelling Stokes wave. Initial conditions on symmetry of Y and asymmetry of Φ

$$Y(\xi, 0) = Y(-\xi, 0) \qquad \text{and} \qquad \Phi(\xi, 0) = -\Phi(-\xi, 0). \tag{5.16f}$$

A solution, $Y(\xi, t)$ and $\Phi(\xi, t)$, to the above set of equations has the associated nondimeninsional constants B, F, and θ, two of which will be determined as eigenvalues through the imposition of the energetic and standing/travelling constraints (5.16d) and (5.16e).

We employ a shooting method to solve system (5.16), in which we begin with initial data at $t = 0$. This is evolved to $t = 1$, at which point we seek to minimise the difference between the solutions at $t = 0$ and $t = 1$ with Newton iteration. A detailed overview of this method is now provided.

(i) Initial guess.

An initial guess for $Y(\xi, 0)$, $\Phi(\xi, 0)$, and the constant eigenvalues θ and one of B or F, is taken either from the linear theory of §5.2.2, a previously computed numerical solution, or for $\beta = 0.25$, a steadily travelling wave calculated from Shelton et al. (2021) for which we take $\Phi = -\mathcal{H}[Y]$. In discretising the spatial domain ξ with N grid points, such that $\xi_i = -1/2 + i/N$ for $i = 0, \dots, N-1$, we define the solutions evaluated at each of these collocation points by $Y_i(t) = Y(\xi_i, t)$ and $\Phi_i(t) = \Phi(\xi_i, t)$. At $t = 0$, $Y_i(0)$ and $\Phi_i(0)$ then contribute to $2N$ unknown quantities. Including the two unknown eigenvalues then yields a total of $2N + 2$ unknowns.

(ii) Time evolution.

We discretise the time interval $t \in (0, 1)$ into $M + 1$ points, which yields $t_l = l/M$ for $l = 0, \dots, M$. The fourth-order Runge-Kutta method is used to advance the solution from timestep t_l to t_{l+1}. With knowledge of $Y_i(t_l)$ and $\Phi_i(t_l)$, the conjugate functions $X_i(t_l)$ and $\Psi_i(t_l)$ are calculated from the harmonic relations (5.5c). We use the Fourier transform to evaluate the derivatives and Hilbert transforms that appear in equations (5.16a) and (5.16b). For instance, since the Fourier symbols for differentiation and the Hilbert transform are $2\pi\mathrm{i}k$ and $\mathrm{i} \cdot \mathrm{sgn}(k)$, we have $Y_\xi = \mathcal{F}^{-1}[2\pi\mathrm{i}k\mathcal{F}[Y]]$ and $\mathcal{H}[Y] = \mathcal{F}^{-1}[\mathrm{i} \cdot \mathrm{sgn}(k)\mathcal{F}[Y]]$, where $\mathcal{F}$ denotes the Fourier transform. The fast Fourier transform algorithm is utilised to evaluate these identities. This allows for the calculation of $X_i(t_{l+1})$ and $\Phi_i(t_{l+1})$.

We resolve aliasing errors on the solutions at each time step by setting the highest $N/2$ Fourier modes to zero.

(iii) Function to minimise.

The previous step may be repeated until $Y_i(1)$ and $\Phi_i(1)$ are known. We then employ Newton iteration on this system to minimise the following $2N + 4$ conditions:

$$\left.\begin{array}{lll} Y_i(0) - \bar{Y}_i(1), & \Phi_i(0) - \bar{\Phi}_i(1), & \text{Temporal periodicity,} \\ E^* - E, & \beta^* - \beta, & \text{Constants (5.16d, 5.16e),} \\ \mathrm{Im}[\mathcal{F}[Y(\xi, 0)]], & \mathrm{Re}[\mathcal{F}[\Phi(\xi, 0)], & \text{Symmetry at } t = 0. \end{array}\right\} \tag{5.17}$$

In the above, E^* and β^* are the desired values of the energy and the travelling/standing parameter, while E and β are the corresponding values of the current numerical solution, calculated from equations (5.16d) and (5.16e). Furthermore, since we are computing solutions that return to a phase shift, θ, of their initial profiles at $t = 1$, this phase shift is calculated in Fourier space by $\bar{Y} = \mathcal{F}^{-1}[\mathrm{e}^{\mathrm{i}k\theta}\mathcal{F}[Y(\xi, 1)]]$, where k is the wavenumber. In (5.17) above, we have then defined $\bar{Y}_i = \bar{Y}(\xi_i)$ and $\bar{\Phi}_i(1) = \bar{\Phi}(\xi_i)$.

As we had only $2N + 2$ unknowns, the resultant system is overdetermined. We note that there is a degree of freedom in the initial condition, (we could evolve from $t = 1/2$ to $t = 3/2$) for instance, and the additional symmetry conditions at $t = 0$, from (5.16f), specify this.

5.4 Numerical results for fixed energy

In the following sections, numerical solutions are found for fixed energy, E, and travelling/standing parameter, β. We begin in section 5.4.1 by overviewing the solutions found by Wilkening (2021). These solutions neglect the effects of surface tension with $B = 0$, and serve to demonstrate the gravity wave profiles that emerge for different values of β. In section 5.4.2, we proceed to consider gravity-capillary waves, where $B \neq 0$, for the value of $\beta = \pi/2$. This corresponds to standing waves.

5.4.1 *Temporally periodic gravity waves*

In this section, numerical solutions are computed for zero surface tension ($B = 0$), for different values of the travelling/standing parameter, β. In using the numerical scheme detailed in section 5.3, we initialise the shooting method with a linear solution derived in section 5.2.2. This linear solution has

$$F^2 = \frac{1}{2\pi}, \tag{5.18}$$

and an initial profile with one period in both time and space ($m = 1, k = 1$) given by

$$Y(\xi, 0) = \epsilon \hat{a}_1^{(1)} \cos(2\pi\xi) \qquad \text{and} \qquad \Phi(\xi, 0) = \epsilon \bar{b}_1^{(1)} \sin(2\pi\xi), \tag{5.19}$$

from equation (5.14). Since $Y(\xi, 1/4) = \epsilon \bar{b}_1^1 \sin(2\pi\xi)$, specification of the parameter β yields

$$\beta = \text{Arg}\left[\hat{a}_1^{(1)} + \text{i}\bar{b}_1^{(1)}\right], \tag{5.20}$$

and provides a relationship between $\hat{a}_1^{(1)}$ and $\bar{b}_1^{(1)}$. All that remains is to choose an appropriate value for $\epsilon\hat{a}_1^{(1)}$ in (5.19), which we typically take to be 10^{-5}. The discretisation of this linear initial condition the yields the starting value for our shooting scheme.

Once a small amplitude solution is computed via Newton iteration, we search for a new solution with a larger value of the energy from (5.16d) (typically the energy is increased by a multiple of 1.05 for each run, but this factor may be as large as 1.2 when the energy is small). This process continues until we compute a solution with the desired energy, $\mathscr{E} = 0.4$. In this section, we use $N = 200$ spatial gridpoints and $M = 500$ time steps. Each solution takes approximately 5-10 minutes to compute.

In figure 5.1 we show six different solutions for the free surface, $y = \zeta$, for the values of $\beta = \{0.25\pi, 0.3\pi, 0.35\pi, 0.4\pi, 0.45\pi, 0.5\pi\}$, and energy $\mathcal{E} = 0.4$. The free surfaces are shown at different values of time, and for clarity only the dynamics between $t = 0$ and $t = 0.5$ are pictured. In (a) we have for $\beta = 0.25\pi$ a purely travelling gravity wave, which is steady in the co-moving frame. Solution (f) is a standing gravity wave, with $\beta = 0.5\pi$. This standing wave begins at $t = 0$ as a flat wave, and reaches its maximum value at $t = 0.25$. the values of the free surface between $t = 0.25$ and $t = 0.5$ are then the same as that found between $t = 0$ and $t = 0.25$. Profiles (b)-(e) have $0.25\pi < \beta < 0.5\pi$, and are seen to contain both travelling and standing components.

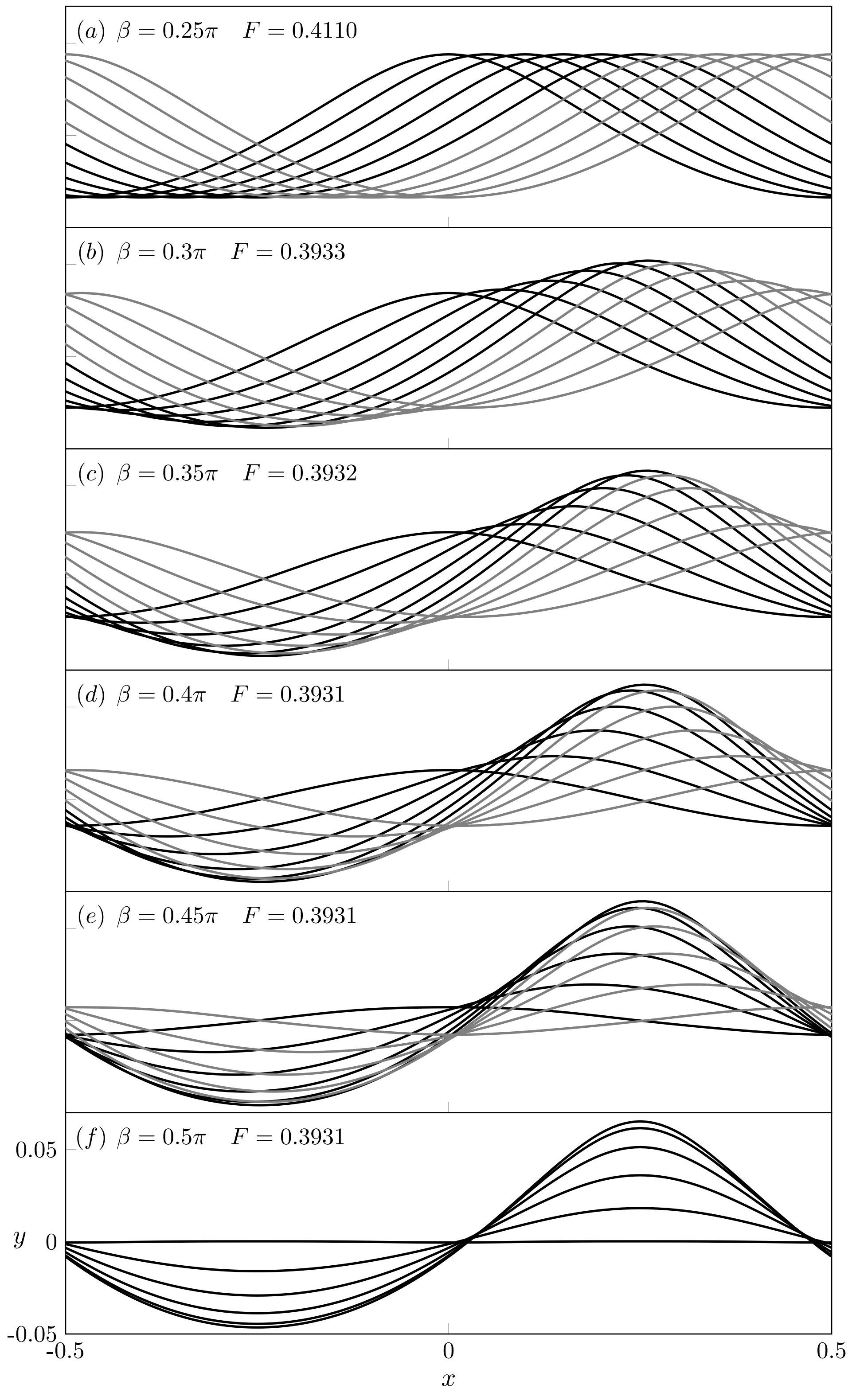

Figure 5.1: Temporally periodic solutions, computed by the numerical scheme of section 5.3 are shown for six different values of the travelling / standing parameter, β. Solution (a) is a travelling gravity wave with $\beta = 0.25\pi$, and solution (f) is a gravity standing wave with $\beta = 0.5\pi$. All six solutions have $B = 0$, $\mathscr{E} = 0.04$, and are computed with $N = 200$ spatial grid points and $M = 500$ time steps. The solution profile is shown by black lines at time intervals $t = \{0, 0.05, 0.1, 0.15, 0.2, 0.25\}$ and gray lines at $t = \{0.3, 0.35, 0.4, 0.45, 0.5\}$. Note that only the first half of the temporally periodic dynamics for $0 \leq t \leq 0.5$ has been shown.

5.4.2 *Structure of gravity-capillary standing waves*

We now consider standing gravity capillary waves, for which we fix $\beta = 0.5\pi$. We saw in section 5.4 that when $B = 0$, the standing gravity wave for fixed energy begins with a flat wave profile at $t = 0$, reaches a maximum at $t = 0.25$, and returns to a flat profile at $t = 0.5$. The dynamics for $0.5 < t < 1$ are then similar to this initial period, with the difference that at $t = 0.75$, the location in x that contained a trough at $t = 0.25$ is now a crest. Analogous to the bifurcation structure that emerged in chapter 3 for steady waves, we expect to find solutions, for small values of B, that are a perturbation of the $B = 0$ solution.

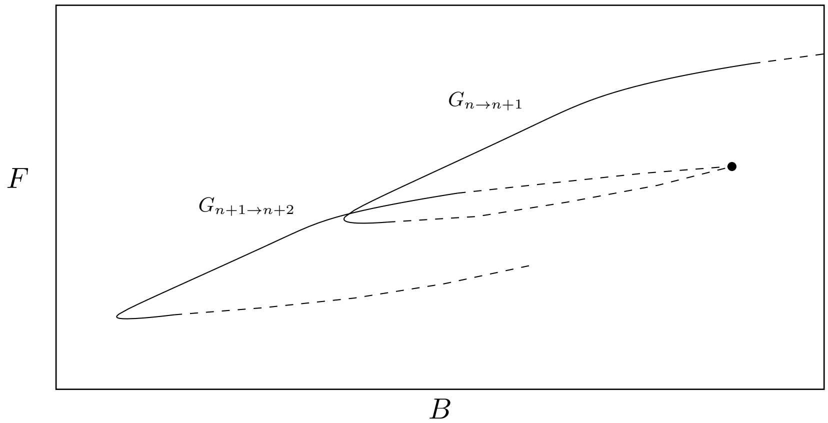

Figure 5.2: Two anticipated (B, F) solution branches are sketched. The solutions along these contain high-frequency parasitic ripples, which we use to characterise the solution branches. Since these transition from solutions with n ripples to $n+1$ ripples and the Bond number decreases, these branches are denoted by $G_{n\to n+1}$. Solid lines denote the portion of the branches we have been able to compute. Dashed lines represent the anticipated connection between these branches, which we have been unable to compute. The black dot represents the anticipated bifurcation point, which based on the steady results of chapter 3 is likely to be a standing wave with $n+1$ spatial periods and $n+1$ temporal oscillations.

Most of the numerical solutions displayed in this section use $N = 200$ spatial gridpoints and $M = 1000$ time steps, taking approximately 10 minutes to compute. This however was insufficient in order to calculate the entire solution branch. To explore further along these branches, we used $N = 300$ spatial gridpoints and $M = 2000$ time steps, which required approximately 60 to 120 minutes for Newton iteration to converge to a solution. Two anticipated solution branches, denoted by $G_{n\to n+1}$ are shown in figure 5.2. Black lines indicate the portion of the branches we have been able to compute, and the dashed lines show the anticipated location of solutions we have been unable to compute. A preliminary (B, F) bifurcation diagram is shown in figure 5.3 for $\mathscr{E} = 0.4$. We see that solution branches emerge, and these appear to become self-similar as the surface tension decreases. Each of these branches is associated with a certain number of crests in the high-frequency parasitic ripple, and the number of these crests increases as $B \to 0$. We note that these high-frequency ripples also oscillate in time faster than the underlying wave, which is predominantly attributed to the effects of gravity. While this underlying wave contains one vertical oscillation between $t = 0$ and $t = 1$, the high-frequency ripples, with k spatial periods, contain k vertical oscillations between $t = 0$ and $t = \pi$, and thus have a fundamental time period of $1/k$. This behaviour is shown in figure 5.4, in which three solutions from branch $G_{12\to 13}$ are shown. Interestingly, the fingers of solutions, across which

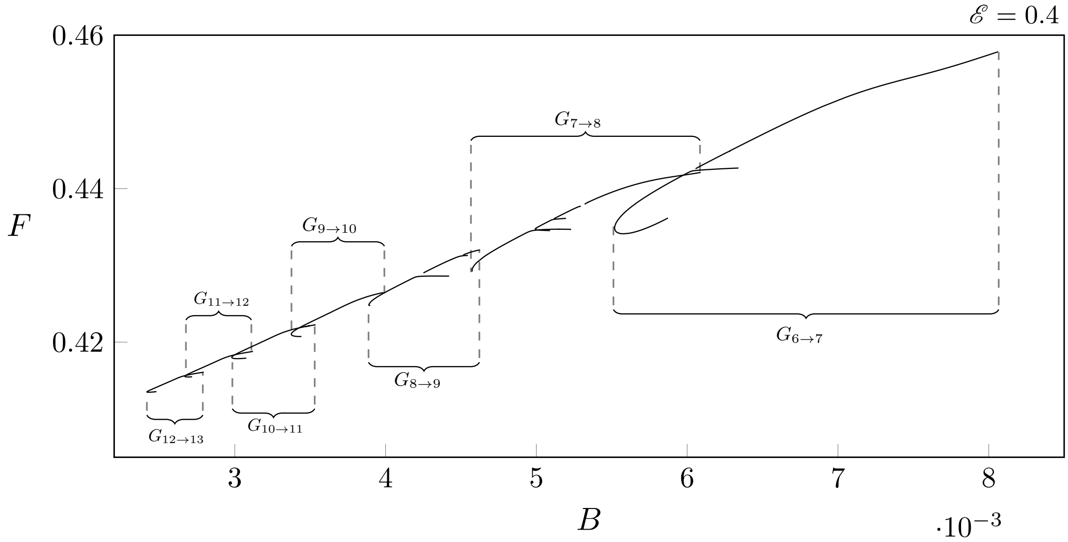

Figure 5.3: A portion of the Bond-Froude bifurcation space is shown for $\mathscr{E} = 0.4$. Multiple solution branches are shown. The solutions on these are gravity-capillary standing waves, and the branches may be characterised by the number of high-frequency parasitic ripples present in the solution. The branches are denoted $G_{n\to n+1}$ since as the Bond number decreases along each of these, the solution profile transitions from containing n ripples to $n+1$ ripples. Three solutions from branch $G_{12\to13}$ are shown in figure 5.4.

the number of ripples transitions from n to $n+1$, appear to split when n is small. Due to the difficulty encountered in exploring these branches further, we have not been able to explain why this occurs. Note also that the Froude number of the gravity standing wave, with $B = 0$ and $\mathscr{E} = 0.4$, is $F = 0.3931$. The top regions of the solution branches appear to be tending to this value as $B \to 0$.

Unlike the gravity standing waves, which are flat at $t = 0$, the free surface of these gravity-capillary standing waves contains oscillations at $t = 0$. This is shown in figure 5.5, in which we display wave profiles at $t = 0$, from the middle of each of the solution branches $G_{n\to n+1}$ shown in figure 5.3. These contain both an $O(B)$ component, and a high-frequency component. The asymptotic scaling of these parasitic ripples is unclear, and requires the computation of more numerical solutions for smaller values of B.

5.5 Conclusion

We have numerically computed gravity-capillary standing waves for small values of the surface tension. Much like that seen in chapter 3 by Shelton et al. (2021) for steadily travelling waves, solutions are found that display high-frequency (in both space and time) parasitic ripples. Solution branches are seen to be characterised by the number of ripples within the periodic domain; the number of which increases as the surface tension decreases.

5.6 Discussion

The computation of the time-dependent solutions presented in this chapter requires significant computation power, and we have only begun to explore the vast bifurcation space of gravity-capillary standing waves. We may anticipate based on the steady

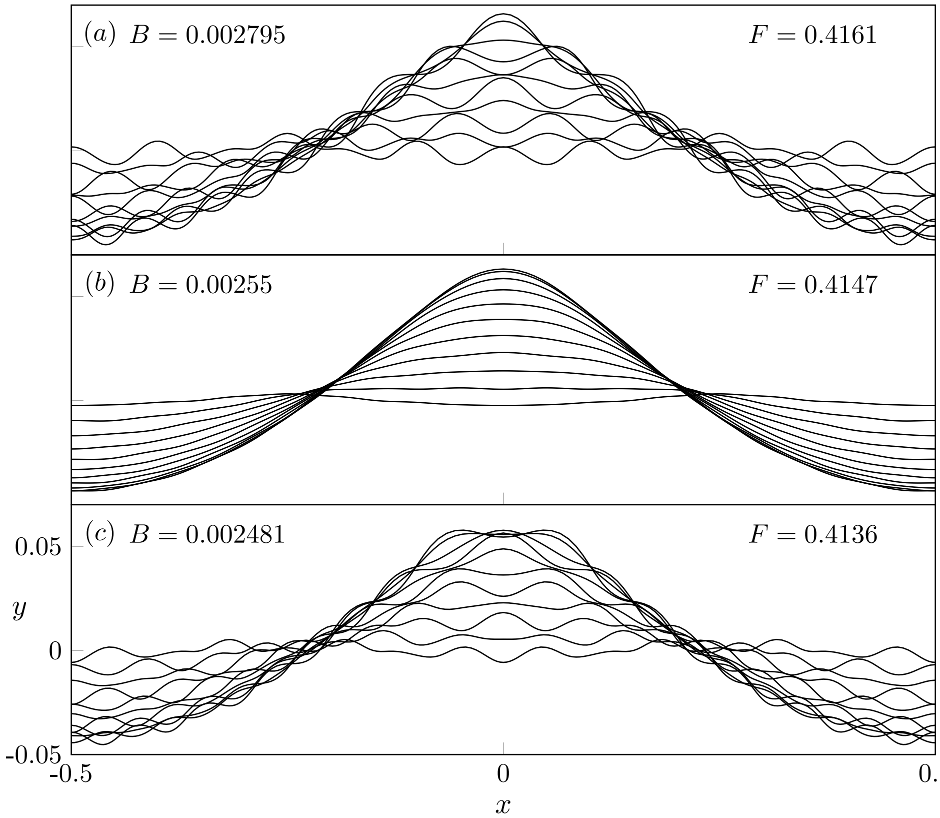

Figure 5.4: Three solutions from branch $G_{12\to13}$ are shown, with $\mathscr{E} = 0.4$. Each solution profile is shown at the eleven values of $t = \{0, 0.025, 0.05, 0.075, 0.1, 0.125, 0.15, 0.175, 0.2, 0.225, 0.25\}$. Note that we have shifted the profile horizontally such that the crest develops at $x = 0$. Profile (b) is from the middle of the solution branch, and profiles (a) and (c) are from each end of the computed solution branch.

solutions of chapter 3 that the adjacent branches displayed in figure 5.3, $G_{10\to11}$ and $G_{11\to12}$ for instance, bifurcate from the same location on a highly periodic branch of solutions. However, bifurcations different to those seen in chapter 3 are observed. For instance, the branches $G_{7\to8}$ and $G_{8\to9}$ in figure 5.3 appear to split in multiple locations. The reason for this is unclear.

If the high-frequency parasitic ripples observed in these standing wave solutions are indeed exponentially small as $B \to 0$, then their analytic treatment would require the extension of the exponential asymptotics of chapter 4 to a time-dependent PDE. One main difference is that the leading order solution would be a nonlinear standing gravity wave. The singular points in the analytically continued domain of this solution would then move in time, and thus require careful attention. Further discussion of this occurs in the summary of section 9.4.

We began by formulating this problem with a travelling/standing parameter β from (5.16e). For $\beta = \pi/4$ travelling waves were found, and $\beta = \pi/2$ yielded standing waves. It is well known that the steadily travelling Stokes wave can approach a limiting formulation in which the wave surface develops a crest singularity [cf. Stokes (1880), Toland (1978), Amick et al. (1982)]. However, whether this is also true for standing waves is unclear. It was conjectured by Penney and Price (1952) that this limiting standing wave would occur, but following an extensive numerical investigation by Wilkening (2011), no bifurcation towards a limiting standing wave was found. It

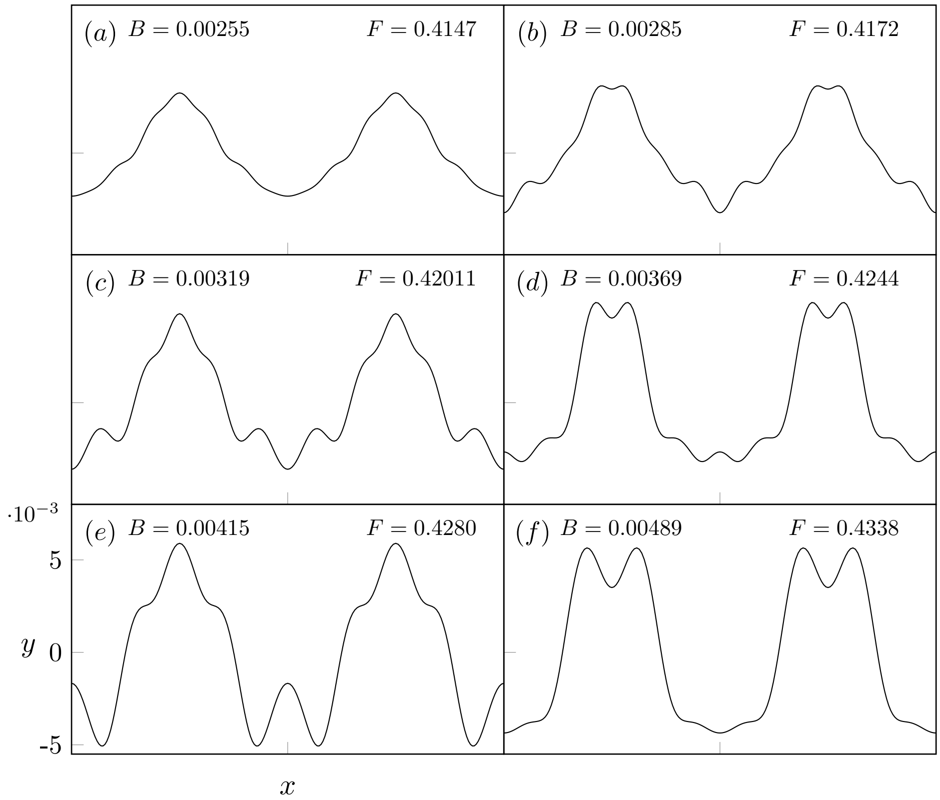

Figure 5.5: Initial profiles at $t = 0$ are shown for six different solutions, each of which has been selected from the middle of the respective solution branch. The dominant component with two wavelengths in the domain is of $O(B)$, and the high-frequency ripples are anticipated to be exponentially-small as $B \to 0$.

is thus natural to ask whether very steep Stokes waves can be numerically continued away from $\beta = \pi/4$. For a small numerical perturbation away from $\beta = \pi/4$ can the limiting formulation still be reached in a self-similar manner? If so, this indicates that continuation in the travelling/standing parameter towards $\beta = \pi/2$ would reveal further information about whether the limiting Standing wave conjectured by Penney and Price can be smoothly approached in a self-similar manner.

6 EXTENSIONS AND POINT VORTICIES

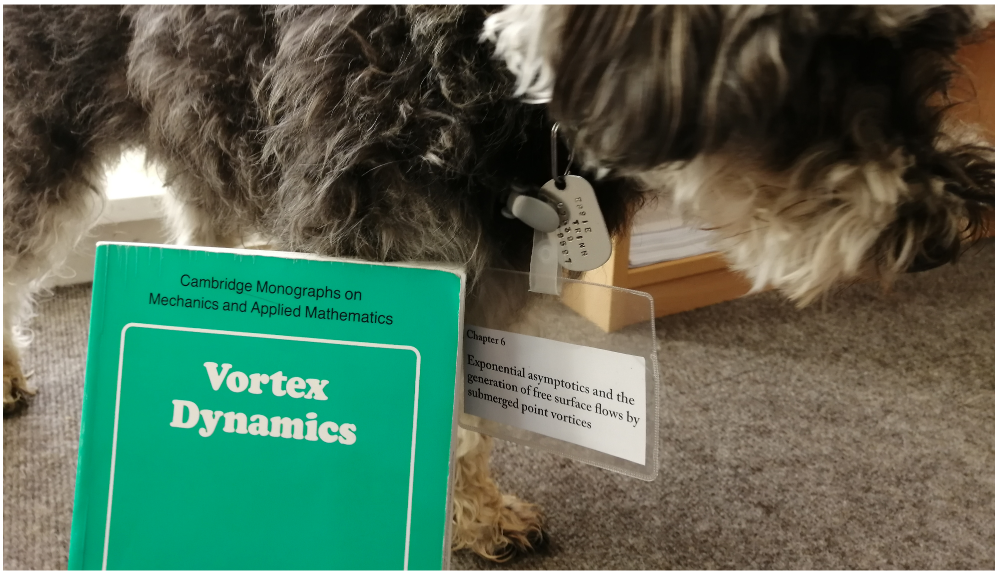

6.1 Introduction

In most classical studies on water waves, the effects of vorticity are neglected. Recently however, there has been a growing interest in the study of vortical effects on water waves. Numerical investigations of this include (Simmen and Saffman 1985, Da Silva and Peregrine 1988, Vanden-Broeck 1996, Vanden-Broeck 1994, McCue and Forbes 1999, Kang and Vanden-Broeck 2000, McCue and Forbes 2002, Choi 2009, Ribeiro et al. 2017, and Dyachenko and Hur 2019). Exact solutions that include vortical effects within the fluid, such as those found by Hur and Wheeler (2020), are much more sparse.

In this section we consider the rotational effects to be localised within the fluid at individual point vortices. This approach is motivated by historical developments in vortex dynamics, for which point vortices were considered significantly earlier than the equivalent formulations that include distributed vorticity within the domain. An example of this is in the study of the wake generated by a staggered vortex street, studied for point vortices by Von Karman and Rubach (1912) and areas of constant vorticity (*vortex patches*) by Christiansen and Zabusky (1973).

We consider a free surface, for which the vorticity is concentrated at submerged points. The fluid is otherwise irrotational, and the free surface $(x(s), y(s))$, parameterised by the arclength, s, is a solution of Bernoulli's equation

$$\frac{F^2}{2}\left[\phi'(s)\right]^2 + y(s) = \frac{F^2}{2},$$

where ϕ is the velocity potential. Note that there are two other equations relating $\phi(s)$, $x(s)$, and $y(s)$. In the low-speed limit of $F \to 0$, Bernoulli's equation is singularly perturbed, and exponentially-small waves are present in the solution profiles. In this chapter, these are derived using the techniques of exponential asymptotics. We also solve for the two vortex case, for which trapped waves, confine to lie between the vortices, emerge for certain values of F. These techniques are expected to be of use in the study of other singular perturbative effects of water waves with submerged point vortices. This includes the small surface tension limit, for which the leading order solutions of the asymptotic expansion would then be determined exactly by the methods by Crowdy and Nelson (2010), Crowdy and Roenby (2014), and Crowdy (2022) for instance.

Appendix B: Statement of Authorship

This declaration concerns the article entitled:	
Exponential asymptotics and the generation of free surface flows by submerged point vortices	
Publication status:	**Draft manuscript** ☐ **Submitted** ☐ **In review** ☐ **Accepted** ● **Published** ☐
Publication details	Authors - Josh Shelton, Philippe H. Trinh Accepted in *Journal of Fluid Mechanics*
Copyright status:	The material has been published with a CC-BY license ☐ The publisher has granted permission to replicate the material included here ☐
Candidate's contribution to the paper	All authors contributed equally to the conceptualisation and methodology used in the article (50%) All analytical calculations were performed by the author of this thesis (100%) All numerical computations were performed by the author of this thesis (100%) The original draft and bulk of the final presentation has been written by the author of this thesis (90%)
Statement from Candidate	This paper reports on original research I conducted during the period of my Higher Degree by Research candidature.
Signed	**Date** 30/12/22

Exponential asymptotics and the generation of free-surface flows by submerged point vortices

Josh Shelton† and Philippe H. Trinh‡

Department of Mathematical Sciences, University of Bath, Bath BA2 7AY, UK

(Received xx; revised xx; accepted xx)

There has been significant recent interest in the study of water waves coupled with non-zero vorticity. We derive analytical approximations for the exponentially-small free-surface waves generated in two-dimensions by one or several submerged point vortices when driven at low Froude numbers. The vortices are fixed in place, and a boundary-integral formulation in the arclength along the surface allows the study of nonlinear waves and strong point vortices. We demonstrate that for a single point vortex, techniques in exponential asymptotics prescribe the formation of waves in connection with the presence of Stokes lines originating from the vortex. When multiple point vortices are placed within the fluid, trapped waves may occur, which are confined to lie between the vortices. We also demonstrate that for the two-vortex problem, the phenomenon of trapped waves occurs for a countably infinite set of values of the Froude number. This work will form a basis for other asymptotic investigations of wave-structure interactions where vorticity plays a key role in the formation of surface waves.

1. Introduction

In this paper we study the steady-state nonlinear flow of an ideal fluid past a submerged line vortex. As the vortices have fixed depth and horizontal displacement, they reduce to point vortices in the two-dimensional flows considered. The inviscid and incompressible fluid of infinite depth is assumed to be irrotational everywhere, with the exception of at the point vortices themselves. For a flow in the complex $z = x + \mathrm{i}y$-plane, with a vortex at $z = z_1$, the complex potential behaves as

$$f = \phi + \mathrm{i}\psi \sim cz - \frac{\mathrm{i}\Gamma}{2\pi} \log{(z - z_1)}, \tag{1.1}$$

where Γ is the circulation of the vortex, and the background flow is of speed c. The non-dimensional system is then characterised by two key parameters: $\Gamma_{\mathrm{c}} = \Gamma/(cH)$, relating vortex strength(s) to inertial effects, and the Froude number, $F = c/\sqrt{gH}$, relating inertial effects to gravitational effects. Here, H is the depth of the point vortex and g is the constant acceleration due to gravity.

The study of such vortex-driven potential flows is complicated by the following fact. The solution of two-dimensional ideal fluid-flow problems involves finding the velocity potential, ϕ, and streamfunction, ψ, in terms of the coordinates x and y, in the functional form $f(z)$. However, it is often convenient to invert this dependency, instead calculating $z(f)$, so that

† Email address for correspondence: j.shelton@bath.ac.uk
‡ Email address for correspondence: p.trinh@bath.ac.uk

the physical variables now have the forms $x(\phi, \psi)$ and $y(\phi, \psi)$. In this formulation, the free surface is a streamline along which ψ is constant, so that the free surface is parameterised by $x(\phi)$ and $y(\phi)$. However, near the point vortex, the local behaviour (1.1), can not be inverted analytically to give $z(f)$. This motivated the work of Forbes (1985), who re-formulated the boundary-integral formulation in terms of a free-surface arclength, s, and a more complex set of governing equations results.

The imposition of a uniform stream as $x \to -\infty$ results in the generation of downstream free-surface waves, as shown in figure 1(a). As hinted in the preliminary numerical investigations of Forbes (1985), the wave amplitude tends to zero as $F \to 0$. In this work, we confirm this behaviour and demonstrate, both numerically and analytically, that the amplitude is exponentially-small in the low-Froude limit. For instance, the amplitude versus $1/F^2$ graph shown in figure 2 demonstrates the fit between our asymptotic predictions of §3 and numerical results of §4. We note that this theory is nonlinear in the vortex strength, Γ_c, and the assumption of small Γ_c need not apply.

The purpose of this paper is to thus characterise the formation of water waves using the framework of exponential asymptotics. We show that these exponentially-small waves smoothly switch-on as the fluid passes beyond the vortex, resulting in oscillations as $x \to \infty$ in the far field. When two submerged vortices are considered, the waves switched-on due to each of the vortices may be out of phase with one another and cancel for certain values of the Froude number. This yields trapped waves between the vortices, and a free surface whose derivative decays to zero as $x \to \infty$. A trapped wave solution is depicted in figure 1(b). This phenomenon of trapped waves has previously been studied for obstructions both within the fluid, and for flows of finite depth past lower topography. For instance, both Gazdar (1973) and Vanden-Broeck & Tuck (1985) detected these numerically for flows over a specified lower topography. More recent works, such as those by Dias & Vanden-Broeck (2004), Hocking *et al.* (2013), and Holmes *et al.* (2013), have focused on detecting parameter values for which these trapped wave solutions occur in various formulations.

The work in this paper provides a first step towards extending many of the existing ideas and techniques of exponential asymptotics, previously developed for purely gravity- or capillary-driven waves (e.g. Chapman & Vanden-Broeck 2002, 2006) to wave phenomena with vortices. As noted above, because the governing equations require an alternative formulation (originally developed by Miksis *et al.* 1981) the asymptotic formulation we present can be extended to other wave-structure interactions where the more general arc-length formulation of the water-wave equations is required. In addition, there has been significant recent interest in the study of water-wave phenomena with dominant vorticity effects, and we reference the recent extensive survey by Haziot *et al.* (2022) and references therein. The exponential-asymptotic techniques developed in this work can also be extended to situations where capillary ripples are forced on the surface of steep vortex-driven waves. The leading order solution in these asymptotic regimes would then be known analytically from the works of *e.g.* (Crowdy & Nelson 2010; Crowdy & Roenby 2014; Crowdy 2022). These, and other exciting future directions, we shall discuss in §6.

2. Mathematical formulation and outline

We consider the typical configurations shown in 1. Following Forbes (1985), in nondimensional form, the system is formulated in terms of the arclength, s, along the free surface, with unknown velocity potential $\phi = \phi(s)$, and free-surface positions, $(x(s), y(s))$. Then, the governing equations are given by Bernoulli's equation, an arclength relation between x and y, and a boundary-integral equation.

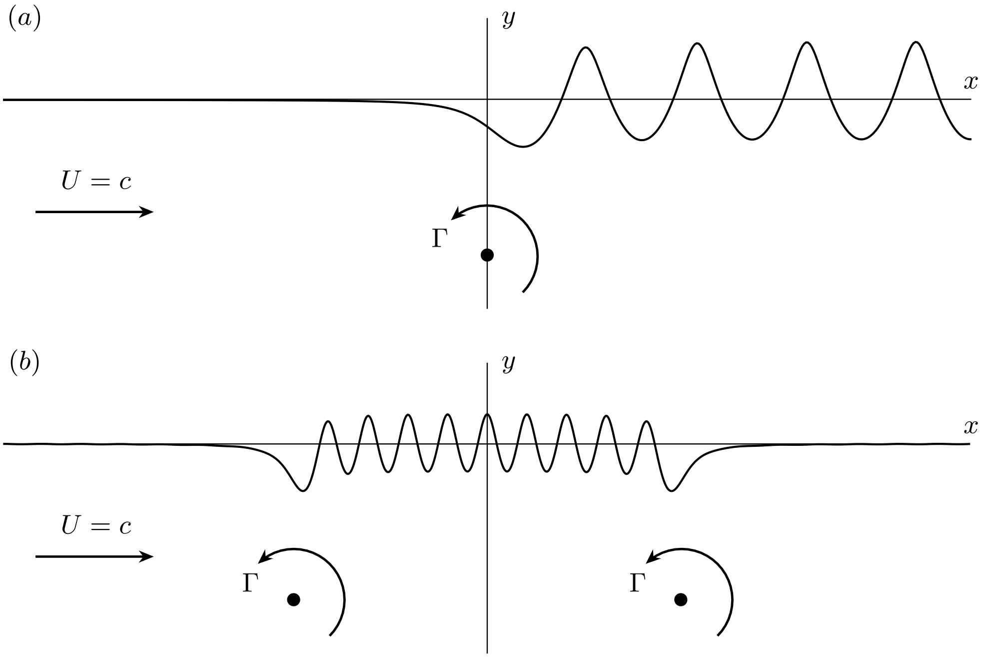

Figure 1: The two physical regimes of underlying point vortices considered within this paper are shown. In (a), a single point vortex with circulation Γ is placed within the fluid. In (b), two point vortices, each with circulation Γ, are located at the same depth within the fluid. These solutions have been computed using the numerical scheme detailed in §4.

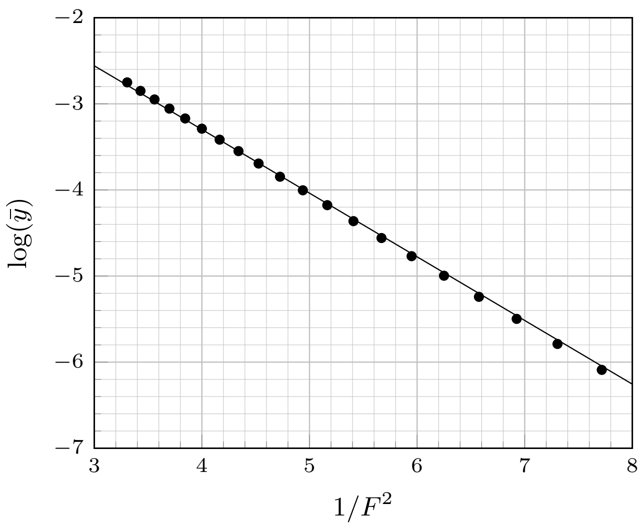

Figure 2: The amplitude, $\bar{y}$, of the free-surface waves is shown for $\log(\bar{y})$ vs $1/F^2$ for the analytical (line) and numerical (dots) solutions of §3 and §4. These have a fixed value of the nondimensional vortex strength, $\Gamma_{\rm c} = 0.25$. The graph confirms exponential smallness of the waves. The solid line has a gradient of ≈ 0.7395, computed using the exponential asymptotic theory of §4.

For a single submerged point vortex at $(x, y) = (0, -1)$, the three equations are

$$\frac{F^2}{2}\left[\phi'(s)\right]^2 + y(s) = \frac{F^2}{2}, \tag{2.1a}$$

$$\left[x'(s)\right]^2 + \left[y'(s)\right]^2 = 1, \tag{2.1b}$$

$$\phi'(s)x'(s) - 1 = \frac{\Gamma_{\rm c}}{\pi}\frac{y(s)+1}{[x(s)]^2 + [y(s)+1]^2} + \mathcal{I}[x, y, \phi']. \tag{2.1c}$$

In the above, two nondimensional parameters appear: the Froude number, F, and the vortex strength, Γ_c, defined by

$$F = \frac{c}{\sqrt{gH}} \quad \text{and} \quad \Gamma_c = \frac{\Gamma}{cH}. \tag{2.2}$$

Here, c is the speed of the fluid, H is the depth of the submerged point vortex, g is the constant acceleration due to gravity, and Γ is the circulation of the point vortex. Furthermore, we have also introduced $\mathcal{I}$ as the nonlinear principle-valued integral defined by

$$\mathcal{I}[x, y, \phi'] = \frac{1}{\pi} ⨍_{-\infty}^{\infty} \frac{[\phi'(t) - x'(t)][y(t) - y(s)] + y'(t)[x(t) - x(s)]}{[x(t) - x(s)]^2 + [y(t) - y(s)]^2} \, \mathrm{d}t. \tag{2.3}$$

When the configuration with two point vortices is considered in §3.5, the boundary-integral equation (2.1c) will need to be modified to (3.23).

2.1. *Analytic continuation*

In the exponential asymptotic procedure of §3, we study the exponentially small terms that display the Stokes phenomenon across Stokes lines of the problem. These Stokes lines originate from singularities of the leading order asymptotic solution, which are located in the analytic continuation of the domain, the arclength s. The analytic continuation of the governing equations (2.1a)-(2.1c) is studied in this section.

We now analytically continue the domain $s \mapsto \sigma$, where $\sigma \in \mathbb{C}$. Bernoulli's equation (2.1a) and the arclength relation (2.1b) may be analytically continued in a straightforward manner, with all dependence on s replaced by the complex valued variable σ. The analytic continuation of the boundary integral equation (2.1c) is more complicated, due to the principal value integral $\mathcal{I}$ defined in (2.3). The analytic continuation of this integral is given by

$$\mathcal{I}[x, y, \phi'] = \widehat{\mathcal{I}}[x, y, \phi'] - a\mathrm{i}\phi'(\sigma)y'(\sigma), \tag{2.4}$$

where $a = \pm 1$ denotes the direction of analytic continuation into $\mathrm{Im}[\sigma] > 0$ or $\mathrm{Im}[\sigma] < 0$, respectively, and $\widehat{\mathcal{I}}$ is the complex-valued integral. Equation (2.4) may be verified by taking the limit of either $\mathrm{Im}[\sigma] \to 0^+$, or $\mathrm{Im}[\sigma] \to 0^-$, which yields half of a residue contribution associated with the singular point at $t = s$ of the integrand.

Substitution of (2.4) into (2.1c) then yields the analytically continued equations, given by

$$\frac{F^2}{2}\left[\phi'(\sigma)\right]^2 + y(\sigma) = \frac{F^2}{2}, \tag{2.5a}$$

$$\left[x'(\sigma)\right]^2 + \left[y'(\sigma)\right]^2 = 1, \tag{2.5b}$$

$$\phi'(\sigma)x'(\sigma) - 1 + a\mathrm{i}\phi'(\sigma)y'(\sigma) = \frac{\Gamma_c}{\pi}\frac{y(\sigma) + 1}{[x(\sigma)]^2 + [y(\sigma) + 1]^2} + \widehat{\mathcal{I}}[x, y, \phi']. \tag{2.5c}$$

The analytic continuation for situations with multiple point vortices is similarly done, with the only difference being the inclusion of additional point vortices in (2.5c).

2.2. *Outline of paper*

In this work, we will consider the following two regimes depicted in figure 1:

(i) A single submerged point vortex, which is the formulation originally considered by Forbes (1985). Imposing free stream conditions as $x \to -\infty$ results in surface waves generated by the vortex. Their amplitude is exponentially-small as $F \to 0$. This is the limit considered by Chapman & Vanden-Broeck (2006) in the absence of vortical effects.

(ii) Two submerged point vortices of the same circulation. For certain critical values of the Froude number, F, the resultant waves are confined to lie between the two vortices. The amplitude of these is also exponentially small as $F \to 0$.

We begin in §3 by determining these exponentially small waves using the techniques of exponential asymptotics. This relies on the optimal truncation of an algebraic asymptotic series for small Froude number, F, and deriving the connection of this to the Stokes phenomenon that acts on the exponentially small waves. The case for two submerged point vortices is then studied in §3.5, where we derive the critical values of the Froude number for which the waves are trapped. Numerical solutions are computed in §4, where comparison occurs with the exponential asymptotic predictions for the single vortex and double vortex cases.

3. Exponential asymptotics

3.1. *Early orders of the solution*

We begin by considering the following asymptotic expansions, in powers of F^2, for the solutions, which are given by

$$x(\sigma) = \sum_{n=0}^{\infty} F^{2n} x_n(\sigma), \quad y(\sigma) = \sum_{n=0}^{\infty} F^{2n} y_n(\sigma), \quad \phi'(\sigma) = \sum_{n=0}^{\infty} F^{2n} \phi'_n(\sigma). \tag{3.1}$$

Substitution of expansions (3.1) into equations (2.5*a*)-(2.5*c*) yields at leading order three equations for the unknowns x_0, y_0, and ϕ'_0. The first of these, Bernoulli's equation (2.5*a*), yields $y_0(\sigma) = 0$. This may be substituted into the second equation, (2.5*b*), to find $(x'_0)^2 = 1$, for which we consider $x'_0 = 1$ without any loss of generality. This may be integrated to find $x_0 = \sigma$, where the constant of integration has been chosen to set the origin at $x_0(0) = 0$. Next, ϕ'_0 is determined from equation (2.5*c*). Since $y_0 = 0$, the integral $\widehat{\mathcal{I}}$ does not enter the leading order equation. This yields the leading order solutions as

$$y_0(\sigma) = 0, \qquad x_0(\sigma) = \sigma, \qquad \phi'_0(\sigma) = 1 + \frac{\Gamma_c}{\pi} \frac{1}{(1+\sigma^2)}. \tag{3.2}$$

Note that there is a singularity in ϕ'_0 above whenever $\sigma^2 = -1$. This corresponds to the point vortex within the fluid at $\sigma = -\mathrm{i}$, as well as another singularity at $\sigma = \mathrm{i}$, which will produce a complex-conjugate contribution to the exponentially-small solution along the free surface.

Next at order $O(F^2)$, y_1 is found explicitly from (2.5*a*). We then find the equation $x'_1 = 0$ from (2.5*b*), and ϕ_1 is determined explicitly from (2.5*c*). This yields

$$\left.\begin{aligned} y_1(\sigma) &= \frac{1}{2}\Big(1 - (\phi'_0)^2\Big), \qquad x_1(\sigma) = 0, \\ \phi'_1(\sigma) &= -a\mathrm{i}\phi'_0 y'_1 + \frac{\Gamma_c(\sigma^2-1)}{\pi(1+\sigma^2)^2} y_1 + \widehat{\mathcal{I}}_1(\sigma), \end{aligned}\right\} \tag{3.3}$$

where $\widehat{\mathcal{I}}_1$ is the $O(F^2)$ component of the complex-valued integral $\widehat{\mathcal{I}}$, originally defined along the real axis in equation (2.3).

3.2. *Late-term divergence*

Our derivation of the exponentially-small terms and associated Stokes phenomenon of §3.4 requires knowledge of the late-terms of the solution expansion (3.1), x_n, y_n, and ϕ'_n, as

$n \to \infty$. We begin by determining the $O(F^{2n})$ components of equations (2.5*a*)-(2.5*c*). The late-terms of Bernoulli's equation are given by

$$y_n + \phi_0'\phi_{n-1}' + \phi_1'\phi_{n-2}' + \cdots = 0, \tag{3.4a}$$

for the arclength relation we have

$$x_0'x_n' + x_1'x_{n-1}' + \cdots + y_1'y_{n-1}' + y_2'y_{n-2}' + \cdots = 0, \tag{3.4b}$$

and finally the boundary integral equation yields

$$x_0'\phi_n' + x_1'\phi_{n-1}' + \phi_0'x_n' + \cdots + a\mathrm{i}\left[\phi_0'y_n' + \phi_1'y_{n-1}' + y_1'\phi_{n-1}' + \cdots\right] + \frac{\Gamma_\mathrm{c}}{\pi}\left[\frac{y_n}{1+x_0^2} - \frac{2y_n}{(1+x_0^2)^2} + \cdots\right] - \widehat{\mathcal{I}}_n(\sigma) = 0. \tag{3.4c}$$

In (3.4*a*)-(3.4*c*) above, only the terms that will appear at the first two orders of n as $n \to \infty$ have been included.

In (3.4*c*), the $O(F^{2n})$ component of the complex-valued integral, $\widehat{\mathcal{I}}$ has been denoted by $\widehat{\mathcal{I}}_n$. The dominant components of this integral, as $n \to \infty$, require the integration of late-term asymptotic solutions that are either a function of the real valued integration domain, such as $y_n(t)$, or a function of the complex domain, such as $y_n(\sigma)$. The first of these, $y_n(t)$, is integrated along the real-valued free surface, away from any singular behaviour. It is thus subdominant to the other terms appearing in equation (3.4*c*). This is analogous to neglecting the late terms of the complex-valued Hilbert transform in similar free-surface problems in exponential asymptotics [c.f. Xie & Tanveer (2002), Chapman & Vanden-Broeck (2002), Chapman & Vanden-Broeck (2006)]. All that remains is to integrate the components of $\widehat{\mathcal{I}}_n$ that involve late-term solutions evaluated in the complex-valued domain. Of these, only that involving $y_n(\sigma)$ appears in the two leading orders, as $n \to \infty$, of equation (3.4*c*). This component is given by

$$\widehat{\mathcal{I}}_n \sim -\frac{y_n(\sigma)}{\pi}\int_{-\infty}^{\infty}\frac{\phi_0'(t)-1}{(t-\sigma)^2}\mathrm{d}t = -\frac{\Gamma_\mathrm{c}}{\pi}\frac{y_n(\sigma)}{(\sigma+a\mathrm{i})^2}, \tag{3.5}$$

for which the integral was evaluated by substituting for ϕ_0' from equation (3.2). Note that integration of $y_n(\sigma)$ was not required due to the lack of any dependence on the domain of integration, t.

Recall that the leading order solutions were singular at $\sigma = \pm i$. For each of the three solution expansions, this singularity first appeared in ϕ_0', y_1, and x_2. Since successive terms in the asymptotic expansion involve differentiation of previous terms (for instance, equation (3.4*a*) for y_n involves ϕ_{n-1}', whose determination in equation (3.4*c*) requires knowledge of y_{n-1}'), the strength of this singularity will grow as we proceed into the asymptotic series. Furthermore, this growing singular behaviour will also lead to the divergence of the late-term solutions as $n \to \infty$, which we capture analytically with the factorial-over-power ansatzes of

$$x_n \sim X(\sigma)\frac{\Gamma(n+\alpha-1)}{[\chi(\sigma)]^{n+\alpha-1}}, \quad y_n \sim Y(\sigma)\frac{\Gamma(n+\alpha)}{[\chi(\sigma)]^{n+\alpha}}, \quad \phi_n \sim \Phi(\sigma)\frac{\Gamma(n+\alpha)}{[\chi(\sigma)]^{n+\alpha}}. \tag{3.6}$$

Here, α is a constant, χ is the singulant function that will capture the singular behaviour of the solution at $\sigma = \pm\mathrm{i}$, and X, Y, and Φ are functional prefactors of the divergent solutions. It can be seen from the dominant balance as $n \to \infty$ of equations (3.4*a*) and (3.4*b*) that $x_{n+1} = O(y_n)$ and $y_n = O(\phi_n)$, which has motivated our precise ordering in n in the ansatzes (3.6).

Substitution of ansatzes (3.6) into the $O(F^{2n})$ equations (3.4*a*)-(3.4*c*) yields at leading order in n the three equations

$$Y - \phi_0'\chi'\Phi = 0, \qquad \chi'\left(X + y_1'Y\right) = 0, \qquad \chi'\left(\Phi + ai\phi_0'Y\right) = 0. \tag{3.7}$$

While the last two of these equations permit the solution $\chi' = 0$, this is unable to satisfy the first equation in (3.7). The remaining solutions can be solved to give $\chi' = ai(\phi_0')^{-2}$, which we integrate to find

$$\chi_a(\sigma) = ai\int_{ai}^{\sigma}\left[1 + \frac{\Gamma_c}{\pi}\frac{1}{(1+t^2)}\right]^{-2}\mathrm{d}t. \tag{3.8}$$

Here, we have introduced the notation $\chi_a = \chi$, where $a = \pm 1$, to discern between each singulant generated by the two singular points of ϕ_0', which are given by $\sigma = \mathrm{i}$ and $\sigma = -\mathrm{i}$. The starting point of integration in (3.8) is $\sigma = \pm\mathrm{i}$ to ensure that $\chi_a(ai) = 0$. This condition is required in order to match with an inner solution near this singular point. Integration of (3.8) yields

$$\begin{aligned}\chi_a(\sigma) =ai\Bigg[\sigma &+ \frac{\Gamma_c^2\sigma}{2(\Gamma_c+\pi)(\pi\sigma^2+\Gamma_c+\pi)} - \frac{\Gamma_c(3\Gamma_c+4\pi)}{2\sqrt{\pi}(\Gamma_c+\pi)^{3/2}}\tan^{-1}\left(\frac{\sqrt{\pi}\sigma}{\sqrt{(\Gamma_c+\pi)}}\right)\Bigg]\\ &+ 1 + \frac{\Gamma_c}{2(\Gamma_c+\pi)} - \frac{\Gamma_c(3\Gamma_c+4\pi)}{2\sqrt{\pi}(\Gamma_c+\pi)^{3/2}}\tanh^{-1}\left(\frac{\sqrt{\pi}}{\sqrt{\Gamma_c+\pi}}\right).\end{aligned} \tag{3.9}$$

3.3. *Solution of the late-term amplitude equations*

We now determine the amplitude functions, Φ, X, and Y, of the late term solutions. Note that if one of these amplitude functions is known, then the other two may be determined by the last two equations in (3.7). Thus, only one equation is required for the amplitude functions, which we find at the next order of n in the late term equation (3.4*a*). This equation is given by

$$\phi_0'\Phi' = \phi_1'\chi'\Phi, \tag{3.10}$$

which may be integrated to find the solution

$$\Phi(\sigma) = \Lambda\exp\left(ai\int_0^{\sigma}\frac{\phi_1'(t)}{[\phi_0'(t)]^3}\mathrm{d}t\right). \tag{3.11}$$

In the above, Λ is a constant of integration, which is determined by matching with an inner solution near the singular points $\sigma = ai$. Once Φ is known, the remaining amplitude functions are determined by the equations $Y = ai(\phi_0')^{-1}\Phi$ and $X = ai\phi_0''\Phi$.

We now calculate the constant, α, that appears in the factorial-over-power ansatzes (3.6). This is determined by ensuring that the singular behaviour, as $\sigma \to ai$, of each ansatz is consistent with the anticipated singular behaviours of

$$x_n = O\Big((\sigma - ai)^{1-3n}\Big), \qquad y_n = O\Big((\sigma - ai)^{1-3n}\Big), \qquad \phi_n = O\Big((\sigma - ai)^{-3n}\Big). \tag{3.12}$$

In taking the inner limit of Φ from (3.11), we have $\Phi = O(\sigma - ai)^{3/2}$. Furthermore since $\chi = O\big((\sigma - ai)^3\big)$, derived later in equation (A 5), equating the power of the singularities for ϕ_n between the ansatz (3.6) and the anticipated singular behaviour above in (3.12) yields the value of $\alpha = 1/2$. The constant of integration, Λ, that appears in solution (3.11) for the amplitude function, Φ, is derived in Appendix A by matching the inner limit of the divergent solution, ϕ_n, with an inner solution at $\sigma = ai$. This yields

$$\alpha = \frac{1}{2} \qquad \text{and} \qquad \Lambda = -\frac{\Gamma_c(-ai)^{1/2}\mathrm{e}^{-\mathcal{P}(ai)}}{6\pi}\left(-\frac{4ai\pi^2}{3\Gamma_c^2}\right)^{\alpha}\lim_{n\to\infty}\left(\frac{\hat{\phi}_n}{\Gamma(n+\alpha+1)}\right), \tag{3.13}$$

where $\hat{\phi}_n$, determined via recurrence relation (A 10), is a constant appearing in the series expansion for the outer limit of the inner solution for ϕ, and $\mathcal{P}(\sigma)$ is defined in equation (A 13).

To conclude, the late-term divergence of the asymptotic expansions (3.1) diverge in a factorial-over-power manner specified by the ansatzes (3.6). Evaluation of this divergence requires the constants α and Λ from equation (3.13), as well as the singulant function $\chi(\sigma)$ from (3.9) and amplitude function $\Phi(\sigma)$ from (3.11). These will be required in the derivation of the exponentially-small terms considered in the next section.

3.4. *Stokes smoothing and Stokes lines*

The exponentially-small components of the solutions are now determined. We truncate the asymptotic expansions (3.1) at $n = N - 1$ and consider a remainder, yielding

$$x = \underbrace{\sum_{n=0}^{N-1} F^{2n} x_n}_{x_r} + \bar{x}, \qquad y = \underbrace{\sum_{n=0}^{N-1} F^{2n} y_n}_{y_r} + \bar{y}, \qquad \phi' = \underbrace{\sum_{n=0}^{N-1} F^{2n} \phi'_n}_{\phi'_r} + \bar{\phi}, \tag{3.14}$$

where the truncated asymptotic expansions have been denoted by x_r, y_r, and ϕ'_r. When N is chosen optimally at the point at which the divergent expansions reorder as $n \to \infty$, given by

$$N \sim \frac{|\chi|}{F^2} + \rho \tag{3.15}$$

where $0 \leqslant \rho < 1$ to ensure that N is an integer, the remainders to the asymptotic expansions (3.14) will be exponentially-small.

Equations for these remainders are found by substituting the truncated expansions (3.14) into the analytically continued equations (2.5*a*)–(2.5*c*). These are given by

$$(F^2\phi'_0 + F^4\phi'_1)\bar{\phi}' + \bar{y} = -\xi_{\mathrm{a}}, \tag{3.16a}$$

$$2\bar{x}' + 2F^2 y'_1 \bar{y}' = -\xi_{\mathrm{b}}, \tag{3.16b}$$

$$\bar{\phi}' + a\mathrm{i}\phi'_0\bar{y}' = -\xi_{\mathrm{c}}. \tag{3.16c}$$

In equations (3.16) above, nonlinear terms such as $\bar{x}^2$ were neglected as they will be exponentially subdominant. In anticipating that $\bar{x} = O(F^2\bar{y}) = O(F^2\bar{\phi})$, terms of the first two orders of F^2 have been retained on the left-hand side of (3.16*a*). Motivated by the late-term analysis, in which equations for the amplitude functions were obtained at leading order for the last two governing equations, we have only retained the leading order terms in equations (3.16*b*) and (3.16*c*). Furthermore, the forcing terms introduced in equations (3.16) are defined by

$$\left.\begin{aligned} \xi_{\mathrm{a}} &= \frac{F^2}{2}(\phi'_r)^2 + y_r - \frac{F^2}{2}, \qquad \xi_{\mathrm{b}} = \left(x'_r\right)^2 + \left(y'_r\right)^2 - 1, \\ \xi_{\mathrm{c}} &= \phi'_r x'_r - 1 + a\mathrm{i}\phi'_r y'_r - \frac{\Gamma_{\mathrm{c}}}{\pi}\frac{y_r + 1}{(x_r)^2 + (y_r+1)^2} - \widehat{\mathcal{I}}[x_r, y_r, \phi'_r]. \end{aligned}\right\} \tag{3.17}$$

Since each order of these forcing terms will be identically zero up to and including $O(F^{2(N-1)})$, they will be of $O(F^{2N})$. Only knowledge of ξ_{a} will be required in the Stokes smoothing procedure of this section, and this is given by

$$\xi_{\mathrm{a}} \sim \phi'_0\phi'_{N-1}F^{2N}. \tag{3.18}$$

Homogeneous solutions to equations (3.16), for which the forcing terms on the right-hand

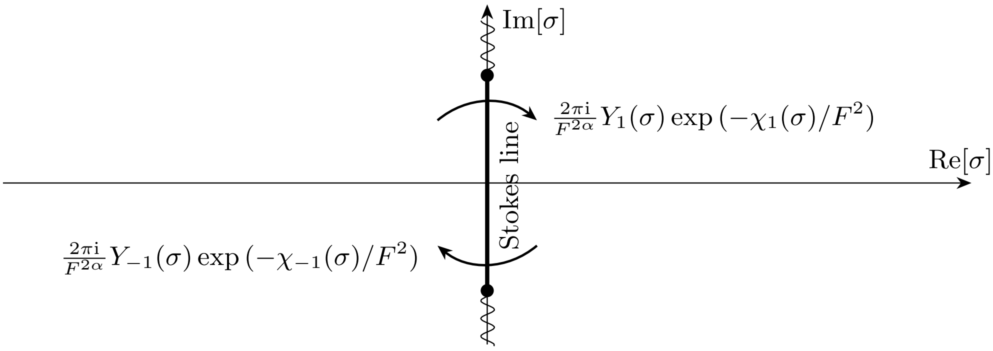

Figure 3: The Stokes lines (bold) lie along the imaginary axis between the two singular points of $\sigma = -\mathrm{i}$ and $\sigma = \mathrm{i}$. Branch cuts are shown with a wavy line.

sides are omitted, are $\bar{x} \sim F^2 X \mathrm{e}^{-\chi/F^2}$, $\bar{y} \sim Y \mathrm{e}^{-\chi/F^2}$, and $\bar{\phi} \sim \Phi \mathrm{e}^{-\chi/F^2}$, where the singulant χ and amplitude functions X, Y, and Φ satisfy the same equations as those found for the late-term solutions in §3.2. Next, we solve for the particular solutions of equations (3.16) through variation of parameters by multiplying the homogeneous solutions by an unknown function, $\mathcal{S}(\sigma)$, giving

$$\left.\begin{aligned} \bar{x} &\sim \mathcal{S}(\sigma) F^2 X(\sigma) \mathrm{e}^{-\chi(\sigma)/F^2}, \\ \bar{y} &\sim \mathcal{S}(\sigma) Y(\sigma) \mathrm{e}^{-\chi(\sigma)/F^2}, \\ \bar{\phi} &\sim \mathcal{S}(\sigma) \Phi(\sigma) \mathrm{e}^{-\chi(\sigma)/F^2}, \end{aligned}\right\} \tag{3.19}$$

where $Y = a\mathrm{i}\Phi/\phi_0'$ and $X = -y_1' Y$. The function $\mathcal{S}$ is called the Stokes multiplier, as it will display the Stokes phenomenon across Stokes lines of the problem, which is demonstrated next. An equation for $\mathcal{S}$ is obtained by substituting (3.19) into equation (3.16*a*), yielding $F^2 \phi_0' \Phi \mathrm{e}^{-\chi/F^2} \mathcal{S}'(\sigma) \sim -\xi_{\mathrm{a}}$. In substituting for the dominant behaviour of ξ_{a} from (3.18) and the factorial-over-power divergence of ϕ_{N-1}' from (3.6), and changing derivatives of $\mathcal{S}$ from σ to χ, we find

$$\frac{\mathrm{d}\mathcal{S}}{\mathrm{d}\chi} \sim \frac{\Gamma(N+\alpha)}{\chi^{N+\alpha}} F^{2(N-1)} \mathrm{e}^{\chi/F^2}. \tag{3.20}$$

In expanding as $N \to \infty$, and substituting for $N \sim |\chi|/F^2 + \rho$ from equation (3.15), the right-hand side of equation (3.19) is seen to be exponentially-small, except for in a boundary layer close to contours satisfying

$$\mathrm{Im}[\chi] = 0 \quad \text{and} \quad \mathrm{Re}[\chi] > 0. \tag{3.21}$$

These are the Stokes line conditions originally derived by Dingle (1973). Across the Stokes lines, the solution for the Stokes multiplier $\mathcal{S}$,

$$\mathcal{S}(\sigma) = S_a + \frac{\sqrt{2\pi}\mathrm{i}}{F^{2\alpha}} \int_{-\infty}^{\sqrt{|\chi|}\frac{\arg(\chi)}{F}} \exp(-t^2/2)\mathrm{d}t, \tag{3.22}$$

rapidly varies from the constant S_a to $S_a + 2\pi\mathrm{i}/F^{2\alpha}$. This is the Stokes phenomenon, and the contours satisfying the Dingle conditions (3.21) are shown in figure 3 to lie along the imaginary axis. For the one vortex case studied in this section, the upstream condition as $\mathrm{Re}[\sigma] \to -\infty$ requires that $S_1 = 0$ and $S_{-1} = -2\pi\mathrm{i}/F^{2\alpha}$.

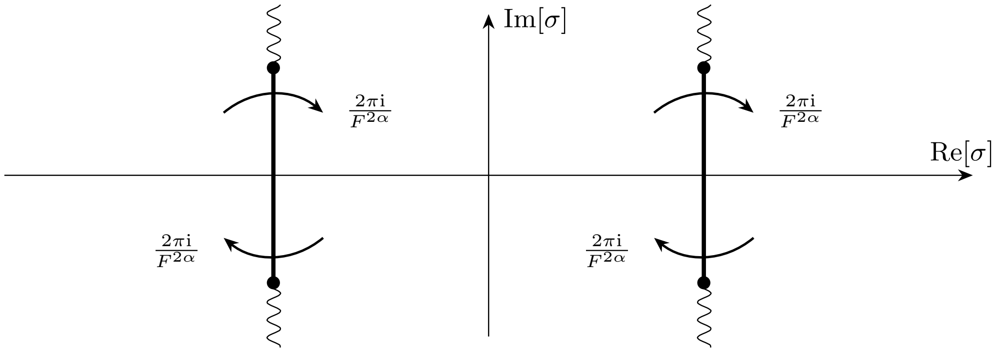

Figure 4: The Stokes lines (bold) generated by the four singular points are shown.

3.5. *Trapped waves generated by two submerged vortices*

We have so far studied the case of a single submerged point vortex. When multiple point vortices are placed within the fluid, the only change is to the boundary integral equation, previously specified in (2.5*c*) for a single vortex. In this section we study the formulation of two submerged point vortices of the same nondimensional strength, Γ_c, located at $z = x + iy = \pm\lambda - i$, for which the analytically continued boundary integral equation is given by

$$\phi'(\sigma)x'(\sigma) - 1 + ai\phi'(\sigma)y'(\sigma) = \frac{\Gamma_c}{\pi}\left[\frac{y(\sigma)+1}{[x(\sigma)-\lambda]^2 + [y(\sigma)+1]^2} + \frac{y(\sigma)+1}{[x(\sigma)+\lambda]^2 + [y(\sigma)+1]^2}\right] + \widehat{\mathcal{I}}[x, y, \phi]. \tag{3.23}$$

Unlike the case for a single submerged point vortex that produces waves in the far field for $x \to \infty$, two identical point vortices can produce solutions for which the waves are confined to lie between the vortices, $-\lambda < \mathrm{Re}[\sigma] < \lambda$. This occurs for critical values of the Froude number, which we now predict using the techniques of exponential asymptotics developed in the previous sections.

The first two orders of the asymptotic solution for ϕ are now given by

$$\phi_0'(\sigma) = 1 + \frac{\Gamma_c}{\pi}\left[\frac{1}{1+(\sigma+\lambda)^2} + \frac{1}{1+(\sigma-\lambda)^2}\right], \tag{3.24a}$$

$$\phi_1'(\sigma) = -ai\phi_0'y_1' + \frac{\Gamma_c y_1}{\pi}\left[\frac{(\sigma+\lambda)^2-1}{[1+(\sigma+\lambda)^2]^2} + \frac{(\sigma-\lambda)^2-1}{[1+(\sigma-\lambda)^2]^2}\right] + \widehat{\mathcal{I}}_n(\sigma), \tag{3.24b}$$

which are singular at the four locations $\sigma = -\lambda + ai$ (from the vortex at $z = -\lambda - i$) and $\sigma = \lambda + ai$ (from the vortex at $z = \lambda - i$). Note that we have again defined $a = \pm 1$ to indicate whether $\mathrm{Im}[\sigma] > 0$ or $\mathrm{Im}[\sigma] < 0$. These four singular points each have associated Stokes lines, shown in figure 4. In general, the waves switched on across the first Stokes lines, emanating from the points $\sigma = -\lambda + ai$, will be out of phase with the waves switched on across the second Stokes lines, from $\sigma = \lambda + ai$. However, for certain values of F, the wave switched on across the first Stokes line is then switched off by the second Stokes line, yielding solutions with no waves for $\mathrm{Re}[\sigma] > \lambda$. An example of this trapped solution was shown earlier in figure 1(b).

Thus, in using the Stokes switching prediction for $\bar{\phi}$ shown in figure 4 and writing $\bar{y} =$

$a\mathrm{i}\bar{\phi}/\phi_0'$, we require for the two contributions of

$$\left.\begin{aligned} \bar{y}_1 &\sim -\frac{2\pi}{F^{2\alpha}\phi_0'}\Phi_1(\sigma)\exp\left(-\frac{\chi_1(\sigma)}{F^2}\right) + c.c., \\ \bar{y}_2 &\sim -\frac{2\pi}{F^{2\alpha}\phi_0'}\Phi_2(\sigma)\exp\left(-\frac{\chi_2(\sigma)}{F^2}\right) + c.c., \end{aligned}\right\} \tag{3.25}$$

to cancel with one another for $\mathrm{Re}[\sigma] > \lambda$. Here, we denoted χ_1 and Φ_1 as the singulant and amplitude function arising from the $\sigma = -\lambda + a\mathrm{i}$ singularities, and χ_2 and Φ_2 as those arising from the $\sigma = \lambda + a\mathrm{i}$ singularities. The first of (3.25), $\bar{y}_1$, is the contribution switched on as we pass from left to right across the Stokes lines associated with the singular points $\sigma = -\lambda + a\mathrm{i}$. The second, $\bar{y}_2$, is the contribution switched on from left to right by the Stokes lines associated with the $\sigma = \lambda + a\mathrm{i}$ singular point. Note that the specified contributions in (3.25) are from the $a = 1$ contribution, and the unspecified complex-conjugate components are from that with $a = -1$.

We now simplify each of the expressions given in equation (3.25) by substituting for the amplitude functions Φ_1 and Φ_2, which satisfy the same equation as that found previously in (3.10). The only difference will be the constants of integration, which we denote by Λ_1 and Λ_2. This yields

$$\left.\begin{aligned} \bar{\phi}_1 &\sim -\frac{4\pi|\Lambda_1|}{F^{2\alpha}\phi_0'}\exp\left(-\frac{\mathrm{Re}[\chi_1]}{F^2}\right)\cos\left(\int_0^\sigma \frac{\phi_1'(t)}{[\phi_0'(t)]^3}\mathrm{d}t + \arg[\Lambda_1] - \frac{\mathrm{Im}[\chi_1]}{F^2}\right), \\ \bar{\phi}_2 &\sim -\frac{4\pi|\Lambda_2|}{F^{2\alpha}\phi_0'}\exp\left(-\frac{\mathrm{Re}[\chi_2]}{F^2}\right)\cos\left(\int_0^\sigma \frac{\phi_1'(t)}{[\phi_0'(t)]^3}\mathrm{d}t + \arg[\Lambda_2] - \frac{\mathrm{Im}[\chi_2]}{F^2}\right). \end{aligned}\right\} \tag{3.26}$$

Note that $|\Lambda_1| = |\Lambda_2|$. This may be verified by matching with an inner solution, much like that considered in Appendix A for the case of a single point vortex. In fact, the same inner equation emerges regardless of the number of vortices considered, and the only difference encountered in the matching procedure is in the inner limit of the outer divergent solution. Furthermore, through integration of $\chi' = a\mathrm{i}(\phi_0')^{-2}$ and imposing the boundary conditions $\chi_1(a\mathrm{i}-\lambda) = 0$ and $\chi_2(a\mathrm{i}+\lambda) = 0$, it may be verified that along the free-surface, $\mathrm{Im}[\sigma] = 0$, we have $\mathrm{Re}[\chi_1] = \mathrm{Re}[\chi_2]$. Thus, the prefactors multiplying each of the cosine functions in (3.26) are identical, and the condition for them to cancel, $\bar{y}_1 + \bar{y}_2 = 0$, yields

$$\begin{aligned} \cos&\left(\int_0^\sigma \frac{\phi_1'(t)}{[\phi_0'(t)]^3}\mathrm{d}t + \frac{\arg[\Lambda_1] + \arg[\Lambda_2]}{2} - \frac{\mathrm{Im}[\chi_1 + \chi_2]}{2F^2}\right) \\ &\times \cos\left(\frac{\arg[\Lambda_1] - \arg[\Lambda_2]}{2} - \frac{\mathrm{Im}[\chi_1 - \chi_2]}{2F^2}\right) = 0. \end{aligned} \tag{3.27}$$

Note that since χ_1 and χ_2 satisfy the same differential equation, $\chi' = a\mathrm{i}(\phi_0')^{-2}$, originally derived in §3.2, the only difference between them are their constants of integration. Therefore $\mathrm{Im}[\chi_1 + \chi_2]$ will be a function of σ, and $\mathrm{Im}[\chi_1 - \chi_2]$ will be constant. Thus, only the second cosine component of (3.27) is capable of satisfying the identity for $\mathrm{Re}[\sigma] > \lambda$. Since this cosine function is zero when the argument equals $\pm\pi/2$, $\pm 3\pi/2$, and so forth, we find

$$F_k = \sqrt{\frac{\mathrm{Im}[\chi_1 - \chi_2]}{\arg[\Lambda_1] - \arg[\Lambda_2] + \pi(2k+1)}}. \tag{3.28}$$

for $k = 0, 1, 2, \ldots$, and so forth. Equation (3.28) yields the discrete values of the Froude number, F_k, for which the waves are confined to lie between the two submerged vortices.

All that remains is to evaluate $\mathrm{Im}[\chi_1 - \chi_2]$, $\arg[\Lambda_1]$, and $\arg[\Lambda_2]$. Each of these singulants are found by integrating $\chi' = \mathrm{i}(\phi_0')^{-2}$, where ϕ_0' is specified in equation (3.24), from the corresponding singular point. We may decompose each singulant into a real-valued integral along the Stokes line, and an imaginary-valued integral along the free-surface. Thus, $\mathrm{Im}[\chi]$ is an integral along the free-surface, $\mathrm{Im}[\sigma] = 0$, from the intersection of the Stokes line to σ. This yields

$$\mathrm{Im}[\chi_1(\sigma) - \chi_2(\sigma)] = \int_{-\lambda}^{\lambda} \left[1 + \frac{\Gamma_\mathrm{c}}{\pi}\left(\frac{1}{1+(t+\lambda)^2} + \frac{1}{1+(t-\lambda)^2}\right)\right]^{-2} \mathrm{d}t. \tag{3.29}$$

In the numerical results of §4.2, the integral in (3.29) is evaluated with a symbolic programming language. Note that the Stokes lines depicted in figure 4 are not truly vertical, and are slightly curved such that they intersect the free surface at the points $-\lambda^*$ and λ^*. Thus, the range of integration in (3.29) should actually lie between $-\lambda^* < t < \lambda^*$; however since λ^* is very close in value to λ (for $\lambda = 8$ and $\Gamma_c = 0.3$, $\lambda^* \approx 7.99998$), this subtlety has been ignored.

Comparisons between the analytical prediction of F_k from (3.28) and numerical results are performed in §4.2.

4. Numerical results

We begin in §4.1 by verifying with numerical results our analytical predictions for the exponentially-small scaling as $F \to 0$ for the case of a single vortex. This is given by the singulant function, χ, from (3.9), and comparisons are made for a range of values of the vorticity, Γ_c. The analytical predictions of the Froude numbers for trapped waves between two point vortices, given in (3.28), are then compared to numerical predictions in §4.2.

A detailed description of the numerical method used is given by Forbes (1985), which we will briefly summarise here.

(i) The real-valued domain, s, is truncated to lie between the values of s_L and s_R. N discretisation points are used, such that the numerical domain is given by $s_k = s_\mathrm{L} + (k-1)(s_\mathrm{R} - s_\mathrm{L})/(N-1)$ for $1 \leqslant k \leqslant N$. The unknown solution is taken to be $y'(s)$, which we define at each gridpoint by $y_k' = y'(s_k)$. The radiation conditions are imposed by enforcing $y_1 = 0$, $y_1' = 0$, $x_1' = 1$, $\phi_1' = 1$, $x_1 = s_1$, and $\phi_1 = s_\mathrm{L}$, and the initial guess for y_k' is either zero or a previously computed solution.

(ii) Since we assume that y_k' is known at the next gridpoint, the arclength relation (2.1*b*) yields x_k'. Trapezoidal-rule integration then determines values for x_k and y_k, which we use to find ϕ_k' from Bernoulli's equation (2.1*a*). This process is repeated for $k = 2$ to $k = N$ to find function values at every gridpoint.

(iii) The boundary-integral equation (2.1*c*) is evaluated at each gridpoint with the known values of x_k, y_k, ϕ_k', x_k', and y'. To avoid the singularity associated with the principal-valued integral $\mathcal{I}[x, y, \phi']$, each unknown that is not a function of the integration variable, t, is instead evaluated between gridpoints by interpolation.

(iv) This yields $N-1$ nonlinear equations from evaluating the boundary-integral equation between each gridpoint, $(s_k + s_{k+1})/2$, which is closed by the $N-1$ unknowns y_k' for $k = 2$ to $k = N$. Solutions are found by minimising the residual through Newton iteration. For the trapped waves studied in §4.2, we impose an additional constraint of symmetry about $s = 0$ in the real-valued solution, $y(s)$, such that the Froude number, F, is determined as an eigenvalue.

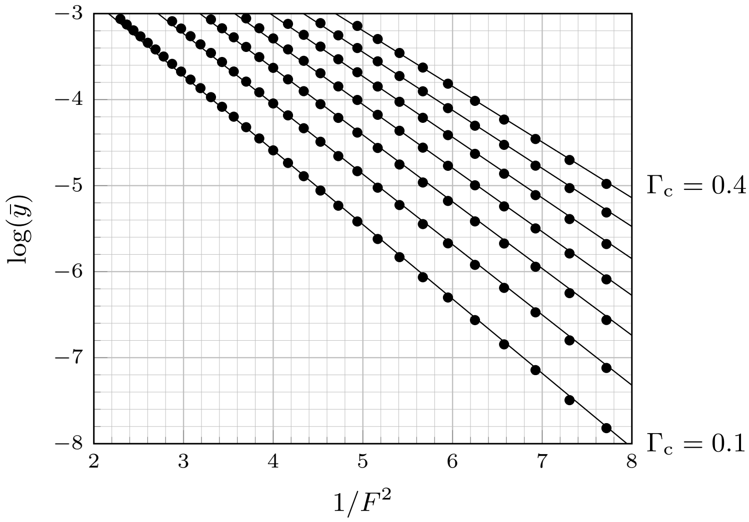

Figure 5: The exponentially-small dependence of the wave amplitude is shown (dots) for numerical results for seven different values of $\Gamma_c = \{0.1, 0.15, 0.2, 0.25, 0.3, 0.35, 0.4\}$. Solid lines represent the analytical gradient found from the real part of χ in equation (3.9). The behaviour of this gradient for different values of the vortex strength Γ_c is shown in figure 6.

4.1. *Waves generated by a single vortex*

For the numerical results presented in this section, we have used $N = 2000$ grid points, and a domain specified by $s_L = -40$ and $s_R = 40$. In computing numerical solutions for a wide range of Froude numbers, and the values of $\Gamma_c = \{0.1, 0.15, 0.2, 0.25, 0.3, 0.35, 0.4\}$, the exponentially-small scaling as $F \to 0$ of the high-frequency waves present for $s > 0$ may be measured. This is shown in the semilog plot of figure 5. We see that these lines, each of which represents solutions with a different value of Γ_c, are straight and thus the amplitude of these ripples is exponentially small as $F \to 0$. The gradient of each of these lines is expected to closely match the exponential scaling predicted analytically, given by the singulant χ. Along the free surface, this is given by $\mathrm{Re}[\chi]$ from equation (3.9) which takes constant values. In figure 6, this analytical prediction is compared to the numerical values from figure 5, and good agreement is observed. Note that there are small instabilities present in the numerical solution which decay when the truncated domain is extended; upon which we expect the numerical results to tend towards the analytical prediction shown in figure 6.

Comparison between a numerical and asymptotic solution profile is shown in figure 7 for $F = 0.45$ and $\Gamma_c = 0.4$. The numerical solution is determined by the scheme detailed at the beginning of §4, with $N = 2000$ discretisation points in the arclength, $-40 \leqslant s \leqslant 40$. The asymptotic solution plots $x(s) = x_0(s) + F^2 x_1(s) + \bar{x}(s)$ against $y(s) = y_0(s) + F^2 y_1(s) + \bar{y}(s)$. These early order solutions, x_0, x_1, y_0, and y_1 are specified in equations (3.2) and (3.3). The exponentially-small components, $\bar{x}$ and $\bar{y}$, are implemented from expression (3.19). This requires knowledge of the singulant, χ, given in (3.9), the amplitude functions $Y = a\mathrm{i}\Phi/\phi_0'$ and $X = -y_1'Y$ determined from Φ in (3.11), and the Stokes multiplier, $\mathcal{S}$, given in (3.22). A real-valued asymptotic solution is obtained through evaluating the sums $\bar{x}|_{a=1} + \bar{x}|_{a=-1}$ and $\bar{y}|_{a=1} + \bar{y}|_{a=-1}$ on the real-valued domain, $\sigma = s$, for $\mathrm{Im}[\sigma] = 0$. Note that in the determination of the constant Λ, its magnitude, $|\Lambda|$, has been fitted to equal that found from the corresponding numerical solution, and its argument (corresponding to a phase shift of the resultant wave) is determined from relation (3.13) as $\arg[\Lambda] = a\pi/2$.

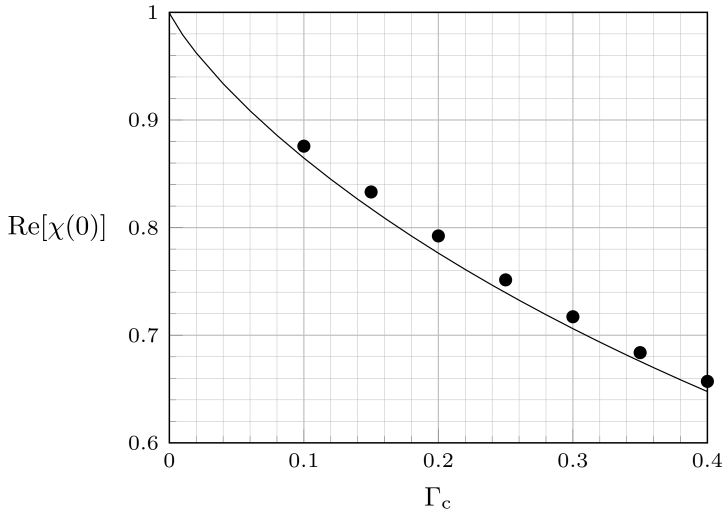

Figure 6: The analytical prediction for $\mathrm{Re}[\chi]$ along the free surface $\mathrm{Im}[\sigma] = 0$ from equation (3.9) is shown against the vorticity Γ_c (line). The numerical predictions, corresponding to the slopes of the semilog plot in figure 5, are shown circled.

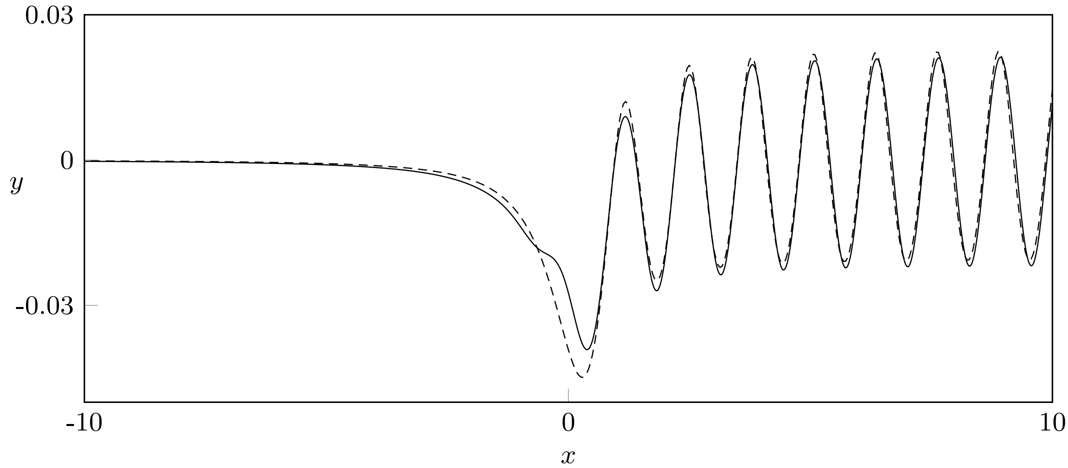

Figure 7: For $F = 0.45$ and $\Gamma_\mathrm{c} = 0.4$, a numerical solution (dashed) is compared to an analytical solution (line) determined in §3.

4.2. *Trapped gravity waves between two vortices*

We considered the case of two submerged point vortices analytically in §3.5. When each vortex had the same nondimensional circulation, Γ_c, and depth equal to unity, trapped waves were seen to occur for certain discrete values of the Froude number, F_k. In this section, we compare the analytical prediction for F_k from (3.28) with numerical results. These trapped numerical solutions are found with the method detailed at the beginning of §4. In imposing the additional constraint of symmetry to eliminate waves downstream of the vortices, the special Froude number, F_k, is determined as an eigenvalue. These results were performed for $N = 4000$ grid points, a domain between $s_\mathrm{L} = -60$ and $s_\mathrm{R} = 60$, and horizontal vortex placement specified as $\lambda = 8$.

In figure 8, we plot the tail amplitude (for $s > \lambda$) of the asymptotic solutions for the values of $0.3 < F < 0.5$, $\Gamma_\mathrm{c} = 0.3$, and $\lambda = 8$. This amplitude is equal to zero at the values of F_k from equation (3.28). The figure also contains additional markers denoted by (a),

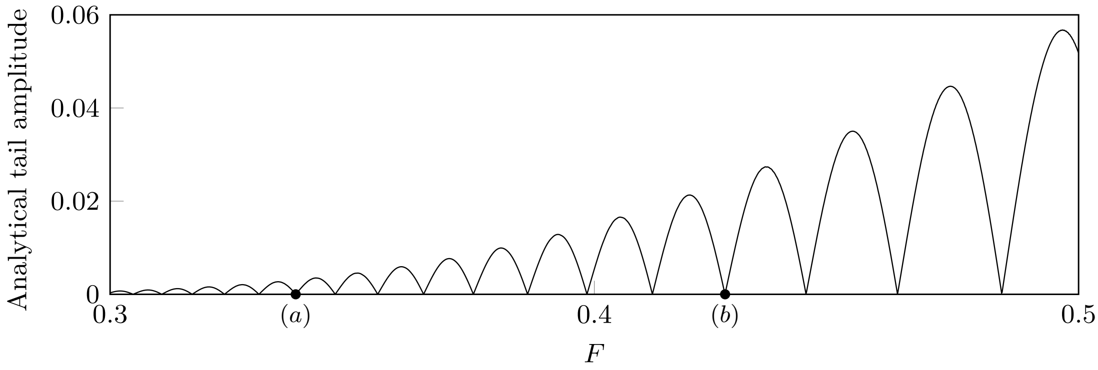

Figure 8: The amplitude of oscillations present for $s > \lambda$ in the asymptotic solutions is shown against the Froude number, F. Here, $\Gamma_c = 0.3$ and $\lambda = 8$. This amplitude is equal to zero at the locations F_k derived in equation (3.28). The two points marked (a) and (b) correspond to the profiles shown in figure 9.

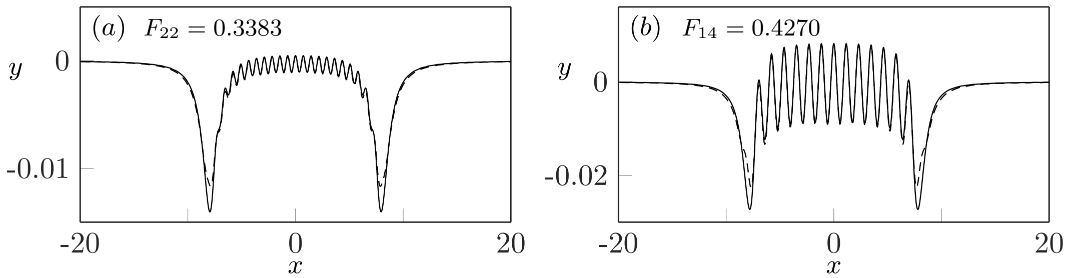

Figure 9: Two different trapped wave solutions are shown for $\Gamma_c = 0.3$ and $\lambda = 8$ corresponding to (a) $F = 0.3383$ and (b) $F = 0.4270$. Asymptotic solutions (solid line) are compared to numerical solutions (dashed) for (a) $k = 22$ and (b) $k = 14$. In each inset, the two curves are nearly indistinguishable to visual accuracy.

where $F = 0.3383$, and (b), where $F = 0.4270$. This corresponds to the figure 9 where we compare numerical solutions obtained in this section, and asymptotic solutions from §3 for those given values of F. The fit is excellent and the corresponding curves are nearly visually indistinguishable at the scale of the graphic.

Finally, in figure 10, we compare the values of F_k obtained analytically and numerically. The straight lines are the analytical prediction from (3.28), and dots represent the numerical values for F_k.

5. Conclusion

We have shown, through both numerical and analytical investigations, that the waves generated by submerged point vortices are exponentially small in the low-speed limit of $F \to 0$. Furthermore, when two submerged vortices are considered, oscillatory waves vanish downstream for certain values of the Froude number, F. Through the techniques of exponential asymptotics, we have demonstrated how these values may be derived. Their prediction relies on the understanding of singularities in the analytically continued domain that generate a divergent asymptotic expansion. The remainder to this series is exponentially small as $F \to 0$, and the study of the associated Stokes phenomenon yields discrete values of F for which the waves are trapped between each vortex.

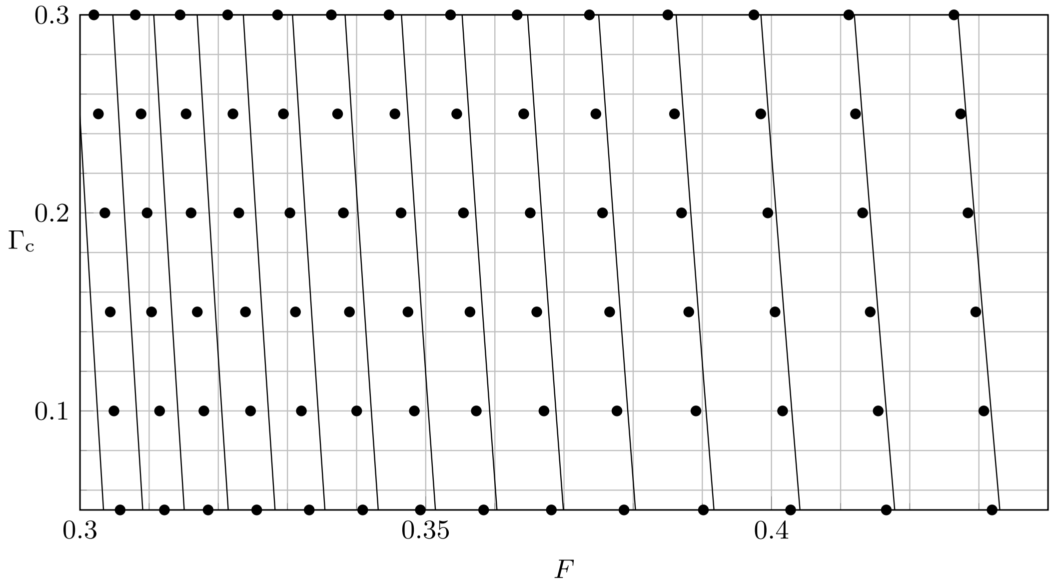

Figure 10: Values of the Froude number, F_k, for which the waves are trapped between each submerged vortex are shown. The numerical results of §4.2 are shown circled, and the analytical results from equation (3.28) are shown with lines. Here, $\lambda = 8$, and for the numerical solutions $N = 4000$, $s_L = -60$, and $s_R = 60$.

6. Discussion

The work presented here forms a basis for a number of interesting extensions involving exponentially-small water waves with gravity, capillarity, and/or vorticity providing singular perturbative effects.

First, it should be remarked that the classical exponential-asymptotics theories by *e.g.* Chapman & Vanden-Broeck (2002, 2006) for capillary- and gravity-driven surface waves produced in flows over topographies rely upon the existence of closed-form conformal maps. In such problems, the governing equations for the free-surface can be written in terms of a single complex-valued unknown (*e.g.* the complex velocity), with the velocity potential serving as the independent variable. This includes situations such as flows past polygonal boundaries (related to the availability of the Schwarz-Christoffel mapping). The arclength formulation we have used in this work provides a more general setting for wave-structure interactions with arbitrary bodies, including for instance, flows past smoothed bodies specified in (x, y)-coordinates. Here, we have demonstrated that the exponential asymptotics can be generalised to such formulations. We expect that many of the interesting wave-structure interactions studied by *e.g.* Holmes *et al.* (2013) (symmetric bottom topography), Hocking *et al.* (2013) (submerged semi-ellipse), and Elcrat & Miller (2006) (submerged point vortex with lower topography) can be attacked using the technology we have developed here.

Secondly, the phenomenon of trapped waves is an interesting one. The exponential asymptotics interpretation, whereby waves switched-on at one location (the Stokes line intersection) must be switched-off at another, provides an intuitive explanation for how trapped waves form in singularly perturbative limits. The context, in our problem, relates to vortices fixed within the fluid for modelling submerged obstructions, such as the submerged cylinders studied numerically by Tuck & Scullen (1998). However, trapped waves have been detected numerically in other geometries including submerged bumps (Hocking *et al.* 2013), a semi-ellipse (Holmes *et al.* 2013), a trigonometric profile (Dias & Vanden-Broeck 2004), spikes (Binder *et al.* 2005), and a rectangular bump (Lustri *et al.* 2012). We expect that the 'selection mechanism' that produces the countably infinite set of values (3.28) is a kind of universality in eigenvalue problems (cf. Chapman *et al.* 2022 for further discussion and examples).

Finally, we note that in this paper, the forcing mechanism producing the waves was via the complex-plane singularities associated with the point vortices—then, we found that the waves were singularly perturbed due to the inertial term in Bernoulli's equation, thus producing exponentially small waves, scaling as $\exp(-\mathrm{const.}/F^2)$. Recently, analytical solutions have been developed for pure-vorticity-driven water waves, notably in the works by Crowdy & Nelson (2010); Crowdy & Roenby (2014); Crowdy (2022). In essence, we believe these solutions can serve as leading-order approximations in the regime of small surface-tension; it might be expected that exponentially-small parasitic ripples then exist on the surface of such vorticity-driven profiles. This would then be similar to the work of Shelton *et al.* (2021); Shelton & Trinh (2022) for parasitic capillary ripples on steep gravity waves. Numerical and analytical work on this class of problems is ongoing.

Acknowledgements. We are grateful for many stimulating and motivating discussions that took place during the recent LMS-Bath symposium "New Directions in Water Waves" held at the University of Bath in July 2022. PHT is supported by the Engineering and Physical Sciences Research Council [EP/V012479/1].

Declaration of interests. The authors report no conflict of interest.

REFERENCES

Binder, B. J., Vanden-Broeck, J.-M. & Dias, F. 2005 Forced solitary waves and fronts past submerged obstacles. *Chaos* **15** (3), 037106.

Chapman, S. J., Dallaston, M. C., Kalliadasis, S., Trinh, P. H. & Witelski, T. P. 2022 The role of exponential asymptotics and complex singularities in transitions and branch merging of nonlinear dynamics. *In review.* .

Chapman, S. J. & Vanden-Broeck, J.-M. 2002 Exponential asymptotics and capillary waves. *SIAM J. Appl. Math.* **62 (6)**, 1872–1898.

Chapman, S. J. & Vanden-Broeck, J.-M. 2006 Exponential asymptotics and gravity waves. *J. Fluid Mech.* **567**, 299–326.

Crowdy, D. G. 2022 Exact solutions for steadily travelling water waves with submerged point vortices. *In review* .

Crowdy, D. G. & Nelson, R. 2010 Steady interaction of a vortex street with a shear flow. *Phys. Fluids* **22** (9), 096601.

Crowdy, D. G. & Roenby, J. 2014 Hollow vortices, capillary water waves and double quadrature domains. *Fluid Dyn. Res.* **46** (3), 031424.

Dias, F. & Vanden-Broeck, J.-M. 2004 Trapped waves between submerged obstacles. *J. Fluid Mech.* **509**, 93–102.

Dingle, R. B. 1973 *Asymptotic Expansions: Their Derivation and Interpretation*. Academic Press, London.

Elcrat, A. R. & Miller, K. G. 2006 Free surface waves in equilibrium with a vortex. *Eur. J. Mech. B-Fluid.* **25** (2), 255–266.

Forbes, L. K. 1985 On the effects of non-linearity in free-surface flow about a submerged point vortex. *J. Eng. Math.* **19** (2), 139–155.

Gazdar, A. S. 1973 Generation of waves of small amplitude by an obstacle placed on the bottom of a running stream. *J. Phys. Soc. Japan* **34** (2), 530–538.

Haziot, S., Hur, V., Strauss, W., Toland, J., Wahlén, E., Walsh, S. & Wheeler, M. 2022 Traveling water waves—the ebb and flow of two centuries. *Quart. Appl. Math.* **80** (2), 317–401.

Hocking, G. C., Holmes, R. J. & Forbes, L. K. 2013 A note on waveless subcritical flow past a submerged semi-ellipse. *J. Eng. Math.* **81** (1), 1–8.

Holmes, R. J., Hocking, G. C., Forbes, L. K. & Baillard, N. Y. 2013 Waveless subcritical flow past symmetric bottom topography. *Eur. J. Appl. Math.* **24** (2), 213–230.

Lustri, C. J., McCue, S. W. & Binder, B. J. 2012 Free surface flow past topography: a beyond-all-orders approach. *Euro. J. Appl. Math.* **23** (4), 441–467.

Miksis, M., Vanden-Broeck, J.-M. & Keller, J. B. 1981 Axisymmetric bubble or drop in a uniform flow. *J. Fluid Mech.* **108**, 89–100.

Shelton, J., Milewski, P. & Trinh, P. H. 2021 On the structure of steady parasitic gravity-capillary waves in the small surface tension limit. *J. Fluid Mech.* **922**.

Shelton, J. & Trinh, P.H. 2022 Exponential asymptotics for steady parasitic capillary ripples on steep gravity waves. *J. Fluid Mech.* **939**.

Tuck, E. O. & Scullen, D. C. 1998 Tandem submerged cylinders each subject to zero drag. *J. Fluid Mech.* **364**, 211–220.

Vanden-Broeck, J.-M. & Tuck, E. O. 1985 Waveless free-surface pressure distributions. *J. Ship Res.* **29** (03), 151–158.

Xie, X. & Tanveer, S. 2002 Analyticity and nonexistence of classical steady Hele-Shaw fingers. *Commun. Pur. Appl. Math.* **56** (3), 353–402.

Appendix A. Inner analysis at the singularities $\sigma = \pm\mathrm{i}$

In order to determine the constant of integration of the amplitude function $\Phi(\sigma)$ from equation (3.10), knowledge of the inner solutions at the singularities $\sigma = \mathrm{i}$ and $\sigma = -\mathrm{i}$ is required. In this section, we study the inner boundary layer at both of these locations, for which matching with the inner limit of the outer solutions determines the constant of integration.

First, we note that in the outer region, where $\sigma = O(1)$, the asymptotic series first reorder whenever

$$\phi_0'(\sigma) \sim F^2\phi_1'(\sigma), \qquad y_1(\sigma) \sim F^2 y_2(\sigma), \qquad x_2(\sigma) \sim F^2 x_3(\sigma). \tag{A 1}$$

In substituting for the early orders of the asymptotic solutions specified in equations (3.2), (3.3), and (3.5), we see that each of (A 1) reorder in a boundary layer of the same width, given by $\sigma - a\mathrm{i} = O(F^{2/3})$. We thus introduce the inner variable, $\hat{\sigma}$, by the relation

$$\sigma - a\mathrm{i} = \hat{\sigma}F^{2/3}, \tag{A 2}$$

for which $\hat{\sigma} = O(1)$ in the inner region. Since the asymptotic series each reorder near the two locations of $\sigma = \mathrm{i}$ and $\sigma = -\mathrm{i}$, we have again used the notation $a = \pm 1$ to distinguish between these two cases.

Next, to determine the form of the inner solutions, we take the inner limit of the outer series expansions for ϕ', x, and y, by substituting for the inner variable $\hat{\sigma}$ defined in (A 2) and expanding as $F \to 0$. This yields

$$\phi' \sim \frac{1}{F^{2/3}}\left[-\frac{a\mathrm{i}\Gamma_{\mathrm{c}}}{2\pi}\frac{1}{\hat{\sigma}} + \cdots\right], \quad y \sim F^{2/3}\left[\frac{\Gamma_{\mathrm{c}}^2}{8\pi^2}\frac{1}{\hat{\sigma}^2} + \cdots\right], \quad x \sim a\mathrm{i} + F^{2/3}\left[\hat{\sigma} + \cdots\right], \tag{A 3}$$

where the omitted terms, represented by $(\cdots)$, are from the inner limit of lower order terms of the outer asymptotic expansion. For instance, the next term in the inner limit of ϕ' is of $O(F^{-2/3}\hat{\sigma}^{-4})$. The form of the inner limits in (A 3) motivates our definition of the inner solutions, $\hat{\phi}(\hat{\sigma})$, $\hat{y}(\hat{\sigma})$, and $\hat{x}(\hat{\sigma})$, through the equations

$$\phi' = -\frac{a\mathrm{i}\Gamma_{\mathrm{c}}}{2\pi F^{2/3}}\frac{\hat{\phi}(\hat{\sigma})}{\hat{\sigma}}, \qquad y = \frac{\Gamma_{\mathrm{c}}^2 F^{2/3}}{8\pi^2}\frac{\hat{y}(\hat{\sigma})}{\hat{\sigma}^2}, \qquad x = a\mathrm{i} + \hat{\sigma}F^{2/3}\hat{x}(\hat{\sigma}). \tag{A 4}$$

The form of the inner variables introduced in (A 4) ensures that the first term in the series expansion for their outer limit will be equal to unity. Furthermore, based on the form of the inner limit of the singulant, χ, from equation (3.8),

$$\chi \sim -\frac{4ai\pi^2}{3\Gamma_c^2}\hat{\sigma}^3 F^2, \tag{A 5}$$

the outer limit of the inner solutions will be a series expansion in inverse powers of $-4ai\pi^2\hat{\sigma}^3/(3\Gamma_c)$. We thus introduce the variable z, defined by

$$z = -\frac{4ai\pi^2}{3\Gamma_c^2}\hat{\sigma}^3, \tag{A 6}$$

to ensure that these series expansions are in inverse powers of z alone.

A.1. *Inner equation*

The leading order inner equations, as $F \to 0$, may now be derived by substituting (A 4) for the inner variables into the outer equations (2.5*a*)-(2.5*c*), yielding

$$\hat{y} - \hat{\phi}^2 = 0, \tag{A 7a}$$

$$\left(\hat{x} + 3z\hat{x}'\right)^2 - \left(\frac{1}{3z}\hat{y} - \frac{1}{2}\hat{y}'\right)^2 = 1, \tag{A 7b}$$

$$\hat{\phi}\left(\hat{x} - \frac{1}{6z}\hat{y}\right)\left(\hat{x} + 3z\hat{x}' - \frac{1}{3z}\hat{y} + \frac{1}{2}\hat{y}'\right) = 1. \tag{A 7c}$$

The inner solutions, $\hat{\phi}(z)$, $\hat{y}(z)$, and $\hat{x}(z)$, will satisfy equations (A 7*a*)-(A 7*c*). Rather than solve these inner equations exactly, knowledge of the inner solutions is only required under the outer limit of $z \to \infty$ in order to match with the inner limit of the outer solutions to determine their divergent form. Thus, we will consider the following series expansions for these inner unknowns,

$$\hat{\phi}(z) = \sum_{n=0}^{\infty}\frac{\hat{\phi}_n}{z^n}, \qquad \hat{y}(z) = \sum_{n=0}^{\infty}\frac{\hat{y}_n}{z^n}, \qquad \hat{x}(z) = \sum_{n=0}^{\infty}\frac{\hat{x}_n}{z^n}, \tag{A 8}$$

which hold as $z \to \infty$.

At leading order as $z \to \infty$ we have, by the definition on the inner solutions in equation (A 4),

$$\hat{\phi}_0 = 1, \qquad \hat{y}_0 = 1, \qquad \hat{x}_0 = 1. \tag{A 9}$$

Determination of $\hat{\phi}_n$, $\hat{y}_n$, and $\hat{x}_n$, as $n \to \infty$, requires the evaluation of a recurrence relation, which is now given. Firstly, substitution of expansions (A 8) into the inner equation (A 7*b*) yields

$$\hat{x}_1 = 0, \qquad 2(1-3n)\hat{x}_n = \frac{1}{36}\sum_{m=0}^{n-2}(2+3m)(2n-3m-4)\hat{y}_m\hat{y}_{n-m-2} + \sum_{m=1}^{n-1}(1-3m)(3n-3m-1)\hat{x}_m\hat{x}_{n-m}, \qquad \text{for } n \geqslant 2. \tag{A 10a}$$

Next, we substitute the same expansions into the inner equation (A 7c), yielding

$$\hat{\phi}_1 = \frac{1}{2}, \qquad \hat{\phi}_n = \sum_{m=2}^{n}\sum_{q=1}^{m-1} \frac{(3q-1)\hat{\phi}_{n-m}}{36}\Big(6\hat{x}_q - \hat{y}_{q-1}\Big)\Big(6\hat{x}_{m-q} - \hat{y}_{m-q-1}\Big)$$
$$- \sum_{m=1}^{n} \frac{\hat{\phi}_{n-m}}{6}\Big(6(2-3m)\hat{x}_m + (3m-2)\hat{y}_{m-1}\Big), \qquad \text{for } n \geqslant 2. \tag{A 10b}$$

Lastly, a recurrence relation for $\hat{y}_n$ is found from equation (A 7a) to be

$$\hat{y}_1 = 1, \qquad \hat{y}_n = \sum_{m=0}^{n} \hat{\phi}_m \hat{\phi}_{n-m}, \qquad \text{for } n \geqslant 2. \tag{A 10c}$$

Assuming that $\hat{\phi}_{n-1}$, $\hat{y}_{n-1}$, and $\hat{x}_{n-1}$ are known, $\hat{x}_n$ can be determined from equation (A 10a), which then yields a value for $\hat{\phi}_n$ from equation (A 10b). Lastly, $\hat{y}_n$ is found by evaluating equation (A 10c).

A.2. *Matching and determination of the constant* Λ

We now match the outer limit of the inner solution, $\hat{\phi}$, with the inner limit of the outer solution, ϕ'. In writing the outer limit of the inner solution in outer variables, we have

$$\phi' = \frac{-a\mathrm{i}\Gamma_\mathrm{c}}{2\pi} \sum_{n=0}^{\infty} \frac{F^{2n}\hat{\phi}_n}{\left(-\frac{4a\mathrm{i}\pi^2}{3\Gamma_\mathrm{c}^2}\right)^n (\sigma - a\mathrm{i})^{3n+1}}, \tag{A 11}$$

and for the inner limit of the outer solution,

$$\phi' = \sum_{n=0}^{\infty} F^{2n}\phi'_n \sim \sum_{n=0}^{\infty} -F^{2n}\chi'\Phi\frac{\Gamma(n+\alpha+1)}{\chi^{n+\alpha+1}}$$
$$\sim \sum_{n=0}^{\infty} -\frac{4\pi^2\Lambda}{\Gamma_\mathrm{c}^2(-a\mathrm{i})^{1/2}}\mathrm{e}^{\mathcal{P}(a\mathrm{i})} \frac{F^{2n}\Gamma(n+\alpha+1)}{\left(-\frac{4a\mathrm{i}\pi^2}{3\Gamma_\mathrm{c}^2}\right)^{n+\alpha+1}(\sigma - a\mathrm{i})^{3n+3\alpha-1/2}}. \tag{A 12}$$

In the above, the inner limit of the amplitude function Φ from equation (3.11) has been taken by defining

$$\mathcal{P}(\sigma) = \int_0^\sigma \left[\frac{a\mathrm{i}\phi_1'(t)}{[\phi_0'(t)]^3} - \frac{3}{2(t-a\mathrm{i})}\right]\mathrm{d}t, \tag{A 13}$$

such that $\mathcal{P}(\sigma) = O(1)$ as $\sigma \to a\mathrm{i}$. Matching (A 11) with (A 12), and substituting for $\alpha = 1/2$ from (3.13), determines the constant, Λ, as

$$\Lambda = \frac{a\mathrm{i}\mathrm{e}^{-\mathcal{P}(a\mathrm{i})}}{3\sqrt{3}} \lim_{n\to\infty}\left(\frac{\hat{\phi}_n}{\Gamma(n+\alpha+1)}\right). \tag{A 14}$$

PART II

Exponentially small instability of the equatorial Kelvin wave and divergent eigenvalue expansions


PART II
Exponentially small instability of th
equatorial Kelvin wave and divergent
eiegenvalue expansions

7 THE HERMITE-WITH POLE EQUATION

7.1 Introduction

In the exponential asymptotic study of chapter 4, we considered an asymptotic expansion for small surface tension ($B \to 0$) of a problem with an eigenvalue (the Froude number, F). In order to satisfy each order of the amplitude constraint, it was necessary to also expand the eigenvalue in asymptotic powers of the small parameter. Thus, in addition to expanding the solution as an asymptotic series, we also considered this eigenvalue to take the form

$$F = F_0 + BF_1 + \cdots + B^{N-1}F_{N-1} + \bar{F},$$

where $\bar{F}$ is the exponentially small remainder to the truncated base expansion, and $N = O(1/B)$. However the effects of F_{N-1} on the $O(B^{N-1})$ equation and $\bar{F}$ on the remainder equation were neglected. These effects are both considered in Appendix B. It is demonstrated in B.1 that F_n diverges as $n \to \infty$ in a factorial-over-power manner. Since these all take constant values and are real-valued, this precise determination of F_n and $\bar{F}$ is largely insignificant and serves only to demonstrate the theory that may be required in problems for which these eigenvalue expansions are important.

In this chapter, we consider a problem for which this is the case: the equatorial Kelvin wave instability, for which the small parameter ϵ is weak latitudinal shear. In considering travelling wave solutions of the form

$$u(y) = u(y)\mathrm{e}^{\mathrm{i}k(x-ct)},$$

the wavespeed, c, is an eigenvalue of the problem and must also be expanded as $\epsilon \to 0$ as

$$c = \underbrace{c_0 + \epsilon^2 c_1 + \cdots + \epsilon^{2(N-1)} c_n}_{\text{real valued}} + \underbrace{\bar{c}}_{\text{complex valued}}.$$

Here, while the base expansion for c is real-valued, the exponentially small component, $\bar{c}$, is complex-valued. This corresponds to an exponentially-small instability that destabilises the equatorial Kelvin wave.

We begin by developing the associated theory for the determination of this geophysical instability for the model *Hermite-with-pole* problem considered by Boyd and Natarov (1998). This analysis by Shelton et al. (2023a), presented in the next section, is quite technical and includes techniques beyond the scope of the exponential asymptotic introduction of chapter 4. One of these is the *higher-order Stokes phenomenon*, for which the late terms themselves of the asymptotic solution display the Stokes phenomenon. This can, and for this problem does, lead to inactive and partially active Stokes lines. Furthermore, the Stokes phenomenon displayed by the exponentially small component of the solution is induced by two different sources. In addition to the standard forcing introduced in chapter 4 from the divergent series, the exponentially-small component of the eigenvalue also produces an associated divergent expansion that contributes to the same Stokes phenomenon.

Appendix B: Statement of Authorship

This declaration concerns the article entitled:	
Pathological exponential asymptotics for a model problem of an equatorially trapped Rossby wave	
Publication status: Draft manuscript ● Submitted ☐ In review ☐ Accepted ☐ Published ☐	
Publication details	Authors - Josh Shelton, Jonathan Chapman, Philippe H. Trinh
Copyright status: The material has been published with a CC-BY license ☐ The publisher has granted permission to replicate the material included here ☐	
Candidate's contribution to the paper	All authors contributed equally to the conceptualisation and methodology used in the article (33%) Most analytical calculations were performed by the author of this thesis (90%) All numerical computations were performed by the author of this thesis (100%) The original draft and bulk of the final presentation has been written by the author of this thesis (80%)
Statement from Candidate	This paper reports on original research I conducted during the period of my Higher Degree by Research candidature.
Signed	**Date** 30/12/22

PATHOLOGICAL EXPONENTIAL ASYMPTOTICS FOR A MODEL PROBLEM OF AN EQUATORIALLY TRAPPED ROSSBY WAVE

JOSH SHELTON*, S. JONATHAN CHAPMAN†, AND PHILIPPE H. TRINH‡

Abstract. We examine a misleadingly simple linear second-order eigenvalue problem (the Hermite-with-pole equation) that was previously proposed as a model problem of an equatorially-trapped Rossby wave. In the singularly perturbed limit representing small latitudinal shear, the eigenvalue contains an exponentially-small imaginary part; the derivation of this component requires exponential asymptotics. In this work, we demonstrate that the problem contains a number of pathological elements in exponential asymptotics that were not remarked-upon in the original studies. This includes the presence of dominant divergent eigenvalues, non-standard divergence of the eigenfunctions, and inactive Stokes lines due to the higher-order Stokes Phenomenon. The techniques developed in this work can be generalised to other linear or nonlinear eigenvalue problems involving asymptotics beyond-all-orders where such pathologies are present.

Key words. Exponential asymptotics, beyond-all-orders analysis, Stokes phenomenon

AMS subject classifications.

1. Introduction. The motivation of this work stems from an interesting mathematical model that was proposed in 1998 by Boyd & Natarov [4] in order to describe equatorially-trapped Rossby waves when the mean shear flow is only a function of the latitude. In such cases, the eigenfunctions are modelled by the so-called *Hermite-with-pole* equation

$$\frac{\mathrm{d}^2 u}{\mathrm{d}z^2} + \left[\frac{1}{z} - \lambda - \left(z - \frac{1}{\epsilon}\right)^2\right] u = 0, \tag{1.1a}$$

$$u(z) \to 0 \quad \text{as} \quad z \to \pm\infty, \tag{1.1b}$$

$$u(0) = 1. \tag{1.1c}$$

Here, ϵ corresponds to the shear strength, u corresponds to a normal mode amplitude, and λ is an eigenvalue determined by the boundary condition at $z = 0$. Although this resembles the standard parabolic cylinder equation with Hermite functions as eigenfunctions, the pole at $z = 0$ lies in the interval of consideration. Boyd & Natarov consider the pole at $z = 0$ as emerging from a singularity in the analytic continuation, which approaches the real axis as viscosity tends to zero. As it turns out, the associated eigenvalue to (1.1a) is complex-valued; in the limit $\epsilon \to 0$, the eigenvalue contains an exponentially-small imaginary part, $\mathrm{Im}[\lambda] = O(\mathrm{e}^{-1/\epsilon^2})$. One of the aims of the analysis is to derive this exponentially-small eigenvalue component.

In their work, Boyd & Natarov [4] note that an asymptotic expansion of $u(z)$ in integer powers of ϵ diverges, and they develop a procedure for approximating $\mathrm{Im}[\lambda]$ with the use of an integral property from Sturm-Louville theory. Their approach relies upon the use of special functions theory and the niceties of the linear differential equation. In contrast, the emphasis of our work here will be on developing a framework that is applicable for more general differential equations—particularly for nonlinear problems where special functions theory is unavailable. Our goal is to study the divergence

*Department of Mathematical Sciences, University of Bath, BA2 7AY, UK
†Oxford Centre for Industrial and Applied Mathematics, Mathematical Institute, University of Oxford, OX1 3LB, UK
‡Department of Mathematical Sciences, University of Bath, BA2 7AY, UK

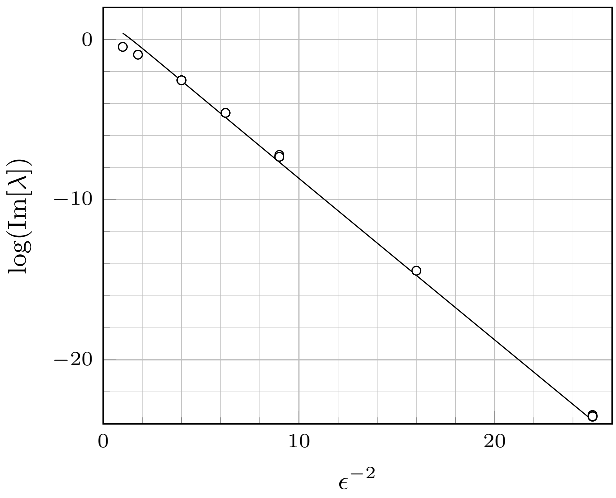

Fig. 1.1. *The imaginary component of the eigenvalue,* λ*, is shown for the numerical solutions of Boyd & Natarov [4] (circles) and the analytical prediction of Im*$[\lambda] = \sqrt{\pi}[1 - 2\epsilon\log(\epsilon) + \epsilon(\log(2)+\gamma)]\mathrm{e}^{-1/\epsilon^2}$ *(line). Here,* $\gamma \approx 0.577$ *is the Euler-Macheroni constant.*

of the asymptotic expansion for the eigenfunction and examine its connection, via the Stokes phenomenon, to the exponentially-small components. In §8 we discuss the significance in the application of techniques developed in this paper, both to the more complete geophysical problem discussed by Natarov & Boyd [15], as well as other problems involving singular perturbations.

For analysis, there is a more convenient form of (1.1a), which is found by shifting

$$y = z - \frac{1}{\epsilon}, \tag{1.2}$$

where now $y = 0$ corresponds to the equator. Then we have, for $u = u(y)$,

$$\frac{\mathrm{d}^2u}{\mathrm{d}y^2} + \left[\frac{\epsilon}{1+\epsilon y} - y^2\right]u = \lambda u. \tag{1.3}$$

This intermediary equation contains a turning point at $y = -1/\epsilon$ which we study by rescaling with $y = Y/\epsilon$. We then set $u(y) = \mathrm{e}^{-y^2/2}\psi(Y)$ which yields the system

$$\epsilon^2\psi'' - 2Y\psi' + \frac{\epsilon\psi}{1+Y} = (\lambda+1)\psi, \tag{1.4a}$$

$$\mathrm{e}^{-Y^2/2\epsilon^2}\psi(Y) \to 0 \quad \text{as} \quad Y \to \pm\infty, \tag{1.4b}$$

$$\psi(0) = 1. \tag{1.4c}$$

In (1.4a) and henceforth, we use primes (′) to denote differentiation in Y.

2. A roadmap of the methodology and main results. As it turns out, the Hermite-with-pole problem (1.4a) has a number of non-trivial elements that were not remarked upon in the original studies; the treatment of which has required the development of new techniques in exponential asymptotics. We explain some of these aspects in the context of singularly perturbed linear eigenvalue problems of the form (1.4a), $\mathcal{L}(\psi;\epsilon) = \lambda\psi$, although many of the same ideas apply more generally to nonlinear eigenvalue problems.

Firstly, asymptotic expansions for $\psi = \psi_0 + \epsilon\psi_1 + \cdots$ and $\lambda = \lambda_0 + \epsilon\lambda_1 + \cdots$ are sought, but these expansions are divergent and must be optimally truncated. The solution is then expressed as a truncated series with a remainder by considering

$$\psi(Y) = \sum_{n=0}^{N-1} \epsilon^n \psi_n(Y) + \mathcal{R}_N(Y), \tag{2.1}$$

with a similar expression for the eigenvalue, λ. When N is chosen optimally [later shown to be of $O(\epsilon^{-2})$] the remainder $\mathcal{R}_N(Y)$ is exponentially-small, and satisfies the linear eigenvalue problem of

$$\mathcal{L}(\mathcal{R}_{\mathcal{N}}; \epsilon) \sim -\epsilon^N \psi''_{N-2}. \tag{2.2}$$

The remainder, $\mathcal{R}_N$, will exhibit the Stokes Phenomenon, in which its magnitude rapidly varies across certain contours in the complex Y-plane. Indeed, as we shall show, this behaviour can be predicted by estimating the growth of the forcing term ψ''_{N-2}. Thus, the late-term behaviour of the divergent series, ψ_N with $N \to \infty$, is required in order to correctly resolve the Stokes phenomenon on the remainder $\mathcal{R}_N(Y)$. This 'decoding' of divergence is one of the hallmarks of exponential asymptotics.

One of our main results of this paper is that for the Hermite-with-pole problem, additional components of the late-term divergence, ψ_n, are required. It is well known, according to the principles of exponential asymptotics (cf. Chapman & Vanden-Broeck [9]) that the nth-order approximation of most singularly perturbed differential equations exhibits a factorial-power-divergence of a form similar to

$$\psi_n \sim \frac{Q(Y)\Gamma\left(\frac{n}{2} + \alpha\right)}{\chi(Y)^{\frac{n}{2}+\alpha}} \quad \text{as } n \to \infty, \tag{2.3}$$

where different problems may involve slight modifications to the above form. Thus for instance, the fractional coefficient of n that appears above may be modified to ensure the correct dominant balance arises in the equation. The functions Q and χ and the constant α prescribe the divergent behaviour.

However in this work we demonstrate that the Hermite-with-pole problem exhibits a very atypical divergence of the form

$$\psi_n \sim \begin{cases} \mathcal{S}(Y)\Big[L(Y)\log(n) + Q(Y)\Big]\dfrac{\Gamma(\frac{n}{2}+\alpha_0)}{\chi^{n/2+\alpha_0}} \\ \qquad\qquad + Q_0(Y)\log^2(n)\Gamma\left(\dfrac{n+1}{2} + \alpha_0\right) & \text{for } n \text{ even}, \\ \underbrace{\mathcal{S}(Y)}_{\text{HOSP}} \underbrace{R(Y)\dfrac{\Gamma(\frac{n}{2}+\alpha_1)}{\chi^{n/2+\alpha_1}}}_{\text{naive divergence}} + \underbrace{R_1(Y)\log(n)\Gamma\left(\dfrac{n+1}{2} + \alpha_1\right)}_{\chi'=0 \text{ divergence}} & \text{for } n \text{ odd}, \end{cases} \tag{2.4}$$

where the singulant, $\chi(Y)$, takes a value of zero at singularities in the early orders of the asymptotic expansion. This is also associated with a divergent eigenvalue of the form

$$\lambda_n \sim \begin{cases} \Big[\delta_0 \log(n) + \delta_1\Big]\Gamma\Big(\dfrac{n+1}{2} + \alpha_0\Big) & \text{for } n \text{ even}, \\ \delta_2\Gamma\Big(\dfrac{n+1}{2} + \alpha_1\Big) & \text{for } n \text{ odd}. \end{cases} \tag{2.5}$$

Once these components are derived, a procedure for the derivation of the exponentially-small remainders can be followed.

We now comment on the following pathologies related to (2.4) and (2.5):

1. *Divergent eigenvalues.*
Although exponential asymptotics has been applied to other eigenvalue problems (cf. Tanveer [20], Kruskal & Segur [14], Chapman & Kozyreff [7], and Shelton & Trinh [19]), in such cases, the eigenvalue divergence has not been noted as significant. In the present work, the divergence of λ_n affects the leading-order prediction of the eigenfunction divergence in (2.4), and is required to satisfy the associated boundary conditions on the late-term solution. We note that other problems for which a real-valued eigenvalue expansion has an imaginary beyond-all-orders component have been tacked by analysing special function solutions by Paris & Wood (1989) [16] and Brazel (1989) [5] for a model problem arising in optical tunnelling.
2. *Spurious singularities in the late-term approximation.*
It is known (cf. Dingle [11], Berry [1], Chapman *et al.* [6]) that typically, divergence of the late terms is captured by a factorial-over-power ansatz of the form displayed in (2.3). This factorial-over-power divergence is often taken as a universality of many problems in singularly perturbed asymptotics.
However, we find that in the Hermite-with-pole problem, an additional singularity beyond that of $Y = -1$ is predicted by the divergent ansatz. This misleadingly suggests that the late-order divergence of the asymptotic series is attributed to a point where no singularity appears in the early orders. This unusual aspect is associated with the following item.
3. *The higher-order Stokes Phenomena (HOSP).*
The Hermite-with-pole problem exhibits a pathology where the anticipated Stokes Phenomenon is suppressed in certain regions of the complex plane. This complexity is an example of the higher-order Stokes Phenomena, for which a general analytic understanding from the viewpoint of the divergent series has remained elusive (c.f. Howls et al. [13], Olde Daalhuis [10], Body et al. [2], and Chapman & Mortimer [8]). An introduction of the HOSP is given in §5.1, using the general analytical techniques developed by the current authors [17].
4. *Atypical boundary layers in the late terms.*
The factorial-over-power divergence (2.4) is unable to satisfy boundary condition (1.4c) at $Y = 0$, due to the functional prefactor growing without bound as $Y \to 0$. A boundary layer of vanishing size as $n \to \infty$ must be introduced, and the consideration of additional divergences with $\chi' = 0$, shown in (2.4), are required to satisfy the matching criteria.
5. *Even-and-odd pairing of the late terms.*
Consecutive terms in the asymptotic expansion exhibit different singular behaviour at $Y = -1$: one is purely algebraic, and the other is the product of a logarithmic and an algebraic singularity. Consequently the late-term representation (2.4) requires a different ansatz for n even and n odd.

It is the resolution of these complicated issues within that separates our work from the previous work by Boyd & Natarov [4]. In the end, despite its misleadingly simple form, the Hermite-with-pole problem turns out to be quite a pathological investigation of beyond-all-orders asymptotics.

3. An Initial Asymptotic Expansion. We begin by considering the asymptotic expansions

$$\psi(Y) = \sum_{n=0}^{\infty} \epsilon^n \psi_n(Y) \qquad \text{and} \qquad \lambda = \sum_{n=0}^{\infty} \epsilon^n \lambda_n. \tag{3.1}$$

At leading order in equation (1.4a) we find the solution $\psi_0 = C_0 Y^{-(1+\lambda_0)/2}$, where C_0 is a constant of integration. In general this solution is singular or contains a branch point at $Y = 0$. In order to apply the leading-order boundary condition of $\psi_0(0) = 1$ at the same location, a boundary layer should typically be considered. However, we can verify through an inner-matching procedure that the leading-order eigenvalue is $\lambda_0 = -1$. Then the boundary condition at $Y = 0$ gives $C_0 = 1$ and no boundary-layer theory is required. This yields our leading-order solution of

$$\psi_0 = 1 \qquad \text{and} \qquad \lambda_0 = -1. \tag{3.2}$$

We emphasise that the singularity at $Y = 0$ in the leading-order solution has been removed by the choice of the eigenvalue, $\lambda_0 = -1$. A similar argument will be applied in subsequent orders to enforce regularity of the solution at $Y = 0$.

At the next order, $O(\epsilon)$, of equation (1.4a), we find the solution

$$\psi_1 = C_1 + \frac{(1-\lambda_1)}{2}\log(Y) - \frac{1}{2}\log(1+Y), \tag{3.3}$$

which contains singularities at both $Y = 0$ and $Y = -1$. To apply the boundary condition $\psi_1(0) = 0$, we require $\lambda_1 = 1$, which then determines the constant of integration as $C_1 = 0$. Thus, our $O(\epsilon)$ solution is

$$\psi_1 = -\frac{1}{2}\log(1+Y) \qquad \text{and} \qquad \lambda_1 = 1. \tag{3.4}$$

Note that the above is singular at $Y = -1$. Since successive terms in the asymptotic series for ψ in (3.1) rely on repeated differentiation of previous terms, the logarithmic singularity will result in the divergence of the series for ψ_n as $n \to \infty$. It is this divergence that we wish to characterise. Note that in the $n \to \infty$ limit, on the assumption that ψ_n is divergent, there exists a dominant balance between the two terms $\epsilon^2\psi''$ and $-2Y\psi'$ of (1.4a). Thus, we must continue to derive additional early orders of the solution until the effects of the $\epsilon^2\psi''$ term become apparent. Since the singularity at $Y = -1$ in ψ_1 first appears at $O(\epsilon)$, the effects of this term will begin at $O(\epsilon^3)$.

The same procedure is applied at $O(\epsilon^2)$ and $O(\epsilon^3)$, for which we find the solutions

$$\psi_2 = \frac{1}{8}\log^2(1+Y), \qquad \lambda_2 = 0, \tag{3.5a}$$

$$\psi_3 = -\frac{Y}{4(1+Y)} - \frac{1}{48}\log^3(1+Y) - \frac{1}{4}\log(1+Y), \qquad \lambda_3 = \frac{1}{2}. \tag{3.5b}$$

Note that while the singularities at $Y = -1$ in ψ_1 and ψ_2 were logarithmic, the dominant singularity in ψ_3 is algebraic and of order unity. Typically the order of the singular behaviour of successive terms in the asymptotic series would increase linearly in a predictable fashion (see *e.g.* the work of Chapman *et al.* in [6]). This is not the case for our current problem, which can be seen by progressing to the next order, which has the solution

$$\psi_4 = -\frac{\log(1+Y)}{8(1+Y)} - \frac{Y}{8(1+Y)} + \frac{\log^4(1+Y)}{384} + \frac{\log^2(1+Y)}{8} \quad \text{and} \quad \lambda_4 = \frac{1}{4}. \tag{3.6}$$

From (3.5b) and (3.6), we find the singular scalings, as $Y \to -1$, of

$$\psi_3 \sim \frac{1}{4(1+Y)} \qquad \text{and} \qquad \psi_4 \sim \frac{-\log(1+Y)}{8(1+Y)}. \tag{3.7}$$

From this, we anticipate that the singular behaviour as $Y \to -1$ of the asymptotic series will proceed in the pairwise fashion of

$$\psi_{2k-1} = O\left(\frac{1}{(1+Y)^{k-1}}\right) \qquad \text{and} \qquad \psi_{2k} = O\left(\frac{\log(1+Y)}{(1+Y)^{k-1}}\right) \tag{3.8}$$

for integer $k \geq 2$, and hence the order of the algebraic singularity increases every other term. As it turns out, the above form in (3.8), which predicts the behaviour of the late-order terms as $Y \to -1$ and $n \to \infty$ also hints at the proper ansatz for $n \to \infty$ in general. In the late-term analysis that follows we will employ separate divergent predictions for ψ_n, distinguishing between the cases of n even and n odd.

4. Typical exponential asymptotics and the naive divergence. The goal of the exponential asymptotics procedure is to predict the exponentially-small eigenvalue and eigenfunction solutions. We shall see in §7 that these exponentially-small terms are connected to the divergence of the expansion (3.1).

Our task in this section is to derive the analytical form of the late terms of (3.1) in the limit of $n \to \infty$. For this, we follow the procedure of introducing an ansatz for the factorial-over-power divergence. However, this ansatz, given in equation (4.2) below, takes an unusual form due to the inclusion of a $\log(n)$ divergent scaling for even values of n. It is demonstrated in §4.1.2, through an inner analysis at the singularity, why the divergent ansatz must take this form.

At $O(\epsilon^n)$ in (1.4a), we have

$$\psi''_{n-2} - 2Y\psi'_n - \frac{Y}{1+Y}\psi_{n-1} = \lambda_3\psi_{n-3} + \cdots + \lambda_{n-1}\psi_1 + \lambda_n, \tag{4.1a}$$

and the boundary-condition of (1.4c) yields at $O(\epsilon^n)$

$$\psi_n(0) = 0. \tag{4.1b}$$

The late-order solutions, ψ_n, will contain a singularity at $Y = -1$ in the manner prescribed by equation (3.8). Moreover, since subsequent orders are determined by differentiation of earlier terms in the expansion, we anticipate that the divergence of the solution, introduced in (2.4), will be captured by the factorial-over-power ansatz,

$$\psi_n \sim \begin{cases} \Big[L(Y)\log(n) + Q(Y)\Big]\dfrac{\Gamma(\frac{n}{2}+\alpha_0)}{[\chi(Y)]^{n/2+\alpha_0}} & \text{for } n \text{ even}, \\[2ex] R(Y)\dfrac{\Gamma(\frac{n}{2}+\alpha_1)}{[\chi(Y)]^{n/2+\alpha_1}} & \text{for } n \text{ odd}. \end{cases} \tag{4.2}$$

As we have warned, the analysis to follow is quite involved. In essence, our first task is to derive the so-called *naive divergence* that appears in (2.4) and above in (4.2). This is done in §4.2 by considering the homogeneous form of the $O(\epsilon^n)$ equation. Before we do this, however, we shall motivate its unusual form by considering in the next section the outer limit of an inner solution at the boundary-layer near $Y = -1$.

4.1. Inner problem for the singularity of $Y=-1$. First, we note that the early orders of expansion (3.1) reorder as we approach the singularity at $Y=-1$. Instead of consecutive terms in the outer expansion reordering, those with an odd and even powers of ϵ will reorder amongst themselves. For instance, the reordering occurs with the odd terms for $\epsilon^3\psi_3 \sim \epsilon^5\psi_5$ and even terms for $\epsilon^4\psi_4 \sim \epsilon^6\psi_6$. Since $\psi_3 \sim (1+Y)^{-1}$ and $\psi_5 \sim (1+Y)^{-2}$ from the singular behaviour introduced in equation (3.8), we balance $(1+Y)^{-1} \sim \epsilon^2(1+Y)^{-2}$ to find the width of the boundary layer to be of $O(\epsilon^2)$. The same width is found by considering the even reordering. We thus introduce the inner-variable, $\hat{y}$, by the relation

$$(1+Y)=\epsilon^2\hat{y}, \tag{4.3}$$

for which $\hat{y}$ will be of $O(1)$ in the zone of consideration. The inner equation may then be derived by substituting for $\hat{y}$, giving

$$\frac{\mathrm{d}^2\hat{\psi}}{\mathrm{d}\hat{y}^2}+2(1-\epsilon^2\hat{y})\frac{\mathrm{d}\hat{\psi}}{\mathrm{d}\hat{y}}+\frac{\epsilon\hat{\psi}}{\hat{y}}=\epsilon^2(1+\lambda)\hat{\psi}, \tag{4.4}$$

where we denote the inner solution by $\hat{\psi}$.

4.1.1. Inner limit of the early orders. To motivate the correct form for the inner solution, we take the inner limit of the outer solution by substituting for $\hat{y}$ and expanding as $\epsilon \to 0$. This yields

$$\begin{aligned}\psi_{\text{outer}} \sim 1-\epsilon\log(\epsilon)+\epsilon\left[-\frac{\log(\hat{y})}{2}+\frac{1}{4\hat{y}}+\cdots\right]+\frac{\epsilon^2\log^2(\epsilon)}{2}\\ +\epsilon^2\log(\epsilon)\left[\frac{\log(\hat{y})}{2}-\frac{1}{4\hat{y}}+\cdots\right]+\epsilon^2\left[\frac{\log^2(\hat{y})}{8}-\frac{\log(\hat{y})}{8\hat{y}}+\frac{1}{8\hat{y}}+\cdots\right]+\cdots.\end{aligned} \tag{4.5}$$

More specifically, this is the six-term inner limit (since we neglect terms of order $\epsilon^3\log^3\epsilon$ after this limit has been taken) of the first five terms, up to and including ψ_4, of the outer expansion. The inclusion of further terms in the outer series would affect this result since they may reorder into terms of either $O(\epsilon)$ or $O(\epsilon^2)$. For instance, including ψ_5 would yield an extra term of $\epsilon\hat{y}^{-2}$ in (4.5).

4.1.2. Outer limit of the inner solution. In Appendix C, we solve the inner equation (4.4) by considering an inner solution, motivated by (4.5), of the form $\hat{\psi}=\hat{\psi}_0+\epsilon\log(\epsilon)\hat{\psi}_{(1,1)}+\epsilon\hat{\psi}_1+\epsilon^2\log^2(\epsilon)\hat{\psi}_{(2,2)}+\epsilon^2\log(\epsilon)\hat{\psi}_{(2,1)}+\epsilon^2\hat{\psi}_2$. In order to find the correct form for the outer solution, where $Y=O(1)$, we will write the inner solution from (C.1) in outer variables by substituting for $\hat{y}=(1+Y)/\epsilon^2$ from (4.3). This outer limit (of the first six terms of the inner series) yields

$$\begin{aligned}\hat{\psi} \sim 1-\epsilon\frac{\log(1+Y)}{2}+\epsilon^2\frac{\log^2(1+Y)}{8}+\sum_{k=1}^{\infty}\frac{\epsilon^{1+2k}}{2}\frac{\Gamma(k)}{[2(1+Y)]^k}\\ +\sum_{k=1}^{\infty}\frac{\epsilon^{2+2k}}{4}\frac{[4b_k-\log(1+Y)\Gamma(k)]}{[2(1+Y)]^k}.\end{aligned} \tag{4.6}$$

In the above, the divergent constant b_k is determined by the recurrence relation (C.9). This may be solved under the limit of $k\to\infty$, as performed in (C.12), to find $b_k \sim \frac{1}{2}(\log(k)+\gamma)\Gamma(k)$. It is this extra factor of $\log(k)$ in the expansion for b_k that causes the unusual $\log(n)$ divergent form introduced in (4.2). In order to compare (4.6) with the late-terms of the outer solution at $O(\epsilon^n)$, we substitute $n = 1 + 2k$ for the first sum on the right-hand side of (4.6) and $n = 2 + 2k$ for the second. The $O(\epsilon^n)$ of this outer limit yields

$$\hat{\psi} \sim \begin{cases} \epsilon^n \left[\dfrac{1}{2}\log(n) + \dfrac{\gamma - \log(2)}{2} - \dfrac{1}{4}\log(1+Y) \right] \dfrac{\Gamma(\frac{n}{2}-1)}{[2(1+Y)]^{\frac{n}{2}-1}} & \text{for } n \text{ even,} \\ \dfrac{\epsilon^n}{2} \dfrac{\Gamma(\frac{n-1}{2})}{[2(1+Y)]^{\frac{n-1}{2}}} & \text{for } n \text{ odd,} \end{cases} \tag{4.7}$$

where we expanded $b_{n/2-1} \sim \frac{1}{2}[\log(n) + \gamma - \log(2)]\Gamma(\frac{n}{2} - 1)$ for $n \to \infty$ as in (C.12).

To summarise, the goal of the analysis in this section was to characterise the outer limit of the inner solution, near $Y = -1$. Having done so, we have obtained (4.7). This form motivates the dominant scaling of $\log(n)$ for even values of n that we had previously introduced in the factorial-over-power ansatz (4.2). We are now ready to return to study the divergence of the outer solution.

4.2. Divergence of the homogeneous late-term equation. From the $O(\epsilon^n)$ equation (4.1a), we begin by considering solutions to the homogeneous equation

$$\psi''_{n-2} - 2Y\psi'_n - \frac{Y}{1+Y}\psi_{n-1} = \lambda_3\psi_{n-3} + \cdots . \tag{4.8}$$

Here, we have removed the inhomogeneous terms on the right-hand side, such as $\lambda_n\psi_0$. Later in §6, these terms will be seen to produce particular solutions that are subdominant as $n \to \infty$ near the singularity of $Y = -1$. In order for the divergent ansatz from (4.2) to match with the outer limit of the inner solution from (4.7) we must have

$$\alpha_0 = -1 \qquad \text{and} \qquad \alpha_1 = -\frac{1}{2}. \tag{4.9}$$

Next, we substitute the factorial-over-power ansatz (4.2) into the homogeneous equation (4.8). Once we have done so, the dominant behaviour of the terms in the equation are then of $O(\log(n)\Gamma(n/2)/\chi^{n/2})$ for n even and $O(\Gamma(\frac{n+1}{2})/\chi^{\frac{n+1}{2}})$ for n odd. We divide out by the factorial-over-power component of these scalings, and this results in an equation with terms of orders $O(1)$, $O(n^{-1})$, and so forth for n odd, and $O(\log n)$, $O(1)$, $O(n^{-1}\log n)$, $O(n^{-1})$ and so forth for n even.

At leading order as $n \to \infty$, the same equation is found for both cases of n even or odd, and this provides an equation for the singulant function, $\chi(Y)$, given by

$$\chi'(\chi' + 2Y) = 0, \tag{4.10}$$

of which there are two solutions. The singular behaviour of ψ_n will be captured by the non-trivial solution, $\chi' = -2Y$. We require $\chi(-1) = 0$ in order to match with the inner solution near the singularity from (4.7). Thus we obtain

$$\chi(Y) = 1 - Y^2. \tag{4.11}$$

Equations for the functional prefactors, $L(Y)$, $R(Y)$, and $Q(Y)$, of the divergent ansatz are now found by considering the subsequent orders in n of equation (4.8). At $O(n^{-1}\log n)$ for n even we find an equation for $L(Y)$. Similarly, the $R(Y)$ and $Q(Y)$

equations are found at $O(n^{-1})$ for the cases of n odd and n even, respectively. These equations are

$$L'(Y) + \frac{1}{Y}L(Y) = 0, \qquad R'(Y) + \frac{1}{Y}R(Y) = 0, \tag{4.12a}$$

$$Q'(Y) + \frac{1}{Y}Q(Y) = \frac{R(Y)}{2(1+Y)} + \frac{2YL(Y)}{1-Y^2}, \tag{4.12b}$$

which may be integrated directly to find the solutions

$$L(Y) = \frac{\Lambda_{\mathrm{L}}}{Y}, \qquad R(Y) = \frac{\Lambda_{\mathrm{R}}}{Y}, \tag{4.13a}$$

$$Q(Y) = \frac{\Lambda_{\mathrm{Q}}}{Y} + \frac{\Lambda_{\mathrm{R}}}{2Y}\log(1+Y) - \frac{\Lambda_{\mathrm{L}}}{Y}\log\left(1-Y^2\right). \tag{4.13b}$$

Above, Λ_{L}, Λ_{R}, and Λ_{Q} are constants of integration.

Substitution of these solutions for $L(Y)$, $R(Y)$, and $Q(Y)$ from equations (4.13a) and (4.13b) back into the ansatz (4.2) gives our divergent prediction for ψ_n, with $n \to \infty$ as

$$\psi_n \sim \begin{cases} \left[\frac{\Lambda_{\mathrm{L}}}{Y}\log(n) + \left(\frac{\Lambda_{\mathrm{Q}}}{Y} + \frac{\Lambda_{\mathrm{R}}}{2Y}\log(1+Y) \right.\right. & \\ \qquad \left.\left. - \frac{\Lambda_{\mathrm{L}}}{Y}\log\left(1-Y^2\right)\right)\right] \dfrac{\Gamma(\frac{n}{2}-1)}{[\chi(Y)]^{n/2-1}} & \text{for } n \text{ even}, \\ \dfrac{\Lambda_{\mathrm{R}}}{Y}\dfrac{\Gamma(\frac{n-1}{2})}{[\chi(Y)]^{(n-1)/2}} & \text{for } n \text{ odd}. \end{cases} \tag{4.14}$$

We will refer the late-order form of (4.14) as corresponding to the *naive divergence*. There are two noticeable issues present:

1. The boundary condition, $\psi_n(0) = 0$, is unable to be satisfied as our current form is unbounded at $Y = 0$;
2. There are additional locations at which the singulant, $\chi(Y)$, is equal to zero. Since $\chi(Y) = 1 - Y^2$, our late term expression predicts singularities at both $Y = -1$ and $Y = 1$. This is in contrast to the early orders of the expansion, which are singular at $Y = -1$ only.

The first of these issues will be resolved in §6.1. There, we demonstrate that as $n \to \infty$, a boundary layer emerges in the late-order solution near $Y = 0$. This boundary layer is of diminishing width as $n \to \infty$. A matched asymptotic approach then allows us to develop an inner solution that satisfies the boundary condition of $\psi_n(0) = 0$.

Regarding the the second issue, we demonstrate in §5 that the late terms (4.14) in fact switch off for $Y > 0$ as a surprising consequence of the higher-order Stokes Phenomenon. This unusual phenomenon is linked to the presence of the additional divergent component of the solution corresponding to $\chi = 0$ from the singulant equation (4.10).

4.3. Determination of the constants Λ_{L}, Λ_{R}, and Λ_{Q}. It remains to find values for the three constants Λ_{L}, Λ_{R}, and Λ_{Q} that appear in the late-term solution for ψ_n in (4.14). These are determined through matching with the outer limit of the inner solution about the singularity at $Y = -1$ given in equation (4.7). Expanding the outer solution for ψ_n from (4.14) as $Y \to -1$, we have

$$\psi_n \sim \begin{cases} \Bigg[-\Lambda_{\mathrm{L}} \log(n) + \Bigg(\Lambda_{\mathrm{L}} \log(2) - \Lambda_{\mathrm{Q}} \\ \qquad + \Big[\Lambda_{\mathrm{L}} - \dfrac{\Lambda_{\mathrm{R}}}{2} \Big] \log(1+Y) \Bigg) \Bigg] \dfrac{\Gamma(\frac{n}{2}-1)}{[2(1+Y)]^{n/2-1}} & \text{for } n \text{ even}, \\ -\Lambda_{\mathrm{R}} \dfrac{\Gamma(\frac{n-1}{2})}{[2(1+Y)]^{(n-1)/2}} & \text{for } n \text{ odd}. \end{cases} \tag{4.15}$$

This form may now be compared to the outer limit of the inner solution in (4.7) to find the following solutions for the constant prefactors of the factorial-over-power solution of

$$\Lambda_{\mathrm{R}} = -\frac{1}{2}, \qquad \Lambda_{\mathrm{L}} = -\frac{1}{2}, \qquad \Lambda_{\mathrm{Q}} = -\frac{\gamma}{2}, \tag{4.16}$$

for which $\gamma \approx 0.577$ is the Euler-Macheroni constant.

5. Stokes lines and the higher-order Stokes phenomenon. The main goal of this section is to discuss the unusual arrangement of Stokes lines in this problem, and to explain the connection with the higher-order Stokes Phenomena. As we know from the works of *e.g.* Dingle [11], Boyd [3], and Chapman *et al.* [6], Stokes lines are expected along the contours that satisfy

$$\mathrm{Im}[\chi(Y)] = 0 \quad \text{and} \quad \mathrm{Re}[\chi(Y)] \geq 0, \tag{5.1}$$

with $Y \in \mathbb{C}$. Here the singulant function, χ, from (4.11) is given by $\chi = 1 - Y^2$. With this, equations (5.1) yields Stokes lines along the real axis between -1 and 1, and along the entire imaginary axis; this is shown in figure 5.1. We note that the

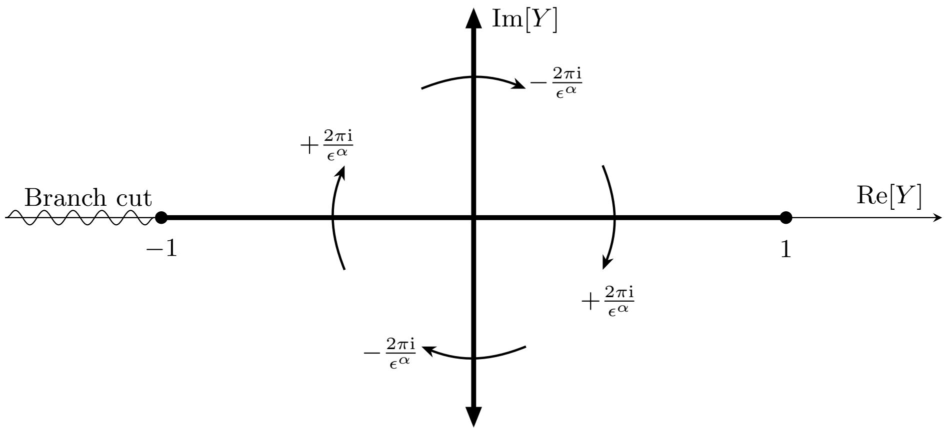

FIG. 5.1. *Classical Stokes lines predicted by the naive divergence with $\chi = 1 - Y^2$. The structure is unusual, and contains both a segment along the real axis with $Y \in [-1, 1]$, but also an infinite line along the imaginary axis.*

arrangement seen is unusual—in previous works on exponential asymptotics, Stokes lines can typically be traced back to the originating singularity along a smooth curve; this is in contrast to what occurs here at the origin, $Y = 0$.

According to the exponential asymptotics theory, a remainder to the regular asymptotic solution (3.1) will contain exponentially-small terms in ϵ that rapidly switch-on or switch-off in magnitude across the Stokes lines. This switching, known as the *Stokes Phenomenon*, occurs within a boundary layer about the Stokes line with diminishing width as $\epsilon \to 0$; the analytical derivation of this transition was first given by Berry [1] in 1989. We shall review the derivation of the exponentially-small terms and discuss its impact on the current problem in §7.

However, there currently exists a glaring issue with our current factorial-over-power prediction in (4.14). This concerns the apparent presence of an additional singularity at $Y = 1$ (at which $\chi = 1 - Y^2$ is zero). Note that because the perturbative procedure of §3 is linear, singularities in the late terms must either arise in the early asymptotic orders [cf. (3.6)], or must appear as singularities or turning points of the differential equation. Here, $Y = 1$ is neither, and so we expect the late terms to be regular at this point. In addition, we may verify that a singularity at $Y = 1$ is not seen to develop in the exact solution for ψ_n obtained up to $n = 50$ using a symbolic programming language. As it turns out, our late-term solution (4.14) is invalid in a region of the complex plane, including $Y = 1$, due to the higher-order Stokes Phenomena—this is explained in §5.1.

In fact, we can provide evidence of the correct form for ψ_n from this numerical study. In figure A.2, we plot ψ_n evaluated at $Y = -1/2$ and $Y = 1/2$ up to $n = 50$. We

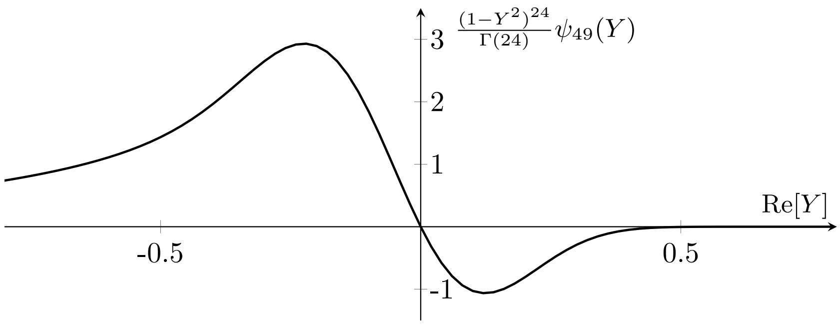

FIG. 5.2. *The* 49*th order solution,* ψ_{49}*, computed using a symbolic programming language in Appendix A, is shown for real values of* Y *(bold line). The anticipated factorial-over-power scaling has been divided out.*

see that the asymptotic solution diverges in the predicted factorial-over-power manner at $Y = -1/2$ for A.2(a). However, a different scaling is observed at $Y = 1/2$ in A.2(b); this is the purely factorial divergence attributed to the additional late-order terms with $\chi' = 0$ introduced briefly in (2.4). We thus conclude that the naive divergence has “switched off” somewhere between these two points. Further study of this divergence demonstrates that this change occurs about a boundary-layer along the imaginary axis. We thus believe that, for a general point $Y \in \mathbb{C}$, the corrected form to (4.14) should be

$$\psi_n \sim \begin{cases} \mathcal{S}(Y)\Big(L(Y)\log(n) + Q(Y)\Big)\dfrac{\Gamma(\frac{n}{2}-1)}{\chi^{n/2-1}} & \text{for } n \text{ even,} \\ \mathcal{S}(Y)R(Y)\dfrac{\Gamma(\frac{n-1}{2})}{\chi^{(n-1)/2}} & \text{for } n \text{ odd,} \end{cases} \tag{5.2}$$

where $\mathcal{S}(Y)$ is the Stokes smoothing function shown in figure 5.3, that takes a value of $\mathcal{S}(Y) = 1$ for $Y < 0$ and $\mathcal{S}(Y) = 0$ for $Y > 0$. This form displays Stokes phenomenon in the late terms themselves, which is one sign of the higher-order Stokes Phenomena, which we discuss next.

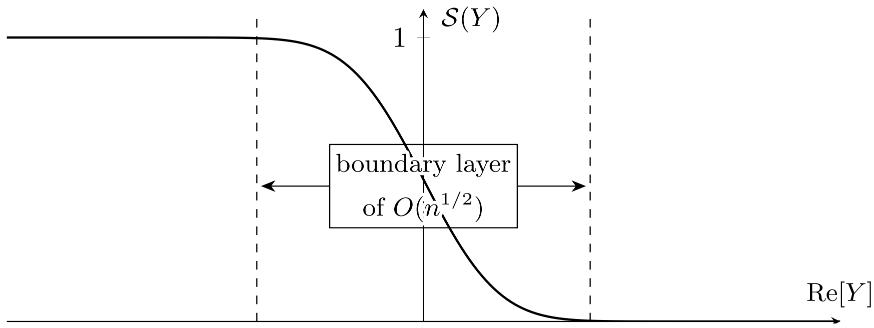

FIG. 5.3. *The Stokes prefactor, $\mathcal{S}(Y)$ is shown along the real Y-axis. This transitions from a value of* 1 *to* 0 *across a boundary layer of diminishing width as $n \to \infty$.*

5.1. An overview of the higher-order Stokes Phenomena. The higher-order Stokes phenomenon (HOSP) concerns two connected phenomena that often arise in the study of singularly perturbed problems with multiple turning points or singularities. These are:

1. *Stokes switching of the late-terms of an asymptotic series.*
Typically, the Stokes phenomenon occurs on exponentially-small components of the asymptotic solution due to the forcing of a divergent Poincare series. However, the late-terms of a divergent series are occasionally observed to undergo a similar phenomena in which they too rapidly change in magnitude across certain contours in the complex plane (higher-order Stokes lines). The link between this behaviour, studied by Mortimer & Chapman [8] for instance by analysing a recurrence relation as $n \to \infty$, and divergence remains elusive. We demonstrate in §5.2 that this Stokes switching on the late-terms is linked to a further divergent series in powers of n^{-1} appearing in the late-term representation of the solution. This new divergent component may contain additional singularities in the functional prefactor of its factorial-over-power approximation. Thus, lower-order terms, in n, of the late-terms contain stronger singular behaviour, and this forces a new divergent series (in n) at each order of the original divergent series. The optimal truncation and Stokes smoothing analysis, to be performed in future work by the current authors [17], provides an analytical link between the HOSP on the late-terms and the concept of divergence.
2. *Inactive (or partially active) Stokes lines.*
The Stokes lines naively predicted by enforcing the Dingle conditions (5.1) on the singulant, χ, found from the late-terms are often seen to be inactive. This is the behaviour studied by *e.g.* Howls *et al.* [13] and Honda *et al.* [12]. It is related to item (1), since if the late-terms have been switched off due to the HOSP across the higher-order Stokes lines, then they are no longer present to induce the classical Stokes phenomenon. A Stokes line is termed inactive if it passes through these regions. Furthermore, if a Stokes line intersects with a higher-order Stokes line, across which the late-terms can no longer be assumed constant, then it is denoted to be partially-active since the late-terms are partially present across this boundary layer, which results in a non-standard Stokes smoothing function.

In general, the conditions for a higher-order Stokes line generated by two different singulants, χ_1 and χ_2, are

$$\mathrm{Im}[\chi_1] = \mathrm{Im}[\chi_2] \qquad \text{and} \qquad \mathrm{Re}[\chi_1] \geq \mathrm{Re}[\chi_2]. \tag{5.3}$$

Since one of our singulants takes the value of unity and the other is $\chi = 1 - Y^2$, the conditions for our problem are

$$\mathrm{Im}[-Y^2] = 0 \qquad \text{and} \qquad \mathrm{Re}[-Y^2] \geq 0, \tag{5.4}$$

which confirms that the higher-order Stokes lines for our problem lie along the imaginary axis. We now motivate conditions (5.4) analytically in the next section.

5.2. Resolution of the higher-order Stokes Phenomena. It is possible to analytically derive the Stokes-switching behaviour encountered in the late-terms due to the HOSP. However, on account of the many complications arising in our Hermite-with-pole problem, these techniques are easiest understood when applied to a simpler problem displaying the HOSP, which has been the focus of present work by the some of the current authors [17]. A simplified overview of this procedure is now presented.

There exists additional components of the late-term solution characterised by $\chi' = 0$, which we briefly introduced in (2.4). These have $\chi = 1$ and take a form analogous to

$$\psi_n \sim R(Y)\Gamma(n/2 + \alpha), \qquad \text{where} \qquad R(Y) \sim \frac{\text{const.}}{Y} \quad \text{as} \quad n \to \infty. \tag{5.5}$$

These contain a singularity at $Y = 0$ in the prefactor, $R(Y)$. One can also derive lower orders (in n) of the late-term divergence, which we preform in Appendix B, by expanding

$$R(Y) \sim R_0(Y) + \frac{\log{(n)}}{n} M_1(Y) + \frac{R_1(Y)}{n} + \cdots. \tag{5.6}$$

The power of the singularity at $Y = 0$ grows as we proceed into this new series. This forces the divergence of the series, which must be optimally truncated. This yields

$$R(Y) \sim R_0(Y) + \frac{\log{(n)}}{n} M_1(Y) + \frac{R_1(Y)}{n} + \cdots + \frac{R_p(Y)}{n^p} + \mathcal{R}(Y), \tag{5.7}$$

where the new series diverges, on account of the singularity at $Y = 0$, as

$$R_p(Y) \sim \frac{\tilde{R}(Y)\Gamma(p + \tilde{\alpha})}{\tilde{\chi}^{p+\tilde{\alpha}}}, \tag{5.8}$$

with $\tilde{\chi} = -Y^2$. Since the divergence (5.8) is generated by the solution (5.5), which had $\chi' = 0$, $\tilde{R}(Y)$ will satisfy the same equation as that found for the prefactor of the $\chi = 1 - Y^2$ late-terms.

Next, we study the exponentially-small remainder, $\mathcal{R}(Y)$, appearing in expansion (5.7). Since this is the remainder to the late-term difference equation, as opposed to the standard Stokes smoothing procedure which acts on a differential equation, the exponentially-small solution will be of the following atypical form,

$$\mathcal{R}(Y) = \mathcal{S}(Y)\tilde{R}(Y)\exp\bigg(-\frac{n}{2}\log{(1 - Y^2)}\bigg). \tag{5.9}$$

Note that while the singulant appearing in (5.9) satisfies the same equation as that for the late-late-terms, $\tilde{\chi}' = -2Y$, the constant of integration differs as now we require $\log(\tilde{\chi}(0)) = 0$ as opposed to $\tilde{\chi}(0) = 0$.

The exponentially-small solution in (5.9) displays the Stokes phenomenon through the function $\mathcal{S}(Y)$, about boundary layers of diminishing width as $n \to \infty$. Substitution into (5.5) then yields

$$\psi_n = \mathcal{S}(Y)\tilde{R}(Y)\frac{\Gamma(n/2+\alpha)}{(1-Y^2)^{n/2}}. \tag{5.10}$$

This is the Stokes switching present in the late terms that we are searching for. Note that the conditions for a higher-order Stokes line are derived by enforcing the Dingle criteria on $\tilde{\chi} = -Y^2$, which yields (5.4).

To summarise, the late-term switching is caused by other components of the late terms, for which an expansion in powers of $1/n$ diverges on account of additional singular points. When this new series is optimally truncated, the remainder displays the Stokes phenomenon.

5.3. Inactive Stokes lines. We demonstrated in §5.1 that there are higher-order Stokes lines along the imaginary axis. Within the vicinity of these, the naive divergence of ψ_n will smoothly switch off as we transition from $Y < 0$ to $Y > 0$. Since the form of the late-terms now differs significantly from that used to generate the initial Stokes lines of figure 5.1, this structure may change. The main effects of the HOSP on the Stokes line structure for the exponentially-small terms in ϵ will be:

1. *An inactive Stokes line*
   Since the non trivial components of the late-terms have been switched off in the sector containing the Stokes line between $Y = 0$ and $Y = 1$, they are no longer present to induce the classical Stokes phenomenon. We thus refer to this segment of the Stokes line as being inactive.
2. *Partially-active Stokes lines*
   The Stokes lines along the imaginary axis coincide with the higher-order Stokes lines. Across these, the late-terms with $\chi = 1 - Y^2$ transition from $\mathcal{S}(Y) = 1$ to $\mathcal{S}(Y) = 0$. Since the late-terms are now partially present across this Stokes line, it too will be partially-active when considering its contribution to the classical Stokes phenomenon. It is anticipated that the switching contribution arising from this Stokes line will be halved due to this. We will refer to this segment of the Stokes line as being half-active.

Later in §7.1 we incorporate both of these effects in figure 7.1, in which the Stokes lines associated with the base asymptotic series are shown.

6. The late-term boundary layer at $Y = 0$. Recall that in the early orders of the expansion, each order of the eigenvalue was determined by enforcing the boundary condition at $Y = 0$. Similarly, we anticipate that the late-terms of the eigenvalue, λ_n, will also be determined by applying the boundary condition on the late-term solution, ψ_n. However, our current form for the naive divergence in (5.2) is unbounded at $Y = 0$ and can not satisfy the condition of $\psi_n(0) = 0$ from (4.1b).

In fact, there is a boundary layer about $Y = 0$ that must be considered to enforce the boundary condition and correctly determine λ_n. This boundary layer arises as a consequence of the singularity in the late-terms at $Y = 0$. In considering lower-order solutions by expanding the functional prefactor as $R_0(Y) + n^{-1}\log(n)M_1(Y) + n^{-1}R_1(Y) + \cdots$ for odd values of n, we will see that the singularity in the leading order, of the form $R_0 \sim Y^{-1}$, forces a stronger singularity at the next order, that behaves as $R_1 \sim Y^{-3}$. Thus, this series reorders as $Y = 0$ is approached. We will demonstrate that additional components of the late-term solution are required, with a constant value of the singulant, in order to satisfy the matching criteria. the solutions with $\chi' = 0$ arise from both the $\chi' = 0$ homogeneous solution previously neglected in (4.10) as well as the particular solution which balances with λ_n in the late term equation (4.1a).

6.1. Reordering of the late-terms as $Y \to 0$. In order to determine the width of this boundary layer in the late-term solution, we introduce in Appendix B a factorial-over-power ansatz of the form

$$\psi_n \sim \begin{cases} \left[L_0(Y)\log(n) + Q_0(Y) + \dfrac{\log(n)}{n} L_1(Y) + \cdots\right] \dfrac{\Gamma(\frac{n}{2}-1)}{\chi^{n/2-1}} & \text{for } n \text{ even}, \\ \left[R_0(Y) + \dfrac{\log(n)}{n} M_1(Y) + \dfrac{R_1(Y)}{n} + \cdots\right] \dfrac{\Gamma(\frac{n-1}{2})}{\chi^{(n-1)/2}} & \text{for } n \text{ odd}. \end{cases} \tag{6.1}$$

Here, the leading order solutions of $L_0(Y)$, $R_0(Y)$, and $Q_0(Y)$ have the same solution as $L(Y)$, $R(Y)$, and $Q(Y)$ derived previously in (4.13a) and (4.13b). The solutions of $M_1(Y)$, $L_1(Y)$, and $R_1(Y)$ are presented in equations (B.3) and (B.4). For the purposes of observing the reordering of these series near $Y = 0$, it is sufficient to display only their singular behaviour here, of the form

$$L_0 \sim \frac{\Lambda_{\mathrm{L}}}{Y}, \qquad L_1 \sim \frac{\Lambda_{\mathrm{L}}}{Y^3}, \qquad R_0 \sim \frac{\Lambda_{\mathrm{R}}}{Y}, \qquad R_1 \sim \frac{\Lambda_{\mathrm{R}}}{Y^3}. \tag{6.2}$$

The series expansions of ψ_n reorder when the two consecutive terms in each of (6.1) are of the same order as $n \to \infty$. This occurs for

$$Y = O(n^{-1/2}),$$

from which we introduce the inner variable $\hat{y}$ by the relation

$$\hat{y} = n^{1/2} Y. \tag{6.3}$$

The inner limit of the outer late-term solution ψ_n may now be found by writing equation (5.2) in terms of the inner variable $\hat{y}$ and taking $n \to \infty$. We note here that this procedure is subtly different from that considered for the other boundary layer at $Y = -1$, as in this case the inner limit of the singulant contributes to the leading-order solution. With $\chi = 1 - Y^2$, we have

$$(1 - Y^2)^{-n/2} = \left(1 - \frac{\hat{y}^2}{n}\right)^{-n/2} \sim \mathrm{e}^{\hat{y}^2/2} \quad \text{as} \quad n \to \infty, \tag{6.4}$$

where this last result arises from the limit definition of the exponential function. Furthermore, the scaling of $Q(Y) \sim Y^{-1}$ will increase the argument of the gamma function by one half. We therefore find

$$\psi_n \sim \begin{cases} \mathcal{S}(\hat{y})\left[-\dfrac{\log(n)}{\sqrt{2}} - \dfrac{\gamma}{\sqrt{2}}\right] \dfrac{\mathrm{e}^{\hat{y}^2/2}}{\hat{y}} \Gamma\left(\dfrac{n-1}{2}\right) & \text{for } n \text{ even}, \\ -\mathcal{S}(\hat{y}) \dfrac{1}{\sqrt{2}} \dfrac{\mathrm{e}^{\hat{y}^2/2}}{\hat{y}} \Gamma\left(\dfrac{n}{2}\right) & \text{for } n \text{ odd}. \end{cases} \tag{6.5}$$

Here, we have taken the (Van-Dyke) inner limit of two terms in the outer solution for even values of n, written in inner variables to two terms. For odd values of n we have taken the one-term inner limit, written to a single term in the inner expansion. The form of (6.5) hints at the required form of the inner solution near $Y = 0$.

6.2. Inner equation. Substituting the inner variable, $\hat{y} = n^{1/2}Y$, into the $O(\epsilon^n)$ outer equation (4.1a) yields the inner equation

$$n\frac{\mathrm{d}^2\hat{\psi}_{n-2}}{\mathrm{d}\hat{y}^2} - 2\hat{y}\frac{\mathrm{d}\hat{\psi}_n}{\mathrm{d}\hat{y}} + \frac{\hat{y}}{n^{1/2}}\left(1+\frac{\hat{y}}{n^{1/2}}\right)^{-1}\hat{\psi}_{n-1} = \lambda_3\hat{\psi}_{n-3} + \cdots + \lambda_{n-1}\hat{\psi}_1 + \lambda_n. \quad (6.6)$$

Here, $\hat{\psi}_1 = -\frac{1}{2}\log(1+n^{-1/2}\hat{y}) \sim -\frac{1}{2}n^{-1/2}\hat{y}$.

6.3. An Inner solution. We now consider an inner solution to equation (6.6) with the ansatz

$$\hat{\psi}_n \sim \begin{cases} \left[\widehat{L}(\hat{y})\log(n) + \widehat{Q}(\hat{y})\right]\Gamma\left(\frac{n-1}{2}\right) & \text{for } n \text{ even}, \\ \widehat{R}(\hat{y})\Gamma\left(\frac{n}{2}\right) & \text{for } n \text{ odd}. \end{cases} \quad (6.7)$$

Since the divergent eigenvalues, λ_n, will appear as a forcing term in the equations for $\widehat{L}(\hat{y})$, $\widehat{Q}(\hat{y})$, and $\widehat{R}(\hat{y})$, we introduce a similar ansatz for their form, given by

$$\lambda_n \sim \begin{cases} \left[\delta_0\log(n) + \delta_1\right]\Gamma\left(\frac{n-1}{2}\right) & \text{for } n \text{ even}, \\ \delta_2\Gamma\left(\frac{n}{2}\right) & \text{for } n \text{ odd}. \end{cases} \quad (6.8)$$

Substituting (6.7) and (6.8) into the inner equation (6.6), and isolating the dominant factorial divergence of $\Gamma(\frac{n}{2})$ for n odd and $\Gamma(\frac{n-1}{2})$ for n even, yields at leading order the equations

$$\widehat{R}'' - \hat{y}\widehat{R}' = \frac{\delta_2}{2}, \qquad \widehat{L}'' - \hat{y}\widehat{L}' = \frac{\delta_0}{2}, \qquad \widehat{Q}'' - \hat{y}\widehat{Q}' = \frac{\delta_1}{2}. \quad (6.9)$$

These three equations all have solutions of a similar form. We will now focus on the first equation for $\widehat{R}$, and adapt the following results analogously for $\widehat{L}$ and $\widehat{Q}$. Integrating the first of (6.9), we find

$$\widehat{R}(\hat{y}) = \widehat{B}_{\widehat{R}} + \widehat{A}_{\widehat{R}}\int_0^{\hat{y}} \mathrm{e}^{t^2/2}\,\mathrm{d}t + \frac{\delta_2}{2}\int_0^{\hat{y}} \mathrm{e}^{t^2/2}\left[\int_0^t \mathrm{e}^{-p^2/2}\,\mathrm{d}p\right]\mathrm{d}t, \quad (6.10)$$

for constants $\widehat{A}_{\widehat{R}}$ and $\widehat{B}_{\widehat{R}}$. The inner boundary condition (4.1b) may be enforced on this solution. Since we require that $\hat{\psi}_n(0) = 0$, then necessarily $\widehat{B}_{\widehat{R}} = 0$. Thus, for n odd, this yields an inner solution of

$$\hat{\psi}_n \sim \left(\widehat{A}_{\widehat{R}}\int_0^{\hat{y}} \mathrm{e}^{t^2/2}\,\mathrm{d}t + \frac{\delta_2}{2}\int_0^{\hat{y}} \mathrm{e}^{t^2/2}\left[\int_0^t \mathrm{e}^{-p^2/2}\,\mathrm{d}p\right]\mathrm{d}t\right)\Gamma\left(\frac{n}{2}\right). \quad (6.11)$$

It now remains to take the outer limit of this form to match with the inner limit of the outer solution. Since the outer solution exhibits the Higher order Stokes phenomenon across a boundary-layer of the same width as that studied currently, we will match in §6.5 to the outer solution with $\mathcal{S}(Y) = 1$ for $\hat{y} \to -\infty$ and $\mathcal{S}(Y) = 0$ for $\hat{y} \to \infty$. Taking the outer limit of (6.11), we have firstly for $\hat{y} \to \infty$,

$$\widehat{R}(\hat{y}) \sim \left[\widehat{A}_{\widehat{R}} + \frac{1}{2}\left(\frac{\pi}{2}\right)^{\frac{1}{2}}\delta_2\right]\frac{\mathrm{e}^{\hat{y}^2/2}}{\hat{y}} - \mathrm{i}\widehat{A}\left(\frac{\pi}{2}\right)^{\frac{1}{2}} - \frac{\delta_2}{4}\left(\log(2) + \gamma + \log(-\hat{y}^2)\right), \tag{6.12}$$

where $\gamma \approx 0.577$ is the Euler-Mascheroni constant. Next, the outer limit is taken as $\hat{y} \to -\infty$. Noting that the first integral on the right-hand side of (6.10) is an odd function in $\hat{y}$, and the second integral is an even function, we have

$$\widehat{R}(\hat{y}) \sim \left[\widehat{A}_{\widehat{R}} - \frac{1}{2}\left(\frac{\pi}{2}\right)^{\frac{1}{2}}\delta_2\right]\frac{\mathrm{e}^{\hat{y}^2/2}}{\hat{y}} + \mathrm{i}\widehat{A}\left(\frac{\pi}{2}\right)^{\frac{1}{2}} - \frac{\delta_2}{4}\left(\log(2) + \gamma + \log(-\hat{y}^2)\right). \tag{6.13}$$

We note here that the inner limit of the outer solution with $\chi = 1 - Y^2$ from (6.5) alone can not match to this form. This is because there are other, previously neglected, components of the outer solution with $\chi' = 0$ required. These are derived in the following section.

6.4. The outer constant χ solution. We now consider an outer solution with $\chi' = 0$. Since the $O(\epsilon^n)$ equation is linear in ψ_n, this type of solution may be considered separately to that derived previously in §4.2 with $\chi = 1 - Y^2$. In order to match with the outer limit of $\hat{\psi}(\hat{y})$ from equations (6.12), and (6.13), we require $\chi = 1$. Thus, we posit the following divergent ansatz for their form

$$\psi_n(Y) \sim \begin{cases} \left[Q_0(Y)\log^2(n) + Q_1(Y)\log(n) + Q_2(Y)\right]\Gamma\left(\dfrac{n-1}{2}\right) & \text{for } n \text{ even}, \\ \left[R_1(Y)\log(n) + R_2(Y)\right]\Gamma\left(\dfrac{n}{2}\right) & \text{for } n \text{ odd}. \end{cases} \tag{6.14}$$

Note that while the inner solution from (6.7) has a coefficient of $O(\log(n))$ for n even, and $O(1)$ for n odd, we have introduced in (6.14) the terms Q_0 and R_1 corresponding to orders not seen in the inner solution. These components are required in the outer solution to cancel out with a further $\log(n)$ term arising when the inner limit of Q_1 and R_1 is taken. We note that ansatz (6.14) will include particular solutions arising from the forcing terms in the $O(\epsilon^n)$ equation that include the divergent eigenvalue from (6.8).

Substituting ansatz (6.14) into the $O(\epsilon^n)$ equation (4.1a), we divide out by $\Gamma((n-1)/2)$ for n even and $\Gamma(n/2)$ for n odd. At $O(\log(n))$ for n odd and $O(\log^2(n))$ for n even, we find the equations

$$R_1'(Y) = 0 \qquad \text{and} \qquad Q_0'(Y) = 0, \tag{6.15}$$

which have the solutions

$$R_1(Y) = A_1 \qquad \text{and} \qquad Q_0(Y) = B_0, \tag{6.16}$$

where A_1 and B_0 are constants. Next, for $O(1)$ for n odd and $O(\log(n))$ for n even, we find

$$R_2'(Y) = -\frac{\delta_2}{2Y} \qquad \text{and} \qquad Q_1'(Y) = -\frac{\delta_0}{2Y} - \frac{R_1(Y)}{2(1+Y)}, \tag{6.17}$$

which have the solutions

$$R_2(Y) = A_2 - \frac{\delta_2}{2}\log(Y) \quad \text{and} \quad Q_1(Y) = B_1 - \frac{\delta_0}{2}\log(Y) - \frac{A_1}{2}\log(1+Y), \tag{6.18}$$

where A_2 and B_1 are the constants of integration. At the next order of $O(1)$ for n even, we find

$$Q_2'(Y) = -\frac{\delta_1}{2Y} - \frac{\delta_2}{2Y}\psi_1(Y) - \frac{R_1(Y)}{2(1+Y)}. \tag{6.19}$$

This has the solution

$$Q_2(Y) = B_2 - \frac{\delta_1}{2}\log(Y) - \frac{A_2}{2}\log(1+Y) + \frac{\delta_2}{4}\log(Y)\log(1+Y). \tag{6.20}$$

We now take the inner limit of this outer $\chi' = 0$ solution from (6.14) by substituting for the inner variable $\hat{y} = n^{1/2}Y$ and expanding as $n \to \infty$. This yields

$$\psi_n \sim \begin{cases} \Bigg[\left(B_0 + \dfrac{\delta_0}{4}\right)\log^2(n) + \left(B_1 + \dfrac{\delta_1}{4} - \dfrac{\delta_0}{2}\log(\hat{y})\right)\log(n) \\ \qquad + \left(B_2 - \dfrac{\delta_1}{2}\log(\hat{y})\right)\Bigg]\Gamma\left(\dfrac{n-1}{2}\right) & \text{for } n \text{ even,} \\ \left[\left(A_1 + \dfrac{\delta_2}{4}\right)\log(n) + \left(A_2 - \dfrac{\delta_2}{2}\log(\hat{y})\right)\right]\Gamma\left(\dfrac{n}{2}\right) & \text{for } n \text{ odd.} \end{cases} \tag{6.21}$$

The full outer solution is then given by combining the $\chi' = 0$ solution from equation (6.14) with the $\chi = 1 - Y^2$ solution from equation (5.2), yielding the relevant divergence rate as

$$\psi_n \sim \begin{cases} \mathcal{S}(Y)\Big[L(Y)\log(n) + Q(Y)\Big]\dfrac{\Gamma(\frac{n}{2}-1)}{\chi^{n/2-1}} & \\ +\Big[Q_0(Y)\log^2(n) + Q_1(Y)\log(n) + Q_2(Y)\Big]\Gamma\left(\dfrac{n-1}{2}\right) & \text{for } n \text{ even,} \\ \mathcal{S}(Y)R(Y)\dfrac{\Gamma(\frac{n-1}{2})}{\chi^{(n-1)/2}} + \Big[R_1(Y)\log(n) + R_2(Y)\Big]\Gamma\left(\dfrac{n}{2}\right) & \text{for } n \text{ odd.} \end{cases} \tag{6.22}$$

We may combine this result with the inner limit of the $\chi = 1 - Y^2$ divergent solution from (6.5) to find, for n even

$$\begin{aligned}\psi_n \sim \Bigg[\left(B_0 + \frac{\delta_0}{4}\right)\log^2(n) + \left(-\frac{\mathcal{S}(Y)e^{\hat{y}^2/2}}{\sqrt{2}\hat{y}} + B_1 + \frac{\delta_1}{4} - \frac{\delta_0}{2}\log(\hat{y})\right)\log(n) \\ + \left(\frac{-\mathcal{S}(Y)\gamma e^{\hat{y}^2/2}}{\sqrt{2}\hat{y}} + B_2 - \frac{\delta_1}{2}\log(\hat{y})\right)\Bigg]\Gamma\left(\frac{n-1}{2}\right),\end{aligned} \tag{6.23}$$

and for n odd

$$\psi_n \sim \left[\left(A_1 + \frac{\delta_2}{4}\right)\log(n) + \left(-\frac{\mathcal{S}(Y)e^{\hat{y}^2/2}}{\sqrt{2}\hat{y}} + A_2 - \frac{\delta_2}{2}\log(\hat{y})\right)\right]\Gamma\left(\frac{n}{2}\right). \tag{6.24}$$

6.5. Matching and conclusions. We may now match the inner limit of the outer solution, given above in equations (6.23) and (6.24), with the outer-limit of the inner solution as $\hat{y} \to \infty$ from (6.12) and $\hat{y} \to -\infty$ from (6.13). Firstly, the inner solution contains no terms of $O(\log n)$ for n odd and $O(\log^2(n))$ for n even, requiring that

$$A_1 = -\frac{\delta_2}{4} \qquad \text{and} \qquad B_0 = -\frac{\delta_0}{4}. \tag{6.25}$$

Next, we match the terms of $O(\hat{y}^{-1}\mathrm{e}^{\hat{y}^2/2})$. Taking $\mathcal{S}(Y) = 0$ for $\hat{y} \to \infty$ and $\mathcal{S}(Y) = 1$ for $\hat{y} \to -\infty$, we find at leading order for n odd, and orders $\log(n)$ and $O(1)$ for n even, six equations for the eigenvalue coefficients δ_0, δ_1, and δ_2. These are

$$\left.\begin{aligned} &\widehat{A}_{\widehat{L}} + \delta_0\sqrt{\frac{\pi}{8}} = 0, && \widehat{A}_{\widehat{Q}} + \delta_1\sqrt{\frac{\pi}{8}} = 0, && \widehat{A}_{\widehat{R}} + \delta_2\sqrt{\frac{\pi}{8}} = 0,\\ &\widehat{A}_{\widehat{L}} - \delta_0\sqrt{\frac{\pi}{8}} = -\frac{1}{\sqrt{2}}, && \widehat{A}_{\widehat{Q}} - \delta_1\sqrt{\frac{\pi}{8}} = -\frac{\gamma}{\sqrt{2}}, && \widehat{A}_{\widehat{R}} - \delta_2\sqrt{\frac{\pi}{8}} = -\frac{1}{\sqrt{2}}. \end{aligned}\right\} \tag{6.26}$$

The first of (6.26) yields $\widehat{A}_{\widehat{L}} = -\delta_0\sqrt{\frac{\pi}{8}}$, which we substitute into the second equation for δ_0 in (6.26) to find a value for δ_0. This approach yields the solutions

$$\delta_0 = \frac{1}{\sqrt{\pi}}, \qquad \delta_1 = \frac{\gamma}{\sqrt{\pi}}, \qquad \delta_2 = \frac{1}{\sqrt{\pi}}. \tag{6.27}$$

Note that the $\chi' = 0$ outer solutions were not required to determine the eigenvalue divergence, as their inner limit does not contribute to the $\mathrm{e}^{\hat{y}^2/2}$ terms whose coefficients were matched between the inner and outer regions. These terms are however important to view the divergence of the outer solution for $\mathrm{Re}[Y] > 0$, since the factorial-over-power divergence has been switched off in this region due to the HOSP.

7. Stokes smoothing. We now truncate the divergent expansions for the solution and eigenvalue at $n = N-1$ and consider an exponentially-small remainder. These are taken to be of the form

$$\psi(Y) = \underbrace{\sum_{n=0}^{N-1} \epsilon^n \psi_n(Y)}_{\psi_r(Y)} + \overline{\psi}(Y) \quad \text{and} \quad \lambda = \underbrace{\sum_{n=0}^{N-1} \epsilon^n \lambda_n}_{\lambda_r} + \overline{\lambda}, \tag{7.1}$$

where we have denoted the truncated series by $\psi_r(Y)$ and λ_r and optimally truncated at

$$N = \frac{2|\chi|}{\epsilon^2} + \rho, \tag{7.2}$$

where $0 \leq \rho < 1$ to ensure that N takes integer values. Substitution of these expansions into the Hermite-with-pole equation (1.4a) yields the following linear differential equation of

$$\epsilon^2\overline{\psi}'' - 2Y\overline{\psi}' + \left[\frac{\epsilon}{1+Y} - (1+\lambda_r)\right]\overline{\psi} - \psi_r\overline{\lambda} = \xi_{\mathrm{eq}} + O(\overline{\lambda}\overline{\psi}), \tag{7.3}$$

where the forcing term ξ_{eq} is of $O(\epsilon^N)$ and defined by

$$\xi_{\mathrm{eq}} = (1+\lambda_r)\psi_r - \epsilon^2\psi_r'' + 2Y\psi_r' - \epsilon\frac{\psi_r}{1+Y}. \tag{7.4}$$

Our goal is to determine the leading order divergence of $\bar{\lambda}$ by considering the behaviour of $\bar{\psi}(Y)$ throughout the complex plane. This requires the analytical understanding of the Stokes phenomenon, in which $\bar{\psi}(Y)$ rapidly transitions in magnitude across contours in the Y-plane known as Stokes lines. The details presented here will be brief, and we refer the reader to the geophysical study for the Kelvin wave problem [18] for complete details of this procedure.

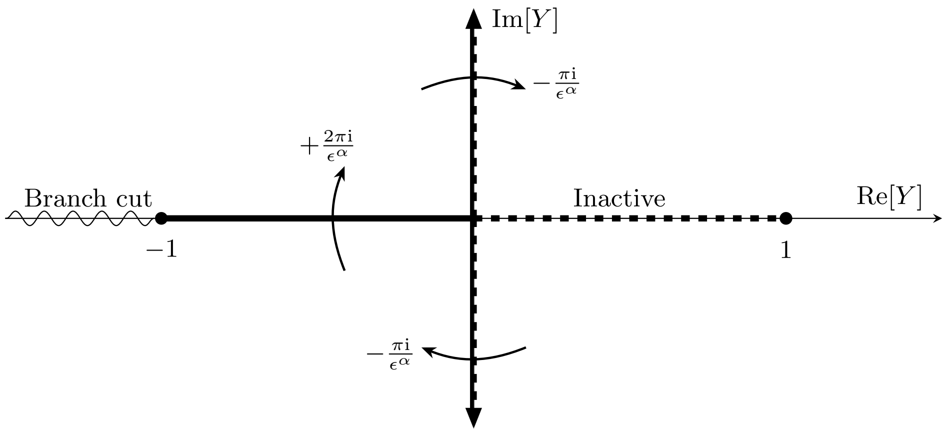

FIG. 7.1. *The Stokes lines generated by the divergent series expansion for our problem are shown (bold). Inactive Stokes lines are shown dashed, and along the imaginary axis the Stokes line is half active.*

7.1. Stokes lines. Across the Stokes lines, shown in figure 7.1, a multiple of the homogeneous solution to equation (7.3) will switch on, due to the inhomogenous forcing term. The homogeneous solution is given by

$$\bar{\psi}(Y) \sim \left(\frac{\bar{\Lambda}_R}{Y} + \epsilon \log(\epsilon) \frac{\bar{\Lambda}_L}{Y} + \epsilon \left[\frac{\bar{\Lambda}_Q}{Y} + \frac{\bar{\Lambda}_R \log(1+Y)}{2Y}\right]\right) e^{-\chi/\epsilon^2}. \tag{7.5}$$

Note that while these constants may take any value, in order to achieve consistency with the anticipated $2\pi i \epsilon^{-\alpha}$ switching, we require

$$\bar{\Lambda}_R = -\frac{1}{2}, \qquad \bar{\Lambda}_L = 1, \qquad \bar{\Lambda}_Q = -\frac{\gamma + \log(2)}{2}. \tag{7.6}$$

These have been found by substituting the optimal truncation point (7.2) into the naive late-term approximation (4.14) and matching orders of ϵ with (7.5).

Thus, across the Stokes line $-1 \le Y < 0$, a $2\pi i \epsilon^{-\alpha}$ multiple of (7.5) will switch on, and across the imaginary axis, $\mathrm{Re}[Y] = 0$, a $\pi i \epsilon^{-\alpha}$ multiple of (7.5) will switch on. This is demonstrated in figure 7.1. Note that this solution alone is unable to satisfy both of the decay conditions as $Y \to \pm\infty$ from (1.4b). This is because in addition to this Stokes switching generated by the base expansion, which appears in equation (7.3) as the forcing term ξ_{eq}, there is another switching generated by a base exponential which is the particular solution associated with the forcing term $\bar{\lambda}$.

This additional Stokes smoothing may be derived by noting that (to the first two orders in ϵ), the particular solution of (7.3) satisfies the equation

$$\epsilon^2 \bar{\psi}'' - 2Y \bar{\psi}' = \bar{\lambda}. \tag{7.7}$$

This equation may be solved in terms of special functions, to which the limits of $Y \to \pm\infty$ may be applied. The solution switches on a contribution of

$$\bar{\psi} \sim \frac{\epsilon\bar{\lambda}\sqrt{\pi}}{2Y}\mathrm{e}^{Y^2/\epsilon^2} \tag{7.8}$$

as we travel from $Y = \infty$ to $Y = -\infty$. In our study of the equatorial Kelvin wave problem [18], we demonstrate how to derive this additional Stokes switching analytically without the use of an integral representation of the particular solution. It is found that there is another Stokes line along the imaginary axis across which (7.8) switches on, generated by a new divergent series expansion within this particular solution.

7.2. Determination of Im[λ]. We now calculate the exponentially-small component of the eigenvalue, λ, by enforcing the decay conditions at $Y \to \pm\infty$ on the exponentially-small solution. We demonstrated in §7.1 that there are two Stokes smoothings that must be considered: one generated by the base expansion for which the Stokes lines are shown in figure 7.1, and another generated by a particular solution, which we denote the base exponential.

In imposing the decay condition at $Y = \infty$, any contributions switched on by the time we reach $Y = -\infty$ must cancel with one other. Note that the decay condition at $Y = -\infty$ may be enforced on different Riemann sheets generated by the singularity at $Y = -1$. The Stokes switching associated with the base expansion thus yields either a switching of $-\pi\mathrm{i}\epsilon^{-\alpha}$, or $+\pi\mathrm{i}\epsilon^{-\alpha}$ if we enter the other Riemann sheet by crossing over the $-1 \leq Y < 0$ Stokes line. This must cancel with the contribution from (7.8), which yields

$$\bar{\lambda} \sim \pm\sqrt{\pi}\mathrm{i}\Big[1 - 2\epsilon\log{(\epsilon)} + \Big(\gamma + \log{(2)}\Big)\epsilon\Big]\mathrm{e}^{-1/\epsilon^2}. \tag{7.9}$$

These are the complex-conjugate pairs for $\bar{\lambda}$, which correspond to growing and decaying temporal instabilities in the solution.

7.3. Conclusion. We have derived the exponentially-small component of the eigenvalue,

$$\mathrm{Im}[\lambda] \sim \pm\sqrt{\pi}\Big[1 - 2\epsilon\log{(\epsilon)} + \Big(\gamma + \log{(2)}\Big)\epsilon\Big]\mathrm{e}^{-1/\epsilon^2},$$

by considering the Stokes phenomenon displayed by the solution, $\psi(Y)$, throughout the complex plane. Since this exponentially-small component of λ is imaginary, it corresponds to a growing temporal instability of the solution associated with weak shear. This is known as a critical layer instability, for which the resolution of the associated equatorial Kelvin wave problem by the current authors in [18] has necessitated this prior study.

8. Discussion. As we noted in §2, the Hermite-with-pole problem posed by Boyd & Natarov [4] as a model for weak latitudinal shear of the equatorial Kelvin wave is an unusually difficult problem in exponential asymptotics. In order to derive the Stokes phenomenon throughout the complex plane, we have had to consider multiple unusual effects. This includes the divergent eigenvalue expansion, for which the solution expansion has an associated particular component which must be considered in detail as it leads to the higher-order Stokes phenomenon. Additionally, determination of the late-terms of the solution required the analysis of a boundary layer at $Y = 0$ of diminishing width as $n \to \infty$.

Nevertheless, in this work, we have shown that these can be handled. Resolution of the boundary layer at $Y=0$ in §6 required the consideration of further components of the late-term divergence in addition to the naive factorial-over-power component that generates the singular behaviour at $Y=-1$.

This work will be followed by a forthcoming study of the full geophysical problem of weak latitudinal shear of the equatorial Kelvin wave. In contrast to equation (1.4a), the physical problem requires the study of three coupled equations for the velocity field $u(y)$, $v(y)$, and depth $h(y)$. However we see that these techniques in exponential asymptotics can be applied to that problem as well by formulating the governing equations into a single second-order differential equation for one of the unknowns.

Acknowledgments. P.H.T. is supported by the Engineering and Physical Sciences Research Council [EP/V012479/1].

Appendix A. Comparison with numerical results. We now validate the analytical predictions for the divergence of the eigenvalue and eigenfunction expansions numerically.

A.1. Divergence of the eigenvalue expansion. Following the approach of Boyd & Natarov [4], we consider a solution to the Hermite-with-pole equation (1.4a), written in the original variable $y=\epsilon^{-1}Y$, in which each order of the solution is expressed as an expansion of Hermite polynomials of the form

$$\psi(y) = \sum_{n=0}^{\infty}\sum_{k=0}^{\infty} \epsilon^n a_{(n,k)} H_k(y). \tag{A.1}$$

Here, $H_k(y)$ is the kth Hermite-polynomial, and $a_{(n,k)}$ is a constant. Substitution of (A.1) into (1.4a) yields at $O(\epsilon^0)$ and $O(\epsilon)$ the solutions

$$\lambda_0 = -1, \qquad a_{(0,0)} = 1, \qquad \lambda_1 = 1, \qquad a_{(1,0)} = 0, \qquad a_{(1,1)} = 0. \tag{A.2}$$

A general expression may be found at $O(\epsilon^n)$, to which we apply the normalisation choice of $a_{(n,0)}=0$. This yields

$$\lambda_n + \sum_{k=1}^{n-1} 2k a_{(n,k)} H_k(y) = (-y)^{n-1} + \sum_{p=2}^{n-1}\sum_{j=0}^{n-p-1}\Big[(-y)^{p-1} - \lambda_p\Big] a_{(n-p,j)} H_j(y) \tag{A.3}$$

for $n \geq 2$. In (A.3), the left-hand side is a polynomial of order $n-1$ containing the unknowns λ_n and $a_{(n,k)}$. The right-hand side is also a polynomial of order $n-1$ in which all the coefficients are known. Equations relating λ_n and $a_{(n,k)}$ for $1 \leq k \leq n-1$ are then found by equating the polynomial coefficients on each side of equation (A.3).

Boyd & Natarov [4] used orthogonality properties of $H_k(y)$ to integrate (A.3) with a symbolic programming language, which yielded λ_n. However, since the left-hand side of (A.3) has only one term containing the highest order polynomial $H_{n-1}(y)$, we may determine $a_{(n,n-1)}$ by equating coefficients with the right-hand side of (A.3). This procedure may be repeated until all of $a_{(n,k)}$ and λ_n are known. In implementing their method, we find that in the time taken for theirs to reach $n=24$ ours exceeds $n=300$.

These results for λ_n are displayed in figure A.1, which show good agreement with our analytical prediction of §6.5.

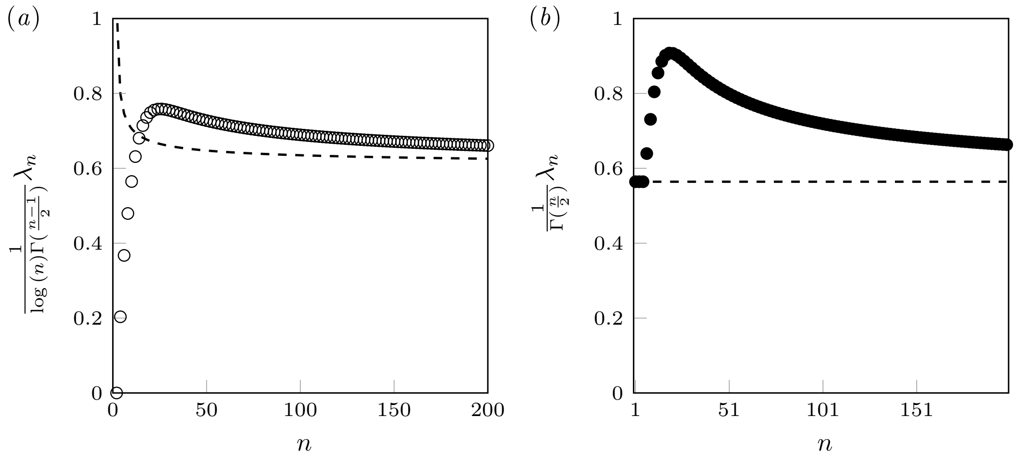

FIG. A.1. *The eigenvalue λ_n, calculated by the Rayleigh-Schrodinger scheme of Appendix A.2, is shown (circles) for n even in (a) and n odd in (b). These are compared to our analytical prediction for λ_n (6.8) (dashed).*

A.2. Divergence of the solution expansion. The Rayliegh-Schrodinger scheme of Appendix A.1 efficiently calculated the divergence of λ_n. However, the normalisation condition required was different to boundary condition (1.4c) used in this work. In this section, we compute each order of the asymptotic solution, $\psi_n(Y)$, up to $n = 50$ with a symbolic programming language in order to compare with our analytical prediction. This allows us to verify two of our analytical predictions:

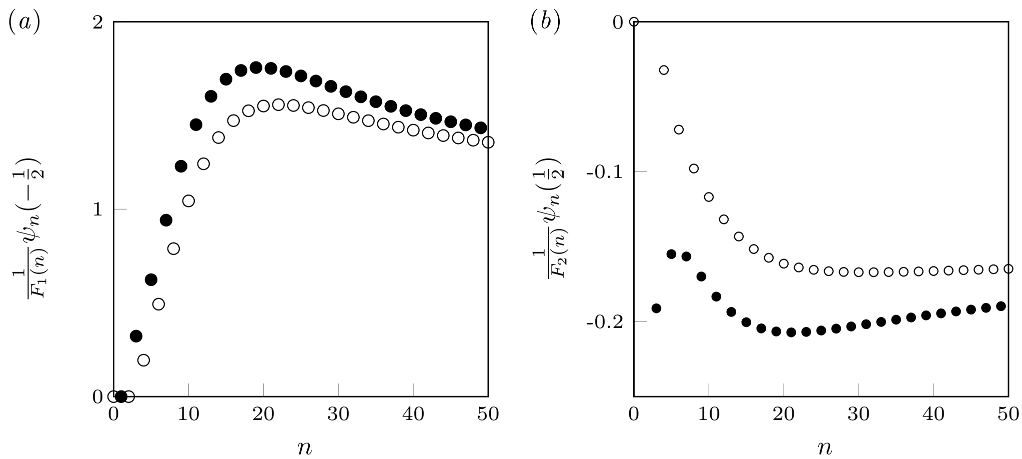

FIG. A.2. *The divergence of the asymptotic solution, ψ_n, solved analytically up to $n = 50$, is shown in (a) for $Y = -1/2$ and in (B) for $Y = 1/2$. For $Y = -1/2$, we have rescaled with $F_1(n) = \log(n)\Gamma(n/2-1)/(1-Y^2)^{n/2-1}$ for n even and $F_1(n) = \Gamma((n-1)/2)/(1-Y^2)^{(n-1)/2}$ for n odd. For $Y = 1/2$, we have taken $F_2(n) = \log^2(n)\Gamma((n-1)/2)$ for n even and $F_2(n) = \log(n)\Gamma(n/2)$ for n odd.*

1. We assumed that the higher-order Stokes phenomenon would switch off the naive late-term solution (2.4) with $\mathcal{S}(Y) = 0$ for $\mathrm{Re}[Y] > 0$. We verify this in figure 5.2, in which we plot $\psi_{49}(Y)$. This indicates that $\psi_n(Y)$ does follow the expected factorial-over-power scaling for $\mathrm{Re}[Y] < 0$, and switches off as we proceed into $\mathrm{Re}[Y] > 0$.

2. In figure A.2, we plot the divergent trends of $\psi_k(Y)$ at the two values of $Y=-1/2$ and $Y=1/2$. We see that the solution diverges in the expected factorial-over-power form at $Y=-1/2$, but at $Y=1/2$ the divergence is seen to be purely factorial. This confirms that our divergent form in (2.4) with $\chi=1$ dominates for $\mathrm{Re}[Y]>0$.

Appendix B. Lower-order divergence of the naive ansatz. As noted in §4.2, the naive factorial-over-power solution to the homogeneous late term equation (4.8) is unable to satisfy the boundary condition at $Y=0$. This is due to a singularity in the prefactors of the divergent ansatz, $L(Y)$, $R(Y)$, and $Q(Y)$, from equations (4.13a) and (4.13b). One may consider lower order terms, as $n\to\infty$, in the divergence of the homogeneous solution by considering a prefactor of the form (for n odd)

$$R(Y)=R_0(Y)+\frac{\log(n)}{n}M_1(Y)+\frac{R_1(Y)}{n}+\cdots, \tag{B.1}$$

where the subsequent terms in this series will be of $O(n^{-2}\log n)$ and $O(n^{-2})$. We will see that the strength of the singularity in $R_0(Y)$ at $Y=0$ increases in later orders and thus forces a reordering of the series as $Y\to 0$.

The method to calculate these lower order solutions is similar to that briefly presented in §4.2 for the leading orders. We substitute an ansatz for $\psi_n(Y)$ of the form

$$\psi_n\sim\begin{cases}\left[L_0(Y)\log(n)+Q_0(Y)+\dfrac{\log(n)}{n}L_1(Y)+\cdots\right]\dfrac{\Gamma(\frac{n}{2}-1)}{\chi^{n/2-1}} & \text{for } n \text{ even},\\[2ex] \left[R_0(Y)+\dfrac{\log(n)}{n}M_1(Y)+\dfrac{R_1(Y)}{n}+\cdots\right]\dfrac{\Gamma(\frac{n-1}{2})}{\chi^{(n-1)/2}} & \text{for } n \text{ odd},\end{cases} \tag{B.2}$$

into the homogeneous equation (4.8). The reordering we seek to capture as $Y\to 0$ will first occur for n even between $L_0(Y)$ and $L_1(Y)$, and for n odd between $R_0(Y)$ and $R_1(Y)$.

Dividing out by the dominant factorial-over-power scaling in the $O(\epsilon^n)$ equation (4.8) yields terms of orders n^0, $n^{-1}\log(n)$, n^{-1}, $n^{-2}\log(n)$, and n^{-2} for odd values of n. The case for even values of n is similar, except for terms of order $\log(n)$ appearing. Distinct equations are found at each of these orders for the cases of n even or n odd.

The first few equations are the same as that considered in §4.2, and yield the singulant $\chi(Y)=1-Y^2$ from equation (4.11) and prefactors $L_0(Y)$, $R_0(Y)$, and $Q_0(Y)$ from (4.12a) and (4.13b).

Equations for $M_1(Y)$ and $L_1(Y)$ are then found at $O(n^{-2}\log(n))$ for odd and even values of n, respectively, which have the solutions

$$\begin{aligned}M_1(Y)&=\Big[\Lambda_{M_1}+\Lambda_{L_0}\log(1+Y)\Big]\frac{(1-Y^2)}{Y},\\ L_1(Y)&=\left[\Lambda_{L_1}+\frac{\Lambda_{M_1}}{2}\log(1+Y)+\frac{\Lambda_{L_0}}{Y^2}+\frac{\Lambda_{L_0}}{4}\log^2(1+Y)\right]\frac{(1-Y^2)}{Y},\end{aligned} \tag{B.3}$$

where Λ_{M_1} and Λ_{L_1} are constants of integration. It remains to determine $R_1(Y)$, the governing equation for which will be found at $O(n^{-2})$ when n is odd. This has the solution of

$$\begin{aligned}R_1(Y)=\Big[&\Lambda_{R_1}+\Lambda_{Q_0}\log(1+Y)+\frac{\Lambda_{R_0}}{Y^2}+\frac{\Lambda_{R_0}}{4}\log^2(1+Y)+\\ &-\Lambda_{M_1}\log(1-Y^2)-\Lambda_{L_0}\log(1+Y)\log^2(1-Y^2)\Big]\frac{(1-Y^2)}{Y},\end{aligned} \tag{B.4}$$

where Λ_{R_1} is a constant of integration.

To conclude, the functional prefactor of a factorial-over-power ansatz for the late-term solution may contain singularities or branch points at locations not seen in the early orders of the expansion. In our case this is the location $Y = 0$. In these instances, it is necessary to consider lower order terms of the ansatz in order to determine the correct inner-variable scaling for the resultant boundary layer matching procedure.

Appendix C. Inner solution at the singularity $Y = -1$. Motivated by the inner limit of the outer solution, (4.5), we consider an inner solution of the form

$$\hat{\psi}_{\text{inner}}(\hat{y}) = \sum_{n=0}^{\infty}\sum_{m=0}^{n} \epsilon^n \log^m(\epsilon)\hat{\psi}_{(n,m)}(\hat{y}). \tag{C.1}$$

Substitution into the inner equation (4.4) yields at $O(1)$, $O(\epsilon\log(\epsilon))$, and $O(\epsilon^2\log^2(\epsilon))$

$$\widehat{\mathcal{L}}[\hat{\psi}_{(0,0)}] = \frac{\mathrm{d}^2\hat{\psi}_{(0,0)}}{\mathrm{d}\hat{y}^2} + 2\frac{\mathrm{d}\hat{\psi}_{(0,0)}}{\mathrm{d}\hat{y}} = 0, \qquad \widehat{\mathcal{L}}[\hat{\psi}_{(1,1)}] = 0, \qquad \widehat{\mathcal{L}}[\hat{\psi}_{(2,2)}] = 0. \tag{C.2}$$

These equations have solutions of a similar form, given by $\hat{\psi}_{(0,0)}(\hat{y}) = A_{(0,0)} + B_{(0,0)}\exp(-2\hat{y})$, $\hat{\psi}_{(1,1)}(\hat{y}) = A_{(1,1)} + B_{(1,1)}\exp(-2\hat{y})$, and $\hat{\psi}_{(2,2)}(\hat{y}) = A_{(2,2)} + B_{(2,2)}\exp(-2\hat{y})$. Matching with the $O(1)$, $O(\epsilon\log(\epsilon))$, and $O(\epsilon^2\log^2(\epsilon))$ components of the inner-limit of ψ_{outer} in (4.5) requires $A_{(0,0)} = 1$, $B_{(0,0)} = 0$, $A_{(1,1)} = -1$, $B_{(1,1)} = 0$, $A_{(2,2)} = 1/2$, and $B_{(2,2)} = 0$. This yields

$$\hat{\psi}_{(0,0)}(\hat{y}) = 1, \qquad \hat{\psi}_{(1,1)}(\hat{y}) = -1, \qquad \hat{\psi}_{(2,2)}(\hat{y}) = \frac{1}{2}. \tag{C.3}$$

At the next orders of $O(\epsilon)$ and $O(\epsilon^2\log\epsilon)$, we find similar equations to (C.2) with the exception of a forcing term that relies on $\hat{\psi}_{(0,0)}(\hat{y})$ and $\hat{\psi}_{(1,1)}(\hat{y})$, respectively. These equations are found to be

$$\widehat{\mathcal{L}}[\hat{\psi}_{(1,0)}] = -\frac{1}{\hat{y}} \quad \text{and} \quad \widehat{\mathcal{L}}[\hat{\psi}_{(2,1)}] = \frac{1}{\hat{y}}, \tag{C.4}$$

where $\widehat{\mathcal{L}}$ is the linear differential operator defined in (C.2). For brevity, only the exact solution of the first of these is provided here. This has the solution of

$$\hat{\psi}_{(1,0)}(\hat{y}) = A_{(1,0)} + B_{(1,0)}\mathrm{e}^{-2\hat{y}} - \mathrm{e}^{-2\hat{y}}\int_0^{\hat{y}} \log(y)\mathrm{e}^{2y}\mathrm{d}y. \tag{C.5}$$

Analogously for the second equation in (C.4) the exact solution will have constants $A_{(2,1)}$ and $B_{(2,1)}$, and a positive sign $(+)$ in front of the last component of the solution in (C.5). To facilitate matching with the $O(\epsilon)$ outer solution, we take the outer-limit of (C.5) as $\hat{y} \to \infty$, yielding

$$\hat{\psi}_{(1,0)}(\hat{y}) \sim -\frac{1}{2}\log(\hat{y}) + \frac{1}{2}\sum_{k=1}^{\infty}\frac{\Gamma(k)}{(2\hat{y})^k} \quad \text{and} \quad \hat{\psi}_{(2,1)}(\hat{y}) \sim \frac{1}{2}\log(\hat{y}) - \frac{1}{2}\sum_{k=1}^{\infty}\frac{\Gamma(k)}{(2\hat{y})^k}. \tag{C.6}$$

Here we set $A_{(1,0)} = 0$, $B_{(1,0)} = 0$, $A_{(2,1)} = 0$, and $B_{(2,1)} = 0$ to match with the $O(\epsilon)$ term of the inner limit of the outer solution from (4.5).

Note that we have been able to construct an exact solution for these. In general, and typically for nonlinear problems, this is not possible and an ansatz must be introduced to capture the series expansion of the outer-limit behaviour of $\hat{\psi}(\hat{y})$, from which the coefficients of this series, in our case $\Gamma(k)$, would determined via the solution to a recurrence relation problem. This will be the approach used when considering the $O(\epsilon^2)$ equation,

$$\widehat{\mathcal{L}}[\hat{\psi}_{(2,0)}] = \frac{\log(\hat{y})}{2\hat{y}} - \sum_{k=1}^{\infty} \frac{\Gamma(k)}{(2\hat{y})^{k+1}}, \tag{C.7}$$

for which we consider a series expansion as $\hat{y} \to \infty$ of the form

$$\hat{\psi}_{(2,0)}(\hat{y}) = \frac{\log^2(\hat{y})}{8} + \log(\hat{y}) \sum_{k=1}^{\infty} \frac{a_k}{(2\hat{y})^k} + \sum_{k=1}^{\infty} \frac{b_k}{(2\hat{y})^k}. \tag{C.8}$$

Substitution of series (C.8) into equation (C.7) yields terms that are either algebraic powers of $(2\hat{y})^{-k}$ or $\log(y)(2\hat{y})^{-k}$. Examining the equations which arise at each of these orders yields the following recurrence relations for a_k and b_k where $k \geq 2$,

$$\begin{aligned} a_1 &= -\frac{1}{4}, \qquad a_k = (k-1)a_{k-1}, \\ b_1 &= \frac{1}{4}, \qquad b_k = (k-1)b_{k-1} + \frac{(2k-1)}{4k}\Gamma(k-1). \end{aligned} \tag{C.9}$$

In substituting for $b_k = \Gamma(k)d_k$, the recurrence relation for b_k may be written in a form with s series solution, yielding for $k \geq 2$

$$a_k = -\frac{\Gamma(k)}{4} \qquad \text{and} \qquad b_k = \left[\frac{1}{2} - \frac{1}{4k} + \frac{1}{2}\sum_{j=2}^{k} \frac{1}{j}\right]\Gamma(k). \tag{C.10}$$

Thus, as $\hat{y} \to \infty$, our $O(\epsilon^2)$ inner solution is given by

$$\hat{\psi}_{(2,0)}(\hat{y}) = \frac{\log^2(\hat{y})}{8} - \frac{\log(\hat{y})}{4} \sum_{k=1}^{\infty} \frac{\Gamma(k)}{(2\hat{y})^k} + \sum_{k=1}^{\infty} \frac{b_k}{(2\hat{y})^k}, \tag{C.11}$$

where b_k is defined in equation (C.10). In §4.1.2, we use the outer limit of this solution to motivate the correct form for the factorial-over-power ansatz of ψ_n as $n \to \infty$. Thus, we are also interested in the limit of $k \to \infty$ of b_k. Expanding b_k given in (C.10) as $k \to \infty$ yields

$$b_k \sim \left[\frac{1}{2}\log(k) + \frac{\gamma}{2} + O(k^{-1})\right]\Gamma(k), \tag{C.12}$$

where $\gamma \approx 0.577$ is the Euler-Macheroni constant.

REFERENCES

[1] M. V. Berry, *Uniform asymptotic smoothing of Stokes discontinuities*, Proc. Roy. Soc. London, A 422 (1989), pp. 7–21.
[2] G. L. Body, J. R. King, and R. H. Tew, *Exponential asymptotics of a fifth-order partial differential equation*, Eur. J. Appl. Math., 16 (2005), pp. 647–681.

8 THE EQUATORIAL KELVIN WAVE INSTABILITY

8.1 Introduction

We demonstrated in the study of the Hermite-with-pole equation of chapter 7 that a divergent asymptotic expansion for an eigenvalue may be real-valued to each algebraic order of ϵ, but still have a non zero imaginary component. For the equatorial Kelvin wave studied in this section, the wavespeed, c, is an eigenvalue of the problem. In the presence of small latitudinal shear, denoted by ϵ, this also has an imaginary component that destabilises the motion of the travelling wave. The purpose of this chapter is to derive this imaginary component asymptotically, which we show is exponentially small as $\epsilon \to 0$. This work both provides the first analytical treatment of this instability, as well as a correction to the numerical work by Natarov and Boyd (2001) who predicted that $\text{Im}[c] = O(\mathrm{e}^{-1/\epsilon^2})$. In this chapter, we demonstrate that the exponentially-small component of the eigenvalue is given by

$$\text{Im}[c] = \pm \frac{1}{4\sqrt{\pi}} \epsilon^3 \mathrm{e}^{-1/\epsilon^2}, \tag{8.1}$$

which comes in complex-conjugate pairs. One of these corresponds to the growing temporal instability of the travelling wave solution.

This result is derived through two different methods. First, by restricting the domain to take real-values, an asymptotic procedure connects two inner solutions, one at $Y = 0$, and another at $Y = 1$, through matching with an outer solution. Secondly, the late-term divergence of the asymptotic expansions, and their exponentially small remainder, are considered for complex values of Y. The exponentially-small component of the eigenvalue is then determined by considering the Stokes line structure and decay conditions as $\text{Re}[Y] \to \pm\infty$, much like that seen for the Hermite-with-pole equation in chapter 7.

Appendix B: Statement of Authorship

<table>
<tr><th colspan="2">This declaration concerns the article entitled:</th></tr>
<tr><td colspan="2">On the exponentially-small instability of the equatorial Kelvin wave</td></tr>
<tr><td colspan="2">Publication status:
Draft manuscript ● | Submitted ☐ | In review ☐ | Accepted ☐ | Published ☐</td></tr>
<tr><td>Publication details</td><td>Authors - Josh Shelton, Stephen D. Griffiths, Jonathan Chapman, Philippe H. Trinh</td></tr>
<tr><td colspan="2">Copyright status:
The material has been published with a CC-BY license ☐ | The publisher has granted permission to replicate the material included here ☐</td></tr>
<tr><td>Candidate's contribution to the paper</td><td>All authors contributed equally to the conceptualisation, motivation, and initial methodology used in the article (25%)

Most analytical calculations were performed by the author of this thesis (75%)

All numerical computations were performed by the author of this thesis (100%)

The original draft and bulk of the final presentation has been written by the author of this thesis (80%)</td></tr>
<tr><td>Statement from Candidate</td><td>This paper reports on original research I conducted during the period of my Higher Degree by Research candidature.</td></tr>
<tr><td>Signed</td><td> | Date | 30/12/22</td></tr>
</table>

On the exponentially-small instability of the equatorial Kelvin wave

Josh Shelton[1] †, Stephen D. Griffiths[2], S. Jonathan Chapman[3] and Philippe H. Trinh[1]

[1]Department of Mathematical Sciences, University of Bath, Bath BA2 7AY, UK

[2]Department of Applied Mathematics, University of Leeds, Leeds, LS2 9JT, UK

[3]Oxford Centre for Industrial and Applied Mathematics, Mathematical Institute, University of Oxford, OX1 3LB, UK

(Received xx; revised xx; accepted xx)

The equatorial Kelvin wave is destabilised by weak shear, which we denote by ϵ. This is caused by an imaginary component of an associated eigenvalue, the wavespeed c, that is exponentially small as $\epsilon \to 0$. We derive this exponentially-small component asymptotically using the techniques of exponential asymptotics. The asymptotic scaling of this instability was studied numerically by Natarov & Boyd (Dynam. Atmos. Oceans, vol. 33, 2001, pp. 191-200), who concluded that $\mathrm{Im}[c] = O(\exp(-1/\epsilon^2))$. We show that this is not the case, and that the correct asymptotic scaling is actually of order $\epsilon^3 \exp(-1/\epsilon^2)$.

1. Introduction

The equatorial Kelvin wave is an oceanographic wave that travels east along the equator without any change of form. However along the equator of the ocean, zonal jets may be present. These travel faster than the fluid at surrounding latitudes and thus introduce latitudinal shear. It is known by the investigation of Boyd & Christidis (1982) that the Kelvin wave is unstable with respect to this weak shear. In writing the solutions in travelling-wave form, the wavespeed c becomes an eigenvalue of the problem. For small shear ($\epsilon \to 0$), the asymptotic expansion for the eigenvalue,

$$c = c_0 + \epsilon^2 c_1 + \epsilon^4 c_2 + \cdots, \tag{1.1}$$

is real-valued to each order of ϵ. However, the Kelvin wave instability is governed by the imaginary component of c, which we show to be given by

$$\mathrm{Im}[c] = \pm \frac{1}{4\sqrt{\pi}} \epsilon^3 \mathrm{e}^{-1/\epsilon^2}. \tag{1.2}$$

Equation (1.2) is the main result of this paper. The difficulty in deriving this analytically is that it lies *beyond-all-orders* of the asymptotic expansion (1.1), our resolution of which relies on the use of sophisticated techniques in asymptotic analysis known as *exponential asymptotics*. In order to understand the cause of this, a simplified toy model, the Hermite-with-pole equation, was proposed by Boyd & Natarov (1998). They were able to determine

† Email address for correspondence: j.shelton@bath.ac.uk

the imaginary component of the associated eigenvalue through the application of an optical theorem. This equation was revisited by Shelton & Trinh (2022) to develop the associated exponential asymptotic theory as a precursor to this present work. However, the imaginary component of the eigenvalue to this model problem differs from (1.2) for the Kelvin wave. Numerical values for $\mathrm{Im}[c]$ were found Natarov & Boyd (2001), which indicated that $\mathrm{Im}[c] = O(\exp(-1/\epsilon^2))$. We demonstrate in this paper that this numerical prediction is incorrect, and that the correct value from equation (1.2) has an additional scaling factor of ϵ^3, which is difficult to detect numerically.

1.1. *Outline of the paper*

In §2, we derive the governing equations of the equatorial Kelvin wave for a specified background shear. Two formulations are derived, both of which contain an eigenvalue: the wave-speed, c. The first is a system of three equations for three unknowns, which we consider in §3, and the second is a single second-order differential equation for a single unknown, which we consider in §4 and §5. The asymptotic limit of small shear is considered with the intention of studying the imaginary component of the eigenvalue. First, in §3, we restrict the domain to take real values and perform a matched asymptotic procedure to determine $\mathrm{Im}[c]$; this is shown to be exponentially small. In §4 and §5, we use exponential asymptotic techniques to derive the exponentially small component of the eigenvalue, which is imaginary. This procedure requires the understanding of singularities in the asymptotic solution, and the connection between the consequent divergent series and the Stokes phenomenon that affects exponentially-small orders of the solution. We conclude in §6 and discussion of this work occurs in §7.

2. Mathematical formulation

We begin by considering a perturbation, Λy, to the zonal flow on the equatorial β-plane. The strength of the shear in this perturbation is Λ. The resultant equations are given by

$$u'_t + \Lambda y u'_x - (\beta y - \Lambda)v' = -p'_x, \tag{2.1a}$$
$$v'_t + \Lambda y v'_x + \beta y u' = -p'_y, \tag{2.1b}$$
$$p'_t + \Lambda y p'_x + c_\mathrm{e}^2(u'_x + v'_y) = 0, \tag{2.1c}$$

where $u'(x,y,t)$ and $v'(x,y,t)$ are the velocity perturbations, and $p'(x,y,t)$ is the pressure perturbation. Here, x and y are the longitudinal and latitudinal distances, respectively. The Coriolis parameter is β, and c_e is the speed of the base zonal flow. We will also impose the decay conditions as $|y| \to \infty$, given by

$$\left[u', v', p'\right] \to 0 \quad \text{as} \quad |y| \to \infty. \tag{2.1d}$$

We now nondimensionalise equations (2.1*a*)-(2.1*c*) with the length scale $L_\mathrm{d} = (c_\mathrm{e}/\beta)^{1/2}$, which is the equatorial radius of deformation, and timescale $L_\mathrm{d}/c_\mathrm{e}$. We also nondimensionalise velocities by c_e, and the pressure by c_e^2. This yields

$$u'_t + \epsilon y u'_x - (y - \epsilon)v' = -p'_x, \tag{2.2a}$$
$$v'_t + \epsilon y v'_x + y u' = -p'_y, \tag{2.2b}$$
$$p'_t + \epsilon y p'_x + u'_x + v'_y = 0, \tag{2.2c}$$

for which a single nondimensional parameter appears, given by

$$\epsilon = \frac{\Lambda}{\sqrt{\beta c_\mathrm{e}}}. \tag{2.3}$$

Since ϵ is proportional Λ, we will refer to it as the nondimensional shear. However, note that by the definition of the equatorial radius of deformation, $L_{\rm d} = (c_{\rm e}/\beta)^{1/2}$, we may also write $\epsilon = \Lambda L_{\rm d}/c_{\rm e}$ or $\epsilon = \Lambda/(\beta L_{\rm d})$. The first of these is a Froude number: the ratio of the background flow, $\Lambda L_{\rm d}$, with the base zonal flow, $c_{\rm e}$. The second is a Rossby number: the ratio of the vorticity induced by the shear, Λ, to the planetary vorticity, $\beta L_{\rm d}$. Within this paper we will be concerned with the limit of $\epsilon \to 0$.

We consider travelling wave solutions of the form

$$u' = \mathrm{Re}\Big[\hat{u}(y)\mathrm{e}^{\mathrm{i}k(x-ct)}\Big], \quad v' = \mathrm{Re}\Big[\mathrm{i}k\hat{v}(y)\mathrm{e}^{\mathrm{i}k(x-ct)}\Big], \quad p' = \mathrm{Re}\Big[\hat{p}(y)\mathrm{e}^{\mathrm{i}k(x-ct)}\Big]. \tag{2.4}$$

Here, k is the prescribed zonal wavenumber which will be both real and positive, and c is the phase speed. It is important to note that c will take complex values, for which the imaginary component will correspond to a growing (or decaying) mode of the solution. As we will find solutions for which the complex phase speed comes in complex conjugate pairs, there will always be a growing temporal instability for $\epsilon \neq 0$. In the limit of $\epsilon \to 0$, $\mathrm{Im}[c] = O(\epsilon^3 \mathrm{e}^{-1/\epsilon^2})$ and thus is exponentially-small in ϵ. The analytical derivation of this imaginary component of c is the main result of our paper. Substitution of the normal mode solutions (2.4) into the nondimensional equations (2.2*a*)-(2.2*c*) yields

$$(\epsilon y - c)\hat{u} - (y - \epsilon)\hat{v} = -\hat{p}, \tag{2.5a}$$
$$-k^2(\epsilon y - c)\hat{v} + y\hat{u} = -\hat{p}', \tag{2.5b}$$
$$(\epsilon y - c)\hat{p} + \hat{u} + \hat{v}' = 0, \tag{2.5c}$$

where primes ($\prime$) now denote differentiation in y. This is the system of equations used by Natarov & Boyd (2001) in their numerical investigation of the limit of $\epsilon \to 0$.

As $y \to \pm\infty$, the solutions of equations (2.5*a*)-(2.5*c*) decay with the behaviour of $\mathrm{e}^{-y^2/2}$. For convenience, we remove this behaviour from the solutions by writing

$$[\hat{u}(y), \hat{v}(y), \hat{p}(y)] = [u(y), v(y), p(y)]\mathrm{e}^{-y^2/2}. \tag{2.6}$$

It will be convenient to rewrite equations (2.5*a*)-(2.5*c*) as a single differential equation for one of the unknowns, much like that considered by Boyd (1978) [cf their equation (3.14)]. We therefore also make the substitution

$$q(y) = \frac{p(y) + u(y)}{2} \qquad \text{and} \qquad r(y) = \frac{p(y) - u(y)}{2}, \tag{2.7}$$

which yields

$$2(\epsilon y - c + 1)q(y) + v'(y) + (\epsilon - 2y)v(y) = 0, \tag{2.8a}$$
$$2(\epsilon y - c - 1)r(y) + v'(y) - \epsilon v(y) = 0, \tag{2.8b}$$
$$q'(y) + r'(y) - 2yr(y) - k^2(\epsilon y - c)v(y) = 0. \tag{2.8c}$$

In addition to these three equations, we also have the decay conditions as $|y| \to \infty$ from (2.1*d*), and a normalisation condition at $y = 0$. Written in terms of the solutions q, r, and v, these are given by

$$\Big[q(y), r(y), v(y)\Big]\mathrm{e}^{-y^2/2} \to 0 \quad \text{as} \quad |y| \to \infty, \tag{2.8d}$$

$$q(0) = v(0) = 1, \qquad r(0) = 0. \tag{2.8e}$$

This system of equations, (2.8*a*)-(2.8*e*) will be used throughout §3, in which we perform a matched asymptotic procedure along the real y-axis to determine $\mathrm{Im}[c]$. A consequence of enforcing boundary condition (2.8*e*) is that c will be determined as an eigenvalue of the problem.

2.1. *Single equation for $V(Y)$*

We now develop a single differential equation for just one of the unknowns in equations (2.8*a*)-(2.8*c*). Note that while each equation of system (2.5) depended on all three unknowns, equations (2.8*a*) and (2.8*b*) each have linear dependence on only two unknowns. Thus, we may substitute into (2.8*c*) expressions for $q(y)$ from (2.8*a*) and $r(y)$ from (2.8*b*) to obtain a single second order linear differential equation for $v(y)$. This resultant equation is similar to that derived by Griffiths (2008) for a general Coriolis force and base flow. We then pose this as an outer solution by rescaling with $Y = \epsilon y$, yielding

$$\begin{aligned}
&\epsilon^2\Big[-(Y-c-1)(Y-c+1)^2-(Y-c-1)^2(Y-c+1)\Big]V''(Y)\\
&+2Y\left[(Y-c-1)(Y-c+1)^2+(Y-c+1)(Y-c-1)^2+\frac{2\epsilon^2(Y-c)^2}{Y}\right]V'(Y)\\
&+\Big[-2Y(Y-c-1)(Y-c+1)^2+2(Y-c-1)^2(Y-c+1)-\epsilon^2(Y-c+1)^2\\
&\quad+(\epsilon^2-2Y)(Y-c-1)^2-2k^2(Y-c)(Y-c+1)^2(Y-c-1)^2\Big]V(Y)=0,
\end{aligned} \tag{2.9a}$$

where primes ($\prime$) denote differentiation in Y. The decay and boundary conditions are now given by

$$V(Y)\mathrm{e}^{-Y^2/2\epsilon^2} \to 0 \quad \text{as} \quad \mathrm{Re}[Y] \to \pm\infty, \tag{2.9b}$$

$$V(0) = 1. \tag{2.9c}$$

Note that we use a different choice of normalisation in the study of equation (2.9*a*), $V(0) = 1$, to that for the coupled system of equations (2.8), $q(0) = v(0) = 1$ and $r(0) = 0$. This has no effect on the eigenvalue, c.

Since in §4 we consider the analytic continuation of Y in order to study the Stokes phenomenon throughout $Y \in \mathbb{C}$, we have now specified decay condition (2.9*b*) to hold only for real values of Y. In fact, the decay condition will also be satisfied more generally for $|Y| \to \infty$ along wedges of $\arg[Y]$ that include $\mathrm{Re}[Y] \to -\infty$ and $\mathrm{Re}[Y] \to \infty$. The specification of these zones in more detail requires the understanding of the exponentially-small solution throughout the complex plane.

3. Along the axis matching for $Y \in \mathbb{R}$

We begin by solving equations (2.8*a*)-(2.8*e*) at each order of ϵ by expanding about the leading order solution of $q_0(y) = 1$, $r_0(y) = v_0(y) = 0$, and $c_0 = 1$ with the following asymptotic series

$$\begin{aligned}
q(y) &= 1 + \epsilon q_1(y) + \epsilon^2 q_2(y) + \cdots, & r(y) &= \epsilon r_1(y) + \epsilon^2 r_2(y) + \cdots,\\
v(y) &= \epsilon v_1(y) + \epsilon^2 v_2(y) + \cdots, & c &= 1 + \epsilon c_1 + \epsilon^2 c_2 + \cdots.
\end{aligned} \tag{3.1}$$

Note that since odd powers of the eigenvalue expansion are identically zero, we later expand in §4 as $c = 1 + \epsilon^2 c_1 + \cdots$. At $O(\epsilon)$, we find from (2.8*a*) an equation for $v_1(y)$, which has the solution $v_1(y) = 1 + 2c_1 e^{y^2}\int_{-\infty}^{y} \mathrm{e}^{-y^2}\,\mathrm{d}y$, where the constant of integration has been specified to satisfy the decay condition (2.8*d*) as $y \to -\infty$. In order to satisfy the same decay condition as $y \to \infty$, we then require $c_1 = 0$, yielding $v_1(y) = 1$. Solutions for $q_1(y)$ and $r_1(y)$ are then similarly found from equations (2.8*b*) and (2.8*c*), which gives

$$q_1(y) = -k^2 y, \qquad r_1(y) = 0, \qquad v_1(y) = 1, \qquad c_1 = 0. \tag{3.2}$$

Next, we proceed to $O(\epsilon^2)$ to find the first non-zero perturbative term, c_2, in the eigenvalue. The analysis proceeds similarly to that used to derive the $O(\epsilon)$ solutions (3.2), yielding

$$\begin{aligned} q(y) &= 1 - \epsilon k^2 y + \epsilon^2 \frac{(2k^4 + k^2 - 1)y}{4} + O(\epsilon^3), \qquad & r(y) &= -\epsilon^2 \frac{(1+k^2)}{4} + O(\epsilon^3), \\ v(y) &= \epsilon - \epsilon^2 k^2 y + O(\epsilon^3), & c &= 1 + \epsilon^2 \frac{1-k^2}{2} + O(\epsilon^3). \end{aligned} \tag{3.3}$$

This analysis may be continued to any algebraic order of ϵ, but the series expansion for the eigenvalue, c, will always be real-valued. The first non-zero imaginary component will be at an asymptotic order that is exponentially-small in ϵ. Typically, this would require a beyond-all-orders analysis in which understanding the Stokes phenomenon throughout $y \in \mathbb{C}$ is required. However, for this current problem it is sufficient to study the imaginary part of the solutions, which we consider next.

As the series expansions in (3.3) reorder as $y \to \infty$, we will introduce in §3.2 the outer variable, Y, defined by $Y = \epsilon y$. In addition to the boundary layer near $Y = 0$ presently studied, there will be another at $Y = 1$. In the following section we will therefore refer y as the inner variable near $Y = 0$.

3.1. *Inner solution near $Y = 0$*

We begin by studying the imaginary component of the solution. In writing $c = c_r + \mathrm{i}c_\mathrm{i}$, $q = q_r + \mathrm{i}q_\mathrm{i}$, $r = r_r + \mathrm{i}r_\mathrm{i}$, and $v = v_r + \mathrm{i}v_\mathrm{i}$, the imaginary components of equations (2.8*a*)-(2.8*c*) yield three equations for q_i, r_i, v_i, with eigenvalue c_i. These equations also involve q_r, r_r, v_r, and c_r, for which the leading order behaviours are already known from (3.3) to be $q_r = 1 + O(\epsilon)$, $r_r = -\epsilon^2(1+k^2)/4 + O(\epsilon^3)$, $v_r = \epsilon + O(\epsilon^2)$, and $c_r = 1 + O(\epsilon^2)$. In substituting for these, we also retain only the dominant behaviour as $\epsilon \to 0$ of the imaginary components of the solutions, yielding

$$2\epsilon y q_\mathrm{i}(y) + v_\mathrm{i}'(y) + -2y v_\mathrm{i}(y) = 2c_\mathrm{i}, \tag{3.4a}$$

$$-4r_\mathrm{i}(y) + v_\mathrm{i}'(y) = -\frac{\epsilon^2}{2}(1+k^2)c_\mathrm{i}, \tag{3.4b}$$

$$q_\mathrm{i}'(y) + r_\mathrm{i}'(y) - 2y r_\mathrm{i}(y) + k^2 v_\mathrm{i}(y) = -\epsilon k^2 c_\mathrm{i}. \tag{3.4c}$$

Since q_i, r_i, and v_i, all have the same asymptotic behaviour as $\epsilon \to 0$, the dominant component of equation (3.4) is $v_\mathrm{i}'(y) - 2y v_\mathrm{i}(y) = 2c_\mathrm{i}$. This may be integrated to find

$$v_\mathrm{i}(y) = 2c_\mathrm{i} \mathrm{e}^{y^2} \int_{-\infty}^{y} \mathrm{e}^{-y^2} \mathrm{d}y, \tag{3.5}$$

where the constant of integration is zero in order to satisfy the decay condition (2.8*d*) as $y \to -\infty$. We may then take the outer limit of $y \to \infty$ of (3.5) to find

$$v_\mathrm{i}(y) \sim 2\sqrt{\pi} c_\mathrm{i} \mathrm{e}^{y^2}. \tag{3.6}$$

This solution currently can not satisfy the decay condition as $y \to \infty$. this is because there is an additional boundary-layer in an outer region at $Y = 1$, across which the component (3.6) is switched off.

3.2. *The outer solution*

Motivated by the reordering of the asymptotic expansion, (3.3), as $y \to \infty$, we introduce the outer variable Y by the relation

$$Y = \epsilon y. \tag{3.7}$$

This outer problem is now considered to determine any boundary layers, in addition to that at $Y = 0$, arising in this problem. This will be demonstrated from the second-order differential equation for $V(Y)$, previously given in (2.9*a*). As $\epsilon \to 0$, the leading order solution is given by

$$V_0(Y) \sim \epsilon(1-Y)^{1/2} \exp\left(\frac{(1-2k^2)Y}{2} + \frac{k^2Y^2}{4}\right), \tag{3.8}$$

where the constant of integration has been specified to ensure that (3.8) matches as $Y \to 0$ to the early orders derived in (3.3).

We see that there is a branch point at $Y = 1$ in (3.8). Since later terms in the asymptotic expansion for $V(Y)$ will require differentiation of earlier orders, this branch point will turn into a singularity in the solution $V_1(Y)$, and cause a reordering of the asymptotic series as $Y \to 1$. We thus have an additional boundary layer at $Y = 1$ that will be considered in §3.3. In order to determine c_i, we will need to match the imaginary component of the outer solution to inner solutions near $Y = 0$ and $Y = 1$. We thus now study the imaginary component of the outer system of equations.

In substituting for $Y = \epsilon y$ in equations (2.8*a*)-(2.8*c*) and taking the imaginary part, we find

$$2\epsilon Y Q_\mathrm{i}(Y) + \epsilon^2 V_\mathrm{i}'(Y) + (\epsilon^2 - 2Y)V_\mathrm{i}(Y) = 2\epsilon c_\mathrm{i} Q_r(Y), \tag{3.9a}$$
$$2(Y-2)R_\mathrm{i}(Y) + \epsilon V_\mathrm{i}'(Y) - \epsilon V_\mathrm{i}(Y) = 2c_\mathrm{i} R_r(Y), \tag{3.9b}$$
$$\epsilon^2 Q_\mathrm{i}'(Y) + \epsilon^2 R_\mathrm{i}'(Y) - 2YR_\mathrm{i}(Y) - \epsilon k^2(Y-1)V_\mathrm{i}(Y) = -\epsilon k^2 c_\mathrm{i} V_r(Y), \tag{3.9c}$$

where the outer solutions are denoted by Q, R, and V. Since the dominant behaviour of these equations includes balances between $\epsilon^2 V_\mathrm{i}' = O(V_\mathrm{i})$ for instance, we consider WKB solutions of the form

$$[Q_\mathrm{i}(Y), R_\mathrm{i}(Y), V_\mathrm{i}(Y)] = [\hat{Q}_\mathrm{i}(Y), \hat{R}_\mathrm{i}(Y), \hat{V}_\mathrm{i}(Y)] \exp\left(\frac{\phi(Y)}{\epsilon^2}\right). \tag{3.10}$$

Matching with the outer limit of the inner solution near $Y = 0$, given in equation (3.6) requires $\phi(Y) = Y^2$, and also yields $\hat{V}_\mathrm{i} = O(c_\mathrm{i})$. Thus, since $V_r = O(1)$ for instance from (3.8), the terms on the left-hand side of equations (3.9*a*)-(3.9*c*) will be exponentially dominant over those on the right-hand side. This is because $V_\mathrm{i} = O(c_\mathrm{i} \mathrm{e}^{Y^2/\epsilon^2})$, and thus $V_\mathrm{i} \gg c_\mathrm{i}$ as $\epsilon \to 0$.

Equations for the leading order behaviour of the amplitude functions $\hat{Q}_\mathrm{i}(Y)$, $\hat{R}_\mathrm{i}(Y)$, and $\hat{V}_\mathrm{i}(Y)$, are then found to be given by

$$2Y\hat{Q}_\mathrm{i}(Y) + \epsilon \hat{V}_\mathrm{i}'(Y) + \epsilon \hat{V}_\mathrm{i}(Y) = 0, \tag{3.11a}$$
$$\epsilon(Y-2)\hat{R}_\mathrm{i}(Y) + Y\hat{V}_\mathrm{i}(Y) = 0, \tag{3.11b}$$
$$2Y\hat{Q}_\mathrm{i}(Y) + \epsilon^2 \hat{R}_\mathrm{i}'(Y) - \epsilon k^2(Y-1)\hat{V}_\mathrm{i}(Y) = 0. \tag{3.11c}$$

From equations (3.11*a*) and (3.11*c*), $\hat{Q}_\mathrm{i}$ may be eliminated to form a relationship between $\hat{R}_\mathrm{i}$ and $\hat{V}_\mathrm{i}$. We then substitute for $\hat{R}_\mathrm{i}$ from equation (3.11*b*) to find

$$\hat{V}_\mathrm{i}'(Y) + \frac{1}{2}\left[k^2(Y-2) + \frac{Y^2 - 4Y + 2}{(Y-1)(Y-2)}\right]\hat{V}_\mathrm{i}(Y) = 0. \tag{3.12}$$

Solving (3.12) then yields an outer solution given by

$$\begin{aligned} V_{\mathrm{i}}(Y) &= \frac{A(2-Y)\mathrm{e}^{-Y/2}\mathrm{e}^{-k^2(Y-2)^2/4}}{(1-Y)^{1/2}}\mathrm{e}^{Y^2/\epsilon^2}, \\ &= \frac{\sqrt{\pi}c_{\mathrm{i}}\mathrm{e}^{-Y/2}(2-Y)\mathrm{e}^{-k^2Y(Y-4)/4}}{(1-Y)^{1/2}}\mathrm{e}^{Y^2/\epsilon^2}, \end{aligned} \tag{3.13}$$

where A is a constant of integration, which has been determined as $A = \sqrt{\pi}c_{\mathrm{i}}\mathrm{e}^{k^2}$ by matching to (3.6) near $Y = 0$. Note the similarity between solution (3.13) and (5.12) derived later for the exponentially-small component of the outer solution. Since the leading order component of the imaginary solution is exponentially-small, these are equivalent.

3.3. *Inner solution near $Y = 1$*

Our goal is now to match the imaginary component of the outer solution (3.13) to an inner solution at $Y = 1$. To study this region, we introduce the inner variable, μ, given by

$$Y - 1 = \frac{\epsilon^2}{2}[\mu + (1-k^2)]. \tag{3.14}$$

Here, the width of the boundary layer is of $O(\epsilon^2)$, and we have written the relationship between the outer variable, Y, and inner variable, μ, in a particular form in order to obtain an inner equation with known special function solutions.

Substitution of relation (3.14) into the differential equation for $V(Y)$ from (2.9*a*) yields at leading order as $\epsilon \to 0$ the equation

$$\mu V''(\mu) - \mu V'(\mu) + \frac{1}{2}V(\mu) = 0. \tag{3.15}$$

This is the confluent hypergeometric equation, which is satisfied by any linear combination of the two solutions $M(-1/2, 0, \mu)$ and $U(-1/2, 0, \mu)$, yielding

$$V(\mu) = AM(-1/2, 0, \mu) + BU(-1/2, 0, \mu), \tag{3.16}$$

where A and B are constants. Note that the solution (3.16) will be complex valued, and as $\mu \to -\infty$ the imaginary component must match to the inner limit of (3.13) as $Y \to 1$. This is how we determine $\mathrm{Im}[c]$ in the next section.

3.4. *Matching and determination of Im$[c]$*

We now match the inner solution near $Y = 1$, derived in §3.3 as a combination of the special functions $U(-1/2, 0, \mu)$ and $M(-1/2, 0, \mu)$, with the outer solution from §3.2. The real part of the outer solution is given in equation (3.8), and the imaginary part in (3.13).

Firstly, we note that as $\mu \to \infty$, $U(-1/2, 0, \mu) = O(\mu^{1/2})$ and $M(-1/2, 0, \mu) = O(\mathrm{e}^{\mu}\mu^{-1/2})$. This exponential growth in the latter is unable to match to the outer solution for $Y > 1$, requiring $A = 0$ in (3.16). Next, since $U(-1/2, 0, \mu) \sim \mu^{1/2}$ as $|\mu| \to \infty$, we have that $V(\mu) \sim \pm \mathrm{i}B|\mu|^{1/2}$ as $\mu \to -\infty$. Here, the plus sign corresponds to the limit taken with $\arg[\mu] = \pi^-$, and the minus sign with $\arg[\mu] = -\pi^+$. This must match with the inner limit of $V_r(Y)$ from (3.8), yielding

$$V(\mu) = \pm\frac{\mathrm{i}\epsilon^2}{\sqrt{2}}\mathrm{e}^{(2-3k^2)/4}U(-1/2, 0, \mu). \tag{3.17}$$

We have now matched the dominant component of $V(\mu)$ to the real part of the outer solution as $\mu \to -\infty$. It remains to match the imaginary component, which will be exponentially-small, to (3.13) under the same limit. This requires knowledge of $\mathrm{Re}[U(-1/2, 0, \mu)]$ as $\mu \to -\infty$, which may be determined by the use of special function theory as $\mathrm{Re}[U(-1/2, 0, \mu)] \sim \mathrm{e}^{\mu}|\mu|^{-1/2}/2$. This yields

$$V_{\mathrm{i}}(\mu) \sim \pm \frac{\mathrm{i}\epsilon^2}{2\sqrt{2}|\mu|^{1/2}} \mathrm{e}^{(2-3k^2)/4} \mathrm{e}^{\mu}, \tag{3.18}$$

which we match to the inner limit of (3.13) to find

$$c_{\mathrm{i}} = \pm \frac{\epsilon^3 \mathrm{e}^{-k^2/2} \mathrm{e}^{-1/\epsilon^2}}{4\sqrt{\pi}}. \tag{3.19}$$

This analytical derivation of c_{i}, combined with the exponential asymptotics approach to find the same prediction in §5, is the main result of this paper. To summarise, we have constructed an outer solution holding for $0 < Y < 1$. This was matched to an inner solution at $Y = 0$, which is the only region in which c_{i} affects the imaginary component of the solution. We then matched the outer solution to a boundary layer at $Y = 1$, yielding c_{i} in (3.19).

4. Exponential asymptotics for $Y \in \mathbb{C}$

We now consider an asymptotic expansion for the solution and eigenvalue of the form

$$V(Y) = \sum_{n=0}^{\infty} \epsilon^{2n} V_n(Y) \qquad \text{and} \qquad c = \sum_{n=0}^{\infty} \epsilon^{2n} c_n, \tag{4.1}$$

for which we have expanded in powers of ϵ^2, which is the small parameter in the differential equation for $V(Y)$. Substituting expansions (4.1) into equation (2.9*a*) for $V(Y)$, we find at leading order in ϵ, $O(\epsilon^0)$, a first-order differential equation for $V_0(Y)$, which has the solution

$$V_0(Y) = A_0(c_0 - Y)^{\frac{1}{2c_0}} \mathrm{e}^{Y/2} \left[Y^{\frac{1}{2}(1-1/c_0)} + (1 - c_0) Y^{-\frac{1}{2}(1+1/c_0)} \right]. \tag{4.2}$$

This form either contains a singularity at $Y = 0$, or has the behaviour $V_0(Y) \to 0$ as $Y \to 0$, depending on the precise value of the eigenvalue, c_0. The exception to this is the choice of $c_0 = 1$, for which $V_0(Y)$ approaches a non-zero constant as $Y \to 0$. Thus, in order to apply the $O(1)$ boundary condition from (2.9*c*), $V_0(0) = 1$, we require that $c_0 = 1$, which yields $A_0 = 1$. This gives the $O(1)$ solution as

$$V_0(Y) = (1 - Y)^{\frac{1}{2}} \mathrm{e}^{Y/2} \qquad \text{and} \qquad c_0 = 1, \tag{4.3}$$

which is the same as that, with $k = 0$, derived in equation (3.8) with a different normalisation condition.

At the next order of equation (2.9*a*) we have terms of $O(\epsilon^2)$, from which we find a first-order differential equation for $V_1(Y)$. Similarly to that seen in the leading order solution eqrefeq:O1sol, this expression is singular at $Y = 0$ and is unable to satisfy the $O(\epsilon^2)$ boundary condition of $V_1(0) = 0$. Typically this would require a boundary-layer matching procedure for an inner solution at $Y = 0$, but we note that the issue is quickly resolved by the choice of $c_1 = (1 - k^2)/2$. This yields

$$V_1(Y) = \left(A_1(1 - Y)^{\frac{1}{2}} + \frac{(1 - Y)^{-1/2}}{16} \left[2 + 2(1 - Y) \log{(Y - 1)} \right] \right) \mathrm{e}^{Y/2}, \tag{4.4a}$$

$$c_1 = \frac{1}{2}. \tag{4.4b}$$

The above procedure may be extended repeatedly to any arbitrary order in ϵ^2, but the analysis becomes considerably more difficult. For instance, at $O(\epsilon^4)$ we are unable to solve the resultant first order differential equation for $V_2(Y)$ using a symbolic programming language. The singular behaviour for $V_2(Y)$ can however be extracted from this equation by considering the limit of $Y \to 0$. Imposition of the boundary condition, $V_2(0) = 0$, requires the singular behaviour near $Y = 0$ to cancel, which yields

$$c_2 = -\frac{1}{8}. \tag{4.5}$$

This difficulty encountered in solving for higher orders of the solution expansion analytically highlights the significance of our approach of §4.1 in which we solve for the leading-order divergent behaviour of $V_n(Y)$ and c_n as $n \to \infty$.

Note that $V_0(Y)$ contains a branch point of the form $V_0(Y) \sim (1-Y)^{1/2}$ as $Y \to 1$. Since the coefficients of the differential equation for $V_1(Y)$ contain derivatives of $V_0(Y)$, the next order of the solution has the singular behaviour of $V_1(Y) \sim (1-Y)^{-1/2}$. We therefore anticipate that the singular behaviour near $Y = 1$ of the asymptotic solution will be of the form

$$V_n(Y) = O\Big((1-Y)^{1/2-n}\Big). \tag{4.6}$$

This result can be proved by induction by working in an inner boundary layer at $Y = 0$, which we consider in Appendix A.

4.1. *Late-term divergence of the expansions*

We now seek to characterise the behaviour of the late-terms of expansions (4.1) for the solution, $V_n(Y)$, and the eigenvalue, c_n, under the limit of $n \to \infty$. At $O(\epsilon^{2n})$ in equations (2.9*a*) and (2.9*c*), we find the equation

$$\begin{aligned} &2Y(1-Y)(Y-2)V''_{n-1}(Y) + 4Y^2(Y-1)(Y-2)V'_n(Y) - (Y^2-2Y+2)V''_{n-2}(Y) \\ &+ 2Y(3Y^2-6Y+4)V'_{n-1}(Y) - 2Y^3(Y-2)V_n(Y) + \cdots \\ &\qquad = c_n\Big[\Big(2Y^3+2Y^2-8Y+8\Big)V_0(Y) - 4Y\Big(Y^2-2Y+2\Big)V'_0(Y)\Big], \end{aligned} \tag{4.7a}$$

and the boundary condition

$$V_n(0) = 0. \tag{4.7b}$$

In (4.7*a*) above, we have included on the left-hand side the two leading orders in n of the homogeneous terms that contribute to the divergence of $V_n(Y)$. On the right-hand side of (4.7*a*) we have retained only the leading order in n of the inhomogeneous forcing term involving the divergent eigenvalue, c_n.

4.2. *The naive divergence*

We begin by considering solutions to the homogeneous $O(\epsilon^{2n})$ equation,

$$\begin{aligned} 2Y(1-Y)(Y-2)V''_{n-1}(Y) + 4Y^2(Y-1)(Y-2)V'_n(Y) - (Y^2-2Y+2)V''_{n-2}(Y) \\ + 2Y(3Y^2-6Y+4)V'_{n-1}(Y) - 2Y^3(Y-2)V_n(Y) = 0, \end{aligned} \tag{4.8}$$

found by ignoring the forcing terms in (4.7*a*) that involve the late-terms of the eigenvalue. For this we follow the approach of *e.g.* Dingle (1973) and Chapman *et al.* (1998) and impose a typical factorial-over-power ansatz for the solution of the form

$$V_n(Y) \sim A(Y)\frac{\Gamma(n+\gamma)}{\chi(Y)^{n+\gamma}}. \tag{4.9}$$

Here, the singulant $\chi(Y)$ is responsible for the growing singular behaviour of $V_n(Y)$ as $n \to \infty$ shown in equation (4.6). The gamma function captures the factorial divergence of the solution, and $A(Y)$ is a functional prefactor. We also assume that γ is constant. With ansatz (4.9), the dominant singular behaviour as $n \to \infty$ of equation (4.8) is of $O(\chi^{-n-\gamma-1}\Gamma(n+\gamma+1))$. Dividing out by this divergence results in terms that are of $O(1)$, $O(n^{-1})$, and so forth.

At leading order, we find the following equation for the singulant,

$$\chi'(\chi' + 2Y) = 0. \tag{4.10}$$

Integrating the non-trivial solution and enforcing the condition $\chi(1) = 0$, required for matching with the inner region near the singularity at $Y = 1$ in Appendix A, we find

$$\chi(Y) = 1 - Y^2. \tag{4.11}$$

At $O(n^{-1})$ in (4.8), we find the equation

$$\frac{A'}{A} = -\frac{(Y^2 - 4Y + 2)}{2(Y-1)(Y-2)}, \tag{4.12}$$

which has the solution

$$A(Y) = \Lambda \frac{(Y-2)}{(1-Y)^{1/2}} \mathrm{e}^{-Y/2}. \tag{4.13}$$

Here, Λ is the constant of integration, which we determine in Appendix A by matching with an inner solution near the singularity at $Y = 1$.

The late-term boundary condition (4.7*b*) can not be satisfied by solution (4.13) alone, as it is unbounded as $Y \to 0$. This is because there are other components of the late-term representation of the solution, with $\chi_c' = 0$ from (4.10), currently neglected. We denote these constant values of the singulant by χ_c. Due to the linearity of the $O(\epsilon^{2n})$ equation, additional components of the late-term solution may be considered independently of one another. These are:

(i) Inhomogeneous contributions from the forcing term in the $O(\epsilon^{2n})$ equation (4.7*a*). The late-terms of the eigenvalue expansion will diverge in the factorial-over-power manner of

$$c_n \sim \delta \frac{\Gamma(n+\gamma_1)}{\Delta^{n+\gamma_1}}, \tag{4.14}$$

where δ and Δ are constants. Since particular solutions to (4.7*a*) are generated by the eigenvalue, c_n, they will be determined by substituting into the (4.7*a*) a factorial-over-power ansatz with $\chi_c = \Delta$;

(ii) Homogeneous solutions with $\chi_c' = 0$. Lower orders in n of the late-term solution are seen in §4.5 to reorder as $Y \to 0$. This necessitates the consideration of an inner solution, for which the associated inner-outer matching procedure requires outer homogeneous solutions with $\chi_c = \chi(0) = 1$.

We note that these solutions with $\chi_c' = 0$ are subdominant when matching to an inner solution near the singularity at $Y = 1$, since $\chi(Y) \to 0$ as $Y \to 1$. Thus, they do not affect the matching procedure that determines the constants γ and Δ, which are found next in §4.3.

4.3. *Determination of the constants γ and Λ*

It remains to determine the constants γ and Λ appearing in our naive factorial-over-power ansatz (4.9). These are determined by matching with an inner solution near the singularity at $Y = 1$. This singular behaviour forces a reordering in the early orders, $V_0 \sim \epsilon^2 V_1$, of the outer expansion (4.1) as $Y \to 1$, which we consider with an inner solution in Appendix A.

Firstly, the constant γ is determined by matching the inner limit of the factorial-over-power ansatz (4.9) with the anticipated singular scaling in the inner region from equation (4.6). This gives

$$-\Lambda e^{-1/2}(1-Y)^{-1/2}\frac{\Gamma(n+\gamma)}{[2(1-Y)]^{n+\gamma}} = O\Big((1-Y)^{1/2-n}\Big), \tag{4.15}$$

from which we compare the power of the singularity as $Y \to 1$ to find

$$\gamma = -1. \tag{4.16a}$$

Next, Λ is determined by matching the inner limit of $V_n(Y)$ with a series expansion for the outer-limit of the inner solution. This is performed in Appendix A, in which we find

$$\Lambda = -\frac{e}{2}\lim_{n\to\infty}\frac{a_n}{\Gamma(n-1)} = \frac{1}{4\pi}. \tag{4.16b}$$

Here, a_n is the coefficient of the nth term in a series expansion of the inner solution near $Y = 1$. It is determined by recurrence relation (A 8*c*), which we iterate to $n = 150$ numerically to find $\Lambda \approx 0.0079$.

4.4. *Stokes lines and the higher-order Stokes phenomenon*

In this section, we demonstrate that the late-term solution with $\chi(Y) = 1 - Y^2$ takes a more complicated form than that considered initially in §4.2 for the homogeneous equation. Typically, only the exponentially-small remainder to an optimally truncated divergent series will display the Stokes phenomenon, in which the functional form rapidly changes in magnitude across a boundary layer of diminishing width as $\epsilon \to 0$. However in our problem, the late terms themselves, $V_n(Y)$, display the Stokes phenomenon across a boundary layer with width of $O(n^{-1})$. This is known as the *higher-order Stokes phenomenon*, to which we refer the reader to the works of Howls *et al.* (2004), Chapman & Mortimer (2005), and Shelton & Trinh (2022).

We will instead consider the late-term divergence to take the modified form

$$V_n(Y) \sim \mathcal{S}(Y)A(Y)\frac{\Gamma(n+\gamma)}{\chi^{n+\gamma}}, \tag{4.17}$$

where $\mathcal{S}(Y)$ is the Stokes smoothing function that takes a value of $\mathcal{S}(Y) = 0$ for $\mathrm{Re}[Y] < 0$ and $\mathcal{S}(Y) = 1$ for $\mathrm{Re}[Y] > 0$. The contour $\mathrm{Re}[Y] = 0$ is a higher-order Stokes line, about which this transition in $\mathcal{S}(Y)$ occurs. Note that previously in the naive divergence (4.9), the singulant $\chi(Y) = 1 - Y^2$ took a value of zero at the locations of $Y = -1$ and $Y = 1$. This incorrectly predicted singularities in the late-terms at $Y = -1$, about which the early orders of §4 are regular. Since the late-terms are now "switched off" with $\mathcal{S}(Y) = 0$ at $Y = -1$ in equation (4.17), this issue is resolved.

It is necessary to consider this switching of the late-terms when the exponentially-small components of the asymptotic solution are determined in §5. This is because the Stokes phenomenon, in which the magnitude of these exponentially-small (in ϵ) terms rapidly changes across Stokes lines, is induced by forcing terms that rely on the late-term divergent solution, $V_n(Y)$. If the late-terms have been switched off in certain regions through the higher-order Stokes phenomenon, then any Stokes lines passing through this region will be inactive. The Stokes lines generated by $V_n(Y)$ are shown in figure 1, for which there are two interesting features to note:

(i) The Stokes line connecting $Y = -1$ and $Y = 0$ in inactive. This is due to the late-terms, $V_n(Y)$, being switched off for $\mathrm{Re}[Y], 0$ through the higher-order Stokes phenomenon;

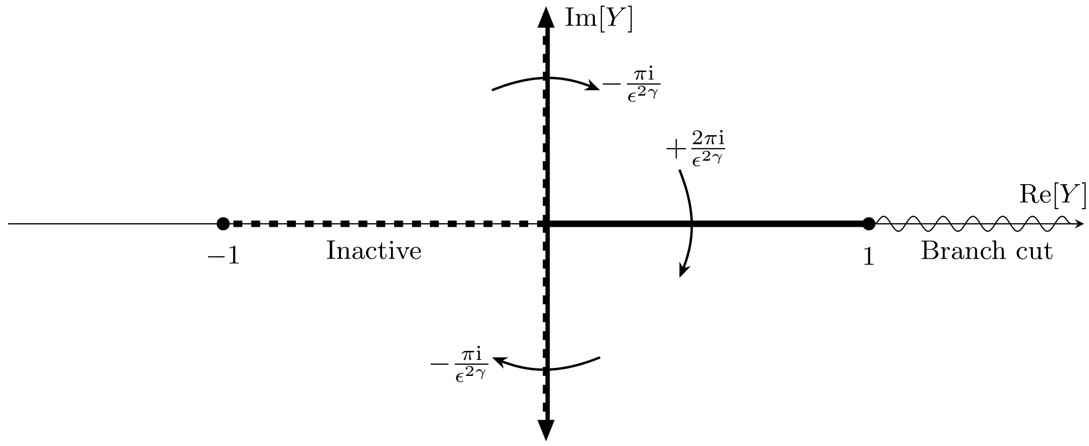

Figure 1: The final Stokes lines generated by the divergent series are shown. Active Stokes lines are shown with bold lines, and inactive Stokes lines dashed.

(ii) The Stokes line along the imaginary axis, $\mathrm{Re}[Y] = 0$, is partially active, as it coincides with the higher-order Stokes line across which the late-terms $V_n(Y)$ switch off.

4.5. *Reordering of the late-terms at $Y = 0$*

Recall that in §4 the early orders of the eigenvalue expansion were determined by enforcing boundary-condition (2.9*c*) at $Y = 0$ on the asymptotic solution. Our current late-term solution (4.17) alone is unable to satisfy this condition. This is because there is a boundary layer near $Y = 0$ that must be considered, which is generated by the reordering of the late-term solution as $Y \to 0$, which we now discuss.

The late-term solution will contain a boundary-layer of width $O(n^{-1/2})$ at $Y = 0$. To see this, one can derive lower orders, in n, of the naive divergence (4.9) by considering a factorial-over-power ansatz of the form

$$V_n(Y) \sim \left[A_0(Y) + \frac{A_1(Y)}{n} + \frac{A_2(Y)}{n^2} + \cdots\right]\frac{\Gamma(n+\gamma)}{\chi^{n+\gamma}}. \tag{4.18}$$

The method to derive the solutions $A_1(Y)$ and $A_2(Y)$ is similar to that considered in §4.2 for $A(Y) = A_0(Y)$. Lower order terms in the $O(\epsilon^{2n})$ equation must be retained, which yields at the subsequent orders in n equations for $A_1(Y)$ and $A_2(Y)$. Near $Y = 0$, these each have the singular scaling of

$$A_0(Y) = O(1), \qquad A_1(Y) = O(Y^{-1}), \qquad A_2(Y) = O(Y^{-3}). \tag{4.19}$$

As $Y \to 0$, the series first reorders for $n^{-1}A_1(Y) \sim n^{-2}A_2(Y)$, from which we introduce in equation (4.20) the inner variable $\hat{y}$ to study this reordering.

4.6. *An inner solution at $Y = 0$ for the late terms*

Since the late-terms, $V_n(Y)$, each reorder as $Y \to 0$, an inner problem must be considered in which we enforce boundary condition (2.9*c*). The associated inner variable, $\hat{y}$, is determined by the reordering of the late-terms from equations (4.18) and (4.19). This is given by

$$Y = \frac{\hat{y}}{n^{1/2}}, \tag{4.20}$$

where we will consider $\hat{y} = O(1)$ in the inner region. We now derive the inner equation for the inner solution $\widehat{V}(\hat{y})$ by substituting (4.20) into the $O(\epsilon^{2n})$ equation (4.7*a*) and expanding as $n \to \infty$. In retaining only the terms that will be seen to appear at leading order in n, we find

$$-\frac{n^{3/2}}{\hat{y}}\frac{\mathrm{d}^2\widehat{V}_{n-1}}{\mathrm{d}\hat{y}^2} + 2n^{1/2}\frac{\mathrm{d}\widehat{V}_n}{\mathrm{d}\hat{y}} + \frac{n^{3/2}}{\hat{y}^2}\frac{\mathrm{d}\widehat{V}_{n-1}}{\mathrm{d}\hat{y}} = \frac{2nc_n}{\hat{y}^2}. \tag{4.21}$$

To view the correct form for the inner solution $\widehat{V}(\hat{y})$ as $n \to \infty$, the inner limit of the outer solution is now considered. Since $\chi^{-(n+\gamma)} = (1 - n^{-1}\hat{y}^2)^{-(n+\gamma)} \sim \mathrm{e}^{\hat{y}^2}$ as $n \to \infty$, we find this to be

$$V_n \sim -2\Lambda\mathcal{S}(Y)\mathrm{e}^{\hat{y}^2}\Gamma(n+\gamma). \tag{4.22}$$

As the higher-order Stokes phenomenon will occur in a boundary layer of the same width in n as that considered currently for $\hat{y}$, we will have $\mathcal{S}(Y) = 1$ as $\mathrm{Re}[Y] \to 0^+$ and $\mathcal{S}(Y) = 0$ as $\mathrm{Re}[Y] \to 0^-$ under this inner limit.

Thus, to facilitate matching with (4.22), we consider an inner solution to (4.21) of the form

$$\widehat{V}_n(\hat{y}) = \widehat{R}(\hat{y})\Gamma(n+\gamma) \qquad \text{and} \qquad c_n \sim \delta\Gamma(n+\gamma-1/2). \tag{4.23}$$

In the above, we have also taken the divergent form for c_n from (4.14) with $\Delta = 1$ and $\gamma_1 = \gamma - 1/2$ to ensure that the divergent eigenvalue and solution both appear at leading order in the inner late-term equation (4.21). If this assumption is incorrect due to the eigenvalue balancing at lower orders of n, then we would expect to find $\delta = 0$, which would require the analysis of lower-order components of solutions (4.23).

Substitution of ansatzes (4.23) into the inner late-term equation (4.21) yields at leading order the second-order differential equation

$$\frac{\mathrm{d}^2\widehat{R}}{\mathrm{d}\hat{y}^2} - \left(2\hat{y} + \frac{1}{\hat{y}}\right)\frac{\mathrm{d}\widehat{R}}{\mathrm{d}\hat{y}} = -\frac{2\delta}{\hat{y}}, \tag{4.24}$$

which has the solution

$$\widehat{R}(\hat{y}) = \hat{B} + \hat{A}\mathrm{e}^{\hat{y}^2} + 2\delta\mathrm{e}^{\hat{y}^2}\int_0^{\hat{y}} \mathrm{e}^{-t^2}\,\mathrm{d}t. \tag{4.25}$$

Imposition of the inner boundary condition $\widehat{R}(0) = 0$ requires that $\hat{B} = -\hat{A}$. The outer limit of (4.25) is now taken for the two cases of $\hat{y} \to \infty$ and $\hat{y} \to -\infty$ in order to match with (4.22). This yields

$$\widehat{R}(\hat{y}) \sim \begin{cases} \left[\hat{A} + \sqrt{\pi}\delta\right]\mathrm{e}^{\hat{y}^2} + \cdots & \text{as } \hat{y} \to \infty, \\ \left[\hat{A} - \sqrt{\pi}\delta\right]\mathrm{e}^{\hat{y}^2} + \cdots & \text{as } \hat{y} \to -\infty, \end{cases} \tag{4.26}$$

where the result for $\hat{y} \to -\infty$ follows from that for $\hat{y} \to \infty$ due to the first integral in solution (4.25) for $\widehat{R}(\hat{y})$ being an odd function about $\hat{y} = 0$.

It is now possible to match the terms of $O(\mathrm{e}^{\hat{y}^2})$ in (4.26) with the inner limit of the outer solution in (4.22), which is performed in §4.7. We note that the omitted terms in the outer limit (4.26), which are of algebraic orders in $\hat{y}$ and also of $O(\log(\hat{y}))$, do not match to the inner limit of the factorial-over-power ansatz (4.22). Their matching requires the consideration of additional inhomogeneous components of the outer divergent solution, with $\chi' = 0$, which are not discussed further here.

4.7. *Matching and conclusions*

We now match the outer limit of the inner solution, from equation (4.26), with the inner limit of the outer factorial-over-power solution. Matching the terms of $O(\mathrm{e}^{\hat{y}^2})$ requires that

$$\hat{A} + \sqrt{\pi}\delta = -2\Lambda \qquad \text{and} \qquad \hat{A} - \sqrt{\pi}\delta = 0, \tag{4.27}$$

where the first equation above arose from matching as $\hat{y} \to \infty$ and the latter from $\hat{y} \to -\infty$. The solution of equations (4.27) is found to be

$$\hat{A} = -\Lambda \qquad \text{and} \qquad \delta = -\frac{\Lambda}{\sqrt{\pi}}. \tag{4.28}$$

We have thus determined the divergence of the eigenvalue to be of the form

$$c_n = -\frac{\Lambda}{\sqrt{\pi}}\Gamma(n + \gamma - 1/2). \tag{4.29}$$

5. Optimal truncation and Stokes smoothing

The goal of this section is to determine the exponentially-small solution and eigenvalue, which are found through optimal truncation of the divergent expansion derived in §4.1. Unlike the base asymptotic expansion for the eigenvalue, c, the exponentially-small component is imaginary valued, which corresponds to a growing temporal instability of the normal mode solution.

We will consider an asymptotic solution of the form

$$V(Y) = \underbrace{\sum_{n=0}^{N-1} \epsilon^{2n} V_n(Y)}_{\text{base expansion}} + \underbrace{B(Y)\mathrm{e}^{-1/\epsilon^2}}_{\chi_c=1} + \underbrace{A(Y)\mathrm{e}^{-(1-Y^2)/\epsilon^2}}_{\chi=1-Y^2}. \tag{5.1}$$

Here, the exponentially-small term with $\chi = 1 - Y^2$ displays the Stokes phenomenon through optimal truncation of the base series $V_n(Y)$, and that with $\chi_c = 1$ arises as a particular solution generated by the exponentially-small eigenvalue.

The exponentially-small component of the eigenvalue will be determined in §5.4 by matching the inner limit of the $\mathrm{e}^{-(1-Y^2)/\epsilon^2}$ exponential with the outer limit of an inner solution near $Y = 0$. However, this current problem displays a very unusual feature, in which the primary Stokes smoothing associated with optimal truncation of the base expansion, performed in §5.2, is insufficient in order to correctly determine the behaviour of the $\mathrm{e}^{-(1-Y^2)/\epsilon^2}$ exponential throughout the complex Y-plane. In fact, there is an additional Stokes switching generated by optimal truncation of an asymptotic expansion for $B(Y)$ in the $\mathrm{e}^{-1/\epsilon^2}$ exponential that also generates terms of order $\mathrm{e}^{-(1-Y^2)/\epsilon^2}$. In expanding

$$B(Y) = B_0(Y) + \epsilon^2 B_1(Y) + \cdots + \epsilon^{2N} B_N(Y) + C(Y)\mathrm{e}^{Y^2/\epsilon^2}, \tag{5.2}$$

there is a singularity at $Y = 0$ in $B_0(Y)$ which forces the divergence of the late-terms, $B_N(Y)$. In §5.3, we show that this new exponential is of order $\mathrm{e}^{Y^2/\epsilon^2}$, which when multiplied by the factor of $\mathrm{e}^{-1/\epsilon^2}$ yields a term of order $\mathrm{e}^{-(1-Y^2)/\epsilon^2}$.

Remark on terminology: Note that while the Stokes phenomenon generated by a divergent series expansion of an exponentially-small term is called the second-generation Stokes phenomenon, since the $\chi_c = 1$ exponential, $\mathrm{e}^{-1/\epsilon^2}$, in (5.8) is uniformly present across the domain, we refer to this as a base exponential for which there is an associated *secondary* Stokes phenomenon.

Both of these Stokes switchings together allow for determination of the exponentially-small eigenvalue when matched to the inner solution, which we discuss next in §5.1.

5.1. *The inner solution at $Y = 0$*

Analogous to the reordering of the late-terms near $Y = 0$ shown in (4.19), the outer solution for $A(Y)$ in (5.8) will also reorder as $Y \to 0$. To study the solution near $Y = 0$, we introduce the inner variable, y, defined by

$$Y = \epsilon y, \tag{5.3}$$

where $y = O(1)$ in the inner region. As the inner limit of the early orders of the outer expansion for $V(Y)$, obtained by substituting for $Y = \epsilon y$ and expanding as $\epsilon \to 0$, yields contributions to each order of ϵ, we consider an inner solution of the form

$$v_{\mathrm{inner}}(y) = \sum_{n=0}^{2N-2} \epsilon^n v_n(y) + \bar{v}(y) \qquad \text{and} \qquad c_n = \sum_{n=0}^{N-1} \epsilon^{2n} c_n + \bar{c}. \tag{5.4}$$

An inner equation for $v_{\mathrm{inner}}(y)$ may also be derived by substituting (5.3) into the outer equation (2.9*a*) for $V(Y)$. Substitution of the expansions (5.4) into this yields the following second-order differential equation for $\bar{v}(y)$, given by

$$\frac{\mathrm{d}^2\bar{v}}{\mathrm{d}y^2} - \left(2y + \frac{1}{y}\right)\frac{\mathrm{d}\bar{v}}{\mathrm{d}y} + \frac{2\bar{c}}{\epsilon y} = -\epsilon\bar{y}\bar{\xi}_{\mathrm{eq}}(y). \tag{5.5}$$

In the above, we have retained only the leading order terms, in ϵ, that involve $\bar{v}(y)$ and $\bar{c}$. The function $\bar{\xi}_{\mathrm{eq}}(y)$ on the right-hand side is a forcing term of order ϵ^{2N-1}, obtained by substituting the base expansions asymptotic expansions for $v(y)$ and c into the inner equation. However, unlike for the outer equation, the particular solution associated with the forcing term will be subdominant as $N \to \infty$ to the solution determined next, and is thus ignored.

The solution to equation (5.5) is

$$\bar{v}(y) = \bar{B} + \bar{A}\mathrm{e}^{y^2} + \frac{2\bar{c}\mathrm{e}^{y^2}}{\epsilon}\int_0^y \mathrm{e}^{-t^2}\,\mathrm{d}t, \tag{5.6}$$

where $\bar{A}$ and $\bar{B}$ are constants of integration. Next, imposing the boundary condition of $\bar{v}(0) = 0$, yields $\bar{B} = -\bar{A}$. We may now take the outer limit as $y \to \pm\infty$ of solution (5.6) to find

$$\bar{v}(y) \sim \begin{cases} \left[\bar{A} + \dfrac{\bar{c}\sqrt{\pi}}{\epsilon}\right]\mathrm{e}^{y^2} - \bar{A} - \dfrac{\bar{c}}{\epsilon y}\left(1 + \displaystyle\sum_{n=1}^{\infty}\frac{\Gamma(n+\frac{1}{2})}{\sqrt{\pi}(-y^2)^n}\right) & \text{as } y \to \infty, \\ \left[\bar{A} - \dfrac{\bar{c}\sqrt{\pi}}{\epsilon}\right]\mathrm{e}^{y^2} - \bar{A} - \dfrac{\bar{c}}{\epsilon y}\left(1 + \displaystyle\sum_{n=1}^{\infty}\frac{\Gamma(n+\frac{1}{2})}{\sqrt{\pi}(-y^2)^n}\right) & \text{as } y \to -\infty, \end{cases} \tag{5.7}$$

where we have included terms of $O(y^{-2n})$ which will later be required in §5.3 to determine the constant prefactor associated with the divergence that forces the secondary Stokes-switching. This form will be matched to the inner limit of an outer solution, determined in §5.2 and §5.3.

5.2. *The Stokes phenomenon induced by $V_n(Y)$*

In this section, we optimally truncate the divergent expansion (4.1) and study the Stokes phenomenon that occurs on the exponentially-small remainder. We consider the truncated asymptotic expansion and remainder for the solution, $V(Y)$, to be of the form

$$V(Y) = \sum_{n=0}^{N-1} \epsilon^{2n} V_n(Y) + \bar{V}(Y). \tag{5.8}$$

The optimal value of N is at the point where the series first reorders as $n \to \infty$. Balancing $V_n \sim \epsilon^2 V_{n+1}$ yields $N \sim |\chi(Y)|/\epsilon^2$, which we shift by the integer $\rho \in (0, 1]$ to ensure that N takes integer values. This yields

$$N = \frac{|\chi(Y)|}{\epsilon^2} + \rho. \tag{5.9}$$

Substitution of the truncated expansion (5.8) for $V(Y)$, and (5.4) for c into the governing equation (2.9*a*) yields an equation for $\bar{V}$ with eigenvalue $\bar{c}$. Terms of orders $\bar{c}^2$, and $\bar{c}\bar{V}$ are neglected as they are exponentially subdominant as $\epsilon \to 0$. Furthermore, since we anticipate solutions of the form $\bar{V}(Y) \sim \mathrm{e}^{-\chi/\epsilon^2}$, we neglect terms of $O(\epsilon^6)$ in the coefficient of $\bar{V}''$, $O(\epsilon^4)$ for $\bar{V}'$, and $O(\epsilon^2)$ for $\bar{V}$ to find

$$\begin{aligned}
&\Big[-2Y(Y-1)(Y-2)\epsilon^2 - (Y^2 - 2Y + 2)\epsilon^4\Big]\bar{V}'' \\
&+ (Y-1)\Big[4Y^2(Y-2) + 2(Y^3 - 2Y - 2)\epsilon^2\Big]\bar{V}' - 2Y^3(Y-2)\bar{V} \\
&+ \frac{2(Y-2)(2Y^2 - 3Y + 2) - 4k^2 Y(Y-2)(Y-1)^3}{(1-Y)^{1/2}}\mathrm{e}^{Y/2}\bar{c} = \xi_{\mathrm{eq}}.
\end{aligned} \tag{5.10}$$

In (5.10) above, ξ_{eq} is the forcing term obtained by substituting the truncated asymptotic expansions (5.8) into equation (2.9*a*). Since each order of this forcing term is identically satisfied up to and including $O(\epsilon^{2N-2})$, ξ_{eq} will be of $O(\epsilon^{2N})$. This yields

$$\xi_{\mathrm{eq}} \sim 2Y(Y-1)(Y-2)V''_{N-1}(Y)\epsilon^{2N}, \tag{5.11}$$

where we have retained only the leading order component as $N \to \infty$ at $O(\epsilon^{2N})$, which is V''_{N-1}.

We will now derive the form of the solution that displays the Stokes phenomenon across Stokes lines associated with the late terms, V_N, of the asymptotic expansion. Note that we will not consider the effect of the exponentially-small eigenvalue, $\bar{c}$, in this section; this will be considered when deriving the secondary generation smoothing in §5.3. We begin by considering the solution to the homogeneous equation, which is found from (5.10) by neglecting the forcing term ξ_{eq} and eigenvalue $\bar{c}$. This equation has solutions of the following WKB form,

$$\bar{V}_{\mathrm{homog}} = A(Y)\mathrm{e}^{-\chi(Y)/\epsilon^2}, \tag{5.12}$$

where $\chi(Y)$ and $A(Y)$ satisfy the same equations found for the late-term analysis in (4.10) and (4.12). Following the method established by Chapman *et al.* (1998), we will describe the Stokes phenomenon induced by the forcing term ξ_{eq} through variation of parameters by considering a solution of the form

$$\bar{V} = \mathcal{S}(Y)A(Y)\mathrm{e}^{-\chi(Y)/\epsilon^2}. \tag{5.13}$$

Here, $\mathcal{S}(Y)$ is the Stokes multiplier that will be seen to rapidly vary across the Stokes lines. Substitution of (5.13) into (5.10) yields on the left-hand side terms that are exponentially-small in ϵ. Since the leading order equation, at $O(\epsilon^{-2}\mathrm{e}^{-\chi/\epsilon^2})$, is identically satisfied due to our choice of $\chi = 1 - Y^2$, the first non-zero order on the left-hand side of (5.10) is of $O(\mathrm{e}^{-\chi/\epsilon^2})$. This will balance with the dominant component of ξ_{eq} as $\epsilon \to 0$ from (5.11) to form a first order differential equation for $\mathcal{S}(Y)$. Upon changing variables from Y to χ, terms involving $2Y(Y-1)(Y-2)A(Y)(\chi')^2$ cancel, and we find

$$\frac{\mathrm{d}\mathcal{S}}{\mathrm{d}\chi} \sim \epsilon^{2N}\frac{\Gamma(N+\gamma+1)}{\chi^{N+\gamma+1}}\mathrm{e}^{\chi/\epsilon^2}. \tag{5.14}$$

This equation for $\mathcal{S}(\chi)$ is now of a similar form to that found by Chapman & Vanden-Broeck (2006). We use Stirling's approximation to expand the gamma function in (5.14) as $N \to \infty$, and substitute for the optimal value of $N = |\chi|/\epsilon^2 + \rho$ from (5.9). In writing $\chi = r\mathrm{e}^{\mathrm{i}\theta}$, this yields a differential equation for $\mathcal{S}(\theta)$ that rapidly changes in form across a boundary layer at $\theta = 0$. This is the Stokes phenomenon along the anticipated contours of $\mathrm{Im}[\chi] = 0$ and $\mathrm{Re}[\chi] \geqslant 0$. The resultant equation for the Stokes prefactor, $\mathcal{S}(Y)$, has the solution of

$$\mathcal{S}(Y) = S_1 + \frac{\sqrt{2\pi}\mathrm{i}}{\epsilon^{2\gamma}}\int_{-\infty}^{\frac{\sqrt{r}\theta}{\epsilon}} \exp\left(-t^2/2\right)\mathrm{d}t, \tag{5.15}$$

where S_1 is a constant. As $\epsilon \to 0$, we see that there is a jump in the expected value of $\mathcal{S}(Y)$ that depends on the sign of θ. For $\theta < 0$, $\mathcal{S}(Y) \to S_1$, and for $\theta > 0$, we integrate the error function to find $\mathcal{S}(Y) \to S_1 + \frac{2\pi\mathrm{i}}{\epsilon^{2\gamma}}$. Thus, we have predicted the jump condition of

$$\mathcal{S}(\theta \to 0+) - \mathcal{S}(\theta \to 0-) = \frac{2\pi\mathrm{i}}{\epsilon^{2\gamma}}, \tag{5.16}$$

where the change occurs smoothly in a boundary layer of width $O(\epsilon)$ about $\theta = 0$.

Note that this condition of $\theta = 0$ and $r > 0$ is equivalent to the Dingle conditions of

$$\mathrm{Im}[\chi] = 0 \qquad \text{and} \qquad \mathrm{Re}[\chi] \geqslant 0, \tag{5.17}$$

which are satisfied along the real axis between $Y = -1$ and $Y = 1$, and the entire imaginary axis. However, due to the higher-order Stokes phenomenon detailed in §4.4, the Stokes line between $Y = -1$ and $Y = 0$ is inactive, and that along the imaginary axis is half-active. These Stokes lines are shown in figure 1, and are also shown alongside additional Stokes lines, generated by the particular solution associated with $\bar{c}$, in figure 2, which we derive next in §5.3.

5.3. *The Stokes phenomenon induced by $\bar{c}$*

Previously in §5.2, we derived the Stokes phenomenon displayed by the exponential $\mathrm{e}^{-(1-Y^2)/\epsilon^2}$ that is forced by the base asymptotic series. However, as briefly discussed at the beginning of §5, there is another Stokes switching that occurs on the prefactor of an $\mathrm{e}^{-1/\epsilon^2}$ exponential generated as a particular solution from $\bar{c}$ in equation (5.10). This new switching also yields terms of order $\mathrm{e}^{-(1-Y^2)/\epsilon^2}$. In conjunction with the classical Stokes smoothing of the previous section, this allows for determination of the exponentially-small eigenvalue, $\bar{c}$.

The particular solution of equation (5.10) is

$$\bar{V}(Y) \sim -\frac{\bar{c}}{Y(1-Y)^{1/2}} \qquad \text{as } Y \to 0, \tag{5.18}$$

which contains a singularity at $Y = 0$. One may also consider lower orders of this particular solution with an expansion of the form

$$\bar{V}(Y) = \bar{c}\sum_{n=0}^{\infty}\epsilon^{2n}B_n(Y). \tag{5.19}$$

Since determination of the next order solution, $B_1(Y)$, requires differentiation of the leading order solution $B_0(Y) = -Y^{-1}(1-Y)^{-1/2}$ from (5.18), the power of the singularity at $Y = 0$ will grow. This results in a divergent series, which we capture with the factorial-over-power ansatz of

$$B_n(Y) \sim \tilde{A}(Y)\frac{\Gamma(n+\tilde{\gamma})}{\tilde{\chi}(Y)^{n+\tilde{\gamma}}}. \tag{5.20}$$

Here, $\tilde{A}$ and $\tilde{\chi}$ are functions of the domain, Y, and $\tilde{\gamma}$ is a constant. Since the solution expansion (5.23) has a value of $\chi' = 0$ within the exponentially-small eigenvalue $\bar{c}$, the equations for $\tilde{\chi}$ and $\tilde{A}$ will be the same as that found for the divergence of the base asymptotic series in §4.2. These are equations (4.10) and (4.12), which we integrate to find

$$\tilde{\chi}(Y) = -Y^2 \qquad \text{and} \qquad \tilde{A}(Y) = \tilde{\Lambda}\frac{(Y-2)}{(1-Y)^{1/2}}\mathrm{e}^{-Y/2}. \tag{5.21}$$

Here, $\tilde{\Lambda}$ is a constant of integration (not necessarily the same as that for $A(Y)$ in (4.12)), and the constant of integration for $\tilde{\chi}$ has been set to zero to satisfy the condition $\tilde{\chi}(0) = 0$.

The constants associated with this divergent form, $\tilde{\gamma}$ and $\tilde{\Lambda}$ may be determined by matching the inner limit of (5.20), with $Y = \epsilon y$, with an inner solution found in §5.1. This is analogous to the matching procedure near $Y = -1$ performed in Appendix A to determine the constants associated with the base divergent series. This yields

$$\tilde{\gamma} = \frac{1}{2} \qquad \text{and} \qquad \tilde{\Lambda} = \frac{\mathrm{i}}{2\sqrt{\pi}}. \tag{5.22}$$

Next, we optimally truncate expansion (5.23) and consider an exponentially-small remainder, $\bar{B}$ by writing

$$\bar{V}(Y) = \bar{c}\left[\sum_{n=0}^{N-1}\epsilon^{2n}B_n(Y) + \bar{B}(Y)\right]. \tag{5.23}$$

This Stokes phenomenon displayed by this remainder is denoted the secondary Stokes phenomenon, as it is forced by an exponentially-small term, as opposed to the base asymptotic expansion. There will be secondary Stokes lines whenever the Dingle conditions of

$$\mathrm{Im}[\tilde{\chi}] = 0 \qquad \text{and} \qquad \mathrm{Re}[\tilde{\chi}] \geqslant 0, \tag{5.24}$$

are satisfied. Moreover, the direction of the switching will be from regions where $\arg[\chi] < 0$ to $\arg[\chi] > 0$. This occurs along the imaginary axis, which is shown in figure 2.

5.4. *Determination of $\bar{c}$*

We now determine the exponentially-small eigenvalue by combining the primary Stokes switching results of §5.2 with those derived in §5.3 for the secondary Stokes switching. Since we require the solution to decay as $Y \to -\infty$, there will be no exponentially-small terms present when $Y < 0$. There are now two ways to proceed to determine the exponentially-small eigenvalue:

(i) We can match along the axis to determine $\bar{c}$. This is the method employed in §3, where we note that the inner solution near $Y = 0$ must decay to zero as we take the outer limit of $y \to -\infty$. This yields an outer limit as $y \to \infty$ of $\bar{v} \sim 2\epsilon^{-1}\bar{c}\sqrt{\pi}\mathrm{e}^{y^2}$ in equation (5.7). When matched to an outer solution obtained from half of the contribution from the $\mathrm{Re}[Y] > 0$ Stokes line, this yields the prediction in equation (5.28);

(ii) The contributions from the primary and secondary Stokes lines must cancel due to the decay conditions.

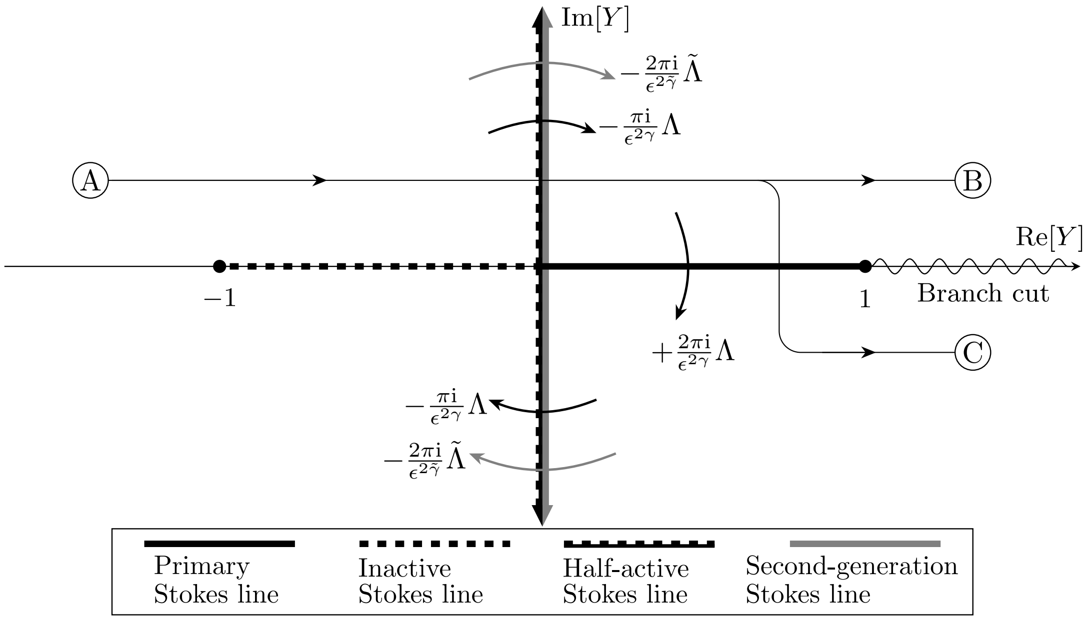

Figure 2: A

It is this second method which we will employ in this section. This is visualised in figure 2, for which we note that there is a subtle choice of which Riemann sheet the decay conditions as $Y \to \infty$ are evaluated on. In starting at point A in figure 2, passing across the imaginary axis yields a contribution of $-\pi i\epsilon^{-2\gamma}\Lambda$ from the primary Stokes line, and $-2\pi i\epsilon^{-2\tilde{\gamma}}\tilde{\Lambda}$ from the secondary Stokes line. We may then stay on the same Reimann sheet and evaluate the decay condition as $Y \to \infty$ at point B, which requires these two contributions to cancel. Alternatively, we may enter the other Riemann sheet associated with the branch point at $Y = 1$ by passing through the $0 < \text{Re}[Y] < 1$ primary Stokes line. The decay condition at point C then requires that the three contributions of $-\pi i\epsilon^{-2\gamma}\Lambda$, $-2\pi i\epsilon^{-2\tilde{\gamma}}\tilde{\Lambda}$, and $2\pi i\epsilon^{-2\gamma}\Lambda$ cancel. This yields a similar prediction for $\bar{c}$, but with a minus sign.

Across the primary Stokes line, we switch on a solution of the form

$$\bar{V}(Y) \sim -\frac{\pi i\Lambda}{\epsilon^{2\gamma}}\frac{(Y-2)}{(1-Y)^{1/2}}e^{-Y/2}e^{-(1-Y^2)/\epsilon^2}, \tag{5.25}$$

and across the secondary Stokes line

$$\bar{V}(Y) \sim -\frac{2\pi i\tilde{\Lambda}}{\epsilon^{2\tilde{\gamma}}}\frac{(Y-2)}{(1-Y)^{1/2}}e^{-Y/2}e^{Y^2/\epsilon^2}\bar{c}, \tag{5.26}$$

switches on. Thus, for the exponentially-small terms to decay as $Y \to \pm\infty$, we require these two contributions to cancel. Since $\gamma = -1$ and $\Lambda = 1/(4\pi)$ from equation (4.16), and $\tilde{\gamma} = 1/2$ and $\tilde{\Lambda} = i/(2\sqrt{\pi})$ from (5.22), we have

$$\bar{c} = \frac{\Lambda}{-2\tilde{\Lambda}}\epsilon^{2(\tilde{\gamma}-\gamma)}e^{-1/\epsilon^2} = \frac{i}{4\sqrt{\pi}}\epsilon^3 e^{-1/\epsilon^2}. \tag{5.27}$$

This is the result for evaluation of the decay condition as $Y \to \infty$ on the Riemann sheet associated with the point B in figure 2. Alternatively, one may evaluate the decay condition at point C on another Riemann sheet, which requires crossing the $0 < \text{Re}[Y] < 1$ Stokes line. This yields a similar prediction for $\bar{c}$ as in (5.27) above, but with a minus sign. Thus, we have derived the complex conjugate pairs of $\bar{c}$, given by

$$\bar{c} = \pm \frac{\mathrm{i}}{4\sqrt{\pi}} \epsilon^3 \mathrm{e}^{-1/\epsilon^2}. \tag{5.28}$$

6. Conclusions

We have analytically determined the imaginary component of the eigenvalue for weak latitudinal shear, ϵ, of the equatorial Kelvin wave. Since the eigenvalue, c, is the phase speed of the travelling wave solutions (2.4), the imaginary component which is exponentially small in ϵ corresponds to a growing temporal instability in the solution. We have employed the following two methods:

(i) Firstly in §3, we restricted the domain, Y, to be real valued. Since the asymptotic expansions for the solution and eigenvalue are then real valued to each algebraic order of ϵ, we have been able to study the imaginary components of the governing equations to extract information about c_{i}. The associated matching procedure to $Y = 0$ and $Y = 1$ then yielded prediction (3.19) for c_{i}.

(ii) Secondly, in §4 and §5, we considered complex values of Y in order to study the Stokes phenomenon and associated Stokes lines, which yield the exponentially-small solution throughout $Y \in \mathbb{C}$. The analysis is difficult, and requires understanding of the higher-order Stokes phenomenon, divergent eigenvalue expansions, and boundary layers of diminishing width as $n \to \infty$ in the late-terms of the asymptotic expansion $V(Y) = \sum_{n=0}^{\infty} \epsilon^{2n} V_n(Y)$.

7. Discussion

Unlike most instability problems in fluid dynamics such as those that are unstable when the Reynolds number exceeds a certain value, the equatorial Kelvin wave is unstable no matter how small we take the latitudinal shear, ϵ. Higher solution modes however, the equatorial Rossby waves, are stable under this limit. Whether this exponentially-small critical latitude instability occurs for other geophysical problems is not clear.

The exponential asymptotic approach of §4 and §5 required the consideration of additional divergent effects that influenced the exponentially-small component of our asymptotic solution. In addition to the Stokes phenomenon generated by the divergent asymptotic series of the solution, studied in §5.2, there was another Stokes phenomenon effect that contributed to terms of the same order, $O(\mathrm{e}^{-(1-Y^2)/\epsilon^2})$. Derived in §5.4, this was generated by a particular solution forced by the exponentially-small component of the eigenvalue. The asymptotic expansion for this particular solution, of $O(\mathrm{e}^{-1/\epsilon^2})$, diverged and upon optimal truncation yielded an exponentially small remainder of $O(\mathrm{e}^{Y/\epsilon^2})$. This is similar to the second-generation switching discussed by Chapman & Mortimer (2005), which is a further Stokes phenomenon induced by an exponentially-small term that itself was switched on by the base asymptotic series.

Acknowledgements. P.H.T. is supported by the Engineering and Physical Sciences Research Council [EP/V012479/1].

Declaration of interests. The authors report no conflict of interest.

Appendix A. Inner analysis at the singularity, $Y = 1$

The constant prefactor, Λ, of the naive late-term solution (4.9) is determined by matching with an inner solution near the singularity at $Y = 1$. Close to this point, the early orders of the asymptotic expansion reorder as $V_0(Y) \sim \epsilon^2 V_1(Y)$. Since $V_0(Y) = O((1-Y)^{1/2})$ and $V_1(Y) = O((1-Y)^{-1/2})$ by taking the limit of $Y \to 1$ in equations (4.3) and (4.4*a*), the width of the boundary layer is of ϵ^2. We thus introduce the inner variable, $\bar{y}$, by the relation

$$(1-Y) = -\epsilon^2 \bar{y}, \tag{A 1}$$

for which $\bar{y} = O(1)$ in the inner region. To observe the correct scaling to take for the inner solution, we take the inner limit of the first order of the outer solution by substituting for $\bar{y}$ from (A 1) and taking the limit of $\epsilon \to 0$. This yields

$$V_0(Y) \sim \epsilon(-\bar{y})^{1/2}\mathrm{e}^{1/2}, \tag{A 2}$$

where we have retained only the leading order terms in ϵ. We may also take the inner limit of our factorial-over-power solution, which yields

$$\epsilon^{2n} V_n(Y) \sim -\epsilon\sqrt{2}\Lambda \mathrm{e}^{-1/2} \frac{\Gamma(n-1)}{(-2\bar{y})^{n-1/2}}. \tag{A 3}$$

Motivated by the form of the inner limit of $V_0(Y)$ in (A 2), we define the inner solution, $\bar{V}(\bar{y})$, by the relation

$$V_{\mathrm{outer}} = \epsilon(-\bar{y})^{1/2}\mathrm{e}^{1/2}\bar{V}_{\mathrm{inner}}. \tag{A 4}$$

We will consider in §A.1 a series expansion for the outer limit of the inner solution, $\bar{V}_{\mathrm{inner}}$, in order to match with (A 3). In taking

$$z = -2\bar{y}, \tag{A 5}$$

the resultant expansion will be in integer powers of z^{-1}.

A.1. *Inner solution*

We now derive the inner equation for $\bar{V}(z)$. Only the leading order, as $\epsilon \to 0$, of the inner solution needs to be considered to match with the inner limit of $\epsilon^{2n}V_n(Y)$ given in (A 3). We substitute for $z = 2(1-Y)/\epsilon^2$ and $\bar{V}$ from (A 4) into the outer equation (2.9*a*) for $V(Y)$, and retain only the leading order as $\epsilon \to 0$, yielding

$$4z^2(z+1)\frac{\mathrm{d}^2\bar{V}}{\mathrm{d}z^2} + 4z(z+1)^2\frac{\mathrm{d}\bar{V}}{\mathrm{d}z} + (z-1)\bar{V}(z) = 0. \tag{A 6}$$

Now we determine the outer-limit, as $z \to \infty$, of the inner solution with a series expansion of the form

$$\bar{V}(z) = \sum_{n=0}^{\infty} \frac{a_n}{z^n}. \tag{A 7}$$

Substitution of (A 7) into the inner equation (A 6) yields equations at each order of z^{-n}. These are

$$4a_1 = a_0, \tag{A 8a}$$

$$8a_2 = a_1 - a_0, \tag{A 8b}$$

$$4(n+1)a_{n+1} = (2n-1)^2 a_n + (2n-3)(2n-1)a_{n-1} \quad \text{for } n \geqslant 2. \tag{A 8c}$$

In matching the inner limits of $V_0(Y)$ and $\epsilon^2 V_1(Y)$ from (A 2) with (A 7) to determine a_0 and a_1, we find

$$a_0 = 1, \qquad a_1 = \frac{1}{4}, \qquad a_2 = -\frac{3}{32}, \tag{A 9}$$

where a_2 above was found from equation (A 8*b*). Values for a_n may the be found numerically by iterating recurrence relation (A 8*c*) to large values of n. With equation (A 4) we can compare the nth order of the inner solution to that of the inner limit of the outer solution from (A 3). This yields

$$-\epsilon \frac{\sqrt{2}\Lambda \mathrm{e}^{-1/2}\Gamma(n-1)}{z^{(n-1/2)}} = \epsilon \left(\frac{z}{2}\right)^{1/2} \mathrm{e}^{1/2} \frac{a_n}{z^n}, \tag{A 10}$$

which we may rearrange and consider the limit of $n \to \infty$ to determine the constant Λ as

$$\Lambda = -\frac{\mathrm{e}}{2} \lim_{n\to\infty} \frac{a_n}{\Gamma(n-1)}. \tag{A 11}$$

Numerically we iterate recurrence relation (A 8*c*) to $n = 150$ to find $\Lambda \approx 0.079$.

REFERENCES

Boyd, J. P. 1978 The effects of latitudinal shear on equatorial waves. part i: Theory and methods. *J. Atmos. Sci.* **35** (12), 2236–2258.

Boyd, J. P. & Christidis, Z. D. 1982 Low wavenumber instability on the equatorial beta-plane. *Geophs. Res. Lett.* **9** (7), 769–772.

Boyd, J. P. & Natarov, A. 1998 A sturm–liouville eigenproblem of the fourth kind: A critical latitude with equatorial trapping. *Stud. Appl. Math.* **101** (4), 433–455.

Chapman, S. J., King, J. R. & Adams, K. L. 1998 Exponential asymptotics and Stokes lines in nonlinear ordinary differential equations. *Proc. R. Soc. Lond. A* **454**, 2733–2755.

Chapman, S. J. & Mortimer, D. B. 2005 Exponential asymptotics and Stokes lines in a partial differential equation. *Proc. R. Soc. A* **461** (2060), 2385–2421.

Chapman, S. J. & Vanden-Broeck, J.-M. 2006 Exponential asymptotics and gravity waves. *J. Fluid Mech.* **567**, 299–326.

Dingle, R. B. 1973 *Asymptotic Expansions: Their Derivation and Interpretation*. Academic Press, London.

Griffiths, S. D. 2008 The limiting form of inertial instability in geophysical flows. *J. Fluid Mech.* **605**, 115–143.

Howls, C. J., Langman, P. J. & Daalhuis, A. B. Olde 2004 On the higher-order Stokes Phenomenon. *Proc. R. Soc. Lond. A* **460**, 2285–2303.

Natarov, A. & Boyd, J. P. 2001 Beyond-all-orders instability in the equatorial kelvin wave. *Dynam. atmos. oceans* **33** (3), 191–200.

Shelton, J. Chapman, S. J. & Trinh, P. H. 2022 Pathological exponential asymptotics for a model problem of an equatorially trapped rossby wave. *In Preperation* .

9 DISCUSSION AND FUTURE WORK

9.1 Summary of thesis

We have demonstrated the crucial role that exponentially-small effects play in water waves. Firstly, the small surface tension limit considered in **Part I** contained high-frequency parasitic ripples, whose amplitude was seen to be exponentially small in the surface tension parameter. This was demonstrated numerically for steadily travelling waves in chapter 3 and standing waves in chapter 5. In these chapters, portions of the bifurcation structure were computed numerically for small surface tension. The analytical work of chapter 4 required the use of exponential asymptotic techniques in order to study these exponentially small parasitic ripples for the steadily travelling formulation.

Motivated by the potential influence of divergent eigenvalues, in **Part II**, we developed exponential asymptotics for two model problems exhibiting this feature. In particular, we studied the limit of vanishing latitudinal shear for the equatorial Kelvin wave. No matter how small this shear was taken, the travelling wave was seen to be unstable. This analysis also required the use of exponential asymptotic techniques, as the instability arose from the imaginary component of the eigenvalue (wavespeed), which was seen to be exponentially small with respect to the weak shear.

Future extensions to the work performed throughout this thesis are now discussed.

9.2 The inclusion of viscosity

In chapter 3, we considered steadily travelling gravity-capillary waves in the absence of viscous effects. Consequently, the numerical solutions found were symmetric with parasitic ripples located on both sides of the wave crest. Experimental solutions however are asymmetric as the parasitic ripples are predominantly located ahead of the crest of the travelling water wave. This could be attributed to any of the physical effects we have neglected, such as viscosity, vorticity, and time dependence. We note that previous authors, such as Longuet-Higgins (1992), Fedorov and Melville (1998), Dias et al. (2008), and Milewski and Wang (2016), have developed models to include the effect of viscosity in a boundary layer near the wave surface. This results in similar dynamic and kinematic boundary conditions for the free surface, but now with a Reynolds number, R_e, multiplying a viscous term, in addition to the Froude, F, and Bond, B, numbers.

This formulation was solved numerically by Fedorov and Melville (1998), who considered steadily travelling solutions for which a pressure forcing was necessary to counteract the viscous dissipation. They presented a few very interesting numerical solutions that, for small surface tension, contained parasitic ripples located ahead of the wave crest. Visually, these solutions agree well with the experimental profiles calculated by Perlin et al. (1993).

It is therefore interesting to ask whether any self-similar bifurcation structure emerges, much like our inviscid investigation of chapter 3, for fixed energy in this viscous formulation. Would the resultant solutions contain parasitic ripples that are exponentially small as the surface tension tends to zero? If so, the resultant exponential asymptotic theory, analogous to our chapter 4, for the determination of these might also produce a solvability condition that forbids certain combinations of values of the speed, c, and wavelength, λ.

9.3 Temporally periodic travelling waves

In chapter 5, we computed a portion of the bifurcation structure of gravity-capillary standing waves. We began this investigation with a more general formulation posed by Wilkening (2021) that contained a travelling/standing parameter, β, for temporally periodic solutions. With $\beta = \pi/2$, standing waves were found; for $\pi/2 > \beta > \pi/4$ travelling/standing waves emerged; and $\beta = \pi/4$ characterised travelling solutions.

Our steadily travelling solutions of chapters 3 and 4 trivially fall into this classification for $\beta = \pi/2$. It is unclear however whether if for $\beta = \pi/4$ there also contain unsteady travelling waves that are temporally periodic. The asymptotic characterisation of these solutions for small surface tension would contain a steadily travelling leading order solution, with unsteadiness first appearing at either algebraic or exponentially-small orders of the surface tension.

Previous authors, such as Jervis (1996) and Murashige and Choi (2017), have studied a similar formulation of this problem. In considering the time-evolution system with an initial condition of a steadily travelling gravity wave at $t = 0$, they subsequently "switched on" the surface tension to a constant value for $t > 0$. Parasitic capillary ripples were observed to develop on the forward face of the solution profile. This is shown in figure 9.1. However, while the parasitic ripples first emerge on the forward face of the

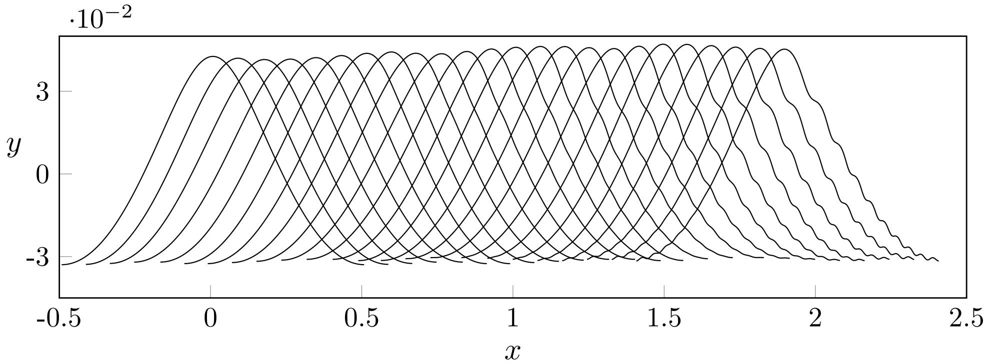

Figure 9.1: The free surface of an unsteady travelling gravity capillary wave is shown at intervals of $t = 0.5$. The initial condition at $t = 0$ is a gravity wave with Froude number $F = 0.4104$, and for $t > 0$ the Bond number is taken to be $B = 0.0084$. The numerical computations have solved the time evolution equations (A.2) with the method detailed in 5.

travelling wave, they eventually spread out to the entire periodic domain and continue to act in an unsteady manner. This led Jervis (1996) to conjecture that temporally periodic solutions may exist in this formulation, possibly with parasitic ripples that move at a different speed to that of the underlying wave.

9.4 Time-dependent exponential asymptotics

We demonstrated in section 5 that, for small surface tension, gravity-capillary standing waves contain high-frequency ripples. these are likely to be exponentially small in amplitude. The exponential asymptotic theory to describe these requires the asymptotic solution to two coupled nonlinear PDEs, for which the leading order solution (a standing gravity wave) is known only numerically. In most previous exponential asymptotic studies on PDEs, for instance that by Chapman and Mortimer (2005), the equations have been linear.

Furthermore, the time-dependent asymptotic study may also be able to reveal whether the temporally periodic solutions discussed in section 9.3 exist. The leading order solution of this study would be a steadily travelling gravity wave, which satisfies a nonlinear ODE. Only the subsequent orders of the asymptotic expansion would then require the solution of PDEs. This is analogous to Lustri and Chapman (2013) and Lustri et al. (2019), in which the initial condition was chosen to be that of the leading order solution, ensuring a steady solution at leading order.

9.5 The higher-order Stokes phenomenon

Our studies of the Hermite-with-pole equation in chapter 7 and the Kelvin wave problem in chapter 8 displayed the higher-order Stokes phenomenon. This is when the late-terms of the asymptotic series display the Stokes phenomenon across higher-order Stokes lines. This can lead to classic Stokes lines, obtained by evaluating $\text{Im}[\chi] = 0$ and $\text{Re}[\chi] > 0$ from Dingle (1973), being inactive, or even partially active (with an atypical Stokes multiplier) if the higher order and classical Stokes lines coincide.

We did not rely on a derivation of this phenomenon, and assumed that the higher-order Stokes lines would lie along the imaginary axis for our examples. Known methods of deriving the higher-order Stokes phenomenon are through integral representations of the solution by Howls et al. (2004), or through asymptotics of the equation directly, such as for the linear PDE studied by Chapman and Mortimer (2005). Extending these ideas for nonlinear PDEs remains an open problem.

BIBLIOGRAPHY

Akylas, T. R. and Yang, T.-S. (1995). On short-scale oscillatory tails of long-wave disturbances. *Stud. Appl. Math.*, 94(1):1–20.

Amick, C. J., Fraenkel, L. E., and Toland, J. F. (1982). On the Stokes conjecture for the wave of extreme form. *Acta Math.*, 148(1):193–214.

Barros, R., Choi, W., and Milewski, P. A. (2020). Strongly nonlinear effects on internal solitary waves in three-layer flows. *J. Fluid Mech.*, 883.

Berry, M. V. (1989). Uniform asymptotic smoothing of Stokes discontinuities. *Proc. Roy. Soc. London*, A 422:7–21.

Binder, B. J., Dias, F., and Vanden-Broeck, J.-M. (2008). Influence of rapid changes in a channel bottom on free-surface flows. *IMA J. Appl. Math.*, 73(1):254–273.

Binder, B. J., Vanden-Broeck, J.-M., and Dias, F. (2005). Forced solitary waves and fronts past submerged obstacles. *Chaos*, 15(3):037106.

Body, G. L., King, J. R., and Tew, R. H. (2005). Exponential asymptotics of a fifth-order partial differential equation. *Eur. J. Appl. Math.*, 16(5):647–681.

Boyd, J. P. (1978). The effects of latitudinal shear on equatorial waves. part i: Theory and methods. *J. Atmos. Sci.*, 35(12):2236–2258.

Boyd, J. P. (1999). The Devil's invention: Asymptotics, superasymptotics and hyperasymptotics. *Acta Applicandae*, 56:1–98.

Boyd, J. P. and Christidis, Z. D. (1982). Low wavenumber instability on the equatorial beta-plane. *Geophs. Res. Lett.*, 9(7):769–772.

Boyd, J. P. and Natarov, A. (1998). A sturm–liouville eigenproblem of the fourth kind: A critical latitude with equatorial trapping. *Stud. Appl. Math.*, 101(4):433–455.

Brazel, N. (1989). A model equation for the optical tunnelling problem using parabolic cylinder functions. Master's thesis, Dublin City University.

Chandler, G. A. and Graham, I. G. (1993). The computation of water waves modelled by Nekrasov's equation. *SIAM J. Numer. Anal.*, 30(4):1041–1065.

Chapman, S. J. (1999). On the role of Stokes lines in the selection of Saffman-Taylor fingers with small surface tension. *Eur. J. Appl. Math.*, 10(6):513–534.

Chapman, S. J., King, J. R., and Adams, K. L. (1998). Exponential asymptotics and Stokes lines in nonlinear ordinary differential equations. *Proc. R. Soc. Lond. A*, 454:2733–2755.

Chapman, S. J. and Kozyreff, G. (2009). Exponential asymptotics of localised patterns and snaking bifurcation diagrams. *Phys. D*, 238(3):319–354.

Chapman, S. J. and Mortimer, D. B. (2005). Exponential asymptotics and Stokes lines in a partial differential equation. *Proc. R. Soc. A*, 461(2060):2385–2421.

Chapman, S. J. and Vanden-Broeck, J.-M. (2002). Exponential asymptotics and capillary waves. *SIAM J. Appl. Math.*, 62 (6):1872–1898.

Chapman, S. J. and Vanden-Broeck, J.-M. (2006). Exponential asymptotics and gravity waves. *J. Fluid Mech.*, 567:299–326.

Chen, B. and Saffman, P. G. (1979). Steady gravity-capillary waves on deep water—I. weakly nonlinear waves. *Stud. Appl. Math.*, 60(3):183–210.

Chen, B. and Saffman, P. G. (1980). Steady gravity-capillary waves on deep water—II. numerical results for finite amplitude. *Stud. Appl. Math.*, 62(2):95–111.

Chen, B. and Sallman, P. G. (1980). Numerical evidence for the existence of new types of gravity waves of permanent form on deep water. *Stud. Appl. Math.*, 62(1):1–21.

Choi, W. (2009). Nonlinear surface waves interacting with a linear shear current. *Math. Comput. Simulat.*, 80(1):29–36.

Choi, W. and Camassa, R. (1999a). Exact evolution equations for surface waves. *J. Eng. Mech.*, 125(7):756–760.

Choi, W. and Camassa, R. (1999b). Fully nonlinear internal waves in a two-fluid system. *J. Fluid Mech.*, 396:1–36.

Christiansen, J. P. and Zabusky, N. J. (1973). Instability, coalescence and fission of finite-area vortex structures. *J. Fluid Mech.*, 61(2):219–243.

Cox, C. S. (1958). Measurements of slopes of high-frequency wind waves. *J. Mar. Res.*, 16:199–225.

Crapper, G. D. (1957). An exact solution for progressive capillary waves of arbitrary amplitude. *J. Fluid Mech.*, 2(6):532–540.

Crapper, G. D. (1970). Non-linear capillary waves generated by steep gravity waves. *J. Fluid Mech.*, 40(1):149–159.

Crew, S. C. and Trinh, P. H. (2016). New singularities for Stokes waves. *J. Fluid Mech.*, 798:256–283.

Crowdy, D. G. (2022). Exact solutions for steadily travelling water waves with submerged point vortices.

Crowdy, D. G. and Nelson, R. (2010). Steady interaction of a vortex street with a shear flow. *Phys. Fluids*, 22(9):096601.

Crowdy, D. G. and Roenby, J. (2014). Hollow vortices, capillary water waves and double quadrature domains. *Fluid Dyn. Res.*, 46(3):031424.

Da Silva, A. F. T. and Peregrine, D. H. (1988). Steep, steady surface waves on water of finite depth with constant vorticity. *J. Fluid Mech.*, 195:281–302.

Deike, L., P. S. and Melville, W. K. (2015). Capillary effects on wave breaking. *J. Fluid Mech.*, 769:541–569.

Dias, F., Dyachenko, A. I., and Zakharov, V. E. (2008). Theory of weakly damped free-surface flows: a new formulation based on potential flow solutions. *Phys. Lett. A*, 372(8):1297–1302.

Dias, F. and Vanden-Broeck, J.-M. (2004). Trapped waves between submerged obstacles. *J. Fluid Mech.*, 509:93–102.

Dingle, R. B. (1973). *Asymptotic expansions: their derivation and interpretation*, volume 48. Academic Press London.

Doak, A., Barros, R., and Milewski, P. A. (2022). Large mode-2 internal solitary waves in three-layer flows. *J. Fluid Mech.*, 953:A42.

Dyachenko, A. I., Zakharov, V. E., and Kuznetsov, E. A. (1996). Nonlinear dynamics of the free surface of an ideal fluid. *Plasma Phys. Rep.*, 22(10):829–840.

Dyachenko, S. A. and Hur, V. M. (2019). Stokes waves with constant vorticity: I. numerical computation. *Stud. Appl. Math.*, 142(2):162–189.

Ebuchi, N., Kawamura, H., and Toba, Y. (1987). Fine structure of laboratory wind-wave surfaces studied under an optical method. *Boundary-Layer Meteorol.*, 39:133–151.

Elcrat, A. R. and Miller, K. G. (2006). Free surface waves in equilibrium with a vortex. *Eur. J. Mech. B-Fluid.*, 25(2):255–266.

Fedorov, A. V. and Melville, W. K. (1998). Nonlinear gravity–capillary waves with forcing and dissipation. *J. Fluid Mech.*, 354:1–42.

Forbes, L. K. (1985). On the effects of non-linearity in free-surface flow about a submerged point vortex. *J. Eng. Math.*, 19(2):139–155.

Gao, T., W.-Z. and Vanden-Broeck, J.-M. (2017). Investigation of symmetry breaking in periodic gravity–capillary waves. *J. Fluid Mech.*, 811:622–641.

Gazdar, A. S. (1973). Generation of waves of small amplitude by an obstacle placed on the bottom of a running stream. *J. Phys. Soc. Japan*, 34(2):530–538.

Grant, M. A. (1973). The singularity at the crest of a finite amplitude progressive Stokes wave. *J. Fluid Mech.*, 59(2):257–262.

Griffiths, S. D. (2008). The limiting form of inertial instability in geophysical flows. *J. Fluid Mech.*, 605:115–143.

Grimshaw, R. (2010). Exponential asymptotics and generalized solitary waves. In *Asymptotic methods in fluid mechanics: survey and recent advances*, pages 71–120. Springer.

Hocking, G. C., Holmes, R. J., and Forbes, L. K. (2013). A note on waveless subcritical flow past a submerged semi-ellipse. *J. Eng. Math.*, 81(1):1–8.

Holmes, R. J. and Hocking, G. C. (2017). A note on waveless subcritical flow past symmetric bottom topography. *Euro. J. Appl. Math*, 28(4):562–575.

Holmes, R. J., Hocking, G. C., Forbes, L. K., and Baillard, N. Y. (2013). Waveless subcritical flow past symmetric bottom topography. *Eur. J. Appl. Math.*, 24(2):213–230.

Honda, N., Kawai, T., and Takei, Y. (2015). *Virtual turning points*, volume 4. Springer.

Howls, C. J., Langman, P. J., and Daalhuis, A. B. O. (2004). On the higher-order Stokes Phenomenon. *Proc. R. Soc. Lond. A*, 460:2285–2303.

Hung, L.-P. and Tsai, W.-T. (2009). The formation of parasitic capillary ripples on gravity–capillary waves and the underlying vortical structures. *J. Phys. Oceanogr.*, 39(2):263–289.

Hur, V. H. and Wheeler, M. H. (2020). Exact free surfaces in constant vorticity flows. *J. Fluid Mech.*, 896.

Jervis, M. T. (1996). *Some effects of surface tension on water waves and water waves at a wall*. PhD thesis, University of Bristol.

Kang, Y. and Vanden-Broeck, J.-M. (2000). Gravity-capillary waves in the presence of constant vorticity. *Euro. J. Mech.*, 19(2):253–268.

Kruskal, M. D. and Segur, H. (1991). Asymptotics beyond all orders in a model of crystal growth. *Stud. Appl. Math.*, 85:129–181.

Longuet-Higgins, M. S. (1963). The generation of capillary waves by steep gravity waves. *J. Fluid Mech.*, 16:138–159.

Longuet-Higgins, M. S. (1989). Capillary-gravity waves of solitary type on deep water. *J. Fluid Mech.*, 200:451–470.

Longuet-Higgins, M. S. (1992). Capillary rollers and bores. *J. Fluid Mech.*, 240:659–679.

Longuet-Higgins, M. S. (1995). Parasitic capillary waves: a direct calculation. *J. Fluid Mech.*, 301:79–107.

Longuet-Higgins, M. S. and Fox, M. J. H. (1977). Theory of the almost-highest wave: The inner solution. *J. Fluid Mech.*, 80(04):721–741.

Longuet-Higgins, M. S. and Fox, M. J. H. (1978). Theory of the almost-highest wave. Part 2. Matching and analytic extension. *J. Fluid Mech.*, 85(04):769–786.

Lustri, C. J. (2013). *Exponential asymptotics in unsteady and three-dimensional flows*. PhD thesis, Oxford University, UK.

Lustri, C. J. and Chapman, S. J. (2013). Steady gravity waves due to a submerged source. *J. Fluid Mech.*, 732:660–686.

Lustri, C. J., McCue, S. W., and Binder, B. J. (2012). Free surface flow past topography: a beyond-all-orders approach. *Euro. J. Appl. Math.*, 23(4):441–467.

Lustri, C. J., Pethiyagoda, R., and Chapman, S. J. (2019). Three-dimensional capillary waves due to a submerged source with small surface tension. *J. Fluid Mech.*, 863:670–701.

Mailybaev, A. A. and Nachbin, A. (2019). Explosive ripple instability due to incipient wave breaking. *J. Fluid Mech.*, 863:876–892.

McCue, S. W. and Forbes, L. K. (1999). Bow and stern flows with constant vorticity. *J. Fluid Mech.*, 399:277–300.

McCue, S. W. and Forbes, L. K. (2002). Free-surface flows emerging from beneath a semi-infinite plate with constant vorticity. *J. Fluid Mech.*, 461:387–407.

Milewski, P. A., Vanden-Broeck, J.-M., and Wang, Z. (2010). Dynamics of steep two-dimensional gravity–capillary solitary waves. *J. Fluid Mech.*, 664:466–477.

Milewski, P. A. and Wang, Z. (2016). Self-focusing dynamics of patches of ripples. *Phys. D*, 333:235–242.

Miyata, M. (1988). Long internal waves of large amplitude. In *Nonlinear water waves*, pages 399–406. Springer.

Moreira, R. M. and Peregrine, D. H. (2010). Nonlinear interactions between a free-surface flow with surface tension and a submerged cylinder. *J. Fluid Mech.*, 648:485–507.

Mortimer, D. B. (2004). *Exponential Asymptotics and Stokes Lines in Partial Differential Equations*. PhD thesis, University of Oxford.

Mui, R. C. Y. and Dommermuth, D. G. (1995). The vortical structure of parasitic capillary waves. *Trans. ASME J. Fluids. Engng.*

Murashige, S. and Choi, W. (2017). A numerical study on parasitic capillary waves using unsteady conformal mapping. *J. Comp. Phys.*, 328:234–257.

Natarov, A. and Boyd, J. P. (2001). Beyond-all-orders instability in the equatorial wave. *Dynam. atmos. oceans*, 33(3):191–200.

Okamoto, H. and Shōji, M. (2001). *The mathematical theory of permanent progressive water-waves*, volume 20. World Scientific.

Olde Daalhuis, A. B. (2004). On higher-order Stokes phenomena of an inhomogeneous linear ordinary differential equation. *J. Comput. Appl. Math.*, 169:235–246.

Olde Daalhuis, A. B., Chapman, S. J., King, J. R., Ockendon, J. R., and Tew, R. H. (1995). Stokes phenomenon and matched asymptotic expansions. *SIAM J. Appl. Math.*, 55(6):1469–1483.

Paris, R. B. and Wood, A. D. (1989). A model equation for optical tunnelling. *IMA J. Appl. Math.*, 43(3):273–284.

Penney, W. G. and Price, A. T. (1952). Part ii. finite periodic stationary gravity waves in a perfect liquid. *Philos. TR. R. Soc. S.-A*, 244(882):254–284.

Perlin, M., Lin, H., and Ting, C.-L. (1993). On parasitic capillary waves generated by steep gravity waves: an experimental investigation with spatial and temporal measurements. *J. Fluid Mech.*, 255:597–620.

Perlin, M. and Schultz, W. W. (2000). Capillary effects on surface waves. *Annu. Rev. Fluid Mech.*, 32(1):241–274.

Ribeiro, R., Milewski, P. A., and Nachbin, A. (2017). Flow structure beneath rotational water waves with stagnation points. *J. Fluid Mech.*, 812:792–814.

Schultz, W. W., Vanden-Broeck, J.-M., Jiang, L., and Perlin, M. (1998). Highly nonlinear standing water waves with small capillary effect. *J. Fluid Mech.*, 369:253–272.

Schwartz, L. W. and Vanden-Broeck, J.-M. (1979). Numerical solution of the exact equations for capillary–gravity waves. *J. Fluid Mech.*, 95(1):119–139.

Shelton, J., Chapman, S. J., and Trinh, P. H. (2023a). Pathological exponential asymptotics for a model problem of an equatorially trapped rossby wave. *In Preperation*.

Shelton, J., Crew, S., and Trinh, P. H. (2023b). Exponential asymptotic and higher-order stokes pheonmenon in singularly perturbed odes. *In Preperation*.

Shelton, J., Griffiths, S., Chapman, S. J., and Trinh, P. H. (2023c). On the exponentially-small instability of the equatorial kelvin wave. *In Preperation*.

Shelton, J., Milewski, P., and Trinh, P. H. (2021). On the structure of steady parasitic gravity-capillary waves in the small surface tension limit. *J. Fluid Mech.*, 922.

Shelton, J. and Trinh, P. H. (2022). Exponential asymptotics for steady parasitic capillary ripples on steep gravity waves. *J. Fluid Mech.*, 939.

Shimizu, C. and Shōji, M. (2012). Appearance and disappearance of non-symmetric progressive capillary–gravity waves of deep water. *Japan J. Ind. Appl. Math.*, 29(2):331–353.

Simmen, J. A. and Saffman, P. (1985). Steady deep-water waves on a linear shear current. *Stud. Appl. Math.*, 73(1):35–57.

Stokes, G. G. (1847). On the theory of oscillatory waves. *Trans. Camb. Phil. Soc.*, 8:411–455.

Stokes, G. G. (1851). On the numerical calculation of a class of definite integrals and infinite series. *T. Cam. Philos. Soc.*, 9:166.

Stokes, G. G. (1864). On the discontinuity of arbitrary constants which appear in divergent developments. *T. Cam. Philos. Soc.*, 10:105.

Stokes, G. G. (1880). Considerations relative to the greatest height of oscillatory irrotational waves which can be propagated without change of form. *Mathematical and physical papers*, 1:225–228.

Tanveer, S. (1991). Singularities in water waves and rayleigh-taylor instablity. *Proc. R. Soc. Lond. A*, 435:137–158.

Tanveer, S. and Xie, X. (2003). Analyticity and nonexistence of classical steady Hele-Shaw fingers. *Commun. Pure Appl. Math.*, 56(3):353–402.

Toland, J. F. (1978). On the existence of a wave of greatest height and Stokes's conjecture. *Proc. R. Soc. Lon. Ser.-A*, 363(1715):469–485.

Toland, J. F. (1996). Stokes waves. *Topol. Method. Nonlinear Anal.*, 7(1):1–48.

Trinh, P. H. (2017). On reduced models for gravity waves generated by moving bodies. *J. Fluid Mech.*, 813:824–859.

Trinh, P. H. and Chapman, S. J. (2013). New gravity–capillary waves at low speeds. part 1. linear geometries. *J. Fluid Mech.*, 724:367–391.

Trinh, P. H., Chapman, S. J., and Vanden-Broeck, J.-M. (2011). Do waveless ships exist? Results for single-cornered hulls. *J. Fluid Mech.*, 685:413–439.

Tuck, E. O. and Scullen, D. C. (1998). Tandem submerged cylinders each subject to zero drag. *J. Fluid Mech.*, 364:211–220.

Vanden-Broeck, J.-M. (1984). Nonlinear gravity–capillary standing waves in water of arbitrary uniform depth. *J. Fluid Mech.*, 139:97–104.

Vanden-Broeck, J.-M. (1986). Steep gravity waves: Havelock's method revisited. *Phys. Fluids*, 29(9):3084–3085.

Vanden-Broeck, J.-M. (1994). Steep solitary waves in water of finite depth with constant vorticity. *J. Fluid Mech.*, 274:339–348.

Vanden-Broeck, J.-M. (1996). Periodic waves with constant vorticity in water of infinite depth. *IMA J Appl. Math.*, 56(3):207–217.

Vanden-Broeck, J.-M. (2010). *Gravity-Capillary Free-Surface Flows*. Cambridge University Press, Cambridge, UK.

Vanden-Broeck, J.-M. and Tuck, E. O. (1985). Waveless free-surface pressure distributions. *J. Ship Res.*, 29(03):151–158.

Von Karman, T. and Rubach, H. (1912). On the mechanism of resistance in fluids. *Physikalische Zeitschrift*, 13(5):351–358.

Wilkening, J. (2011). Breakdown of self-similarity at the crests of large-amplitude standing water waves. *Phys. rev. lett.*, 107(18):184501.

Wilkening, J. (2021). Traveling-standing water waves. *Fluids*, 6(5):187.

Wilkening, J. and Yu, J. (2012). Overdetermined shooting methods for computing standing water waves with spectral accuracy. *Comp. Sci. Discov.*, 5(1):014017.

Wilkening, J. and Zhao, X. (2021). Quasi-periodic travelling gravity–capillary waves. *J. Fluid Mech.*, 915:A7.

Wilton, J. R. (1915). Lxxii. on ripples. *The London, Edinburgh, and Dublin Philosophical Magazine and Journal of Science*, 29(173):688–700.

Yang, T.-S. and Akylas, T. R. (1996). Weakly nonlocal gravity–capillary solitary waves. *Phys. Fluids*, 8(6):1506–1514.

Yang, T.-S. and Akylas, T. R. (1997). On asymmetric gravity–capillary solitary waves. *J. Fluid Mech.*, 330:215–232.

Zufiria, J. A. (1987a). Non-symmetric gravity waves on water of infinite depth. *J. Fluid Mech.*, 181:17–39.

Zufiria, J. A. (1987b). Symmetry breaking in periodic and solitary gravity-capillary waves on water of finite depth. *J. Fluid Mech.*, 184:183–206.

TIME DEPENDENT CONFORMAL MAPPING FOR GRAVITY CAPILLARY WAVES

A

In chapter 5, numerical solutions were found for gravity-capillary standing waves when the Bond number, B, was small. This corresponds to the regime of small surface tension. Computation of these time dependent standing waves required us to conformally map the unknown fluid domain, $-\infty < y \leq \zeta(x,t)$, to a fixed domain. For the steady solutions considered in chapter 3, this conformal mapping was simply the mapping to the potential (ϕ, ψ)-plane. In this case, the free surface was a streamline for which ψ was constant, and was parameterised by the remaining variable: the velocity potential, ϕ. The time dependent case is more complicated, for while the free surface, $y = \zeta(x,t)$, is still a streamline along which the streamfunction, ψ, is constant, this constant will change with time.

We now derive this time-dependent conformal mapping that transforms our equations in the physical (x,y) domain,

$$\phi_{xx} + \phi_{yy} = 0 \qquad \text{for} \quad y \leq \zeta, \tag{A.1a}$$

$$\zeta_t - \phi_y + \zeta_x \phi_x = 0 \qquad \text{at} \quad y = \zeta, \tag{A.1b}$$

$$F^2 \phi_t + \frac{F^2}{2}(\phi_x^2 + \phi_y^2) + y - B\frac{\zeta_{xx}}{(1+\zeta_x^2)^{\frac{3}{2}}} = 0 \qquad \text{at} \quad y = \zeta, \tag{A.1c}$$

$$\phi_x \to 0 \quad \text{and} \quad \phi_y \to 0 \qquad \text{as} \quad y \to -\infty, \tag{A.1d}$$

into the time evolution equations for the free surface variables (found by evaluating x, y, ψ, and ϕ on the free surface $\eta = 0$) in the conformal (ξ, η) domain, given by

$$Y_t = Y_\xi \mathcal{H}\left[\frac{\Psi_\xi}{J}\right] - X_\xi \left(\frac{\Psi_\xi}{J}\right), \tag{A.2a}$$

$$\Phi_t = \frac{1}{2}\left(\frac{\Psi_\xi^2 - \Phi_\xi^2}{J}\right) + \Phi_\xi \mathcal{H}\left[\frac{\Psi_\xi}{J}\right] - \frac{Y}{F^2} + \frac{B}{F^2}\frac{(X_\xi Y_{\xi\xi} - Y_\xi X_{\xi\xi})}{J^{3/2}}. \tag{A.2b}$$

Here, $\mathcal{H}$ is the periodic Hilbert transform. System (A.2) contains two evolution equations for four unknowns, and is closed by the harmonic relations

$$X_\xi = 1 - \mathcal{H}[Y_\xi] \qquad \text{and} \qquad \Psi_\xi = \mathcal{H}[\Phi_\xi]. \tag{A.3}$$

We begin by deriving these harmonic relationships in the following sections. The mapping derived in the following sections originates from the work by Dyachenko et al. (1996) and our presentation follows closely to that by Choi and Camassa (1999a) and Milewski et al. (2010).

A.1 The free-surface variables

The conformal mapping derived in this section maps the physical (x,y)-plane to the conformal (ξ, η)-plane. This is depicted in figure A.1. Note that the free surface, $y = \zeta(x,t)$ is mapped to the line $\eta = 0$. Thus, we define the free surface variables through

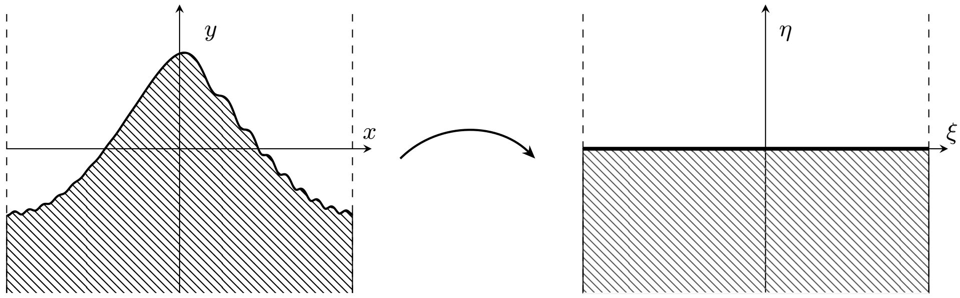

Figure A.1: The conformal map from $-1/2 < x < 1/2$ and $y \leq \zeta(x)$ to $-1/2 < \xi < 1/2$ and $\eta \leq 0$ is shown.

evaluation at $\eta = 0$, yielding

$$\left.\begin{aligned} X(\xi,t) &= x(\xi,0,t), & Y(\xi,t) &= \zeta(x(\xi,0,t),t), \\ \Phi(\xi,t) &= \phi(\xi,0,t), & \Psi(\xi,t) &= \psi(\xi,0,t). \end{aligned}\right\} \tag{A.4}$$

A.2 Harmonic relations between X and Y

The harmonic relationship between $X(\xi,t)$ and $Y(\xi,t)$ is now found by solving the following harmonic system, given by

$$y_{\xi\xi} + y_{\eta\eta} = 0 \qquad \text{for} \quad \eta \leq 0, \tag{A.5a}$$

$$y = Y(\xi,t) \qquad \text{at} \quad \eta = 0, \tag{A.5b}$$

$$y \sim \eta \qquad \text{as} \quad \eta \to -\infty. \tag{A.5c}$$

We will express $y(\xi,\eta,t)$ as a Fourier series in ξ, to which the Cauchy-Riemann equations are applied to form the relationship between the harmonic variables x and y. Evaluation of this relationship on $\eta = 0$ then yields equation (A.3).

In writing

$$y = a_0(t)N_0(\eta) + \sum_{n=1}^{\infty}\left[a_n(t)N_n(\eta)\cos(2n\pi\xi) + b_n(t)M_n(\eta)\sin(2n\pi\xi)\right], \tag{A.6}$$

substitution into equation (A.5a) yields

$$\left.\begin{aligned} N_0''(\eta) &= 0, \\ N_n''(\eta) - (2n\pi)^2 N_n(\eta) &= 0, \\ M_n''(\eta) - (2n\pi)^2 M_n(\eta) &= 0, \end{aligned}\right\} \tag{A.7}$$

where the last two equations in (A.7) hold for $n \geq 1$. Solutions of equations (A.7) are found by integration to be

$$\left.\begin{aligned} N_0(\eta) &= C_0\eta + D_0, \\ N_n(\eta) &= C_n \mathrm{e}^{2n\pi\eta} + D_n \mathrm{e}^{-2n\pi\eta}, \\ M_n(\eta) &= E_n \mathrm{e}^{2n\pi\eta} + F_n \mathrm{e}^{-2n\pi\eta}, \end{aligned}\right\} \tag{A.8}$$

where C_n, D_n, E_n, and F_n are constants of integration.

Boundary condition (A.5c), $y \sim \eta$ as $\eta \to -\infty$ may now be applied to solution (A.6) for $y(\xi,\eta,t)$. This yields $a_0(t)C_0 = 1$, $D_n = 0$, and $F_n = 0$. Substitution of solutions (A.8) into Fourier series (A.6) for y yields

$$y = \eta + D_0 a_0(t) + \sum_{n=1}^{\infty} \Big[\bar{a}_n(t) \mathrm{e}^{2n\pi\eta} \cos(2n\pi\xi) + \bar{b}_n(t) \mathrm{e}^{2n\pi\eta} \sin(2n\pi\xi) \Big], \quad \text{(A.9)}$$

where we have defined $\bar{a}_n(t) = C_n a_n(t)$ and $\bar{b}_n(t) = E_n b_n(t)$ for convenience. Differentiation of solution (A.9) yields the expressions

$$y_\xi = \sum_{n=1}^{\infty} 2n\pi \mathrm{e}^{2n\pi\eta} \Big[-\bar{a}_n(t) \sin(2n\pi\xi) + \bar{b}_n(t) \cos(2n\pi\xi) \Big], \quad \text{(A.10a)}$$

$$y_\eta = 1 + \sum_{n=1}^{\infty} 2n\pi \mathrm{e}^{2n\pi\eta} \Big[\bar{a}_n(t) \cos(2n\pi\xi) + \bar{b}_n(t) \sin(2n\pi\xi) \Big]. \quad \text{(A.10b)}$$

Equations (A.10a) and (A.10b) are now related by using properties of the Hilbert transform,

$$\mathcal{H}[y](\xi') = \fint_{-\infty}^{\infty} \frac{y(\xi, \eta, t)}{\xi - \xi'} \mathrm{d}\xi. \quad \text{(A.11)}$$

Since $\mathcal{H}[\sin(2n\pi\xi)] = \cos(2n\pi\xi)$ and $\mathcal{H}[\cos(2n\pi\xi)] = -\sin(2n\pi\xi)$, we have that $y_\eta = 1 - \mathcal{H}[y_\xi]$. Next, we note that $z = x + \mathrm{i}y$ is an analytic function of $\xi + \mathrm{i}\eta$. Thus, the Cauchy-Riemann equation $x_\xi = y_\eta$ may be applied, and evaluation on $\eta = 0$ yields our anticipated result of

$$X_\xi = 1 - \mathcal{H}[Y_\xi]. \quad \text{(A.12)}$$

A.3 Harmonic relations between Φ and Ψ

Derivation of the harmonic relationship between Φ and Ψ follows similarly to that presented in §A.2 between X and Y. We will solve the following harmonic system for $\phi(\xi, \eta, t)$, given by

$$\phi_{\xi\xi} + \phi_{\eta\eta} = 0 \quad \text{for} \quad \eta \le 0, \quad \text{(A.13a)}$$

$$\phi = \Phi(\xi, t) \quad \text{at} \quad \eta = 0, \quad \text{(A.13b)}$$

$$\phi_\eta \to 0, \quad \phi_\xi \to 0 \quad \text{as} \quad \eta \to -\infty. \quad \text{(A.13c)}$$

Here, the lower boundary conditions as $\eta \to -\infty$ are derived from the equations $\phi_\eta = \phi_x x_\eta + \phi_y y_\eta$ and $\phi_\xi = \phi_x x_\xi + \phi_y y_\xi$, which are obtained by the chain rule for partial derivatives. Since $u = \phi_x \to 0$ and $v = \phi_y \to 0$ as $y \to -\infty$ from (A.1d), and noting that $y \sim \eta$ as $\eta \to -\infty$, we find $\phi_\eta \to 0$ and $\phi_\xi \to 0$ as $\eta \to -\infty$.

In considering a Fourier series solution for ϕ, substitution into equation (A.13a) yields

$$\phi = \sum_{n=1}^{\infty} \mathrm{e}^{2n\pi\eta} \Big[\tilde{a}_n(t) \cos(2n\pi\xi) + \tilde{b}_n(t) \sin(2n\pi\xi) \Big]. \quad \text{(A.14)}$$

This is a similar result to equation (A.9) for y. Thus, we may differentiate (A.14) with respect to both ξ and η, which in using properties of the Hilbert transform yields $\phi_\eta = -\mathcal{H}[\phi_\xi]$. Since the complex velocity, $\phi + \mathrm{i}\psi$ is an analytic function of $\xi + \mathrm{i}\psi$, we may then use the Cauchy-Riemann equation $\phi_\eta = -\psi_\xi$. This yields the relation $\psi_\xi = \mathcal{H}[\phi_{xi}]$, which we evalaute on the free surface, $\eta = 0$, to find

$$\Psi_\xi = \mathcal{H}[\Phi_\xi]. \quad \text{(A.15)}$$

A.4 Time evolution equations for the free-surface variables

We now derive the time evolution equations (A.2a) and (A.2b) by finding expressions for each component of these equations in terms of the free surface variables, X, Y, Φ, and Ψ, introduced in equation (A.4). Expressions for ϕ_x, ϕ_y, ζ_t, ϕ_t, ζ_x, and ζ_{xx} are required. Differentiation of these expressions yields

$$Y_t = \zeta_t + \zeta_x X_t, \tag{A.16a}$$
$$Y_\xi = \zeta_x X_\xi, \tag{A.16b}$$
$$Y_{\xi\xi} = \zeta_x X_{\xi\xi} + \zeta_{xx} X_\xi^2, \tag{A.16c}$$
$$\Phi_t = \phi_x X_t + \phi_y Y_t + \phi_t, \tag{A.16d}$$
$$\Phi_\xi = \phi_x X_\xi + \phi_y Y_\xi, \tag{A.16e}$$
$$\Psi_\xi = \psi_x X_\xi + \psi_y Y_\xi = \phi_x Y_\xi - \phi_y X_\xi, \tag{A.16f}$$

where for the last equation we have used the Cauchy-Riemann equations $\phi_x = \psi_y$ and $\phi_y = -\psi_x$. The last two of these, equations (A.16e) and (A.16f), may be solved to find

$$\phi_x = \frac{Y_\xi \Psi_\xi + X_\xi \Phi_\xi}{X_\xi^2 + Y_\xi^2} \qquad \text{and} \qquad \phi_y = \frac{Y_\xi \Phi_\xi - X_\xi \Psi_\xi}{X_\xi^2 + Y_\xi^2}. \tag{A.17}$$

Next, expressions for ζ_x, ζ_{xx}, ζ_t, and ϕ_t are found from equations (A.16) to be given by

$$\left.\begin{aligned} &\zeta_x = \frac{Y_\xi}{X_\xi}, \quad \zeta_{xx} = \frac{X_\xi Y_{\xi\xi} - Y_\xi X_{\xi\xi}}{X_\xi^3}, \quad \zeta_t = Y_t - \frac{Y_\xi X_t}{X_\xi}, \\ &\phi_t = \Phi_t - \frac{\Psi_\xi (Y_\xi X_t - X_\xi Y_t) + \Phi_\xi (X_\xi X_t + Y_\xi Y_t)}{X_\xi^2 + Y_\xi^2}. \end{aligned}\right\} \tag{A.18}$$

Substitution of these into the kinematic and dynamic boundary conditions (A.1b) and (A.1c) yields

$$\Psi_\xi = Y_\xi(1 + X_t) - X_\xi Y_t, \tag{A.19a}$$

$$\begin{aligned} \Phi_t = &- \frac{(\Phi_\xi^2 + \Psi_\xi^2)}{2J} - \frac{Y}{F^2} + \frac{B}{F^2}\frac{(X_\xi Y_{\xi\xi} - Y_\xi X_{\xi\xi})}{J^{3/2}} \\ &+ \frac{\Psi_\xi}{J}\big[Y_\xi(1 + X_t) - X_\xi Y_t\big] + \frac{\Phi_\xi}{J}\big[X_\xi(1 + X_t) + Y_\xi Y_t\big], \end{aligned} \tag{A.19b}$$

where we have defined $J = X_\xi^2 + Y_\xi^2$. Note that these are not the desired equations as dependence on X_t and Y_t still remains. This can be removed by noting that in defining $Z(\xi, t) = t + X(\xi, t) + \mathrm{i}Y(\xi, t)$, we have

$$\mathrm{Re}\left[\frac{Z_t}{Z_\xi}\right] = \frac{X_\xi(1 + X_t) + Y_\xi Y_t}{J} \quad \text{and} \quad \mathrm{Im}\left[\frac{Z_t}{Z_\xi}\right] = \frac{X_\xi Y_t - Y_\xi(1 + X_t)}{J}. \tag{A.20}$$

This imaginary component is seen from equation (A.19a) to equal $-\Psi_\xi/J$. Since Z, and therefore Z_t/Z_ξ, are analytic functions, their real and imaginary parts satisfy harmonic relations, given by $\mathrm{Re}[Z_t/Z_\xi] = -\mathcal{H}[\mathrm{Im}[Z_t/Z_\xi]]$. Thus, we have that

$$\frac{X_\xi(1 + X_t) + Y_\xi Y_t}{J} = -\mathcal{H}\left[\frac{\Psi_\xi}{J}\right] \quad \text{and} \quad \frac{X_\xi Y_t - Y_\xi(1 + X_t)}{J} = -\frac{\Psi_\xi}{J}. \tag{A.21}$$

These expressions are substituted into equation (A.19b) to find our first time evolution equation,

$$\Phi_t = \frac{1}{2}\left(\frac{\Psi_\xi^2 - \Phi_\xi^2}{J}\right) + \Phi_\xi \mathcal{H}\left[\frac{\Psi_\xi}{J}\right] - \frac{Y}{F^2} + \frac{B}{F^2}\frac{(X_\xi Y_{\xi\xi} - Y_\xi X_{\xi\xi})}{J^{3/2}}. \tag{A.22a}$$

The second time evolution equation is derived by eliminating X_t from equations (A.21), yielding

$$Y_t = Y_\xi \mathcal{H}\left[\frac{\Psi_\xi}{J}\right] - X_\xi\left(\frac{\Psi_\xi}{J}\right), \tag{A.22b}$$

which together with the harmonic relations

$$X_\xi = 1 - \mathcal{H}[Y_\xi] \qquad \text{and} \qquad \Psi_\xi = \mathcal{H}[\Phi_\xi], \tag{A.22c}$$

forms a closed system for X, Y, Φ, and Ψ. Assuming that Y and Φ are known for a certain value of time, $t = t_0$, X_ξ and Ψ_ξ are calculated via the harmonic relations (A.22c). Substitution into time evolution equations (A.22a) and (A.22b) then allows for the numerical determination of Y and Φ at the next time step, $t = t_0 + \Delta t$.

THE DIVERGENT EIGENVALUE OF GRAVITY CAPILLARY WAVES

B

In chapter 4, we considered asymptotic solutions for the small surface tension limit of periodic gravity capillary waves subject to fixed energy,

$$\mathscr{E} = \int_{-1/2}^{1/2} \Big[\mathcal{G}_0(\phi) + B\mathcal{G}_1(\phi) + B^2\mathcal{G}_2(\phi)\Big]\mathrm{d}\phi, \tag{B.1}$$

where

$$\left.\begin{aligned} \mathcal{G}_0(\phi) &= \frac{F^4(1-q^2)}{8q}\Big(3\cos(\theta) - 2q - q^2\cos(\theta)\Big), \\ \mathcal{G}_1(\phi) &= \frac{(1-\cos(\theta))}{q} + \frac{F^2\theta_\phi}{2}\Big(2\cos(\theta) - q - q^2\cos(\theta)\Big), \\ \mathcal{G}_2(\phi) &= \frac{q\theta_\phi^2\cos(\theta)}{2}. \end{aligned}\right\} \tag{B.2}$$

However, in expanding the solutions as

$$q(f) = \sum_{n=0}^{N-1} B^n q_n(f) + \bar{q}(f) \quad \text{and} \quad \theta(f) = \sum_{n=0}^{N-1} B^n\theta_n(f) + \bar{\theta}(f), \tag{B.3}$$

our factorial-over-power representation for the divergence of q_n and θ_n was unable to satisfy the $O(B^n)$ component of the energy condition, as well as periodicity across the domain $-1/2 < \mathrm{Re}[f] \leq 1/2$. This is because we considered only the divergent component that was dominant along the Stokes lines and which led to the Stokes phenomenon. Furthermore, we were also unable to satisfy the exponentially-small component of the energy condition on the remainders $\bar{q}$ and $\bar{\theta}$. The techniques required to fix these issues are discussed in this chapter.

B.1 Analytical solutions for the divergent Froude number

In order to satisfy the energy constraint (B.5a) to each order in B, it is necessary to also expand the eigenvalue, F, as

$$F = \sum_{n=0}^{N-1} B^n F_n + \bar{F}. \tag{B.4}$$

The late-terms, F_n, of this expansion will be determined by enforcing the $O(B^n)$ energy condition and periodicity conditions,

$$\begin{aligned} \int_{-1/2}^{1/2} \Bigg[& F_n\frac{F_0^3(1-q_0^2)}{2q_0}\Big(3\cos(\theta_0) - 2q_0 - q_0^2\cos(\theta_0)\Big) \\ & + \theta_{n-1}'\frac{F_0^2}{2}\Big(2\cos(\theta_0) - q_0 - q_0^2\cos(\theta_0)\Big) \\ & + \theta_n\frac{F_0^4(1-q_0^2)}{8q_0}\Big(q_0^2\sin(\theta_0) - 3\sin(\theta_0)\Big) \\ & - \mathfrak{q}_n\frac{F_0^4}{8q_0^2}\Big(3\cos(\theta_0) - 4q_0^3 - 3q_0^4\cos(\theta_0) + 4q_0^2\cos(\theta_0)\Big)\Bigg]\mathrm{d}\phi = 0, \end{aligned} \tag{B.5a}$$

$$\mathfrak{q}_n(-1/2) = \mathfrak{q}_n(1/2), \tag{B.5b}$$

$$\mathfrak{q}_n'(-1/2) = \mathfrak{q}_n'(1/2). \tag{B.5c}$$

Here, we have retained only the dominant components as $n \to \infty$, and furthermore defined $\mathfrak{q}_n = q_n|_{a=1} + q_n|_{a=-1}$ and $\theta_n = \theta_n|_{a=1} + \theta_n|_{a=-1}$ to combine the contributions from the singularities at $f = f^*$ and $f = -f^*$, where the direction of analytic continuation $a = \pm 1$ into either $\mathrm{Im}[f] > 0$ or $\mathrm{Im}[f] < 0$ discerns between these. Note that rather than consider the periodicity condition, $\mathfrak{q}(f) = \mathfrak{q}(f+1)$, we instead consider the two conditions (B.5b) and (B.5c) in this section. Furthermore, it is not possible to immediately rearrange the energy expression (B.5a) to find F_n, as there will be particular components of the solution containing this divergent eigenvalue.

B.1.1 *Additional components of the late-term solution*

We will demonstrate that in addition to the naive divergent solution, $\mathfrak{q}_n^{(\text{naive})}$, determined in chapter 4, there are three other components required to satisfy periodicity and the energetic condition. These are homogeneous solutions with $\chi' = 0$, denoted by $\mathfrak{q}_n^{(\chi'=0)}$ and two particular solutions. The first particular solution, denoted by $\mathfrak{q}_n^{(F_n)}$, is forced by the divergence of F_n, and the second, $\mathfrak{q}_n^{(\mathcal{H})}$, is forced by the Hilbert transform of the naive solution, $\mathfrak{q}_n^{(\text{naive})}$, which was previously neglected in the late-term analysis. Combined, these yield

$$\mathfrak{q}_n = \mathfrak{q}_n^{(\text{naive})} + \mathfrak{q}_n^{(\chi'=0)} + \mathfrak{q}_n^{(F_n)} + \mathfrak{q}_n^{(\mathcal{H})}. \tag{B.6}$$

In equation (6.1a) of Shelton and Trinh (2022) in chapter 4, we posited the factorial-over-power ansatz for the divergence of q_n, given by

$$q_n(f) \sim Q_a(f)\frac{\Gamma(n+\gamma)}{[\chi_a(f)]^{n+\gamma}}, \tag{B.7}$$

and subsequently found the singulant equation to be

$$\chi_a'(\chi_a' - a\mathrm{i}F_0^2 q_0) = 0. \tag{B.8}$$

Solving for the nontrivial solution, $\chi_a' = a\mathrm{i}F_0^2 q_0$, yields

$$\begin{aligned}\mathfrak{q}_n^{(\text{naive})}(\phi) = \frac{2|\Lambda_1|q_0^2\Gamma(n+\gamma)}{|\chi_1|^{n+\gamma}}\cos\Bigg[&\arg[\Lambda_1] - (n+\gamma)\arg[\chi_1] \\ &+ \int_0^\phi \left(\frac{\cos(\theta_0)}{F_0^2 q_0^3} - F_0^2 q_1 - 2F_0F_1q_0\right)\mathrm{d}t\Bigg].\end{aligned} \tag{B.9}$$

Here, we have used the solution for Q_a from equation (6.7) of Shelton and Trinh (2022) in chapter 4, and written $\Lambda_a = |\Lambda_1|\mathrm{e}^{a\mathrm{i}\arg[\Lambda_1]}$ and $\chi_a(\phi) = |\chi_1(\phi)|\mathrm{e}^{a\mathrm{i}\arg[\chi_1(\phi)]}$; this holds as Λ_1 and Λ_{-1}, as well as χ_1 and χ_{-1}, are the complex conjugate of one another. These complex conjugate relations hold only along the free surface for which ϕ is real. Solution (B.9) is one of the required components of the overall solution (B.6).

B.1.2 *The divergent solution with $\chi_a' = 0$*

The previously neglected singulant solution, $\chi_a' = 0$, yields constant values of χ_a. Since differentiation of the factorial-over-power ansatz (B.7) no longer increases the order in n if χ takes constant values, the leading order terms of the $O(B^n)$ equations change, and are found to be

$$F_0^2 q_0^2 q_n' + 2F_0^2 q_0 q_0' q_n + \cos(\theta_0)\theta_n = -2F_0 F_n q_0^2 q_0', \tag{B.10a}$$

$$q_n + a\mathrm{i} q_0 \theta_n = q_0 \hat{\mathcal{H}}[\theta_n]. \tag{B.10b}$$

In this section, we consider the homogeneous contributions for which the late-terms of the eigenvalue, F_n, are ignored. We consider the divergence of F_n, and the associated particular solution of equation (B.10a), in section B.1.3. For this homogeneous solution with $\chi_a' = 0$, we consider ansatzes of the form

$$q_n(f) \sim R_a(f)\frac{\Gamma(n+\gamma_1)}{\Delta_a^{n+\gamma_1}} \qquad \text{and} \qquad \theta_n(f) \sim T(f)\frac{\Gamma(n+\gamma_1)}{\Delta_a^{n+\gamma_1}}, \tag{B.11}$$

where γ_1 and Δ_a are constants. Substitution of (B.11) into the homogeneous form of equation (B.10) yields

$$a\mathrm{i}F_0^2 q_0^3 T' + \left[3a\mathrm{i}q_0^2 q_0' - \cos(\theta_0)\right]T - 3F_0^2 q_0^2 q_0' \hat{\mathcal{H}}[T] - F_0^2 q_0^3 \hat{\mathcal{H}}[T'] = 0, \tag{B.12a}$$

$$R = q_0 \hat{\mathcal{H}}[T'] - a\mathrm{i} q_0 T. \tag{B.12b}$$

The first of these equations (B.12a) is an integro-differential equation for T, which once known yields R via equation (B.12b).

B.1.3 *Particular solutions of the $O(B^n)$ equation*

In addition to the homogeneous solution (with $\chi'^{=0}$) of the $O(\epsilon^n)$ equation considered in §B.1.2, there are two particular solutions. These were introduced in equation (B.6), and are that from including the divergent Froude number, F_n, and the previously neglected Hilbert transform of the $\chi' = a\mathrm{i}F_0^2 q_0$ divergent solution. The first of these, for which F_n is retained in the $O(\epsilon^n)$ equation results in a modification of equation (B.12a), for which an additional forcing term appears. However, this equation is also unable to be solved explicitly.

The second particular solution, forced by the previously neglected Hilbert transform of the $\chi' \neq 0$ divergence, will be discussed in more detail. We evaluate $\mathscr{H}[\theta_n]$ by substituting for $\theta_n \sim -a\mathrm{i}q_0 q_n$, and using the periodic form of the Hilbert transform. This yields

$$\begin{aligned}\hat{\mathcal{H}}[\theta_n](\phi) &\sim -a\mathrm{i}\fint_{-1/2}^{1/2} \cot[\pi(\phi' - \phi)] q_0(\phi') q_n(\phi')\,\mathrm{d}\phi', \\ &\sim -a\mathrm{i}\Gamma(n+\gamma)\fint_{-1/2}^{1/2} \cot[\pi(\phi'-\phi)] q_0(\phi') Q(\phi') \mathrm{e}^{-(n+\gamma)\log[\chi(\phi')]}\,\mathrm{d}\phi'.\end{aligned} \tag{B.13}$$

The integration contour may now be deformed onto the paths of steepest descent. This procedure is performed in detail in the next section for the integral of q_n appearing in the energy equation. Note that this same procedure is only applicable to (B.13) when the pole, $\phi = \phi'$, lies away from the endpoints of the deformed path of integration.

B.1.4 *Evaluation of $\mathfrak{q}_n^{(naive)}$ in the energy integral*

We write this integral (considering only one component of $\mathfrak{q}_n^{(\mathrm{naive})} = q_n|_{a=1} + q_n|_{a=-1}$) in canonical steepest decent form as

$$\Gamma(n+\gamma) \int_{-1/2}^{1/2} J(\phi)\mathrm{e}^{n\rho(\phi)}\mathrm{d}\phi, \tag{B.14}$$

where

$$J(\phi) = \frac{Q_a(\phi)}{\chi_a^{\gamma}(\phi)} \quad \text{and} \quad \rho(\phi) = -\log\left(\chi_a(\phi)\right). \tag{B.15}$$

Recall that here, Q_a is the amplitude function and χ_a is the singulant associated with the naive component of the late-term solution. Since $\mathrm{Re}[\rho(\phi)] = -\log|\chi_a(\phi)|$ takes the same value at the endpoints $-1/2$ and $1/2$, there is a constant phase path (along which $\mathrm{Re}[\rho]$ is constant) connecting these points, denoted by C'. For $a = 1$, this is a curve in the lower-half plane, and for $a = -1$, C' is a curve in the upper-half plane. Thus, we may deform the path of integration in (B.14) (originally specified for real ϕ) to imaginary values of f over C', yielding

$$\frac{\Gamma(n+\gamma)}{|\chi_a|^n} \int_{C'} J(f)\mathrm{e}^{in\mathrm{Im}[\rho(f)]}\mathrm{d}f. \tag{B.16}$$

This form may now be studied by the method of stationary phase. As $\mathrm{Im}[\rho]' \neq 0$ along C', the dominant contribution of this integral is from the endpoints. This contribution may be found by integration by parts, giving

$$\frac{\Gamma(n+\gamma)}{|\chi_a(1/2)|^n}\left[\frac{Q_a(f)}{\chi_a(f)^{\gamma}}\frac{\mathrm{e}^{in\mathrm{Im}[\rho(f)]}}{in\mathrm{Im}[\rho(f)]'}\right]_{-1/2}^{1/2} = O\left(\frac{\Gamma(n+\gamma-1)}{|\chi_a(1/2)|^{n+\gamma-1}}\right). \tag{B.17}$$

The particular solutions must be of the same order as $q_n \sim \Gamma(n+\gamma)/\chi^{n+\gamma}$ at $\phi = 1/2$ and $\phi = -1/2$ in order to satisfy the periodicity conditions. Since these particular solutions have a constant value of χ, their integration in the energy expression does not change the order in n. Thus, (B.17) will be subdominant to the evaluation of the particular solutions in the $O(\epsilon^n)$ energy expression.

C GENERALISED SOLITARY WAVES OF AN INTERNAL THREE-LAYER FLOW

In the introduction of chapter 2 we considered a model equation for generalised solitary waves to introduce the exponential asymptotics theory used within this thesis. Generalised solitary waves contain far-field oscillations as $x \to \infty$ or $x \to -\infty$, and these solutions occur in many different problems across fluid dynamics. In some of these areas, *embedded solitary waves* are also found; these solutions have no oscillations in the far field and decay to zero as $x \to \pm\infty$. In this chapter, we study the asymptotic properties of these far-field ripples for the steadily travelling waves in a three-layer fluid model. It is found that these ripples are not exponentially small, but appear in the $O(\epsilon)$ solution, where the small parameter, ϵ, is the distance in the bifurcation diagram from an embedded branch of solutions.

We consider the three-layer Euler flow depicted in figure C.1. These three fluids are assumed to be inviscid, and incompressible, and each has a constant density. Here,

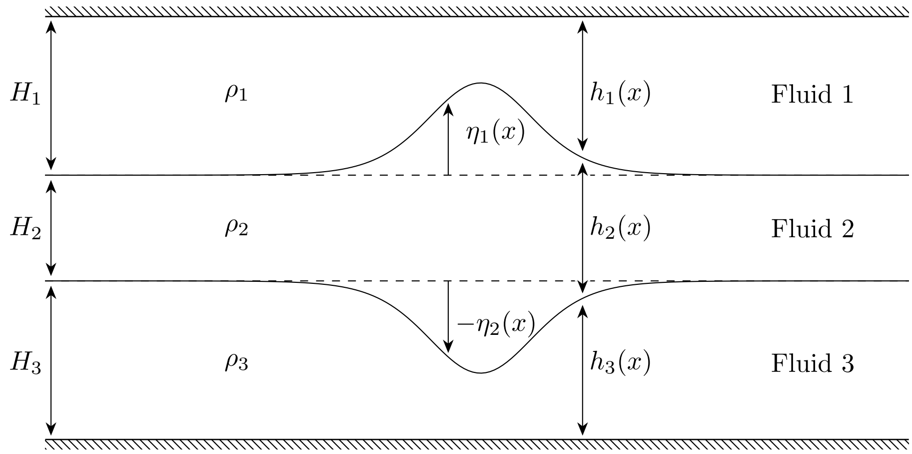

Figure C.1: Our nondimensional three-layer formulation is shown. Each fluid has density ρ_i, and height $h_i(x)$. The interface displacements are denoted by $\eta_1(x)$ and $\eta_2(x)$

these fluids of different densities are confined to lie between a flat bed at $y = 0$ and a rigid lid at $y = 1$. While the horizontal domain of this analytical formulation is $-\infty < x < \infty$, we will numerically consider periodic solutions $-\lambda < x < \lambda$, for which λ is large. To ensure that these travelling solutions are stable, we require that $\rho_3 > \rho_2 > \rho_1$. Since this problem has already been nondimensionalised, we have that the sum of the three constant depths equals unity, $H_1 + H_2 + H_3 = 1$. The interface heights are defined by $\eta_1(x)$ and $\eta_2(x)$, yielding

$$\left.\begin{aligned} h_1(x) &= H_1 - \eta_1(x), \\ h_2(x) &= H_2 + \eta_1(x) - \eta_2(x), \\ h_3(x) &= H_3 + \eta_b(x). \end{aligned}\right\} \tag{C.1}$$

The full Euler equations for this system, considered numerically by Doak et al. (2022) for instance, are difficult to approach analytically. These are a set of coupled integro-differential equations, much like the boundary integral relationship for our single fluid system on infinite depth in chapter 3. Therefore, in this section we consider the 3-layer MCC equations, a generalisation of the Miyata–Choi–Camassa (MCC) equations for two layers by Miyata (1988) and Choi and Camassa (1999b), derived by Barros et al. (2020). These equations preserve nonlinearity and are given by the following two coupled nonlinear differential equations

$$\begin{aligned}2\left(\frac{H_1^2}{h_1}+\frac{H_2^2}{h_2}\right)\eta_1''+\frac{H_2^2}{h_2}\eta_2''+\left(\frac{H_1^2}{h_1^2}-\frac{H_2^2}{h_2^2}\right)\left((\eta_1')^2-3\right)&\\ +2\frac{H_2^2}{h_2^2}\left(\eta_2'\eta_1'+(\eta_2')^2\right)+\frac{6\eta_1}{F_1^2}&=0,\end{aligned} \tag{C.2a}$$

$$\begin{aligned}2\left(\frac{H_2^2}{h_2}+\frac{H_3^2}{h_3}\right)\eta_2''+\frac{H_2^2}{h_2}\eta_1''+\left(\frac{H_2^2}{h_2^2}-\frac{H_3^2}{h_3^2}\right)\left((\eta_2')^2-3\right)&\\ -2\frac{H_2^2}{h_2^2}\left(\eta_1'\eta_2'+(\eta_1')^2\right)+\frac{6\eta_2}{F_2^2}&=0,\end{aligned} \tag{C.2b}$$

for the solutions η_1 and η_2. Here, we have defined the two constants F_1 and F_2 by

$$F_1=\frac{c}{\sqrt{g\Delta_1}} \qquad \text{and} \qquad F_2=\frac{c}{\sqrt{g\Delta_2}}, \tag{C.3}$$

where c is the speed of the travelling waves, and Δ_1 and Δ_2 are the positive density differences defined by $\Delta_1=\rho_2-\rho_1$ and $\Delta_2=\rho_3-\rho_2$.

Since $H_1+H_2+H_3=1$, we treat H_2 as a known constant. System (C.2) therefore is two coupled equations for the unknowns η_1 and η_2, with four unknown constants F_1, F_2, H_1, and H_3. Two of these may be turned into eigenvalues with the imposition of individual amplitude parameters for the two nonlinear interfaces. This parameter space was explored extensively by Doak et al. (2022), who found that whilst most of these parameter values yielded generalised solitary waves (with far-field ripples), for certain values of these constants, embedded solitary waves emerged (with no far field ripples). These embedded solutions were associated with: branches of solutions in a two-dimensional bifurcation diagram; sheets in a 3-dimensional bifurcation diagram; and a three-dimensional space of embedded solutions when all four unknown constants were considered. To simplify our analytical approach, two of these constants will be fixed in the next section.

C.1 The symmetric state for embedded solutions

Under the choice of

$$H_1=H_3 \quad \text{and} \quad \Delta_1=\Delta_2, \tag{C.4}$$

the solutions to the two coupled MCC-3 equations are symmetric about $y=1/2$, yielding $\eta_1(x)=-\eta_2(x)$. Since there is now a streamline at $y=1/2$, this may be considered to be a rigid boundary, and the formulation reduces down to a two-layer model with a single unknown interface. No oscillatory tails appear in the interface of this two-layer formulation, which does not permit generalised solitary waves. Thus, if we break the symmetry of equation (C.4) by a small perturbation, ϵ, we anticipate that oscillatory tails will emerge. The purpose of this section is to study the asymptotic behaviour of these ripples as $\epsilon\to 0$, and we will find their amplitude to be of $O(\epsilon)$ as $\epsilon\to 0$.

C.2 Breaking symmetry with a small perturbation

In breaking the symmetry of section C.1 by defining

$$H_1 = H_3 + \epsilon \quad \text{and} \quad \Delta_1 = \Delta_2, \tag{C.5}$$

we find the constants H_i and depths $h_i(x)$ to be given by

$$\left.\begin{aligned} H_1 &= H_3 + \epsilon, & h_1(x) &= H_3 + \epsilon - \eta_1(x), \\ H_2 &= 1 - 2H_3 - \epsilon, & h_2(x) &= 1 - 2H_3 - \epsilon + \eta_1(x) - \eta_2(x), \\ H_3 &= H_3, & h_3(x) &= H_3 + \eta_2(x). \end{aligned}\right\} \tag{C.6}$$

Thus, the governing equations are given by (C.2) for $\eta_1(x)$ and $\eta_2(x)$, and the unknown constants H_3 and ϵ. We begin in section C.2.1 by solving these equations numerically for specified values of H_3 and ϵ. In section C.2.2, we then consider an asymptotic expansion for these solutions as $\epsilon \to 0$, for which the leading order solution is the $\epsilon = 0$ symmetric state of section C.1. Comparison between these numerical and asymptotic results are performed in section C.2.3.

C.2.1 *Numerical solutions*

We begin by numerically solving equations (C.2), with components H_i and $h_i(x)$ defined in (C.6). In imposing the amplitude condition

$$\mathcal{A} = \int_{-\lambda}^{\lambda} \eta_1(x) \mathrm{d}x, \tag{C.7}$$

we will determine F as an eigenvalue (where since $F_1 = F_2$ due to the choice $\Delta_1 = \Delta_2$, we have relabelled these to F).

The numerical procedure is now detailed for a fixed value of the wave period, 2λ.

(i) First, an initial guess is chosen. This is either a previously computed numerical solution with different values of $\mathcal{A}$, H_3, and ϵ, or the initial guess

$$\eta_1(x) \approx \delta \,\mathrm{sech}\,(x) \quad \text{and} \quad \eta_2(x) \approx -\delta \,\mathrm{sech}\,(x), \tag{C.8}$$

for small δ, where we take $\mathcal{A} = \delta \int_{-\lambda}^{\lambda} \mathrm{sech}\,(x) \mathrm{d}x$.

(ii) Next, we evaluate each component of the coupled equations. In discretising the domain with N points, we have $x_j = \lambda[-1+2(j-1)/N]$, where $1 \leq j \leq N$. Derivatives are then computed spectrally through properties of the Fourier transform, $\eta' = \mathcal{F}^{-1}\left[(\mathrm{i}\pi k/\lambda)\mathcal{F}[\eta]\right]$, where k is the wavenumber. These are evaluated numerically with the fast Fourier transform (FFT) algorithm.

(iii) Lastly, Newton iteration is applied to this system. We have $2N+1$ equations, N from each interface equation, and another from the amplitude condition (C.8). This is closed by $2N+1$ unknowns, N from each of the interfaces, and a final unknown, the eigenvalue F.

An example solution for η_1, with $\lambda = 20$, $H_3 = 0.4$, $\epsilon = 0.005$, and $\mathcal{A} = 0.75$ is shown in figure C.2. It is seen that this yields a generalised solitary wave.

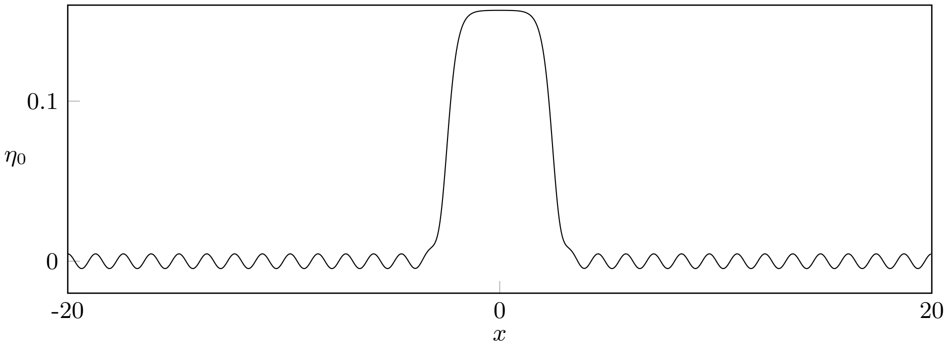

Figure C.2: A numerical solution of the nonlinear equations (C.2) is shown. This profile has an amplitude $\mathcal{A} = 0.75$, half-period $\lambda = 20$, $H_3 = 0.4$, and $\epsilon = 0.005$.

C.2.2 *Asymptotic solutions*

We now consider asymptotic solutions for these generalised solitary waves. In expanding

$$\begin{aligned} \eta_1(x) &= \zeta_0(x) + \epsilon\zeta_1(x) + \cdots , \\ \eta_2(x) &= \vartheta_0(x) + \epsilon\vartheta_1(x) + \cdots , \\ F &= F_0 + \epsilon F_1 + \cdots , \end{aligned} \tag{C.9}$$

we find at leading order the following nonlinear differential equation for $\zeta_0(x)$,

$$\begin{aligned} &\left(\frac{2H_3^2}{(H_3-\zeta_0)} + \frac{(1-2H_3)^2}{(1-2H_3+2\zeta_0)}\right)\zeta_0'' \\ &\quad + \left(\frac{H_3^2}{(H_3-\zeta_0)^2} - \frac{(1-2H_3)^2}{(1-2H_3+2\zeta_0)^2}\right)\left((\zeta_0')^2 - 3\right) + \frac{6\zeta_0}{F^2} = 0, \end{aligned} \tag{C.10a}$$

for which we determine the remaining interface by the condition $\vartheta_0(x) = -\zeta_0(x)$. Note that since $F_1 = F_2$ due to the choice $\Delta_1 = \Delta_2$, we have relabelled this constant to F. Here, H_3 is a free constant, and F will be determined as an eigenvalue through the imposition of the leading order amplitude condition,

$$\mathcal{A} = \int_{-\lambda}^{\lambda} \zeta_0(x)\mathrm{d}x. \tag{C.10b}$$

These equations are solved numerically by Newton iteration analogously to the method detailed in section C.2.1. Example numerical solutions for ζ_0 are shown in figure C.3 for $H_3 = 0.4$, $\mathcal{A} = (0.2, 0.4, 0.6, 0.8, 1)$, and $\lambda = 20$. Note that as the amplitude $\mathcal{A}$ of these solutions increases, the profiles predominantly broaden instead of increase in height.

At $O(\epsilon)$ in system (C.2), we find two coupled equations for the solutions $\eta_1(x)$ and $\zeta_1(x)$. To prevent this thesis from being split into two volumes, these equations are not provided here, and are easiest derived with a symbolic programming language. Assuming that H_3, ζ_0, and ϑ_0 are known from the leading order problem, these coupled $O(\epsilon)$ equations may be solved numerically by Newton iteration, subject to the $O(\epsilon)$ amplitude condition

$$\int_{-\lambda}^{\lambda} \zeta_1(x)\mathrm{d}x = 0. \tag{C.11}$$

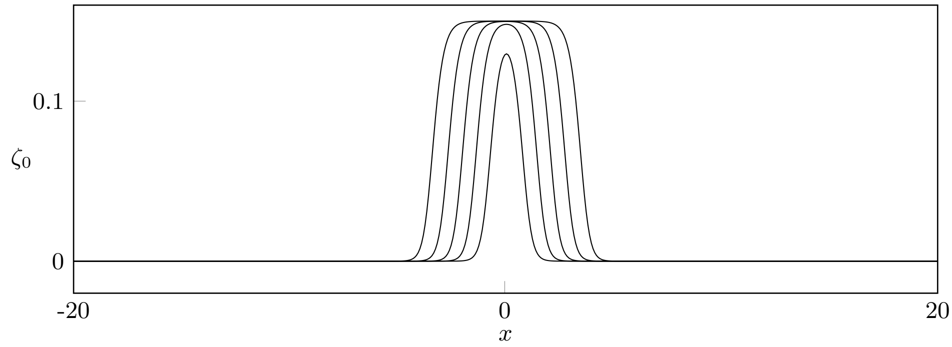

Figure C.3: Solutions of the leading order equation (C.10a) are shown for the five amplitude values of $\mathcal{A} = (0.2, 0.4, 0.6, 0.8, 1)$. We also have $H_3 = 0.4$ and $\lambda = 20$. As the amplitude increases, the central core of the solitary waves widens.

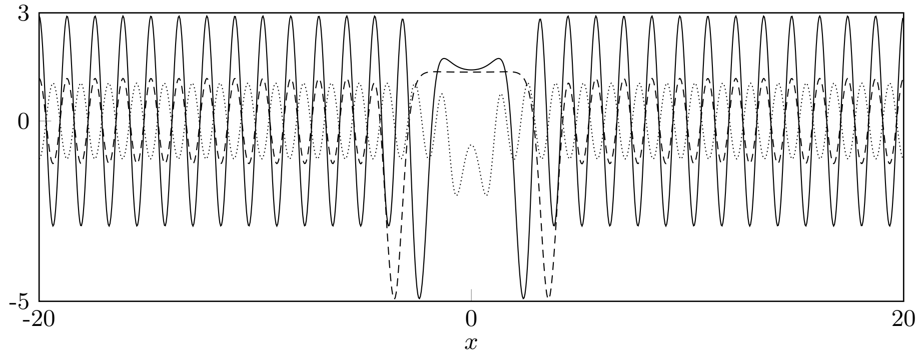

Figure C.4: Three solutions of the $O(\epsilon)$ equations, with $\lambda = 20$ and $H_3 = 0.4$ are shown. The dashed profile has $\mathcal{A} = 1$, the solid profile has $\mathcal{A} = 0.6$, and the dotted profile has $\mathcal{A} = 0.2$.

Three solutions are shown in figure C.4 for the values of $\mathcal{A} = (0.2, 0.6, 1)$ used for the leading order solutions shown in figure C.3.

C.2.3 *Comparison and conclusions*

We now compare the fully nonlinear results of section C.2.1 with the asymptotic solutions from section C.2.2. Both of these are computed numerically. In figure C.5, we compare the asymptotic prediction for the $O(\epsilon)$ solution, ζ_1, with the fully nonlinear prediction η_1. To facilitate comparison, we subtract out the leading order profile, ζ_0, from this fully nonlinear solution, and divide by ϵ. We find that $(\eta_1 - \zeta_0)/\epsilon = O(1)$. Excellent agreement is seen between these for $\mathcal{A} = 1$, and $H_3 = 0.4$. The nonlinear solution used a value of $\epsilon = 0.0001$.

To conclude, embedded solitary waves (with no far-field ripples) are found for certain parameter values of this 3-layer formulation. Changing the values of these parameters can yield generalised solitary waves, with far-field ripples. The amplitude of these ripples is seen to be algebraic with respect to the distance (in the bifurcation space) away from the embedded solution. We demonstrated this for the special case of an embedded solution for which $H_1 = H_3$ and $\Delta_1 = \Delta_2$.

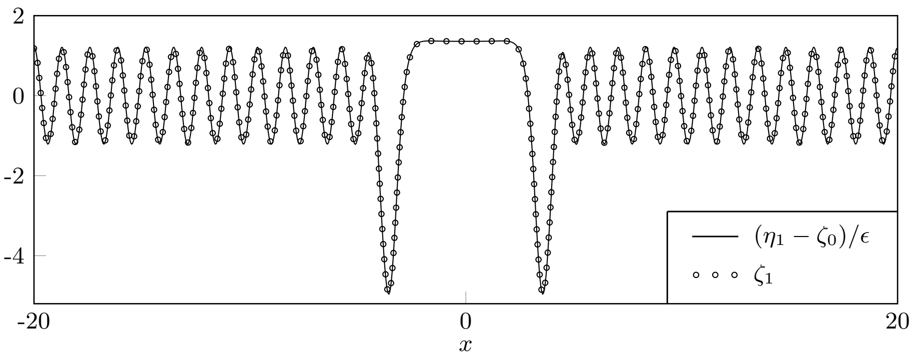

Figure C.5: The asymptotic solution of the $O(\epsilon)$ equations (shown dotted) is compared with the prediction from the fully nonlinear numerical solution (line). Here, $H_3 = 0.4$, $\mathcal{A} = 1$, $\lambda = 20$, and $\epsilon = 0.0001$.